Imaging for scattering properties of the crust : body to surface waves coupling

Andres Camilo Barajas Ramirez

THÈSE

Pour obtenir le grade de

DOCTEUR DE L'UNIVERSITÉ GRENOBLE ALPES

Spécialité : Sciences de la Terre et de l'Univers et de l'Environnement

Arrêté ministériel : 25 mai 2016

Présentée par

Andres BARAJAS

Thèse dirigée par **Michel CAMPILLO**, Professeur
et codirigée par **Ludovic MARGERIN**, DR CNRS, Université Toulouse III - Paul Sabatier

préparée au sein du **Laboratoire Institut des Sciences de la Terre**
dans **l'École Doctorale Sciences de la Terre de l'Environnement et des Planètes**

Imagerie des propriétés de diffraction: le couplage entre ondes de volume et de surface

Imaging for scattering properties of the crust: body to surface waves coupling

Thèse soutenue publiquement le **15 mars 2021**,
devant le jury composé de :

Monsieur Michel CAMPILLO
PROFESSEUR DES UNIVERSITES, UGA, Directeur de thèse
Monsieur Ludovic MARGERIN
DIRECTEUR DE RECHERCHE, CNRS, Co-directeur de thèse
Monsieur Haruo SATO
PROFESSEUR EMERITE, Tohoku University, Rapporteur
Monsieur Christoph SENS-SCHöNFELDER
PROFESSEUR ASSISTANT, German Research Centre for Geosciences GFZ, Potsdam, Rapporteur
Madame Anne PAUL
DIRECTEUR DE RECHERCHE, CNRS, Présidente
Monsieur German PRIETO
PROFESSEUR ASSOCIE, Universidad Nacional de Colombia, Examinateur

Abstract

The analysis of the ambient seismic noise has proven to be a powerful tool to assess velocity changes within Earth's crust using coda-wave interferometry (CWI). CWI is based on the analysis of small waveform changes in the coda of the signals, which can give us information about the structure or dynamic of the internal layers of the earth. The objective of this thesis is to separate and locate at depth the source of these changes. The work here presented is developed in three main stages:

First, we aim to disentangle the processes behind velocity changes detected from a ten-year-long recording of seismic noise made with a single station in the region of Pollino, in the south of Italy. This region is characterized by the presence of aquifers and by a relatively short period of high seismic activity which includes a $M5.0$ earthquake that occurred on the 25th of October 2012. We apply two models that estimate the water level inside the aquifer making a good prediction of the measured apparent $\delta v/v$ which means that the velocity variation is driven by changes in the pore pressure inside the aquifer. A parallel independent confirmation is obtained with geodetic measurements that show a volumetric expansion of the zone that follows the same patterns observed in the models and the velocity variation. The subtraction of these patterns from the measurements reveals a weak elastic response of the crust to the rainfall and unravels the stress drop produced by the seismic event.

Second, we turn to the problem of localizing and imaging the source that generates the changes at depth in the waveform registered at the surface. For this, we use a 3-D wave scalar model that couples naturally body and surface waves. Based on this model we make important deductions of the physical characteristics of the system like a depth-dependent body-to-surface mean free path and a progressive energy transformation from surface to body waves. Using the radiative transfer equations that describe this system we perform a series of Monte-Carlo simulations to estimate the sensitivity kernel. We analyze its most important features and find a good agreement when we compare it with other studies that use full wavefield numerical simulations and independent surface and body wave sensitivities to estimate the sensitivity of the system. We also find that the ratio between the surface wave penetration and the mean free path completely determines the evolution of the system, a feature not seen in previous studies.

Finally, we study the process of locating the sources using the sensitivity kernel and a series of observations: the inversion problem. We design a series of synthetic tests to assess the capacity of the inversion to retrieve a velocity perturbation in different scenarios that involve the depth of the perturbation in the medium, the duration of the coda used in the inversion, and the level of noise in the system. We make a first application of the inversion for the case study in Italy and analyze its most relevant characteristics.

Résumé

L'analyse du bruit sismique ambiant s'est avérée être un puissant outil pour évaluer les changements de vitesse au sein de la croûte terrestre à l'aide de l'interférométrie par onde de coda (CWI). La CWI est basée sur l'analyse des petites variations de forme d'onde dans la coda des signaux, ce qui peut nous donner des informations sur la structure ou la dynamique des couches internes de la terre. L'objectif de cette thèse est de séparer et de localiser en profondeur la source de ces changements. Le travail présenté ici est développé en trois étapes principales :

Premièrement, nous cherchons à dissocier les processus à l'origine des changements de vitesse dans la région de Pollino, dans le sud de l'Italie. Pour cela, nous utilisons un enregistrement de bruit sismique continu d'une durée de dix ans avec une seule station. Cette région est caractérisée par la présence d'aquifères et par une période relativement courte de forte activité sismique, dont un tremblement de terre de $M5$ qui s'est produit le 25 octobre 2012. Nous appliquons deux modèles qui estiment le niveau de l'eau dans l'aquifère permettant une bonne prédiction du $\delta v/v$ apparent mesuré, ce qui signifie que la variation de vitesse est due aux changements de la pression interstitielle à l'intérieur de l'aquifère. Une confirmation parallèle indépendante est obtenue avec des mesures géodésiques qui montrent une expansion volumétrique de la zone qui suit les mêmes patterns que ceux observés dans les modèles et la variation de vitesse. La soustraction de ces modèles de mesures révèle une faible réponse élastique de la croûte aux précipitations et met en évidence la chute de contrainte produite par l'événement sismique.

Ensuite, nous abordons le problème de la localisation et de l'imagerie de la source qui génère les changements en profondeur dans la forme d'onde enregistrée à la surface. Pour cela, nous utilisons un modèle scalaire d'onde 3D qui couple naturellement les ondes de volume et de surface. Sur la base de ce modèle, nous faisons d'importantes déductions sur les caractéristiques physiques du système comme : un libre parcours moyen des ondes de volume avant qu'elles ne se transforment en ondes de surface dépendant de la profondeur ; et une transformation progressive de l'énergie des ondes de surface vers celles de volume. En utilisant les équations de transfert radiatif qui décrivent ce système, nous effectuons une série de simulations de Monte-Carlo pour estimer le noyau de sensibilité. Nous analysons ses caractéristiques les plus significatives et trouvons une bonne concordance lorsque nous le comparons avec d'autres études qui utilisent des simulations numériques du champ d'onde complet et des sensibilités indépendantes des ondes de surface et de volume pour estimer la sensibilité du système. Nous constatons également que le rapport entre la pénétration des ondes de surface et le libre trajet moyen détermine entièrement l'évolution du système, une caractéristique non détectée dans les précédentes études.

Enfin, nous étudions le processus de localisation des sources en utilisant le noyau de sensibilité et une série d'observations : le problème inverse. Nous concevons une série de tests synthétiques pour évaluer la capacité de l'inversion à retrouver une perturbation de vitesse dans différents scénarios qui impliquent la profondeur de la perturbation dans le milieu, la durée de la coda utilisée dans l'inversion et le niveau de bruit dans le système. Nous

faisons une première application de l'inversion pour l'étude de cas en Italie et analysons ses caractéristiques les plus pertinentes.

Acknowledgements

- Thanks to my jury members, Haruo Sato and Christoph Sens-Schönfelder, who attentively read my manuscript, and Anne Paul and German Prieto for their interest in our work.
- Thanks to my two thesis directors, Ludovic Margerin and Michel Campillo, for the opportunity to participate in this exciting project and for all the things they taught me along the way.
- Thanks to the wave team and especially to Léonard Seydoux, Piero Poli, and Qing-Yu Wang for all their support during my Ph.D.
- Thanks to all the wonderful community at Isterre for making my time at Grenoble an unforgettable period of my life.
- Thanks to my parents and family for all their support from the distance.
- Thanks to Estelle for the interesting discussions, for her love, and especially for all the support during the writing of this thesis.

Contents

List of Figures

Chapter 1

Introduction

Understanding the structures and processes in the interior of the earth is one of the main goals of all the different branches of geophysics. In seismology, this problem is approached by analyzing the waveforms that can be recorded at the surface, produced mainly by natural processes that change the distribution of stresses in the crust. One of the most distinctive features of these waveforms is the coda (Aki, 1969) whose formation is associated with the continuous scattering of the seismic field as a result of its interaction with the imperfections and microstructures in the interior of the Earth. Although random in appearance, the fluctuations of amplitude and phase of the coda wave are formed by deterministic interactions and contain a great amount of valuable information about the state and structure of the medium. However, the recording of this type of information is possible only under one condition: the occurrence of seismic events. This limits the eventual analysis of the Earth's interior temporally and geographically to zones that are seismically active.

This limitation partially disappeared when it was recognized that it is possible to retrieve the seismic response (the Green's function) of any region with continuous recordings of ambient seismic noise; this includes both the ballistic (Campillo and Paul, 2003) and the scattered waves (Sens-Schönfelder and Wegler, 2006). Since then, a great number of insightful observations have been made based on the analysis of the ambient seismic noise, especially on how a variety of phenomena like the stress release produced by earthquakes and its posterior recovery (Brenguier et al., 2008a), or all type of meteorological processes like rainfall or variations of the temperature (Wang et al., 2017) affect the velocity of the seismic waves. However, their effects are sometimes complex to analyze because they can act simultaneously making it difficult to distinguish the velocity changes they produce from each other. At the same time, the exact location of the structural changes within the crust that generate the velocity variations is still an interesting open problem that is being approached by different methods. The objective of this thesis goes in both of these directions: the separation and localization at depth of these processes from ambient noise recordings. The work here presented in organized in the following way:

In chapter 2 we present the theoretical context and the main relevant concepts over which this thesis is developed.

In chapter 3 we examine an aquifer system in the south of Italy using seismic, geodetic, and atmospheric data aiming at understanding and separate the seismic processes to those related to the pore pressure in the crust

In chapter 4 we present a scalar model that sustains the formation of surface and body waves, allowing us to deduce a system of radiative transfer equations that couples them in a manner analogous to what happens with the waves that propagate through the earth.

In chapter 5 we developed this model further to estimate the travel-time sensitivity kernel, with the use of Monte Carlo simulations. The main characteristics of the sensitivity of body and surface waves are analyzed

In chapter 6 we focus on the performance and capacity of the travel-time sensitivity kernel to locate velocity perturbations at depth in the inversion problem.

In chapter 7 we summarize the most important finding of this work and present an inversion of the sensitivity kernels to the ambien noise seismic data of chapter 3

Chapter 2

Concepts and methods

2.1 Radiative transfer theory

Seismic recordings evidence the presence of many imperfections in the crust of the earth that continuously scatter the seismic energy. The observed waveforms at the surface can be understood as the superposition of the many scattered seismic fields generated at each of these events. It is reasonable to assume that the phase between all the randomly generated waves cancel with each and therefore, that the energy is the important measurable physical quantity at the receiver (this necessarily implies losing the information about the phases). This is the main assumption of the radiative transfer equation (also called transport theory), which was first introduced from a phenomenological approach in astrophysics to analyze the light coming from stellar objects; here, we will follow this more intuitive approach. The formal connection of the transport theory to wave phenomena is discussed by Margerin (2005) with especial emphasis on seismic wave propagation.

Dainty et al. (1974) had applied a diffusion model to analyze the long coda waves obtained as a result of impacts or seismic events in the moon that is considered a limit case of the multiple scattering transport equation. The radiative transfer equation was first introduced to seismology by Wu (1985) and Wu and Aki (1988) to separate scattering effects from intrinsic attenuation, which allow to model seismograms envelopes. Later, SHANG and GAO (1988) and Sato (1993) presented the solution for isotropic multiple scattering case in a 2-D medium through alternative derivations, and the extension towards a 3-D medium was obtained by Yuehua Zeng, Feng Su, and Aki (1991). Paasschens (1997) presented a solution for an isotropic scattering medium that makes a good predicition of the energy envelope for single and multiple scattering regimes.

A more practical method to estimate the independent contributions of scattering and intrinsic attenuations was developed by Hoshiba (1991), Fehler et al. (1992), and Mayeda et al. (1992) that did not require the estimation of the total energy of the seismogram which can be complicated by the presence of noise. A first application of the radiative transfer equations for surface waves in a spherical earth-like model was developed by Sato and Nohechi (2001) and Maeda, Sato, and Ohtake (2003) for the single scattering case. The elastic case was was first studied for multiple isotropic regime by Yuehua Zeng (1993) and Sato (1994b) which considered mode conversions between P-waves and S-waves. This was extended to non-isotropic cases in 2-D (Sato, 1994a) and in 3-D (Sato, 1995) geometries. Sato, Nakahara, and Ohtake (1997) obtained synthetic seismograms envelopes from a non-isotropic shear dislocation source. This was later applied by Nakahara et al. (1998) in a inversion to estimate the spatial distribution of energy. Radiative transfer equations for the elastic case derived from the wave equation contain also information of the polarization of the shear waves (Weaver, 1990; Ryzhik, Papanicolaou, and Keller, 1996).

Monte Carlo simulations are an ideal framework to analyze and solve the equations formulated by the radiative transfer equations (Bal, Papanicolaou, and Ryzhik, 2000; Lux, 2018).

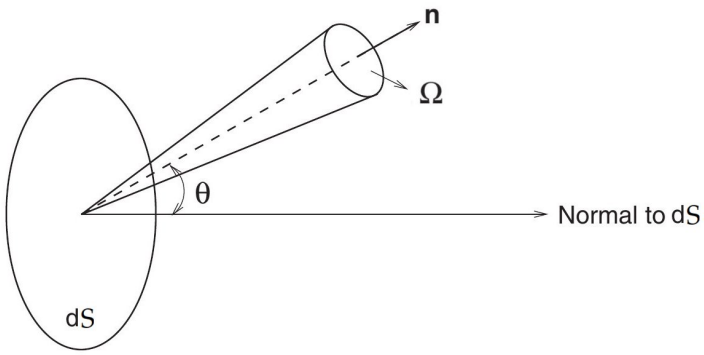

FIGURE 2.1: Definition specific intensity. Modified from Peraiah (2002)

In Monte Carlo simulations, the energy propagation is modeled through a large number of phonons that propagate following a random walk with propagation times statistically controlled by the mean free times. They were first introduced to synthesize seismograms envelopes by Gusev and Abubakirov (1987) and Hoshiba (1991). Margerin, Campillo, and Van Tiggelen (2000) included scattering anisotropy, mode conversions and polarizations and reproduced the known equipartition levels between elastic waves. Przybilla and Korn (2008) confirmed the applicability of the use of Monte Carlo simulations comparing envelopes generated by the technique, with envelopes obtained with finite differences methods of a 3-D elastic medium. Imaging the earth structures have an important applications of the Monte Carlo simulation of transport equations (Margerin, 2003; Mancinelli, Shearer, and Liu, 2016; Sens–Schönfelder, Margerin, and Campillo, 2009; Sanborn and Cormier, 2018).

2.1.1 Radiative transfer equation

The basic entity in transport theory is the specific intensity, defined as

$$I(t, \mathbf{r}, \mathbf{n}) = \frac{dE}{|\mathbf{n} \cdot d\mathbf{S}| d\Omega(\mathbf{n}) d\omega dt} \tag{2.1}$$

that is, the radiated energy dE through a small area $d\mathbf{S}$ into a solid angle $d\Omega$, in a small frequency band $(\omega, \omega + d\omega)$, in small period of time dt, with a direction $\mathbf{n}$ at position $\mathbf{r}$. The dependency of the intensity on the frequency was omitted for simplicity. The dot product accounts for the effective flow through the area dS. This is illustrated in figure 2.1.

In terms of the specific intensity, we can define the local energy current

$$\mathbf{J}(t, \mathbf{r}) = \int_{4\pi} I(t, \mathbf{r}, \mathbf{n}) \mathbf{n} d\Omega(\mathbf{n}) \tag{2.2}$$

and the local energy density

$$\rho(t, \mathbf{r}) = \int_{4\pi} \frac{1}{v(\omega, \mathbf{r})} I(t, \mathbf{r}, \mathbf{n}) d\Omega(\mathbf{n}) \tag{2.3}$$

where v is the group velocity (Ishimaru, 1978; Margerin and Nolet, 2003). Two possible mechanisms that decrease the specific intensity are absorption and scattering. In the first one, the medium absorbs a part of the energy through its interaction with the wave, decreasing the total energy propagating in the medium. In the second one, the energy is scattered into the medium itself, meaning that a part of the incoming intensity is not necessarily lost but projected into other directions. From a macroscopic point of view, the first one produces an

overall decrease of the amplitude on the waveform registered at some point, while the second one has as consequence the elongation of the coda wave. However, in practice, both produce similar decays of the incoming intensity

$$\delta I = -\frac{\delta t}{\tau} I \tag{2.4}$$

where τ is called the mean free time and δt is the time of propagation of the energy through the medium. The solution of this equation, $I = e^{-t/\tau}$, shows that the intensity decay is controlled by the mean free time which quantifies the scattering process. To each process can be associated a mean free time. We could define another associated quantity, the mean free path as $l = v\tau$, related directly with the scattering cross section (Chapman, Cowling, and Burnett, 1990)

In the following, we will assume that there is no absorption so the mean free time makes reference to the scattering process and the overall energy in the system is conserved. This loss of intensity through this process in one direction of propagation, implies necessarily the gain of intensity in another. Therefore the gain in the intensity is the sum of the contributions of all the incoming beams into the volume that may be scattered into the direction of interest $\mathbf{n}$

$$\delta I = \frac{\delta t}{\tau} \int_{4\pi} p\left(\mathbf{n}, \mathbf{n}'\right) I\left(t, \mathbf{r}, \mathbf{n}'\right) d\Omega\left(\mathbf{n}'\right) \tag{2.5}$$

where $p\left(\mathbf{n}, \mathbf{n}'\right)$ represents the probability that a beam traveling in direction $\mathbf{n}'$ is scattered and contributes to the intensity in direction $\mathbf{n}$. The prefactor $\delta t/\tau$ accounts for the decay of the intensity in direction $\mathbf{n}'$ in the same way as shown in equation 2.4. Therefore, the total change in the intensity is

$$\begin{aligned} \frac{dI(t, \mathbf{r}, \mathbf{n})}{dt} &= \left(\frac{\partial}{\partial t} + v\mathbf{n} \cdot \nabla\right) I(t, \mathbf{r}, \mathbf{n}) \\ &= -\frac{I(t, \mathbf{r}, \mathbf{n}')}{\tau} + \frac{1}{\tau} \int_{4\pi} p\left(\mathbf{n}, \mathbf{n}'\right) I\left(t, \mathbf{r}, \mathbf{n}'\right) d\Omega\left(\mathbf{n}'\right) + S(t, \mathbf{r}, \mathbf{n}) \end{aligned} \tag{2.6}$$

where a source term $S(t, \mathbf{r}, \mathbf{n})$ was added. This is the radiative transfer equation. A schematic explanation of the gains and losses of intensity by scattering can be seen in figure 2.2

2.1.2 Diffusion approximation

One very interesting case to analyze is the diffusion approximation. This regime sets in after a large number of scatterings events have occurred in the system, rendering the overall system equipartitioned. We begin expressing the intensity as the first terms of a moment expansion

$$I(t, \mathbf{r}, \mathbf{n}) = \frac{\rho(t, \mathbf{r})v}{4\pi} + \frac{3}{4\pi} \mathbf{J}(t, \mathbf{r}) \cdot \hat{\mathbf{n}} \tag{2.7}$$

In this approximation the angular distribution of the intensity is almost constant, will a small flux of intensity (Ishimaru, 1978). This approximation also implies that the first term in the right hand of equation 2.7 is bigger than the second one, signalling a slower transmission of energy in the system in comparison with the first stages of the system (Khan and Jiang, 2003). Replacing 2.7 into the radiative transfer equation 2.6, and integrating over the whole solid angle, leads to

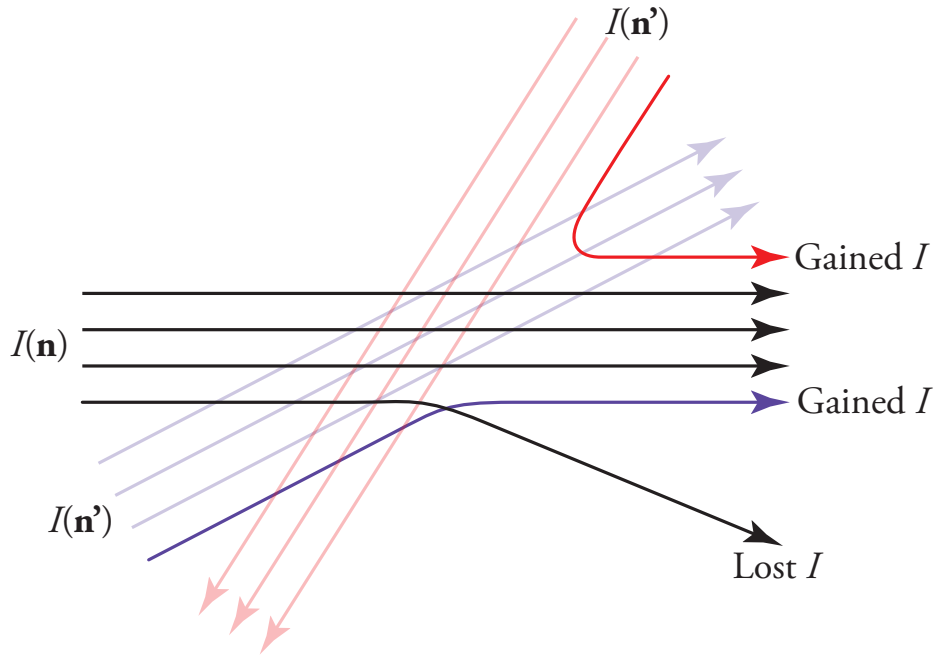

FIGURE 2.2: Schematic view of the gains and losses of intensity by scattering. The black lines represents the incoming specific intensity $I(n)$, and the red and purple lines represent specific intensities that end up contributing to $I(n)$. In this particular case the total intensity increases.

$$\frac{v}{3}\nabla\rho(t,\mathbf{r}) + \frac{1}{v}\frac{\partial \mathbf{J}(t,\mathbf{r})}{\partial t} = -\frac{\mathbf{J}(t,\mathbf{r})}{l}\left(1 - \frac{1}{4\pi}\int_{4\pi} p(\mathbf{n}\cdot\mathbf{n}')\mathbf{n}\cdot\mathbf{n}'\, d\Omega\left(\mathbf{n}'\right)\right) \tag{2.8}$$

The last term in parenthesis accounts for the possible scattering anisotropy of the system between the incoming $\mathbf{n}$ and scattered $\mathbf{n}'$ directions of the intensity. Notice, however, how this term depends in their relative directions only and not in the absolute direction of propagation of the intensity which indicates the isotropy of the medium. Since $\mathbf{n}\cdot\mathbf{n}' = \cos\theta$ where θ is the angle between the two directions, the right hand side term in the parenthesis in equation 2.8 can be interpreted as the weighted average -$\langle\cos\theta\rangle$- of the cosine of the scattering angle over the whole solid angle. Assuming that $\partial\mathbf{J}/\partial t = 0$ we arrive to the first Fick's law of diffusion (Bergman et al., 2011)

$$\mathbf{J}(t,\mathbf{r}) = -D\nabla\rho(t,\mathbf{r}) \tag{2.9}$$

where D is the diffusivity, that on this particular case is $D = vl^\star/3$ where

$$l^\star = \frac{l}{1 - \langle\cos\theta\rangle} \tag{2.10}$$

is called the transport mean free path. This means that the velocity of the diffusion process is controlled by the scattering anisotropy, tending to be higher for bigger values of $l^\star$. In the particular case where the scattering is isotropic $l^\star = l$ and we get the lowest possible value of D. When there is scattering anisotropy, the beam of energy tends to conserve the direction of propagation for a longer distance that the mean free path; in this sense, the transport mean free path can be interpreted as the distance over which the energy lost all information about its original direction.

2.2 Equipartition of the energy

One common feature to all scattering systems is that they eventually reach to a diffusive state in which each normal mode is excited equally, independently of the initial conditions of the field. The amount of energy is proportional to the number of modes that can be sustained in the medium (Hill, 1986; Morse and Bolt, 1944), or in other words, to the density of states; for example, in an elastic medium there can be two transversal modes of propagation (s-waves), and one longitudinal (p-wave). Then, the energy partition between the two types of waves is (Weaver, 1982)

$$R = \frac{E_s}{E_p} = 2\frac{c_\alpha^3}{c_\beta^3} \tag{2.11}$$

where c_α and c_β are the velocities of P-waves and S-waves respectively. The density of states can also be calculated in another way: the Green's function of a linear operator L can be defined as

$$[z - L(\boldsymbol{r})]G\left(\boldsymbol{r}, \boldsymbol{r}'\right) = \delta\left(\boldsymbol{r} - \boldsymbol{r}'\right) \tag{2.12}$$

where z is a complex variable, and L represents the wave equation operator. L has a set of eigenfunctions u_n and eigenvalues λ_n that per definition obey the following relation

$$L(\boldsymbol{r})u_n(\boldsymbol{r}) = \lambda_n u_n(\boldsymbol{r}) \tag{2.13}$$

Each eigenfunction represents the a normal mode in the system. It can be shown that the spectral representation of the Green's function is an analytic function except for the points where $z = \lambda_n$, which means that it diverges at the resonant modes of the system (Economou, 2006). This important property can be used to isolate and count the normal modes of the system with the Green's function. As an example, the density of states ρ for the Helmholtz equation can be expressed as (Sheng and Tiggelen, 2007)

$$\rho(\omega, \mathbf{r}) = -\frac{\mathrm{d}k^2(\omega)}{\mathrm{d}\omega}\frac{1}{\pi}\operatorname{Im} G\left(\omega, \mathbf{r} = \mathbf{r}'\right) \tag{2.14}$$

where ω represents the frequency, and k the wavenumber.

The equipartition of the energy was observed by Shapiro et al. (2000) and later by Hennino et al. (2001) who made a series of observations theoretical estimations of equipartition ratios in different combinations of seismic waves. Margerin, Campillo, and Van Tiggelen (2000) studied numerically the equipartition time in inhomogeneous elastic media using Monte Carlo simulations that included mode conversions and polarization.

2.3 Coda wave interferometry

The seismic wavefronts propagating through the earth get distorted by the interaction with heterogeneities that scatter a fraction of their energy in different directions. This process produces the characteristic coda wave segments after the main arrivals in the seismograms (Aki, 1969). Although complicated to analyze, the coda wave is not random and can be understood as the superposition of all the possible wave fronts that propagated through many different paths when going from the source to the receiver (Sato and Fehler, 2012). This implies that a complex seismogram generated by a seismic event can be reproduced if, by some mean, we repeat the same seismic source at the same position; this has been observed with two or more earthquakes that occur in the same location with very similar magnitudes (Geller

and Mueller, 1980; Poupinet, Ellsworth, and Frechet, 1984; Beroza, Cole, and Ellsworth, 1995). However, although very similar, the received waveforms at the surface are not exactly equal: small variations are produced as a consequence of small changes of the properties of the medium that happen in the period of time between the two seismic events. This is the main principle behind some studies that use these alike earthquakes, called doublets, to track the changes in the velocity (Poupinet, Ellsworth, and Frechet, 1984; Ratdomopurbo and Poupinet, 1995) or in the attenuation (Beroza, Cole, and Ellsworth, 1995) of the crust. We also refer the reader to Sato (1988) for a review of temporal variations of attenuation detected with coda waves. Coda wave interferometry (CWI) is the use of the coda of a waveform to detect an locate all these changes in the medium.

CWI has been applied in experiments to monitor changes of ultrasound waves propagating through granite, (Snieder et al., 2002; Grêt, Snieder, and Scales, 2006), in a volcano using its natural mild repeating explosions(Grêt et al., 2005), in concrete induced by thermal variations (Larose et al., 2006), in the crust as a consequence of earthquakes (Nishimura et al., 2000; Peng and Ben-Zion, 2006), and associated to structural changes preceding eruptions (Ratdomopurbo and Poupinet, 1995; Wegler et al., 2006).

From the assumption of superposition of the field, the travel-time perturbation $\langle\tau\rangle$ produced by a small perturbation of the propagation velocity between a source and a receiver, can be understood as the average of the travel time perturbations τ_P generated between all the possible trajectories P (Pacheco and Snieder, 2005; Snieder, 2006)

$$\delta t = \langle\tau\rangle = \frac{\sum_P I_P \tau_P}{\sum_P I_P} \tag{2.15}$$

where I_P represents the energy intensity of the wave that has propagated along path P. This result is very interesting as it establishes a relationship between the eventual phase perturbations of the coda waves and the energies arriving to a certain point which are the main physical quantity of the radiative transfer theory that assumes that the phases cancel each other at the receiver. This is fundamental in the conceptual development of the sensitivity kernels.

With coda wave interferometry it is possible to relate different type of perturbations to measurements made in the coda. These perturbations can be of different nature: velocity fluctuations, random displacements of punctual scatterers and perturbations in the position of the source (Snieder et al., 2002; Snieder, 2006); here we focus on the first one. A typical phase change in the waveform recorded at the surface, generated by a change in the velocity of a medium can be seen in figure 2.3. The difference between the waveforms obtained with and without the velocity change increases proportionally to the time that the wave has spent traveling in the medium. In this case, the relationship between the velocity variation and the phase delay at different lapse times is $-\delta t/t = \delta v/v$. The quantity $-\delta t/t$ is called the apparent velocity variation, also denoted ε by some authors. The term *apparent* is added because when the velocity is changed in only one part of the medium, there is still a change in the phases at the surface, but the quantity $-\delta t/t$ is not necessarily equal to the velocity pertubation $\delta v/v$ in the medium anymore.

2.3.1 MCSW method

In monitoring, a linear relation between the phase delay and the velocity change in the medium is assumed; therefore, the apparent velocity variation is obtained as the slope of the phase delay δt for different lapse times t. One of the main methods to estimate this slope is the Moving Cross Spectral Window (MCSW) also known as the doublets method, as it was first proposed and used to analyze the phase differences between the coda generated by doublets

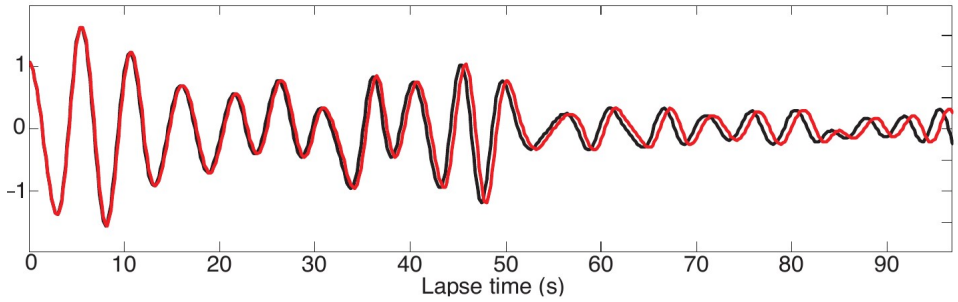

FIGURE 2.3: Effect of the variation of velocity over a seismogram. The red line represents the obtained waveform after a decrease in the velocity of the whole medium in 1% with respect to an unperturbed medium represented by the black line. Taken from Froment (2011)

earthquakes by Poupinet, Ellsworth, and Frechet (1984). The MCSW method is based on a well know property of the Fourier transform: let $u(t)$ represent a signal and $U(\omega) = \mathcal{F}[u(t)]$ its Fourier transform. Then the Fourier transform of temporal shifted version of this signal $u(t \pm \delta t)$ is (Pinsky, 2008)

$$\mathcal{F}[u(t \pm \delta t)] = U(\omega) e^{\pm i\omega\delta t} \tag{2.16}$$

Notice how this temporal shift affects different frequencies at different degrees; a comparison between the Fourier transform of the original and the shifted signals would show a linear relationship between their phase differences and the frequency. In this way, the δt can be estimated for a small section of the coda of the two signals. Since this delay is different for different lapse times, this procedure is repeated over a window that is systematically moved along the coda. This procedure is schematized in figure 2.4. In the end, a linear regression is performed between the obtained values of δt and their respective lapse times to obtained the apparent velocity estimation.

2.4 Seismic interferometry

The link between recordings of correlations of noise and the properties of the medium can be traced back to early works done in helioseismology (Duvall et al., 1993; Giles et al., 1997). Later, a formal connection of these cross-correlations with the retrieval of the Green's function of the medium was established (Weaver and Lobkis, 2004; Lobkis and Weaver, 2001; Wapenaar, 2004). The Green's function represents the response that one part of the system (in this case, the displacements on the surface) would have as a consequence of an impulsive unit source in the medium. This relationship permits the use of tools of analysis in seismology that pass from monitoring to imaging, to regions where there is no presence of active sources. The reconstruction of the Green's function using ambient seismic noise is called Seismic Interferometry (SI).

Let $u(t, \mathbf{x}_1)$ and $u(t, \mathbf{x}_2)$ denote time dependent displacements recordings of noise seismic field at two points over the surface. Then the noise cross correlation over a time interval $[0, T]$ can be written as

$$C_T(\tau, \mathbf{x}_1, \mathbf{x}_2) = \frac{1}{T} \int_0^T u(t, \mathbf{x}_1)\, u(t + \tau, \mathbf{x}_2)\, dt \tag{2.17}$$

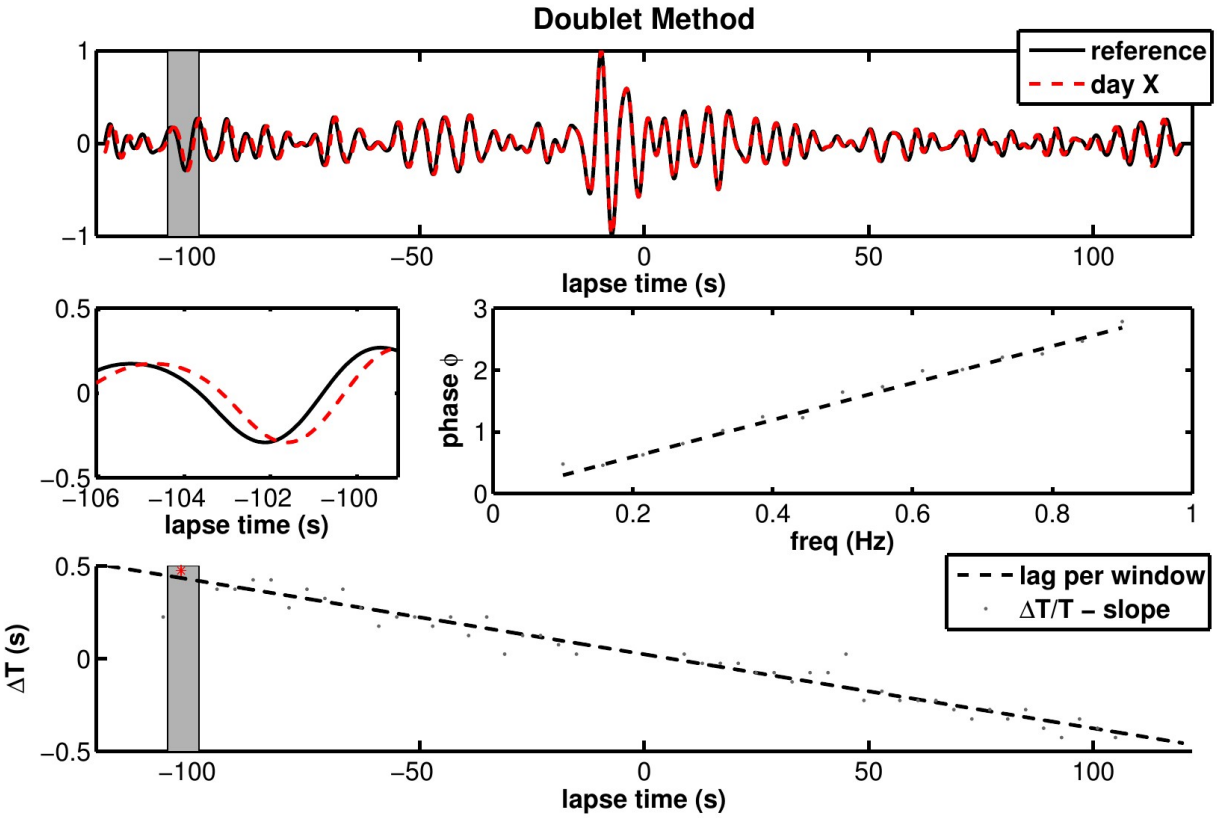

FIGURE 2.4: Moving Cross Spectral Method. Top: a reference signal (black), the signal registered with a velocity perturbation (red), and the window to be analyzed (zone in gray). Middle left: zoom of the differences between the coda segments highligthed section in gray in the top. Middle right: linear relation between the phase and the frequency as product of the time shift between. Bottom: δt measured at different lapse times. Taken from Hadziioannou (2011)

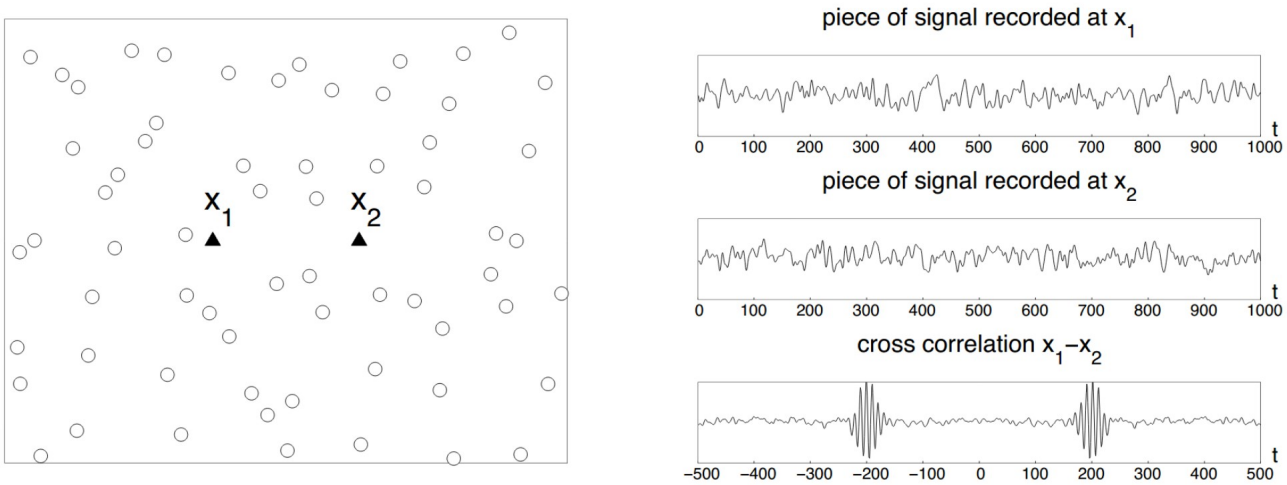

FIGURE 2.5: Cross correlation of recordings at two stations (triangles) from a seismic noise field generated by a random distribution of sources (circles). Taken from Garnier and Papanicolaou (2009)

where τ represents the time lag between the two signals. In a diffusive, equipartitioned field it can be shown that (Snieder, 2004; Roux et al., 2005a)

$$\frac{\partial}{\partial \tau} C_T(\tau, \mathbf{x}_1, \mathbf{x}_2) = G(\tau, \mathbf{x}_1, \mathbf{x}_2) - G(-\tau, \mathbf{x}_1, \mathbf{x}_2) \tag{2.18}$$

as long as T is sufficiently large. The positive and negative parts of the Green's function are related to the causal and anti-causal parts of the cross-correlation, shown in figure 2.5. Each of them represents two possible waves traveling in opposite directions from one station to another. The equipartitioning of the seismic field can be generated with a good distribution of seismic sources, or as a consequence of the scattering produced by heterogeneities in the earth. Several factors can affect the formation of a diffusive field like strong attenuation, an asymmetric distribution of noise sources or a limited observation time window of the coda (Paul et al., 2005; Stehly et al., 2008). in practice, the Green's function is recovered through the average of many correlations obtained with a dense seismic network or over several days. Maybe the most visible feature of the cross-correlations of ambient seismic noise is the reconstruction of the travel times between several stations as is shown in the image 2.6. It has been shown, nonetheless, that even in situations where the Green's function is not perfectly reconstructed, it is still possible to track changes in the medium using the cross-correlation (Hadziioannou et al., 2009).

2.4.1 Passive image interferometry

Sens-Schönfelder and Wegler (2006) showed that not only the ballistic surface waves and P-waves can be retrieved from correlations of continuous recordings of ambient seismic noise (Roux et al., 2005b) but also the scattered waves that form the coda. Coda Wave Interferometry applied to the Green's function coda recovered by ambient seismic noise methods is called Passive Image Interferometry (PSI).

PSI has been used to measure the variation of the seismic field velocity caused by a variety of phenomena like earthquakes (Wegler and Sens-Schönfelder, 2007; Brenguier et al., 2008a; Wegler et al., 2009; Nakata and Snieder, 2011), volcanic activity (Rivet, Brenguier, and Cappa, 2015; Brenguier et al., 2008b), the thermoelastic response of the soil (Meier, Shapiro, and

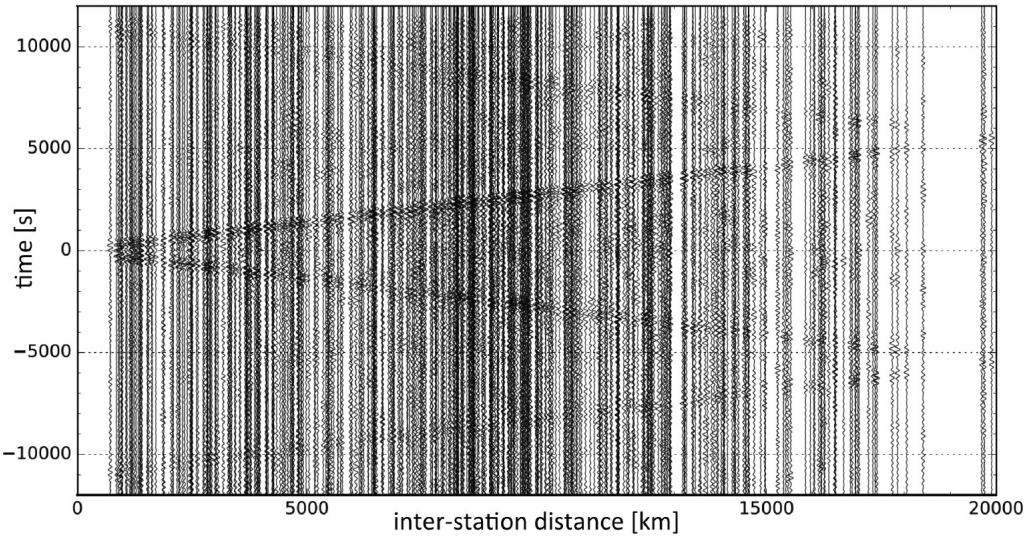

FIGURE 2.6: Cross correlations from stations around the globe. The late arrivals (after and before $\sim \pm 5000s$) correspond to surface waves that have traveled between the two stations making a turn around the earth. Taken from Nakata, Gualtieri, and Fichtner (2019)

Brenguier, 2010), clay landslide (Mainsant et al., 2012), pressurized water injection (Hillers et al., 2015), internal erosion in earthen dams (Planès et al., 2016), the earth tides produced by the sun and the moon (Sens-Schönfelder and Eulenfeld, 2019), temperature variations due to periodic heating of the lunar surface by the sun (Sens-Schönfelder and Larose, 2008), and variations in the loading and pore pressure perturbations over and below the glacial cover (Mordret et al., 2016). Analysis of the ambient noise can also be used to predict earthquake ground motion (Prieto and Beroza, 2008) and study the seismic response of civil structures (Prieto et al., 2010; Nakata et al., 2013).

Many studies focus on the hydrological effects on the $\delta v/v$: Sens-Schönfelder and Wegler (2006) estimated the underground water level using a model developed by Akasaka and Nakanishi (2000), to make a direct relation with the measured velocity variations in a volcano. Meier, Shapiro, and Brenguier (2010) analyze velocity variations within the Los Angeles basin and conclude that the seasonal variations are strongly influenced by groundwater level changes and thermo-elastic strain variations. Tsai (2011) proposed periodic models to recreate displacements and velocity changes from thermo-elastic stresses or hydrological loadings. Wang et al. (2017) found a direct relation between velocity variations and several hydrological and meteorological processes across Japan, mainly based on the pore pressure generated by the rainfall water through a diffusion process. Hillers, Campillo, and Ma (2014) also show the correlation between velocity changes and periodicity of precipitation events in Taiwan.

2.5 Sensitivity kernels

2.5.1 Observation and motivation

The phase fluctuations generated in the surface as a consequence of the presence of a bulk velocity perturbation do not necessarily have a linear relationship with the lapse time; their relationship depends on the position and size of the perturbation. The behavior of the apparent velocity variation $\delta t/t$ for two opposite cases is shown in figure 2.7. These results are obtained in a 2-D elastic medium with both the source and the receivers located at the

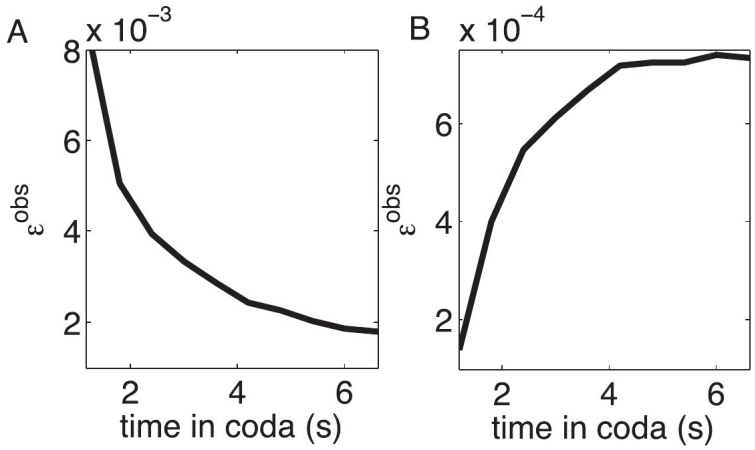

FIGURE 2.7: Apparent velocity variation for a perturbation made in a layer at $20m$ (left) and at $1.5km$ (right) from the surface in an elastic 2-D heterogeneous medium. Taken from Obermann et al. (2013a)

surface. Both are examples of the apparent velocity perturbations measured on the surface when the velocity of a whole layer in a medium is slightly modified. At the left the $\delta t/t$ measurements are obtained when the layer is located close to the surface, and at the right when the perturbation is deeper in the medium. In the first one, the apparent velocity variation at early times is high as the perturbed layer is quickly sampled by most of the energy emitted by the source; however, it quickly decreases as the seismic field expands into deeper regions, making the perturbation relatively smaller in comparison with the total explored area. In the second case, the perturbation is only detected by the front of the propagating energy at the beginning and is later sampled progressively more with the ongoing expansion of the wave field. Notice that the magnitudes also change dramatically: in the latter case, δt is one order of magnitude smaller than in the former case. This simple example shows that the difference of behavior of the apparent velocity variation opens the possibility of estimating the shape and location of the perturbation with the measurements made on the surface: this is the main objective of developing the travel-time sensitivity kernels.

The travel-time sensitivity kernel was first introduced by Pacheco and Snieder (2005) for the diffusive regime, and by Pacheco and Snieder (2006) for the single scattering regime. These sensitivity kernels relate a travel-time perturbation measured between a source and a receiver with all the possible velocity perturbations in the medium around them. For the first one, an analytical expression was obtained for the autocorrelation configuration (coincident source and receiver) for two and three dimensions and was compared against numerical simulations where a small perturbation is introduced. The travel-time sensitivity kernel for the single scattering regime was calculated following the approach of Sato (1977) to obtain the energy density of scattered waves assuming single isotropic. Later Planès et al. (2014) introduced the decorrelation sensitivity kernel that related a perturbation in the medium that alters the paths going from the source to the receiver, with the distortion that it generates to the waveform at the receiver. Later Margerin et al. (2016) made an alternative derivation of this kernel and extended the travel-time sensitivity kernel to include the direction of the energy propagation with the use of the specific intensity. In this work was proposed the idea that the difference between the travel-time and the decorrelation sensitivities depended on whether the perturbation had an active or passive role over the generation of new propagation paths between the source and the receiver. Applications like localizing perturbations in numerical

simulations have been done using the sensitivity kernel. The decorrelation sensitivity kernel was successfully used in locating millimetric holes drilled in a concrete sample (Larose et al., 2010). The sensitivity kernels can be expressed as convolutions of intensity which makes the radiative transfer theory a natural tool for their estimation; Lesage, Reyes-Dávila, and Arámbula-Mendoza (2014), for example, makes use of a solution of the transport equations for 2-D to locate changes produced by volcanic activity. On the other hand, Obermann et al. (2016) makes use of the 3-D radiative transfer solution proposed by Paasschens (1997) to estimate the body wave sensitivity kernel.

The coupling between body and surface waves has remained one challenging factor to the development of the sensitivity kernels in a 3-D halfspace that is the usual setting for most seismic applications. Obermann et al. (2013a) and Obermann et al. (2016) approached this problem by expressing the sensitivity as a linear combination of two independent sensitivities, one for surface and another for body waves, with a controlling factor mediating between them that changes with time, and that is estimated by comparisons with full wavefield numerical simulations. These studies show the predominance of surface waves at early lapse times and of body waves at late lapse times. However, Wu et al. (2016) measured velocity variations from the phase of the Rayleigh waves obtained by seismic interferometry, and observed a progressive decrease of the velocity drop produced by the 2004 Parkfield earthquake (Brenguier et al., 2008a) at lower frequencies. Since the surface waves penetration increases at lower frequencies, they conclude that the velocity variation is mostly constrained in the surface. Furthermore, they concluded that the observations can be explained only by the surface wave dispersion as body wave sensitivity would produce both velocities decreases and increases at different points; this last affirmation was supported by travel-time sensitivity kernels that show that in a spherical geometry, direct shear waves may have alternating early or late arrivals depending on the position on the surface of the receiver (Stein and Wysession, 2009; Zhao, Jordan, and Chapman, 2000). Similar findings were reported by Nakata and Snieder (2011) that found that the magnitude (M_W) 9.0 Tohoku-Oki earthquake produced a shear wave velocity reduction limited to the first $100m$ of the crust, despite being extended to an area $1200km$ wide by comparing arrival times between stations located at the surface and in a borehole in ranges of $100m$ to $337m$ depth. This, however, contradicts Wang et al. (2019) that through an inversion made with seismic and long-period tiltmeters data, found that the same earthquake produced changes that reach $40km$ depth in the crust.

2.5.2 Basic theory of traveltime sensitivity kernels

We begin with a concise derivation of the travel-time sensitivity kernel for a diffusive medium following its intensity interpretation (Pacheco and Snieder, 2005), and later make a connection with the more general version based on the specific intensities (Margerin et al., 2016). Let us imagine a normalized intensity impulse generated at a source, that propagates through a medium. The intensity at lapse time t at a point $\mathbf{r}$ is then described by $P(\mathbf{r}, t)$. If there is no mechanism of intrinsic attenuation acting on the system, the total energy at time t

$$W(V, t) = \int_V P(\mathbf{r}, t) dV(\mathbf{r}) \tag{2.19}$$

is always equal to 1, that is, the total energy emitted by the source. The normalization of the intensity allows us to make two additional interpretations of this quantity: $P(\mathbf{r}, t)$ represents the probability that a particle, following a random walk, arrives or passes by the position $\mathbf{r}$ at time t (Roepstorff, 2012). $P(\mathbf{r}, t)$ can also be understood as the Green's function of the diffusion equation at position $\mathbf{r}$ at time t. The probability that a particle that was

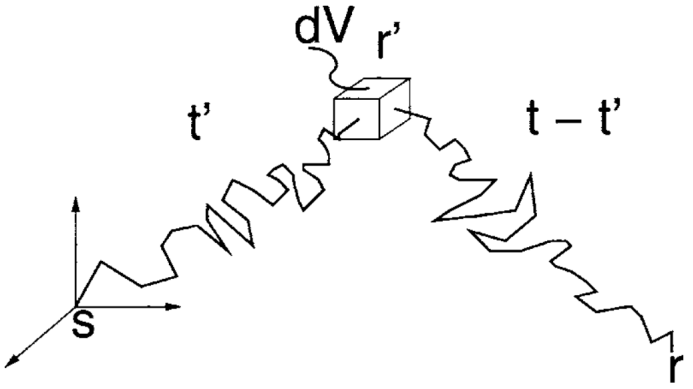

FIGURE 2.8: Random walk of a going from the source, passing through a small volume dV and arriving to the receiver. Taken from Pacheco and Snieder (2005)

emitted at the source at $\mathbf{s}$ arrives to the receiver at $\mathbf{r}$ at time t, can be written in terms of the transit of the phonon through a volume dV located at $\mathbf{r}'$ at time t' (illustrated in figure 2.8).

$$P\left(\mathbf{r},\mathbf{s},t+t'\right)=\int_V P\left(\mathbf{r},\mathbf{r}',t-t'\right)P\left(\mathbf{r}',\mathbf{s},t'\right)dV\left(\mathbf{r}'\right) \tag{2.20}$$

This is the Chapman-Kolmogorov equation (Ross, 2014; Papoulis and Pillai, 2002; Roepstorff, 2012) which states that the probability of going from the source to the receiver can be written by using the intermediate point $\mathbf{r}'$ at a time t', as long as all of them are taken into account. Each of the terms involved in the last equation are transition probabilities; for example

$$P\left(\mathbf{r}',\mathbf{s},t'\right)=P\left(\mathbf{r}',t'|\mathbf{s},t=0\right) \tag{2.21}$$

is the probability that particle transits the position $\mathbf{r}'$ at time t', under the condition that it was emitted from the source at position $\mathbf{s}$ and at time $t=0$. An integration over all the possible travel-times of these equations leads to

$$t=\int_V\left[\int_0^t\frac{P\left(\mathbf{r},\mathbf{r}',t-t'\right)P\left(\mathbf{r}',\mathbf{s},t'\right)}{P(\mathbf{r},\mathbf{s},t)}dt'\right]dV(\mathbf{r}') \tag{2.22}$$

The term inside the square parenthesis is the sensitivity kernel K. One of the most remarkable features of the kernel is that it expresses the travel time as a spatial distribution over the volume around the source and the receiver. An observer that could follow all the phonons going from the source to the receiver, could measure the sensitivity as the average time spent inside each volume of the medium (Margerin et al., 2016); therefore, the sensitivity kernels show which parts of the medium are preferred by the particles when going from the source to the receiver. As such, the regions around the source, the receiver, and between them, are zones that we expect to have high sensitivity as they are probably very frequented by the phonons that travel between the two. A simple schematic explanation of the travel-time sensitivity can be seen in figure 2.9. From equation 2.22 we can estimate the travel-time lags at the surface generated by a velocity perturbation in the medium

$$\frac{\langle\delta t\rangle}{t}=-\int_V K\left(\mathbf{r}',t\right)\frac{\delta v}{v}\left(\mathbf{r}'\right)dV\left(\mathbf{r}'\right) \tag{2.23}$$

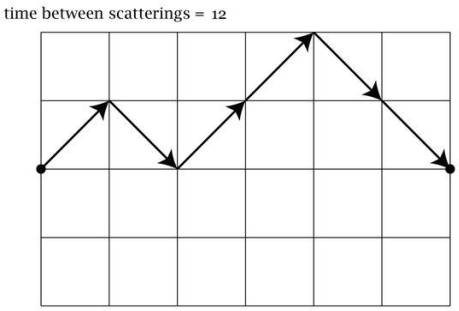

(A) A single particle travels between the source and the receiver

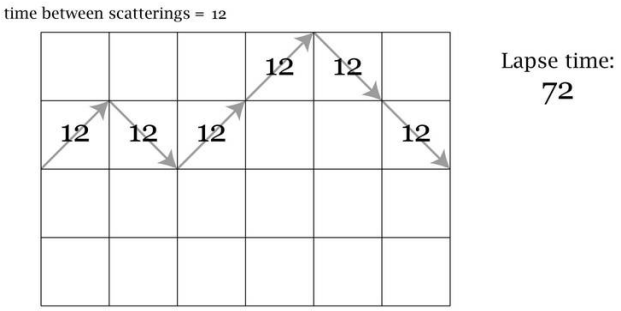

(B) Its travel-time can be *distributed* in small parts through the medium

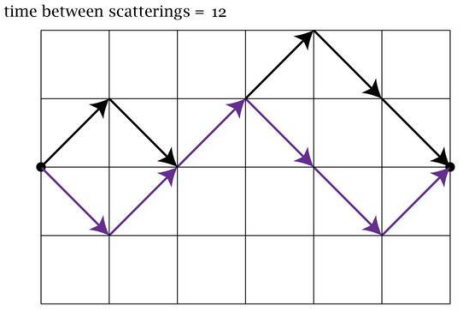

(C) A second particle makes a different path between the source and the receiver

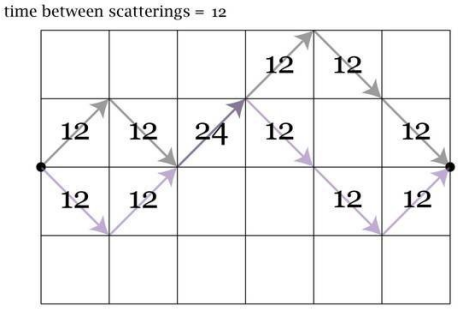

(D) Their travel-times distributions can be added between them

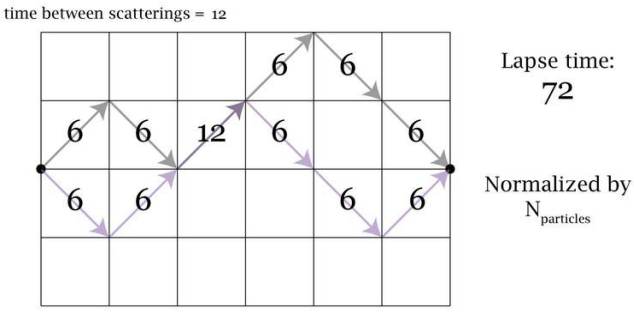

(E) Once normalized we have an image of the sensibility kernel. The sum of all the times in this distribution is equal to the travel time

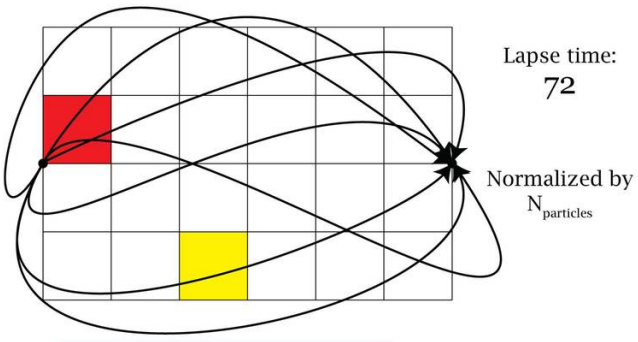

(F) If done with many particles, some areas will have higher sensitivity (red) than others (yellow)

FIGURE 2.9: Explanation of the travel-time sensitivity calculation between a source (at left) and a receiver (at right) with two phonons.

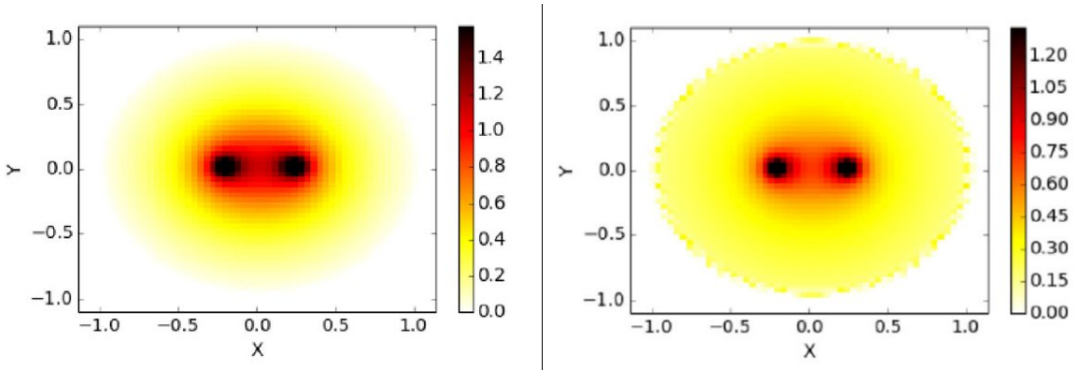

FIGURE 2.10: Travel-time sensitivity kernel for isotropic (left) and strongly anisotropic scattering (right). The kernels are symmetric between a source and the receiver. The distances have been normalized by the mean free path. Taken from Margerin et al. (2016)

where $\langle \cdots \rangle$ represents the average travel time change generated by all the volume elements. This shows that in principle, the location of the perturbation can be done inverting from the information of the phase delays at the surface, and the kernels. However, the estimation of the kernel is usually a complicated task and in most cases, the solutions are estimated through numerical methods.

A second important interpretation can be made from equation 2.22: the sensitivity kernel is a convolution between the intensity perceived at $\mathbf{r}'$ by the pulse generated at the source, and the intensity perceived at the receiver by the pulse generated at $\mathbf{r}'$. Many of the studies done with the sensitivity kernels were based on this kernel for diffusive waves, and the kernel for a single scattering model (Pacheco and Snieder, 2006). Margerin et al. (2016) unified and extended these cases with the use of the specific intensity, allowing them to track the seismic field within its early period, which is strongly marked by the directionality of the energy radiation. With this new approach, the sensitivity kernel can be written as

$$K\left(\mathbf{r}', t; \mathbf{r}, \mathbf{r}_0\right) = S \int_0^t \int_S \frac{P\left(\mathbf{r}, \mathbf{r}', t - t', -\mathbf{n}'\right) P\left(\mathbf{r}', \mathbf{s}, t', \mathbf{n}'\right) dt' dn'}{P\left(\mathbf{r}, \mathbf{s}, t\right)} \tag{2.24}$$

where $\mathbf{n}$ represents the direction of propagation of the phonons in the volume dV, and S represents its area. This kernel introduces the direction of the particles in the Chapman-Kolmogorov equation in addition to their positions. This also allowed the theory to include anisotropic scattering. The travel-time sensitivity kernel obtained for isotropic and strong anisotropic scattering can be seen in image 2.10.

Chapter 3

Separation of phenomena from $\delta v/v$ measurements

Andres Barajas, Piero Poli, Nicola D'Agostino, Ludovic Margerin, Michel Campillo
Article in preparation

There is a wide variety of phenomena that can affect the properties of the crust of the Earth. For this reason, it is usual that measurements of the apparent velocity variation obtained from recordings from ambient seismic noise, present variations that are the sum of the simultaneous action of these phenomena. Identifying to what degree an apparent velocity variation in the surface is caused by a certain physical process is a challenging work that usually requires the cross-examination and comparison with independent sources of information beyond the velocity itself. In this chapter, we present one effort in this direction in the Pollino region, Italy. This area was chosen because most of its seismic activity is limited to a relatively small period within the time frame of study, and because some exploratory measurements of the velocity variation in the zone showed interesting patterns. The advantage of having a period free of seismic activity is the possibility of having a control set against which we can compare the velocity changes when there is seismic activity. Another very important aspect of this region is the presence of aquifers as it is well known that the water content in the crust is one of the main factors behind the velocity variation of the seismic waves. Furthermore, there is a well-preserved record of the rainfall of the zone and a good distribution of GPS stations in the area that make this region an ideal subject of study. In this chapter following the standard notation, the term $\delta v/v$ is referred to as the measured or apparent velocity variation; behind this is the usual assumption of a linear relationship between the actual velocity perturbation at depth and the apparent velocity variation at the surface. However, in later parts of this thesis, the distinction between both will be necessary and therefore $\delta v/v$ will be reserved for the actual variation at depth, and $-\delta t/t$ for the apparent velocity changes measured at the surface.

3.1 Abstract

Analysis of the ambient seismic noise has proven to be a powerful tool to infer the structure or dynamic of the crust through the measure of the variation of the seismic field velocity. However, given the high sensitivity of this method, it's common to register velocity variations produced by many different factors like seismic events or changes in the crust due to atmospheric phenomena. In this study, we aim to disentangle these processes from a ten-year-long recording of seismic noise made with a single station in the region of Pollino, in the south of Italy. This region is characterized by the presence of aquifers and by a relatively short period of high seismic activity which includes slow slip events, and a $M5.0$ earthquake that occurred the 25 October 2012.

We apply two models that estimate the water level inside the aquifer assuming it is continuously recharged from the rainfall of the region. We find that both models make a good prediction of the measured $\delta v/v$ which means that the velocity variation is driven by changes in the pore pressure inside the aquifer: an increase of the water level produces a decrease in the seismic velocity in the zone. Our interpretation of the dynamic inside the aquifer is further confirmed by geodetic measurements which show that in a direction parallel to the strike angle of the fault rupture, the displacement of the zone follows the same patterns observed in the models and in the velocity variation. This could be understood as a poroelastic behavior in which the aquifer expands and contracts due to the pressure generated by the water on its interior, which also causes the velocity changes.

Going one step further, we analyze the nature of the small discrepancies between the measured and modeled velocity variations. We find that these are well correlated with the rainfall and with the vertical geodetic measures, which points to an instantaneous elastic response of the zone to the loading generated by the rain. The comparison between these variables allows us to make a clear identification of the period of seismic activity in the zone, represented by the characteristic drop in the seismic velocity in the period from the beginning of 2012 to mid-2013.

3.2 Introduction

The analysis of the ambient seismic noise (Campillo and Paul, 2003; Shapiro and Campillo, 2004; Campillo, 2006) has permitted estimate changes in the velocity in the crust related to a variety of phenomena, like earthquakes (Brenguier et al., 2008a), volcanic activity (Rivet, Brenguier, and Cappa, 2015; Brenguier et al., 2008b) and the thermoelastic response of the soil (Meier, Shapiro, and Brenguier, 2010), among others. Many studies focus on the hydrological effects on the $\delta v/v$. Sens-Schönfelder and Wegler (2006) estimated the underground water level using a model developed by Akasaka and Nakanishi (2000), to make a direct relation with the measured velocity variations in a volcano. (Meier, Shapiro, and Brenguier, 2010) analyze velocity variations within the Los Angeles basin and conclude that the seasonal variations are strongly influenced by groundwater level changes and thermo-elastic strain variations. Tsai (2011) propose periodic models to recreate displacements and velocity changes from thermoelastic stresses or hydrological loadings. Wang et al. (2017) found a direct relation between velocity variations and several hydrological and meteorological processes across Japan, mainly based on the pore pressure generated by the rainfall water through a diffusion process. Hillers, Campillo, and Ma (2014) shows the correlation between velocity changes and periodicity of precipitation events in Taiwan.

Hydrological deformation processes have also been studied through geodetic data (Bawden et al., 2001; Watson, Bock, and Sandwell, 2002; Borsa, Agnew, and Cayan, 2014; Chanard et al., 2014). In general, the effects of rainfall can be seen in two possible ways: as an elastic response where the water exerts a loading pressure that subsides the surface (Amos et al., 2014; Argus, Fu, and Landerer, 2014; Nof et al., 2012), or as a poroelastic response that generates a rise of the surface as a consequence of the recharge of the porous inner structure of the soil (Galloway and Burbey, 2011; King et al., 2007).

From the aforementioned studies emerge that thermal and hydrologic effects on $\delta v/v$ are significant, and can thus mask velocity changes induced by tectonic processes. It is thus fundamental to quantify the environmental effect to resolve the tectonic induced velocity variations for fault physics studies. Examples of this approach are the study of Hillers et al., 2019, where the seasonal variations were filtered out, to highlight deformation patterns of tectonic origin around the San Jacinto fault, or the work of Poli et al., 2020 where tectonic

and hydrological processes are separated from a single station analysis of the δ/v. In this study we pursue this same objective: we disentangle the influence of the water content inside the crust from the tectonic related events, in a $\delta v/v$ time series obtained from ambient seismic noise recorded in a single station in the region of Calabria, Italy (Figure 3.1).

One of the main characteristics of this zone is the presence of karst aquifers which is likely the driving factor behind geodetic of seismic velocity measurements (Poli et al., 2020; D'Agostino et al., 2018). Furthermore, this area was relatively inactive seismically until the beginning of 2012, when began a seismic swarm that lasted until the middle of 2013, a period that included several earthquakes including a $M5.0$ event on the 25 October 2012 (Passarelli et al., 2015). It has been estimated that 75 percent of 6000 events detected during the swarms are not aftershocks, which means that there may be a transient forcing acting as the driving mechanism behind the swarm. The physical nature of this transient forcing can be fluid filtration, pore pressure diffusion, or aseismic slow slip (Parotidis, Rothert, and Shapiro, 2003; Peng and Gomberg, 2010). This last scenario can also be associated with fluid-related phenomena reducing the normal stress in the fault. It has also been suggested that a big part of the crustal deformation in the zone is accommodated through transient slow slip event (Cheloni et al., 2017).

In this work, we apply two different models that calculate the water level inside the aquifer based on the information of the rainfall and compare the obtained behavior with the seismic noise-based velocity variations. We make an independent verification of the obtained results through horizontal geodetic measures of the zone. We also analyze at a deeper level the velocity variation removing from it, the modeled behavior controlled by the water level inside the aquifer. This allows us to identify a weaker pattern controlled mainly by the immediate elastic response of the zone to the rainfall which is also the main driving factor behind the variations of the vertical geodetic measurements. Finally, this procedure reveals a velocity drop most probably related to the stress release of the zone through seismic activity.

3.3 Data processing description

An overall layout of the data stations can be seen in figure 3.1. The seismic ambient noise is recorded at the station MMNO in Pollino area (Italy) (INGV Seismological Data Centre, 2006). The three components' continuous signals were band-passed between $0.5Hz$ and $1Hz$. For each day, the whole signal is divided into overlapping windows of half an hour (50% overlap). Later, we calculated the cross-correlation between the 30-minutes windows for all the possible combinations of the three available channels; this means that for each 30 minutes segment, we obtain 6 cross-correlations. In the practice, we calculate them simultaneously using the Covet package (Seydoux, Rosny, and Shapiro, 2017). The half-hour cross-correlations are average between them for each day, resulting in 6 cross-correlations per day. Two averaging processes for each combination is performed: the first one consists of making a moving average with the correlations of 30 days around each day to stabilize the obtained signal and reduce possible transient noise sources. The second consists of obtaining six global reference cross-correlations averaging between all the available days. A variation of the velocity can be estimated if we consider that a perturbation in the medium will generate a change in the shape of the cross-correlation with respect to the global average, in the same way, that a pulse emitted in the position of the seismic station would be registered differently if the velocity of the medium change. We calculated this possible change in the frequency domain (Poupinet, Ellsworth, and Frechet, 1984) using the segment of the coda of the cross-correlations between $10s$ and $50s$. All the 6 velocity variations time series are averaged daily and finally, a moving average of 30 days is applied over the resulting $\delta v/v$ series.

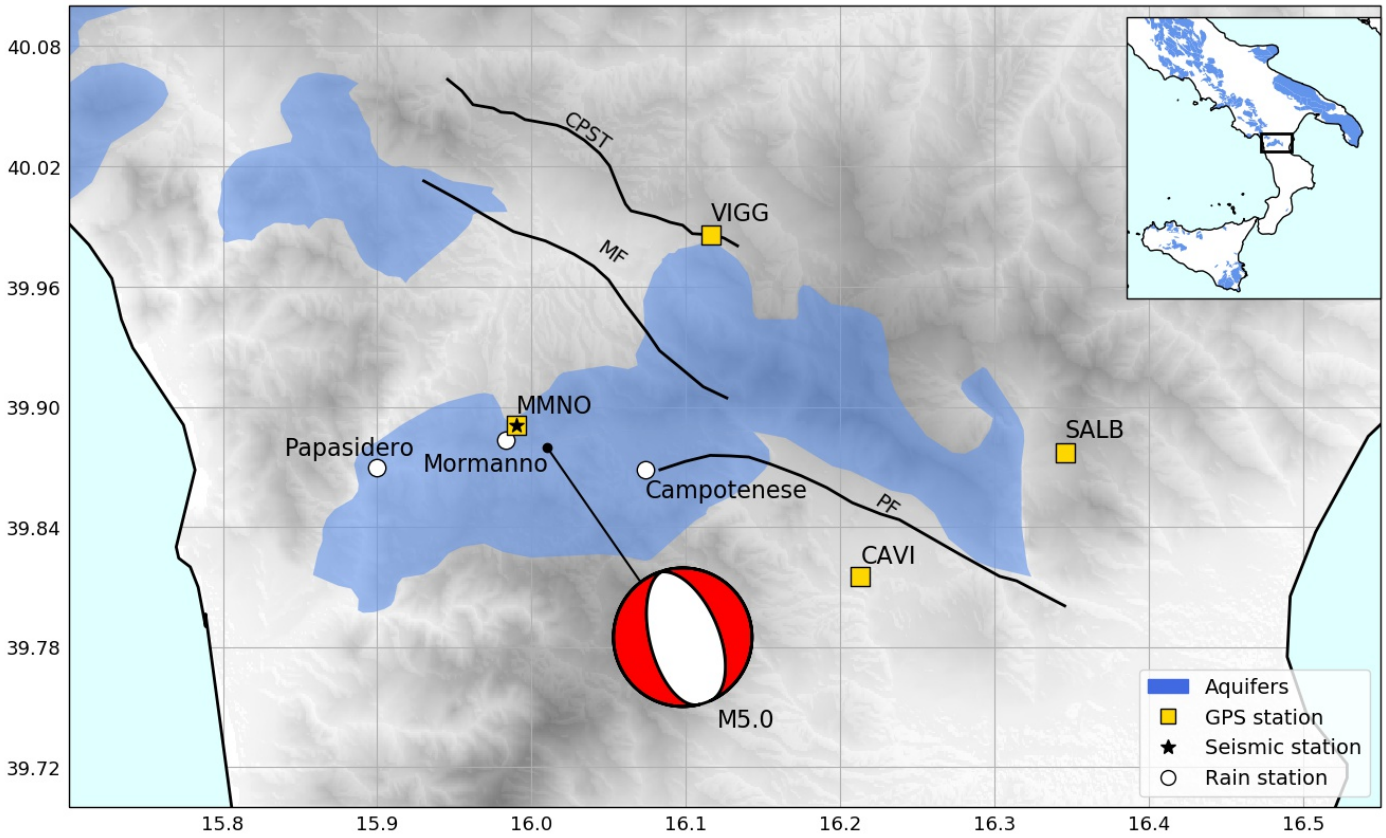

FIGURE 3.1: General disposition of the seismic, rain and GPS stations, the location of the aquifers and the $M5.0$ earthquake in the region of Calabria, Italy. The CPTS, MF and PF lines represent the Castello Seluci-Timpa della Manca, Mercure and Pollino faults respectively. The rain data is obtained from the Multi-risk Functional Centre (*Centro funzionale multirischi della Calabria*).

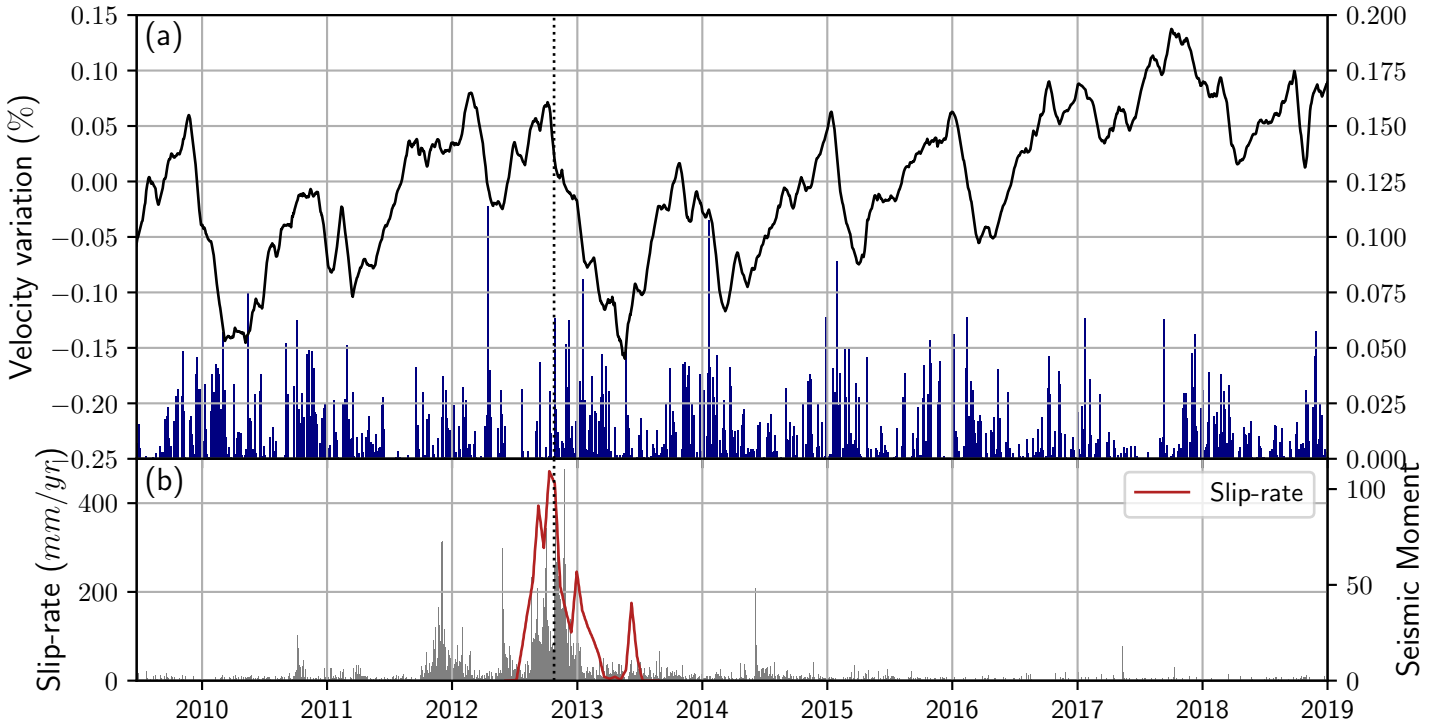

FIGURE 3.2: a) Seismic measurements of $\delta v/v$ and daily rainfall in the region. b) Daily accumulated seismic moment in the region and reported slip-rate by Cheloni et al., 2017. The dashed line marks the date of the $M5.0$ seismic event.

The GPS displacements were obtained from the Rete Integrata Nazionale GPS network (INGV Seismological Data Centre, 2006). This data was processed using the Jet Propulsion Laboratory (JPL) GIPSY-OASIS II software.

The rain data was collected in the 3 closest available stations shown in 3.1. Not all three stations have available data in all the studied period, so the average process is done each day using only the available information. The result of this process gives us the estimation of the regional daily rainfall show in figure 3.2a.

3.4 Procedure and results

3.4.1 Measured and modeled velocity variations

The noise-based velocity variations plotted in figure 3.2a reveal several patterns. We recognize a periodic (1 year) oscillation that is likely to be controlled by the amount of water in the crust. Indeed, the daily rain observed on the region (fig. 3.2a) increase during the winter, with an associated velocity reduction (Sens-Schönfelder and Wegler, 2006). Beyond the periodic signal, a long term trend of increasing velocity is observed for the full period (fig. 3.2a).

To separate hydrologic signal from the possible presence of tectonic stress change effects in the seismic $\delta v/v$ series, we model the induced velocity variations generated by the amount of water in the crust. For this, we developed and applied two different models allowing the estimation of accumulated water inside the aquifer as a function of time.

The aquifer is recharged with the rainfall through a fast process thanks to the characteristic permeable material of the karst. We assume that this happens at a higher velocity than in a normal diffusion process: rainfall is added each day directly to the water level of the aquifer. The discharge process can be described by two different models, both of them related to the stored water inside the aquifer. The first one, the linear reservoir (Fiorillo, 2011), assumes that the aquifer loses water through a flux with its surroundings, at a discharge rate dQ/dt (being Q the stored volume of water) that is proportional to the difference of concentration between the interior and the exterior of the karst $\Delta\phi$, and the contact area between the two A_L

$$\frac{dQ}{dt} = UA_L\Delta\phi + R \tag{3.1}$$

where R is any external source supplying the aquifer. In the last equation U plays the role of a conductance over the surface, that is, the proportionality constant between the flux of water leaving the aquifer (per unit of area) and the concentration difference; in fact, U is the equivalent of the heat transfer coefficient in the heat transfer Newton's law of cooling. From this point of view, this is parallel to obtaining Newton's law of cooling from the heat equation that is described also as a diffusive process. The total quantity of water inside the aquifer can be written in terms of its density and the volume it occupies. The water in the aquifer accumulates at its bottom, and therefore, this volume can be written in terms of the area of the bottom A_B and the height of the column of water h. On the other hand, we assume that the area that transmits water is just the lateral one (no difference-of-concentration flux at the top or at the bottom). Then, the contact area can be written approximately as the multiplication of a perimeter and the height of the column of water $A_L = P * h$. Introducing these changes turn the discharge equation into

$$\frac{d\left(A_B h\right)}{dt} = UPh\Delta\phi + R \tag{3.2}$$

that means that the rate at which the aquifer lose water is proportional to the water level itself

$$\frac{dh(t)}{dt} = -kh(t) + r \tag{3.3}$$

where h is the water level inside the aquifer, r is the source term written in terms of the change it generates in the water level inside the aquifer and $k = UP\Delta\phi/A_B$ that depends on the geometry of the aquifer and the conductance of the medium.

The second model, the Torricelli reservoir (Fiorillo, 2011), assumes that the aquifer works as a container that loses water through a spring at its bottom. The velocity at which the water leaves the aquifer is proportional to the square root of the height of the contained water, as stated by Torricelli's law

$$v = \sqrt{2gh} \tag{3.4}$$

where g represents the gravity. In this case, the discharge can be written in terms of this velocity, and the area through the water is escaping (A_s)

$$\frac{dQ}{dt} = A_s v + R = A_s\sqrt{2gh} + R \tag{3.5}$$

If we write again the volume of water inside the aquifer as $A_B h$, the change on the water level will follow the same mathematical structure ,

$$\frac{dh(t)}{dt} = -k'\sqrt{h(t)} + r \tag{3.6}$$

where $k' = A_s\sqrt{2g}/A_B$, and r represents the source supplying the aquifer in terms of the water level. The constants in both of these equations are related to the physical characteristics of the aquifer, and modifying them changes the strength and the delay of the discharge for a given water quantity inside the aquifer.

Therefore, the water level at each day will be the level of the day before, plus the level gained by the rainfall on that day r, minus the losses that are calculated according to the model:

$$h_{i+1} = h_i - kf(h_i) + r_{i+1} \tag{3.7}$$

Here $f(h_i)$ represents the particular functional dependence of the model in the water level, defined by equation 3.3 or 3.6. At this point it's important to remark the units of the water level as obtained by the models: they are equal to the units of the rainfall, which is measured as mm of water recollected per square meter. This means that only if we have an aquifer of exactly $1m^2$, recollecting the totality of the indicated rainfall (that is most probably not the case), we will have the water levels predicted by the models. Furthermore, if the area that collects the water (the area of the aquifer) is different from the area that supplies the rainfall, the proportion between both units will not be 1-to-1. This implies that both models allow us to predict relative changes in the water level, but not its absolute value. However, this is not a problem as will be clear below.

If the water level controls the velocity variation, the resulting series for h should show the same behavior as the $\delta v/v$, or in other words, there would be a linear relationship between them. We find the value of the constant k in each model that optimizes the linear relation between them with the following grid search:

- A value of k is chosen, and using the rain data as the input, the water level time series is calculated following the recursive formula 3.7
- The water level is shifted towards the zero removing its time average (represented by$\langle\cdot\rangle$):

$$h(t) \to h(t) - \langle h(t)\rangle \tag{3.8}$$

- The proportionality constant between $(\delta v/v)(t)$ and the water level time series is calculated as the ratio between the covariance and the variance: $a = \mathrm{cov}\left((\delta v/v)(t), h(t)\right)/(\mathrm{var}(h(t))$
- The shift or intercept between the two series is estimated as the average of the seismic velocity variation: $b = \langle(\delta v/v)(t)\rangle$
- A synthetic velocity variation $\delta v/v_{syn}$ is obtained from the water level model using both constants a and b:

$$\frac{\delta v}{v}_{syn}(t) = \left\langle \frac{\delta v}{v}(t) \right\rangle + \left(\frac{\mathrm{cov}\left(\frac{\delta v}{v}(t), h(t)\right)}{\mathrm{var}(h(t))} \right) \cdot h(t) \tag{3.9}$$

- For a given constant k, the fit to the data of the model to describe the seismic velocity variation is measured as

$$\sigma^2(k) = \frac{1}{n}\sum_{i=1}^{n} \left(\frac{\delta v}{v}(i) - \frac{\delta v}{v}_{syn}(i,k) \right)^2 \tag{3.10}$$

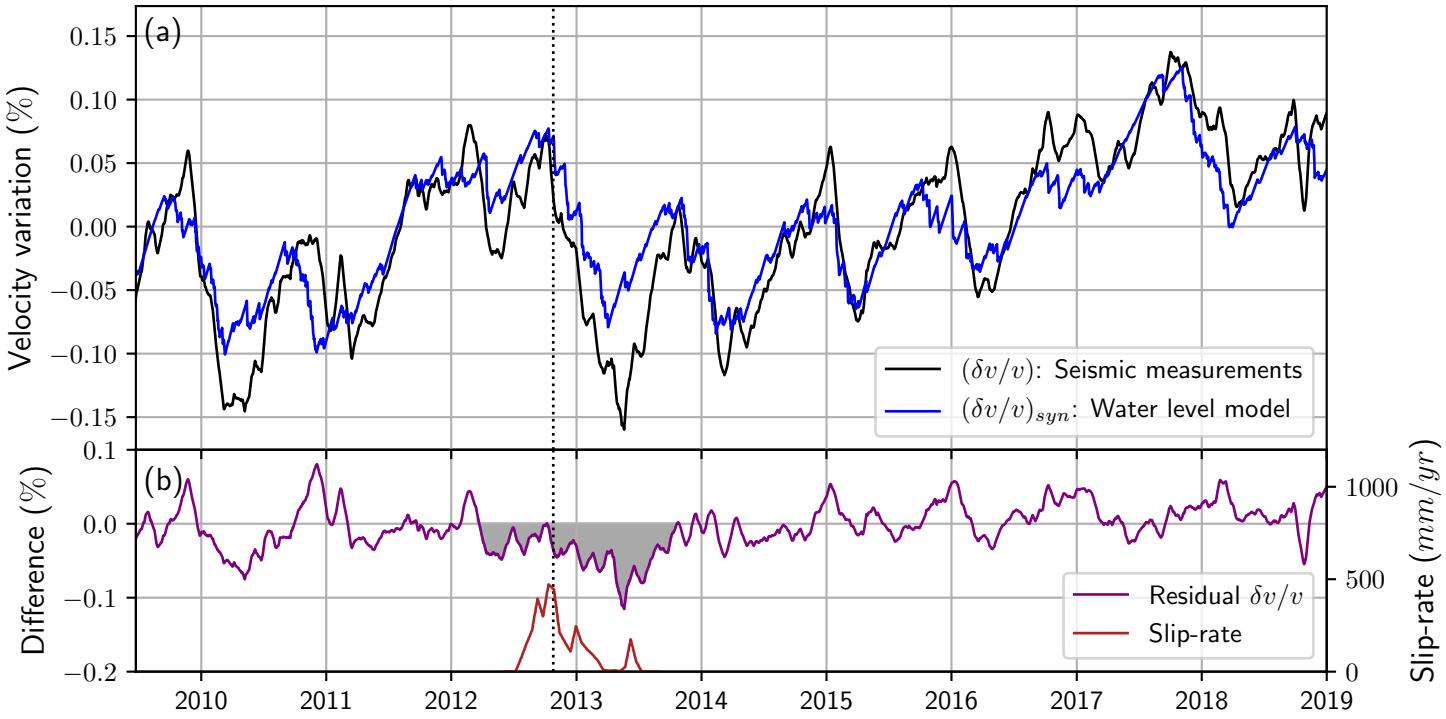

FIGURE 3.3: Seismic noise measurements and water level model. a) Seismic and synthetic $\delta v/v$ obtained from the water level model. b) difference between the model and the measured $\delta v/v$ smoothed with a 30 days window and reported slip-rate by Cheloni et al., 2017. The shaded zone highlights the systematic excess of velocity reduction between the seismic $\delta v/v$ and the rain-based model. The dashed line marks the date of the $M5.0$ seismic event

- The process is repeated for a whole set of values of k and the one with the lowest σ^2 is chosen.

Both the models produce almost indistinguishable results because a daily input will highlight in the long term only a linear dependence with the input itself. The misfit of each model and a comparison between them can be seen in the supplementary material. The predicted velocity variation obtained with the linear reservoir model for the best fitting constant can be seen in figure 3.3a; this will be the model used in the rest of the paper. In both cases the covariance between the seismic measurements and the water level model is negative, which means that they are anti-correlated: the increase of the water content in the aquifer decreases the seismic velocity in the medium. This happens because the presence of water increases the pore pressure, which in turn, reduces the overall effective pressure in the zone and therefore, reduces the seismic velocity. We can see that the models reproduce accurately the seismic-based series, not only on its seasonal patterns but also in the overall multi-year trend, which means that the water content in the aquifer is effectively the main driving factor behind the registered velocity variations. The positive trend observed between 2014-2019 is a regional multi-annual hydrological trend observed also in the spring discharge and in the modulation of seismicity along the Irpinia Fault (D'Agostino et al., 2018).

The difference between measured velocity changes and the modeled velocity changes can be seen in figure 3.3b. It can be seen that there is a periodic misfit between them which

means that a small part of the seismic velocity variation is not predicted by our models. This could be due to a defect of the model or to the presence of a second phenomenon acting in parallel with the water accumulation. Furthermore, the most remarkable feature of this difference is a systematic excess of velocity reduction, that begins at the beginning of 2012 when there is high seismic activity, and that lasts approximately until the end of 2014; the velocity changes measured in the seismic field are not completely accounted by the water level model, that is, by the accumulated water able to increase the hydraulic head and the aquifer pore pressure. Although the 1-month moving average applied over the time series makes it difficult to talk about specific dates, this systematic difference is probably generated by tectonic stress release as it happens simultaneously with the seismic activity. Furthermore, through 2013 this difference seems to increase and seems to have its maximum peak around the same time of the last pulse of the reported slow slip in the zone. It was found that this late slip happened simultaneously with an enlargement of the crustal area affected by the seismicity (Cheloni et al., 2017). However, the systematic difference with our model extends beyond the slow slip event for several months. This extended behavior could be related to the stress change produced by the earthquake and its posterior recovery phase that could last several months (Brenguier et al., 2008a). It could also be possible that the earthquake or the slow slip changed the internal structures of the aquifer which will produce a migration of water that would change temporarily the water level. Whatever may be the cause, the changes in the velocity are completely recovered by the end of 2013.

3.4.2 Analysis of geodetic data

Geodetic measurements are useful to measure displacements related to earthquakes and to slow slip events, and also to analyze hydrological processes inside aquifers (Cheloni et al., 2017; D'Agostino et al., 2018; Silverii et al., 2016). We turn to analyze GPS traces as an independent way to assess the modeled variation of the velocity and its possible mechanisms. For this, we use GPS traces obtained in four stations of the zone which are shown in figure 3.1.

We begin analyzing the relative displacement between the two closest stations to the earthquake, VIGG and MMNO, smoothed with the same 1-month window as was done with the velocity variation. Both relative horizontal components can be seen in figure 3.4a. To simplify the visualization of the GPS traces, all of them have been shifted vertically towards the zero without modifying their behavior or their relative values. This doesn't affect our analysis as we are interested in the patterns described by the traces and not in their absolute values. The relative displacement shows seasonal patterns in all the directions and a clear change of baseline due to the $M5.0$ event.

Perhaps the most interesting feature of the traces in figure 3.4a is the behavior of the NS component from 2014 until the end of the series, as it shows a similar pattern to the one observed in the $\delta v/v$: a yearly seasonal variation over a multiyear increasing behavior, with approximately the same shape. However, this behavior is not present in the EW direction. There are a couple of reasons why this behavior can not be seen in both components. One of these is a possible anisotropic response of the aquifer to hydrostatic pressure in the horizontal direction (Silverii et al., 2016). Commonly, a porous medium like an aquifer presents fractures than can open and close temporarily with the pressure generated by the water in them (Amoruso et al., 2014; Daniele, Braitenberg, and Nagy, 2012). If these fractures happen predominately in a specific direction, the macroscopic expansion-contraction dynamics will be more (or only) visible in such direction, which constitutes an anisotropic response. Another possible reason could be simply the relative position of the GPS station to the aquifer: for example, if we had a GPS station at the north of a perfectly circular aquifer, we would expect

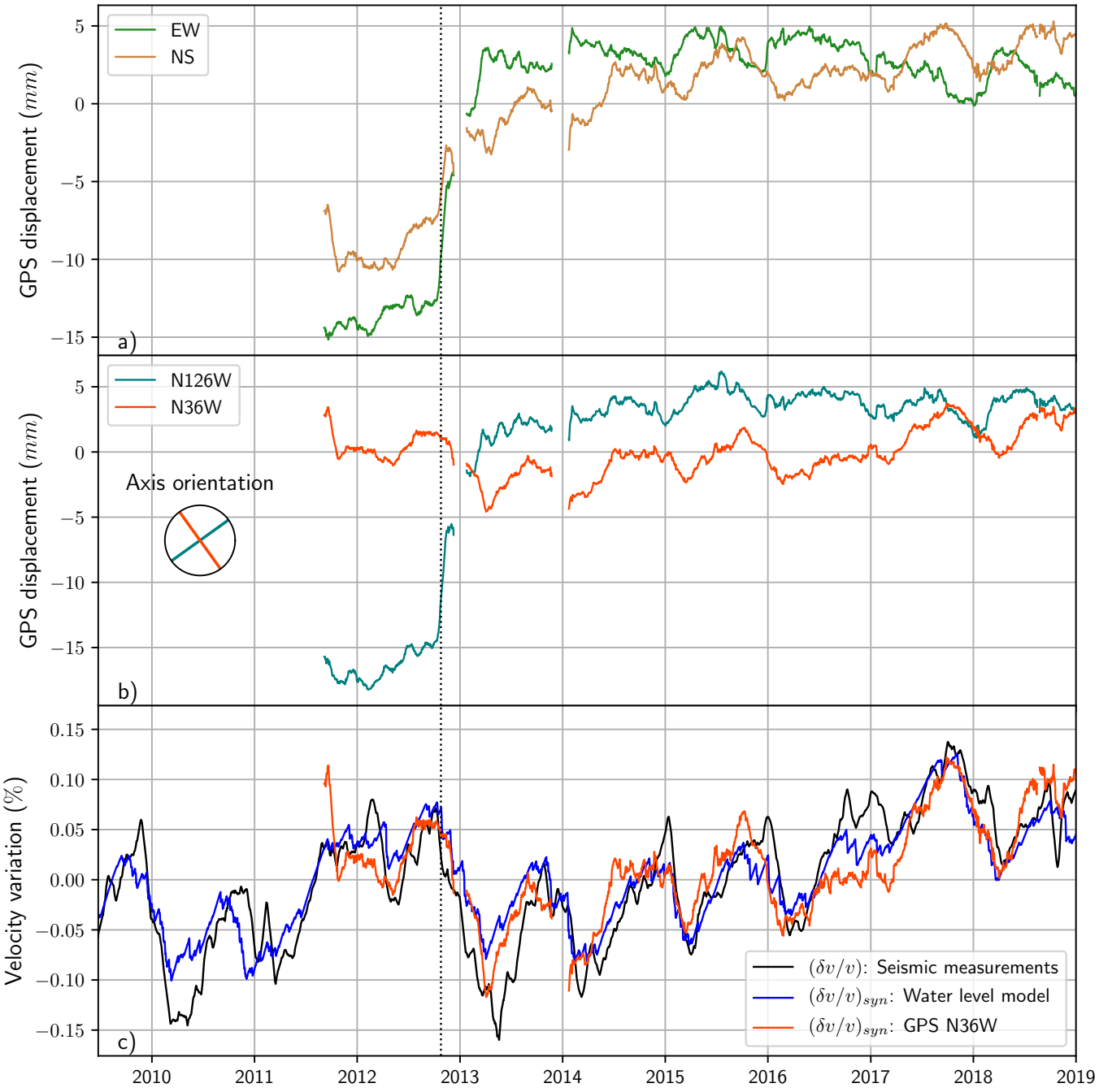

FIGURE 3.4: Modeled velocity variations and GPS relative displacements. a) Relative horizontal GPS displacements between stations MMNO and VIGG. b) GPS horizontal relative displacements rotated by an angle of 36° in clockwise direction. c) Velocity variations measured through seismic noise analysis, predicted from the water level model, and fitted with the rotated $N36W$ horizontal displacement. The dashed line marks the date of the $M5.0$ seismic event.

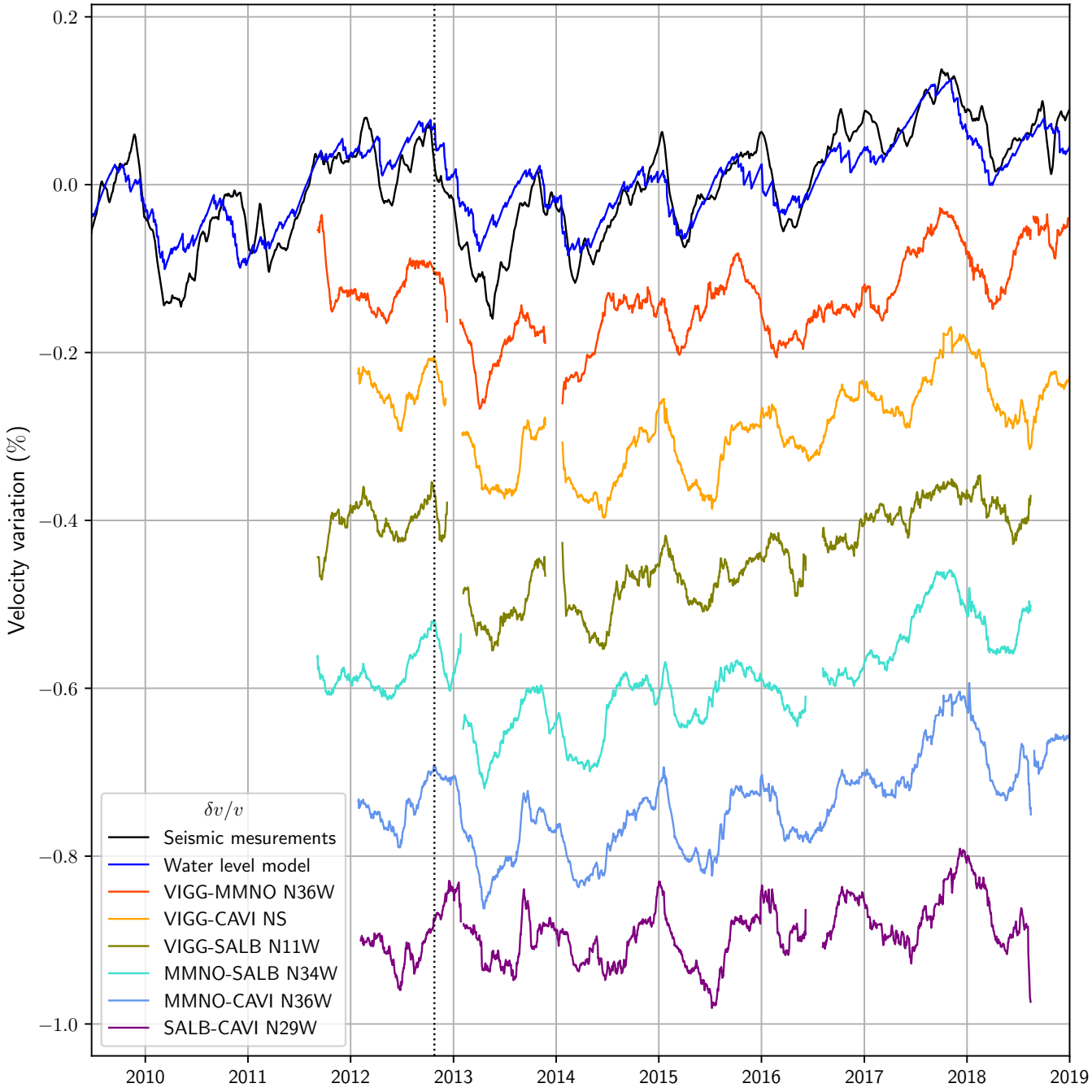

FIGURE 3.5: Comparison between the measured velocity variation (black) and all the synthetic velocity variations obtained with the water level model (blue line) and with rotations of the GPS relative displacements for all the possible combinations between the 4 stations. A shift of 0.15% was introduced between them for visualization purposes. The angle of the rotation that maximizes the fit for each couple is indicated in the label of the line, with exception of VIGG-CAVI where no rotation was needed. The dashed line marks the date of the $M5.0$ seismic event.

to see the expansion-contraction registered only in the NS component and not in the EW component, even in an isotropic fracture system.

Likely, the main expansion-contraction direction is not exactly NS. With this in mind, we perform a rotation of the horizontal GPS traces to find the angle that maximizes the presumed linear relation between the GPS displacement, and the modeled water level inside the aquifer. This is done through a similar grid search like the one implemented before, between one rotated component of the GPS and the measured seismic $\delta v/v$.

The reason why this angle minimizes the fit can be easily seen in figure 3.4c: the trace in the direction N39.3W shows the same behavior of the modeled velocity variations for all times, even in the period in which the earthquake and the slow slip happened. There may be two reasons why this trace reproduces so well the water level in the aquifer: the fist one, the direction of this rotated GPS is the only direction in which the fault rupture of the earthquake is not visible, that is, the direction of the strike angle of the earthquake. This is important as any other direction will show a discontinuity in the horizontal expansion of the aquifer. On the other hand, it's possible that the localization of the GPS station, NW of the aquifer, helps to accentuate the expansion-contraction process in that specific direction.

Beyond the mechanism that accentuates one direction in particular, is clear that the behavior of the displacements is related to the variations seen in both the velocity changes and in the water model, which is coherent with an expansion-contraction dynamics in the aquifer (Cheng, 2000). As the aquifer stretches between the four GPS stations, this process should be visible by different combinations of stations and not only between VIGG and MMNO: in effect, calculating the relative displacement between all the other couples, and finding the best rotation for each case produce a similar pattern, as can be seen in the figure 3.5. Although different GPS combinations are better fitted around different angles, all the combinations that involve the station MMNO (the closest to the seismic event) are maximized around 36 degrees, possibly as a consequence of finding the projection that doesn't show the effect of the earthquake itself. Moreover, it can be seen that different couples produce different levels of intensity between the seismic event and the water-driven pattern, which signals a possible new way to analyze the complexity of the system, and particularly, the directions of volumetric expansion of the zone.

3.5 Loading effect of the rainfall

A deeper inspection of the seismic velocity variations can be made if we analyze the part of it that is not controlled by the water level in the aquifer. This can be done by subtracting one from another as is shown in figure 3.6a. This is the same difference shown in figure 3.3 but processed with a longer smoothing window of 180 days to stabilize the fluctuations and highlight seasonal patterns. The longer smoothing window and the fact that this is the difference between the measured and modeled velocity variations, explains why the obtained pattern amplitude is around 20 percent of the original amplitude of the velocity. As was seen in figure 3.3, this residual velocity is not in phase with the modeled water level in the aquifer. However, a quick inspection of the rainfall smoothed over the same moving window of 180 days (figure 3.6b) reveals that both are in phase, which means that the observed behavior probably comes from the instantaneous loading that the rainfall is generating over the surface. This conclusion is confirmed by the vertical component of the GPS stations in the regions (figure 3.6c) which show an anti-correlation between the rainfall itself and the elevation of the surface. As it would be expected, when the rainfall increases, the loading on the zone increases generating a positive residual velocity variation, and at the same time, produces a downward motion of the vertical position (Meier, Shapiro, and Brenguier, 2010; Lecocq et al.,

2017). This is consistent with regional observations made by Silverii et al. (2016) where they find a correlation between the vertical GPS data and GRACE (Gravity Recovery and Climate Experiment) satellite observations.

This implies that the response of the crust to the rain happens in two ways: in the first one the water generated by the rainfall accumulates in the aquifer and as a result, produces an expansion of the zone which is registered by the horizontal GPS. This is a poroelastic reaction. In the second one, the rainfall generates an instantaneous load over the zone which is measured by the vertical GPS motion. This is an elastic reaction. Although both mechanisms are acting simultaneously, they have peaks that are not in phase. Both are measured with different intensities by the velocity variations of the seismic noise.

Lastly, in figure 3.6 is highlighted a period in which the pattern measured in the velocity variation doesn't match the seasonal loading. The most probable cause of this mismatch is the simultaneously high seismic activity of the zone, including the $M5.0$ earthquake, which happens almost in the middle of the registered anomaly in the velocity variation. All of this is coherent with the temporary velocity drop that dominates this period, which suggests a stress release within the medium (Brenguier et al., 2008a).

3.6 Conclusions

We measure the variations of the seismic velocity during ten years in the region of Calabria, Italy, with a single seismic station. They show a yearly oscillation characteristic of seasonal factors, superimposed over a multi-year pattern. The water content in the soil is usually one of the main factors controlling the velocity variations of a region; for this reason, we use two models that estimate the water level inside the aquifer of the zone, assuming that it is recharged by the rainfall and that it loses water through two different mechanisms. Both models use constants whose values depend on the geometric particularities of the aquifer, that are unknown. For this reason, we perform a grid search comparing the resulting water level models with the velocity variations, for different constants. This comparison consists of recreating a modeled velocity variation that is essentially modifying the water level overall amplitude and mean, to match those of the measured velocity variation, and calculating the root-mean-square error between the two. We find that both the models do a good prediction of the velocity variation showing in both cases an anti-correlation between the levels of water in the aquifer and the velocity of the seismic waves. The increase of pore pressure generated as a consequence of the presence of water leads to a reduction in the effective pressure in the medium and therefore, to a reduction in the seismic velocity. The model recreates the yearly seasonal behavior and the long multi-year trends. This shows that the total water inside the aquifer changes slowly, influenced by long-lasting periods of heavy rains or droughts.

The comparison between the model and the measured $\delta v/v$ also shows a systematic discrepancy between them that lasts between one and two years. In this period, the seismic measurements show that the velocity on the zone is lower than what is predicted by the content of water able to increase the hydraulic head and the aquifer pore pressure. This happens in the same period on which the $M5.0$ earthquake and the slow slip events occur (Cheloni et al., 2017), which suggests that velocity drop discrepancy is produced by a stress release in the tectonic system through seismic activity and transient aseismic deformation. This difference disappears by the end of 2013.

The component NS of the relative displacement between the GPS stations across the fault, VIGG and MMNO, suggests that the deformation in the zone occurs synchronously with both the $\delta v/v$ and the water level of the aquifer, for the period after the seismic activity happening between 2012 and 2013. We found that the relative displacement in the direction

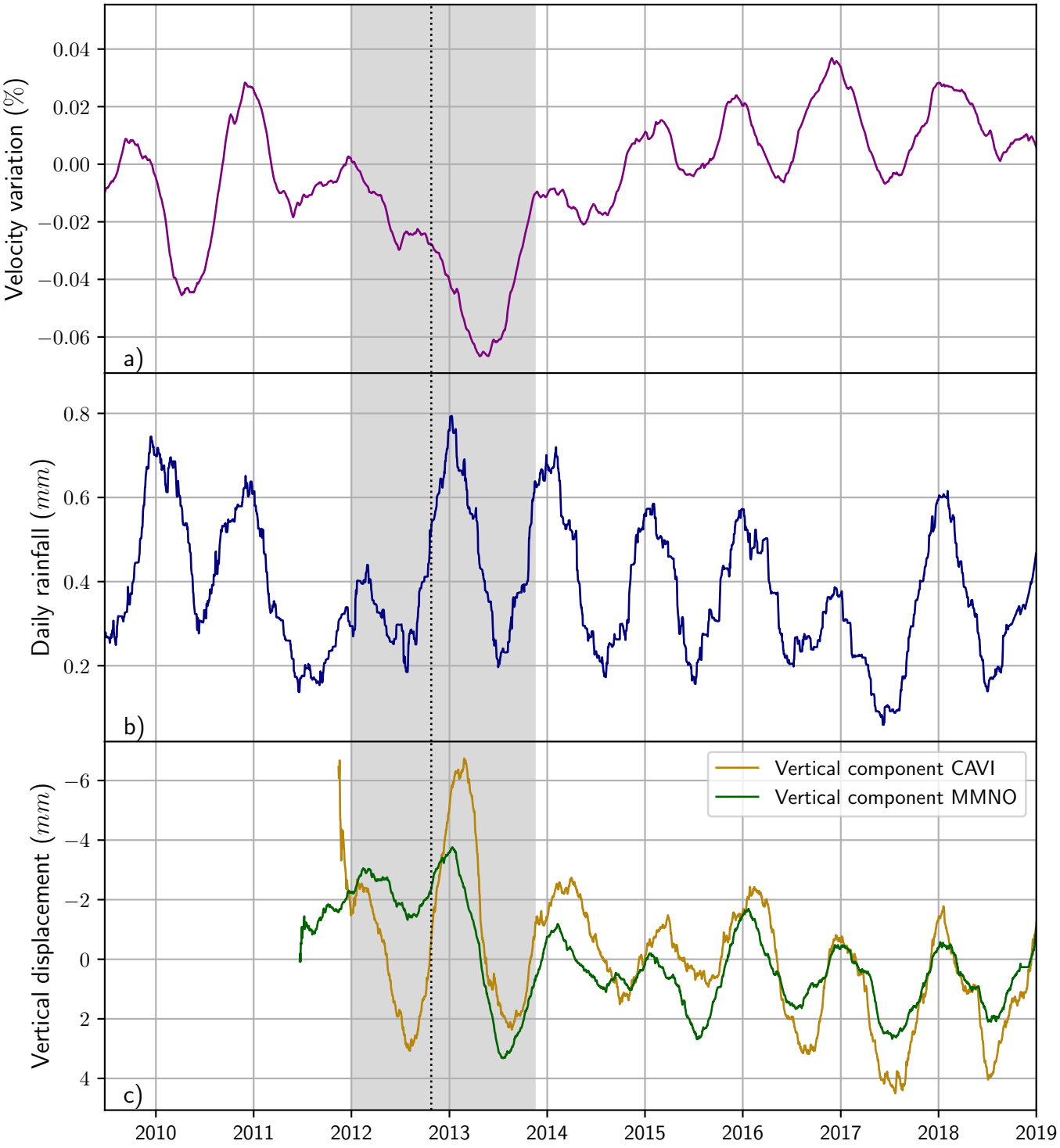

FIGURE 3.6: a) Difference between the measured velocity variation in the seismic noise and the velocity variation of the water level model. b) Rainfall. c) Vertical GPS displacements of stations MMNO and CAVI (inverted). The shaded zone highlights the period on which the velocity variation is not explained by the water content of the soil, and is not in phase with the regional rainfall. The dashed line marks the date of the $M5.0$ seismic event. All the plots are smoothed with a 180 days window

$N36W$ follows the same behavior that both the measured and modeled velocity variations, for the whole period recorded with the GPS. This can be explained by the pressure generated by the water that opens and closes the fractures of the porous media, generating the overall displacements registered by the GPS; this behavior is also seen between all the other stations that are located in the zone. This confirms our assumption of a poroelastic recharge and discharge process of the aquifer, upon which we based the water level models. The angle at which this occurs for the couples that involve the station MMNO is always around 36°, which is close to the angle of the strike fault of the $M5.0$ event (24°), possibly because at this direction the sharp displacement generated by the earthquake is minimized. Moreover, the angles that maximize this expansion-contraction mechanism for the couples that are not close to the earthquake (namely, VIGG-CAVI, VIGG-SALB, and CAVI-SALB), show interesting differences that are possibly related to the shape of the aquifer or local anisotropic behavior.

The subtraction of the predicted velocity variation generated by the water level inside the aquifer from the observed seismic one, reveals a pattern of weaker amplitude that is in phase with the regional rainfall. We also observe that the vertical displacements of the GPS on the zone are well anti-correlated with the rainfall of the zone. This indicates an elastic behavior of the zone that happens in parallel with the described poroelastic dynamics: the rainfall generates an instantaneous loading over the surface that has a consequence, the subsidence of the elevation of the zone (therefore the anti-correlation with the vertical GPS) and a small increase on the stress of the crust (and consequently an increase of the seismic velocity) that is registered in the $\delta v/v$.

Finally, this procedure highlights a period on which an anomalous velocity drop breaks the in-phase behavior between the residual seismic velocity and both the rainfall and the vertical GPS. This happens simultaneously with the period of high seismic activity of the region, which includes the $M5.0$ event. Therefore, the velocity drop is probably related to the stress release associated with the seismic activity of the zone. This means that our analysis allows us to extract the seismic signature of the tectonic stress release, despite having two environment processes, the elastic and the poroelastic response to the precipitation, working simultaneously and dominating the variation of the seismic velocity.

3.7 Supplementary information

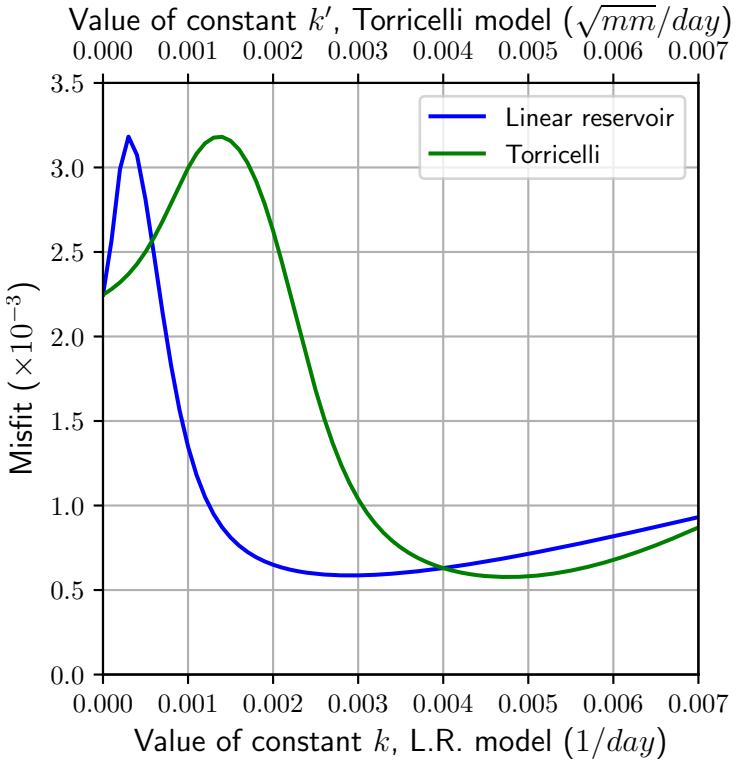

FIGURE 3.7: Misfit of each of the model for different values of k

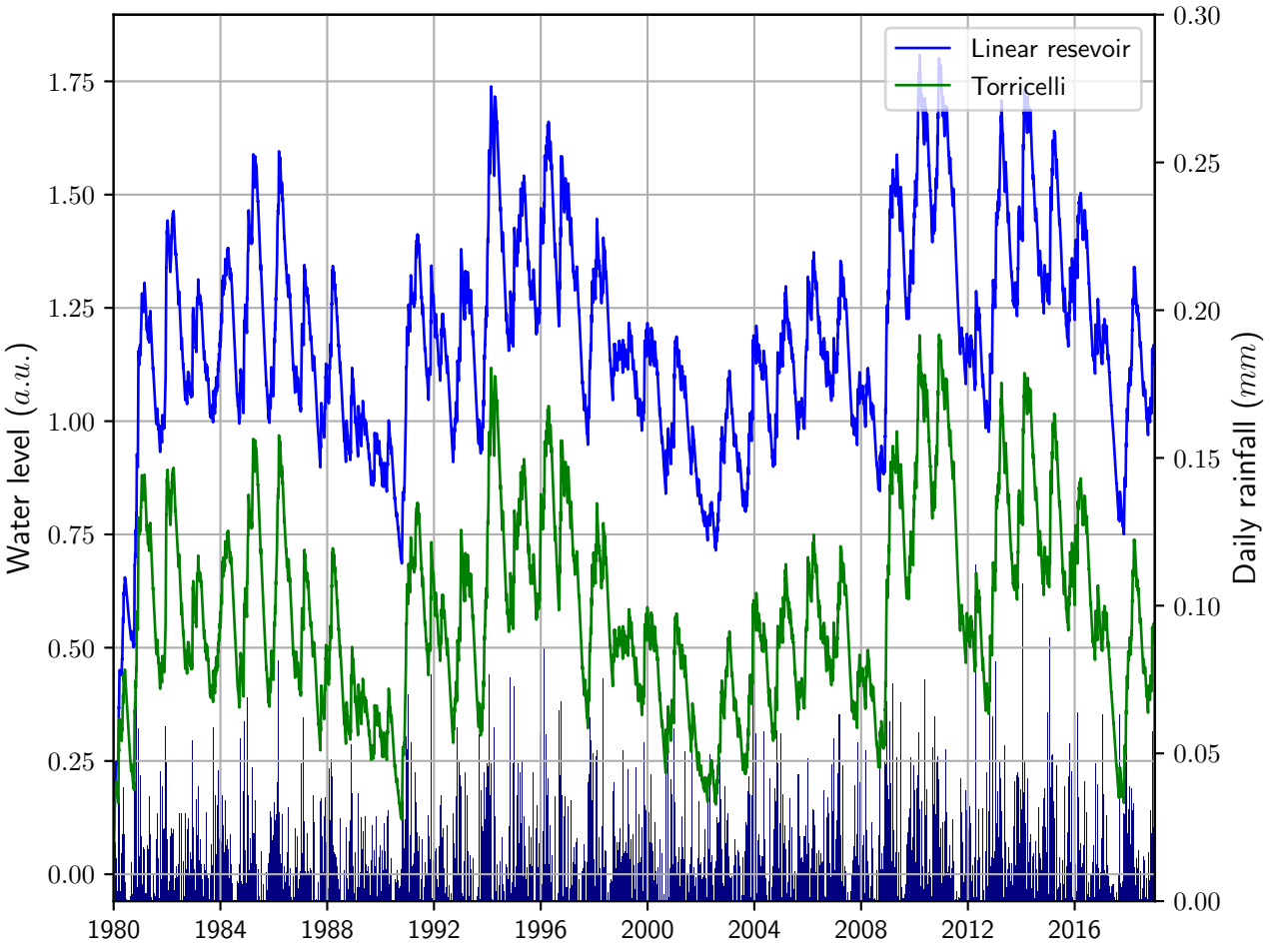

FIGURE 3.8: Water level estimation from both discharge models along with the rainfall.

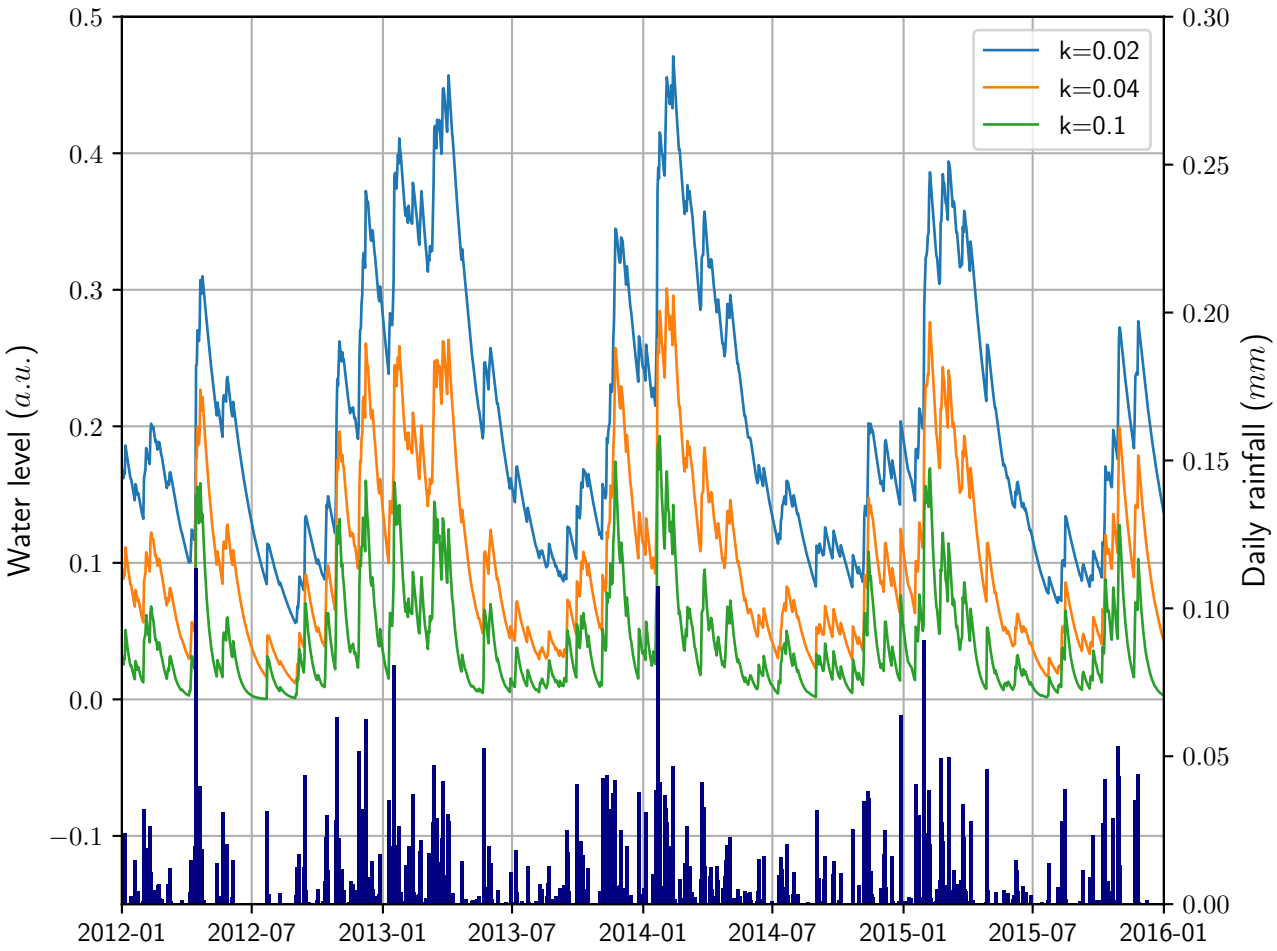

FIGURE 3.9: Water level estimations with the Linear Reservoir model for different values of k. When $k >> 1$ the water model reproduces exactly the rainfall as no water can be accumulated because of the fast discharge.

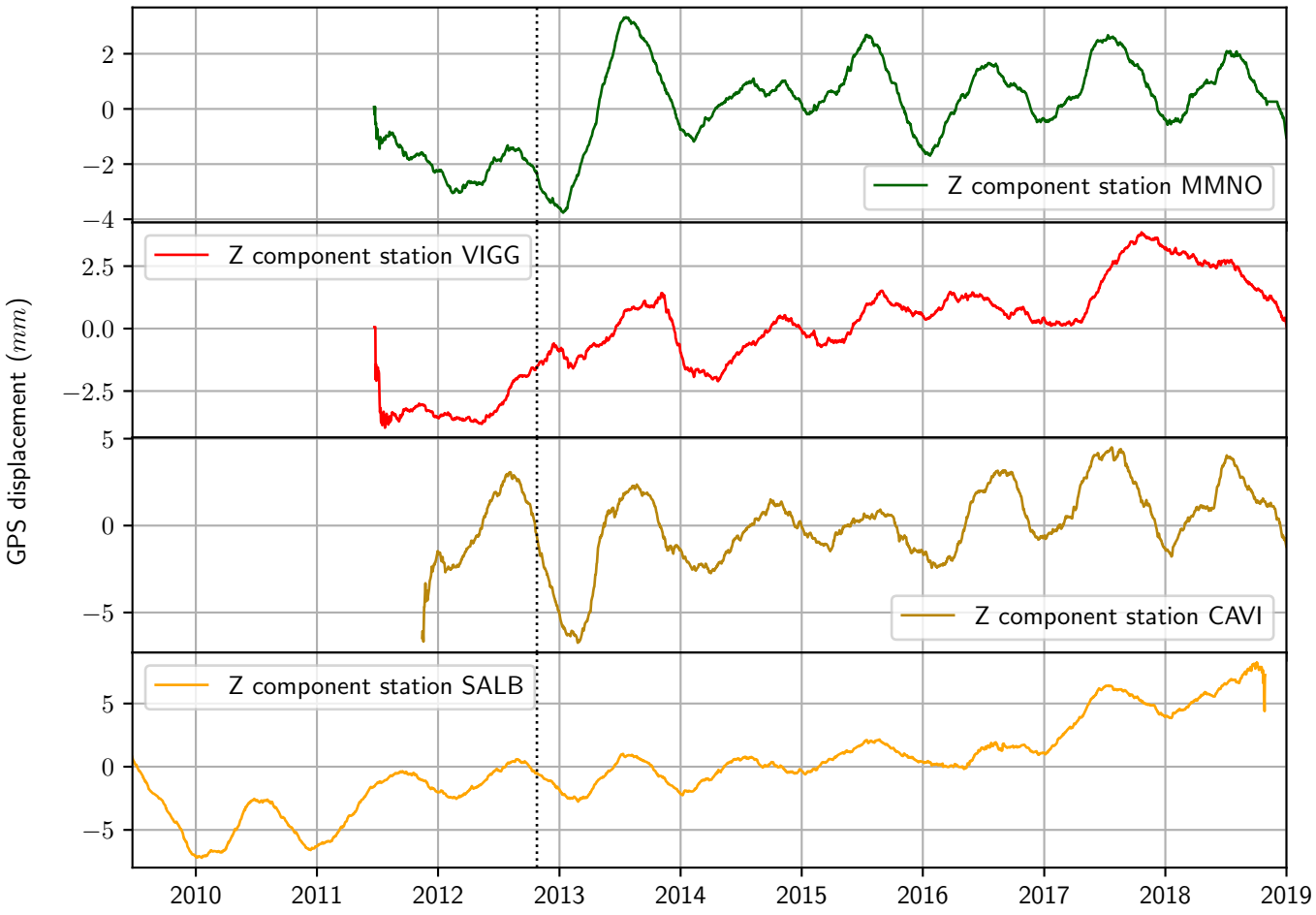

FIGURE 3.10: Vertical GPS components smoothed with a 180 days window. The dashed line marks the date of the $M5.0$ seismic event.

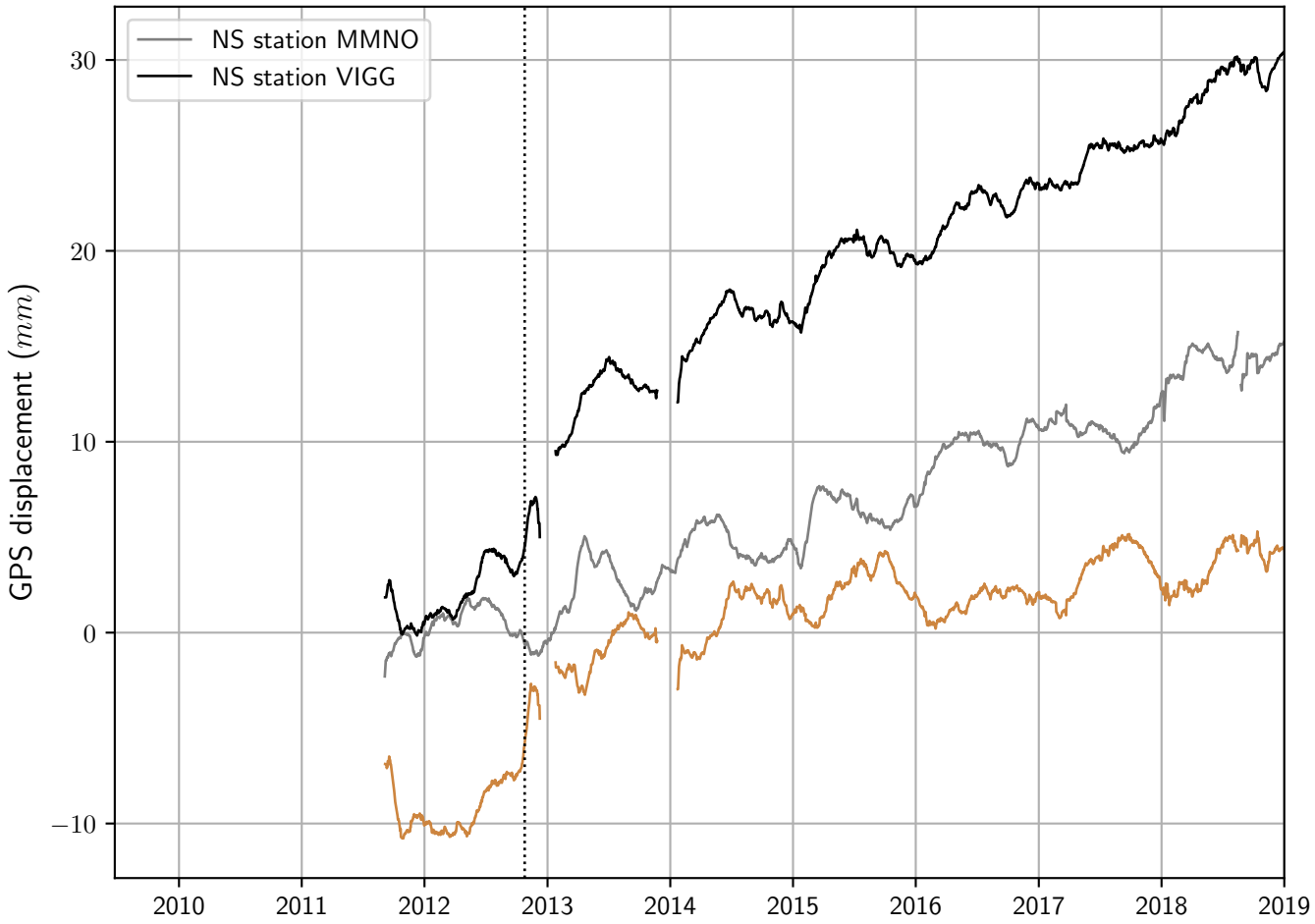

FIGURE 3.11: North-South components of the stations VIGG and MMNO shifted towards zero, and their relative displacement shifted around its mean. All the traces are smoothed with a 30 days window. The dashed line marks the date of the $M5.0$ seismic event.

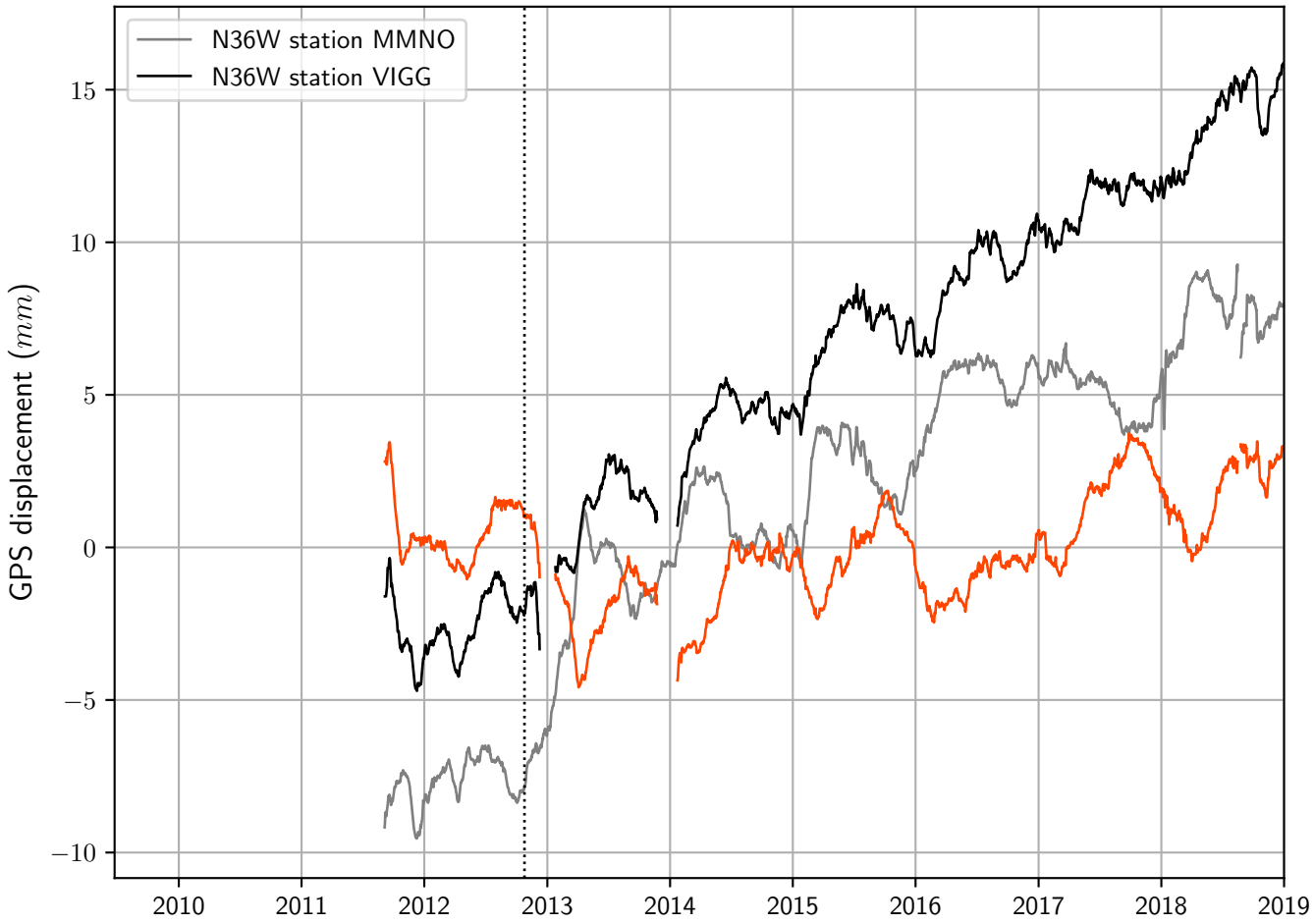

FIGURE 3.12: Rotated North-South components of the stations VIGG and MMNO shifted towards zero, and their relative displacement shifted around its mean. All the traces are smoothed with a 30 days window. The dashed line marks the date of the $M5.0$ seismic event.

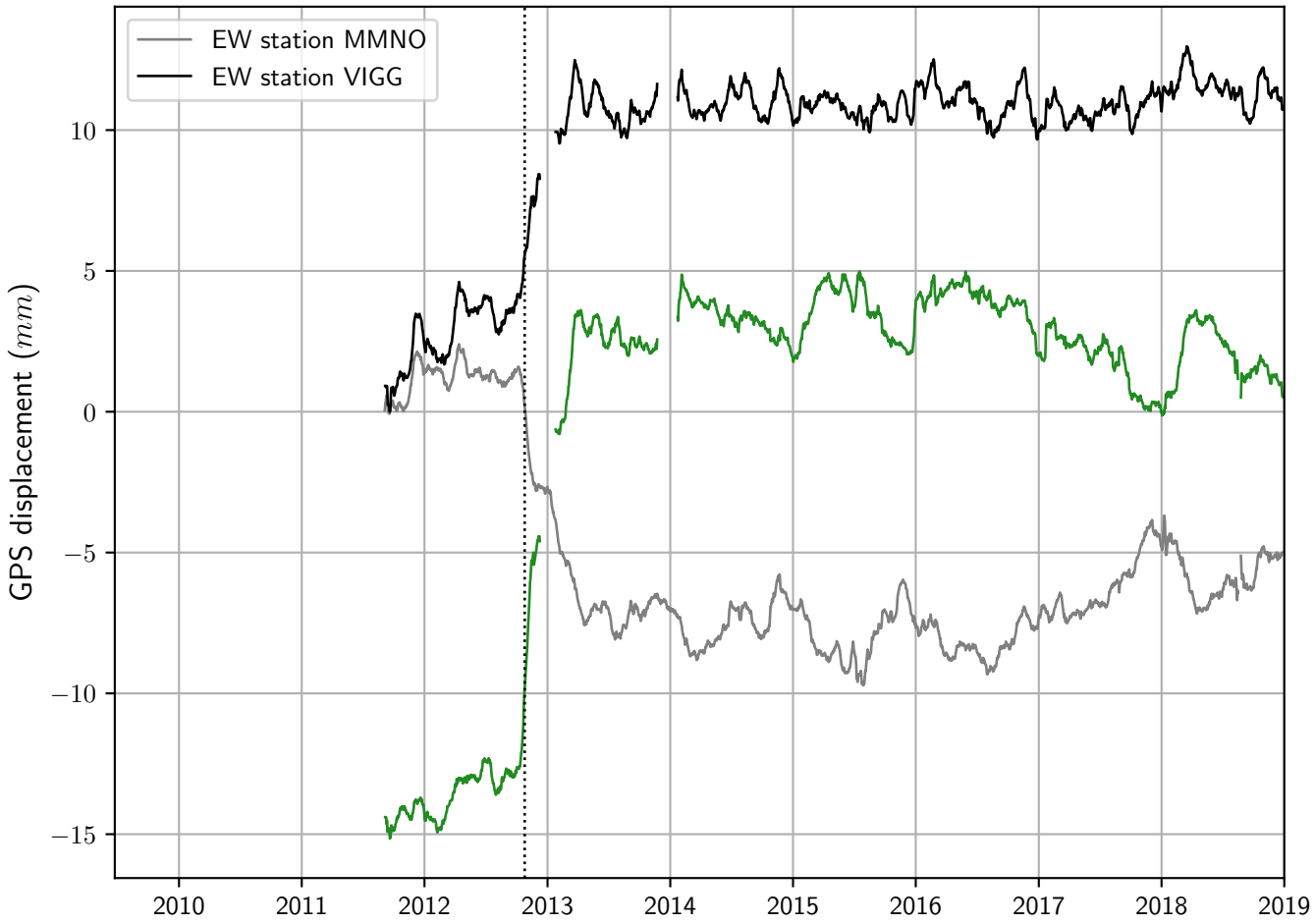

FIGURE 3.13: East-West components of the stations VIGG and MMNO shifted towards zero, and their relative displacement shifted around its mean. All the traces are smoothed with a 30 days window. The dashed line marks the date of the $M5.0$ seismic event.

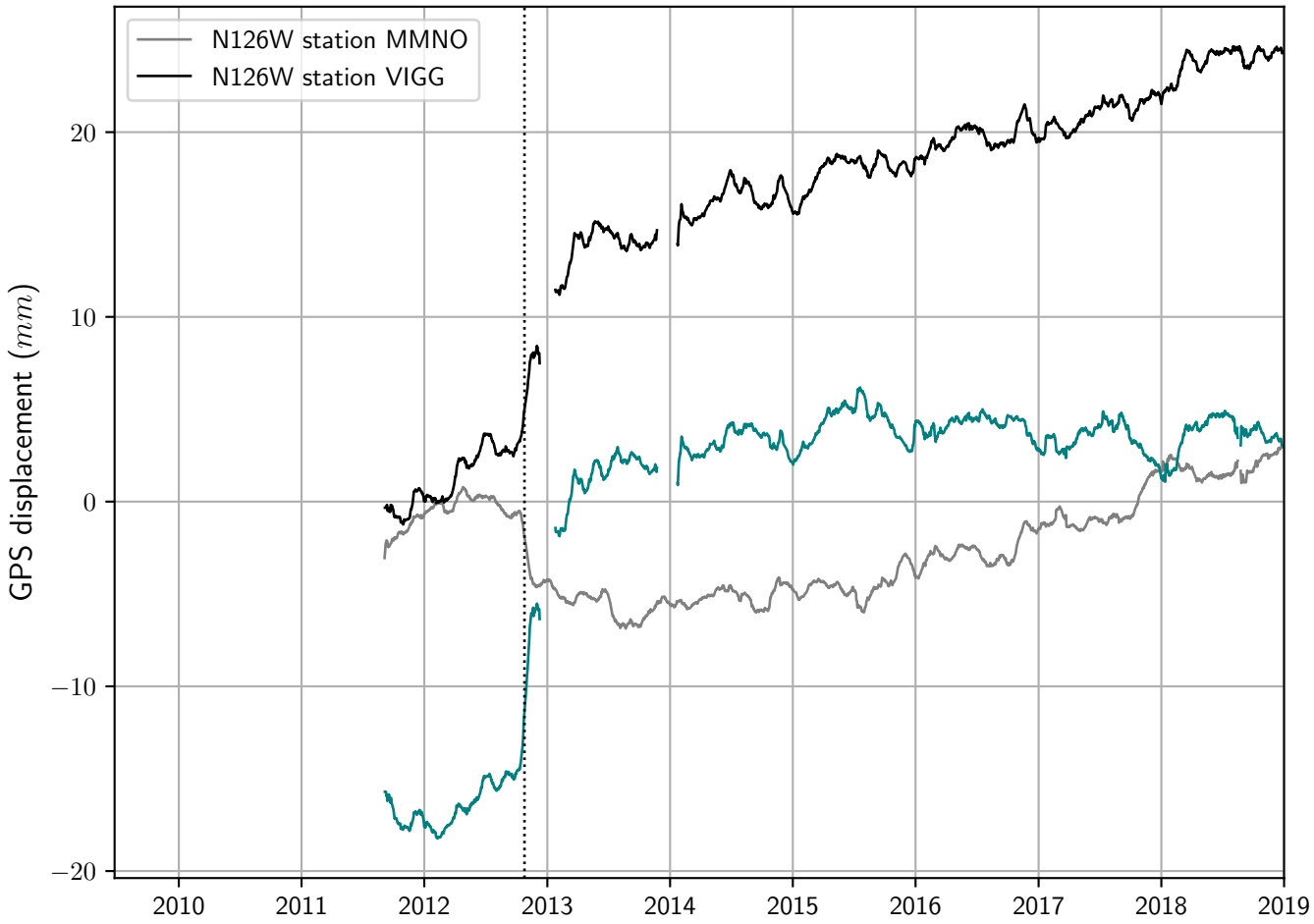

FIGURE 3.14: Rotated east-West components of the stations VIGG and MMNO shifted towards zero, and their relative displacement shifted around its mean. All the traces are smoothed with a 30 days window. The dashed line marks the date of the $M5.0$ seismic event.

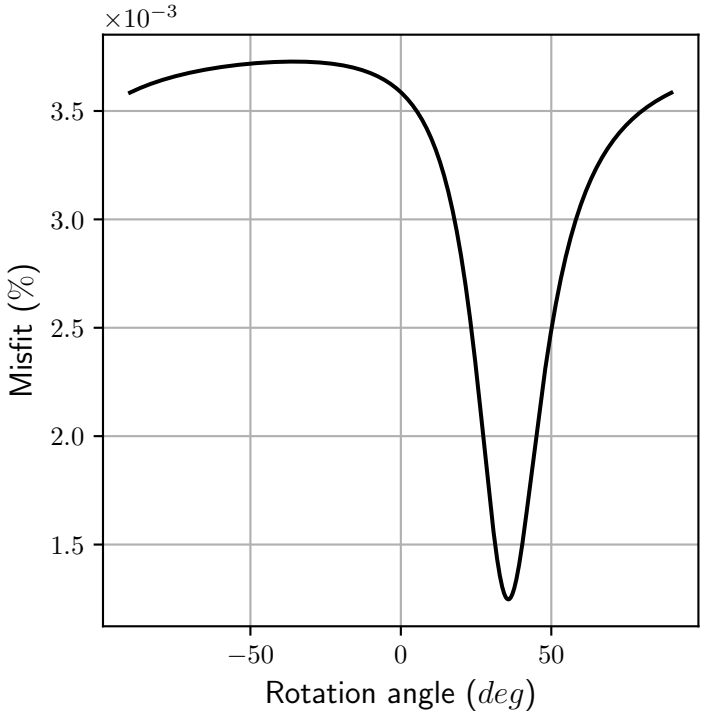

FIGURE 3.15: Misfit between the rotated NS relative displacement and the water level model for different periods.

Chapter 4

Coupling between surface and body waves

Ludovic Margerin, Andres Barajas, Michel Campillo
Article in published in Geophysical Journal International

In the preceding chapter we studied the influence of different factors on the measurements of apparent velocity at the surface, and we proposed a way to separate them using alternative sources of data and physical modeling. However, we want to locate the actual perturbations at depth that generate the phase fluctuations at the surface. This would give us a natural way of separating the phenomena responsible for those changes and a more insightful vision of the processes in the crust of the Earth. The first step towards that objective is to develop a theoretical frame over which we can describe the coupling between surface and body waves, and the energy exchange between them close to the surface. However, developing this model for the elastic case is still an open and challenging problem in seismology. In this chapter, we present a simpler case, a scalar model in the half-space that includes a particular boundary condition that gives rise to the natural formation of surface waves. Based on this model we find fundamental relations of the conversion between surface and body waves and we construct a set of transport equations that will be fundamental for the estimation of the travel-time sensitivity kernel in the next chapter.

4.1 Abstract

To describe the energy transport in the seismic coda, we introduce a system of radiative transfer equations for coupled surface and body waves in a scalar approximation. Our model is based on the Helmholtz equation in a half-space geometry with mixed boundary conditions. In this model, Green's function can be represented as a sum of body waves and surface waves, which mimics the situation on Earth. In a first step, we study the single-scattering problem for point-like objects in the Born approximation. Using the assumption that the phase of body waves is randomized by surface reflection or by interaction with the scatterers, we show that it becomes possible to define, in the usual manner, the cross-sections for surface-to-body and body-to-surface scattering. Adopting the independent scattering approximation, we then define the scattering mean free paths of body and surface waves including the coupling between the two types of waves. Using a phenomenological approach, we then derive a set of coupled transport equations satisfied by the specific energy density of surface and body waves in a medium containing a homogeneous distribution of point scatterers. In our model, the scattering mean free path of body waves is depth dependent as a consequence of the body-to-surface coupling. We demonstrate that an equipartition between surface and body waves is established at long lapse-time, with a ratio which is predicted by usual mode counting arguments. We derive a diffusion approximation from the set of transport equations and

show that the diffusivity is both anisotropic and depth dependent. The physical origin of the two properties is discussed. Finally, we present Monte-Carlo solutions of the transport equations which illustrate the convergence towards equipartition at long lapse-time as well as the importance of the coupling between surface and body waves in the generation of coda waves.

4.2 Introduction

In seismology, Radiative Transfer (RT) has been used for more than three decades to characterize the scattering and absorption properties of Earth's crust (see for instance Fehler et al., 1992; Hoshiba, 1993; Carcolé and Sato, 2010; Eulenfeld and Wegler, 2017). Since its introduction by Wu (1985) for scalar waves in the stationary regime, RT has been considerably improved to bring it in closer agreement with real-world applications. In particular, the coupling between shear and compressional waves was developed in a series of papers by Weaver (1990), Turner and Weaver (1994), Yuehua Zeng (1993), Sato (1994b), and Ryzhik, Papanicolaou, and Keller (1996). The model of Sato (1994b) was applied to data from an active experiment by Yamamoto and Sato (2010) and showed impressive agreement between observations and elastic RT theory. For comprehensive introductions to RT, the reader is referred to the review chapter by Margerin (2005) or the monograph of Sato and Fehler (2012).

Parallel to the physical and mathematical developments of the theory, more and more realistic Monte-Carlo simulations of the transport process were developed over the years. This includes, for example, the treatment of non-isotropic scattering (Abubakirov and Gusev, 1990; Hoshiba, 1995; Gusev and Abubakirov, 1996; Jing, Zeng, and Lin, 2014; Sato and Emoto, 2018), velocity and heterogeneity stratification (Hoshiba, 1997; Margerin, Campillo, and Tiggelen, 1998; Yoshimoto, 2000), coupling between shear and compressional waves (Margerin, Campillo, and Van Tiggelen, 2000; Przybilla, Wegler, and Korn, 2009), laterally varying velocity and scattering structures (Sanborn, Cormier, and Fitzpatrick, 2017). With the growth of computational power, Monte-Carlo simulations opened up new venues for the application of RT in seismology: imaging of deep Earth heterogeneity (Margerin, 2003; Shearer and Earle, 2004; Mancinelli and Shearer, 2013; "On the frequency dependence and spatial coherence of pkp precursor amplitudes"), mapping of the depth-dependent scattering and absorption structure of the lithosphere (Mancinelli, Shearer, and Liu, 2016; Takeuchi et al., 2017), modeling of propagation anomalies in the crust (Sens–Schönfelder, Margerin, and Campillo, 2009; Sanborn and Cormier, 2018), P-to-S conversions in the teleseismic coda (Gaebler, Sens-Schönfelder, and Korn, 2015), to cite a few examples only.

Recently, RT has also been applied to the computation of sensitivity kernels for time-lapse imaging methods such as coda wave interferometry (see e.g. Poupinet, Ellsworth, and Frechet, 1984; Snieder, 2006; Poupinet, Got, and Brenguier, 2008). Coda Wave Interferometry (CWI) exploits tiny changes of waveforms in the coda to map the temporal variations of seismic properties in 3-D. The mapping relies on the key concept of sensitivity kernels, which, in the framework of CWI, were introduced by Pacheco and Snieder (2005) in the diffusion regime and Pacheco and Snieder (2006) in the single-scattering regime. These kernels take the form of spatio-temporal convolutions of the mean intensity in the coda. It was later pointed out by Margerin et al. (2016) that an accurate computation of traveltime sensitivity kernels, valid for an arbitrary scattering order and an arbitrary spatial position, requires the knowledge of the angular distribution of energy fluxes in the coda. These fluxes, or specific intensities, are directly predicted by the radiative transfer model, which makes it attractive for imaging applications.

In noise-based monitoring (Wegler and Sens-Schönfelder, 2007) -also known as Passive Image Interferometry (PII)- the virtual sources and receivers are located at the surface of the medium so that the early coda is expected to contain a significant proportion of Rayleigh waves. At longer lapse-time, the surface waves couple with body waves and the coda eventually reaches an equipartition regime when all the propagative surface and body wave modes are excited to equal energy (Weaver, 1982; Hennino et al., 2001). Because the volumes explored by surface and body waves are significantly different, the knowledge of the composition of the coda wavefield at a given lapse-time in the coda is key to locate accurately the changes at depth in the crust.

Obermann et al. (2013a) and Obermann et al. (2016) proposed to express the sensitivity of coda waves as a linear combination of the sensitivity of surface and body waves, whose kernels are computed from scalar RT theory in 2-D and 3-D, respectively. The relative contribution of the 2-D and 3-D sensitivity kernels at a given lapse-time in the coda is determined by fitting the traveltime shift predicted by the theory against full wavefield numerical simulations in scattering media, where the background seismic velocity is perturbed in a fine layer at a given depth. This method has been validated in the case of 1-D perturbations through numerical tests and has the advantage of modeling exactly the complex coupling between surface and body waves in heterogeneous media. Furthermore, it can easily incorporate realistic topographies, which is important for the monitoring of volcanoes. The main drawbacks of the approach of Obermann et al. (2016) are the numerical cost and the fact that it requires a good knowledge of the scattering properties of the medium, which have to be determined by other methods such as MLTWA (Fehler et al., 1992; Hoshiba, 1993).

This brief overview illustrates that CWI and PII would benefit from a formulation of RT theory which incorporates the coupling between surface and body waves in a self-consistent way. In the case of a slab bounded by two free surfaces, Trégourès and Van Tiggelen, 2002 derived from first principles a quasi 2-D RT equation where the wavefield is expanded onto a basis of Rayleigh, Lamb and Love eigenmodes. Thanks to the normal mode decomposition, this model incorporates the boundary conditions at the level of the wave equation. The energy exchange between surface and body waves is treated by normal mode coupling in the Born approximation. A notable advantage of this formulation is the capacity to predict directly the energy decay in the coda and its parttioning onto different components. The two main limitations for seismological applications are the slab geometry, which may not always be realistic and the fact that the disorder should be weak, i.e., the mean free time should be large compared to the vertical transit time of the waves through the slab.

Zeng (2006) proposed a system of coupled integral equations to describe the exchange of energy between surface waves and body waves in the seismic coda. The formalism used by the author is interesting and bears some similarities with the one developed in this work, although we formulate the theory in integro-differential form. A blind spot in the work of Zeng (2006) is the coupling between surface and body waves, which is introduced in an entirely phenomenological way and differs significantly from our findings. A very promising investigation of the energy exchange between surface and body waves on the basis of the elastodynamic equations in a half-space geometry was performed by Maeda, Sato, and Nishimura (2008). Using the Born approximation, these authors calculated the scattering coefficients between all possible modes of propagation in a medium containing random inhomogeneities. The main limitation of their theory comes from the fact that the conversion from body to surface waves is quantified by a non-dimensional coefficient, which makes it difficult to extend their results beyond the single-scattering regime. The authors argue that the absence of a characteristic scale-length for body-to-surface attenuation is a consequence of the fact that all conversions occur in approximately one Rayleigh wavelength in the vicinity of the surface.

In this work, we revisit the problem of coupling surface and body waves in a RT framework using an approach similar to the one of Maeda, Sato, and Nishimura (2008). For simplicity, we limit our investigations to a scalar model based on the Helmholtz equation with an impedance (or mixed) boundary condition in a half-space geometry. To make the presentation self-contained, we review the most important features of this particular wave equation. Specifically, we recall that the modes of propagation are composed of body waves, and surface waves whose penetration depth depends on the impedance condition only. Hence, our model mimics the situation on Earth while minimizing the mathematical complexity. We then introduce a simple point-scattering model and study its properties in the Born approximation. Using the additional assumption that the surface reflexion randomizes the phase of the reflected wave, we are able to derive simple expressions for the scattering mean free path of both body and surface waves including the coupling between the two. We elaborate on this result to establish a set of two coupled RT equations satisfied by the specific energy density of surface and body waves using a phenomenological approach. Some consequences of our simple theory are explored, in particular the establishment of a diffusion and equipartition regime. Monte-Carlo simulations show the potential of the approach to model the transport of energy in the seismic coda from single-scattering to diffusion.

4.3 Scalar wave equation model with surface and body waves

In this section, we present the basic ingredients of our scalar model based on the Helmholtz equation. We describe how an appropriate modification of boundary conditions at the surface of a half-space gives rise to the presence of a surface wave. We subsequently present an expression of the Green's function and its asymptotic approximation. The concept of density of states, important for later developments, is recalled. For a thorough treatment of the mathematical foundations of our model, the interested reader is refered to the monograph of Hein and Hein R. (2010).

4.3.1 Equation of motion

We consider a 3-D version of the membrane vibration equation in a half-space geometry:

$$(\rho\partial_{tt} - T\Delta)\, u(t, \mathbf{R}) = 0 \tag{4.1}$$

where t is time and $\mathbf{R}$ is the position vector. It may be further decomposed as $\mathbf{R} = \mathbf{r} + z\hat{\mathbf{z}}$ ($z \geq 0$) with $\mathbf{r} = x\hat{\mathbf{x}} + y\hat{\mathbf{y}}$ and $(\hat{\mathbf{x}}, \hat{\mathbf{y}}, \hat{\mathbf{z}})$ denotes a Cartesian system. In Eq. (4.1) u, ρ and T may be thought of as the displacement, the density and the elastic constant of the medium, respectively. The wave Eq. (4.1) is supplemented with the boundary conditions:

$$\begin{aligned} &(\partial_z + \alpha)u(t, \mathbf{R})|_{z=0} = 0 \\ &+\text{radiation condition at } \infty \end{aligned} \tag{4.2}$$

The case of interest to us corresponds to $\alpha > 0$, i.e. when, as recalled below, the boundary can support a surface wave. Equation (4.1) can be derived by applying Hamilton's principle to the following Lagrangian density:

$$L = \frac{1}{2}\left[\rho(\partial_t u(t, \mathbf{R}))^2 - T(\nabla u(t, \mathbf{R}))^2 + \alpha T u(t, \mathbf{R})^2 \delta(z)\right] \tag{4.3}$$

Thanks to the last term of the Lagrangian (4.3), which corresponds to a negative elastic potential energy stored at the surface $z = 0$, the first B.C. in Eq. (4.2) becomes natural in

the sense of variational principles. To make the presentation self-contained, we explain in Appendix 4.8.1 the origin of the delta function in Eq. (4.3) in the simple case of a finite string with mixed boundary conditions at one end and free boundary conditions at the other end.

In the case of a harmonic time dependence $u \propto e^{-i\omega t}$ ($\omega > 0$), the vibrations are governed by Helmholtz Eq.:

$$\Delta u(\mathbf{R}) + \frac{\omega^2}{c^2} u(\mathbf{R}) = 0 \tag{4.4}$$

with $c = \sqrt{T/\rho}$ the speed of propagation of the waves in the bulk of the medium. Eq. (4.4) is complemented with the mixed boundary condition $\partial_z u + \alpha u = 0$ at $z = 0$ and an outgoing wave condition at infinity. From (4.3), we can deduce the energy flux density vector $\mathbf{J}$ and the energy density w using the concept of stress-energy tensor (Morse and Ingard, 1986). For harmonic motions, their average value over a period can be expressed as:

$$\mathbf{J} = -\frac{T}{2} \mathrm{Re}\left\{ i\omega u^* \nabla u \right\} \tag{4.5}$$

$$w = \frac{1}{4}\left\{ \rho\omega^2 |u|^2 + T|\nabla u|^2 - \alpha T |u|^2 \delta(z) \right\} \tag{4.6}$$

In the following section, we recall the consequences of mixed boundary conditions on the Helmoltz Eq., in particular the fact that it gives rise to a surface wave mode.

4.3.2 Eigenfunctions and Green's function

Due to the translational invariance of the medium, we look for eigen-solutions of Eq. (4.4) in the form $u = \psi(z) e^{i\mathbf{k}_\parallel \cdot \mathbf{r}}$ with $\mathbf{k}_\parallel = (k_x, k_y, 0)$. This leads to a self-adjoint eigenvalue problem in the z variable only. For $\alpha > 0$, part of the spectrum is discrete with eigenfunction :

$$u_s(\mathbf{r}, z) = \sqrt{2\alpha} e^{-\alpha z} \frac{e^{i\mathbf{k}_\parallel \cdot \mathbf{r}}}{2\pi} \tag{4.7}$$

with $\mathbf{k}_\parallel \cdot \mathbf{k}_\parallel - \alpha^2 = \dfrac{\omega^2}{c^2}$. The rest of the spectrum forms a continuum of body waves with normalized eigenfunctions:

$$u_b(\mathbf{r}, z) = \frac{1}{(2\pi)^{3/2}} (e^{-iqz} + r(q) e^{iqz}) e^{i\mathbf{k}_\parallel \cdot \mathbf{r}}, q \geq 0 \tag{4.8}$$

with $q^2 + \mathbf{k}_\parallel \cdot \mathbf{k}_\parallel = \dfrac{\omega^2}{c^2}$ and:

$$r(q) = \frac{q + i\alpha}{q - i\alpha} \tag{4.9}$$

Note the relations: (1) $q = (\omega \cos j)/c = k \cos j$ with j the incidence angle of the body wave and (2) $|r(q)|^2 = 1$, i.e., there is total reflection at the surface. For later reference, we introduce a specific notation for the vertical eigenfunction of body waves:

$$\psi_b(\hat{\mathbf{n}}, z) = (e^{-ikz\hat{\mathbf{n}}\cdot\hat{\mathbf{z}}} + r(k\hat{\mathbf{n}} \cdot \hat{\mathbf{z}}) e^{ikz\hat{\mathbf{n}}\cdot\hat{\mathbf{z}}}) \tag{4.10}$$

with $\hat{\mathbf{n}} \cdot \hat{\mathbf{z}} = \cos j$. Note that throughout the paper, we use a hat to denote a unit vector. The surface waves (4.7) and body waves (4.8) are normalized and orthogonal in the sense of the scalar product $\langle u | v \rangle = \int_{\mathbb{R}^3_+} u(\mathbf{R})^* v(\mathbf{R}) d^3R$, where u and v are arbitrary square integrable

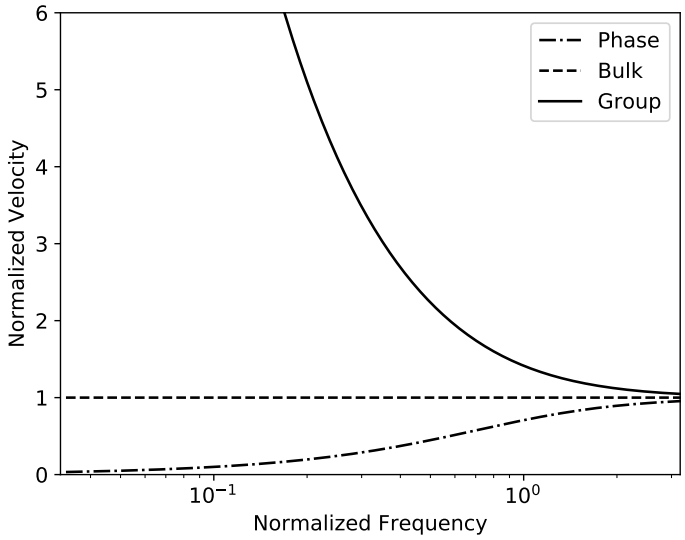

FIGURE 4.1: Dispersion of surface waves in a half-space with mixed boundary conditions. On the horizontal axis, the normalized frequency is defined as $\omega\alpha/c$. On the vertical axis, the velocity is normalized by the speed of body waves c.

functions. The surface wave phase velocity c_ϕ is given by:

$$c_\phi = \frac{c}{\sqrt{1 + \dfrac{c^2\alpha^2}{\omega^2}}} \tag{4.11}$$

and is always smaller than the bulk wave velocity c. The group velocity may be obtained in two different manners, namely, (1) using the classical formula based on the interference of a wave packet:

$$v_g = \frac{d\omega}{dk} = \frac{c^2}{c_\phi} = c\sqrt{1 + \frac{c^2\alpha^2}{\omega^2}} \tag{4.12}$$

and (2) using the principle of energy conservation:

$$\mathbf{v}_s^E = \frac{\langle \mathbf{J} \rangle}{\langle w \rangle} = v_g \hat{\mathbf{k}}_\parallel \tag{4.13}$$

where the brackets indicate an integration over the whole depth range.

The dispersion properties of the surface wave in our scalar model are illustrated in Figure 4.1. As is evident from Eqs (4.11)-(4.12), the group velocity is always faster than both the phase and body wave velocity. In the high-frequency limit, the phase and group velocity tend to the common value c. Using definition (4.13) it is possible to define the energy velocity of a body wave eigenmode (see Eq. 4.8):

$$\mathbf{v}_b^E = \lim_{h\to\infty} \frac{\langle \mathbf{J} \rangle_h}{\langle w \rangle_h} = c \sin j \hat{\mathbf{k}}_\parallel, \tag{4.14}$$

where $\langle\rangle_h$ denotes an integration from the surface to depth h. The depth averaging smoothes out the oscillations of $\mathbf{J}$ and w caused by the interference between the incident and reflected amplitudes. The passage to the limit is necessary because the integrals over depth diverge. Eq. (4.14) can be interpreted as follows. In the full-space case, the current vector of a single unit-amplitude plane wave with wavevector $\mathbf{k} = k(\cos j\hat{\mathbf{z}} + \sin j\hat{\mathbf{k}}_\parallel)$ is given by $\mathbf{J} = \rho\omega c^2 \mathbf{k}/2$

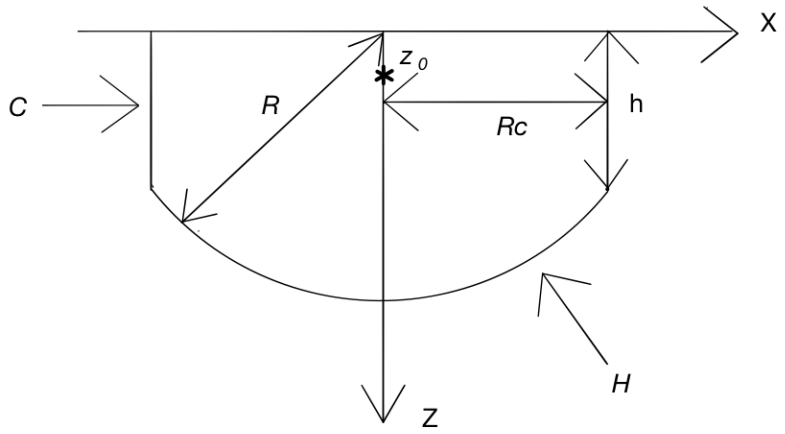

FIGURE 4.2: Geometry of the surface employed to compute the energy radiation of a point source located at $(0, 0, z_0)$. C is a cylindrical surface of radius R_c and height h. H is a hemispherical surface of radius R.

and carries an energy density $w = \rho\omega^2/2$. If we define $\mathbf{k}_r$ as the mirror image of $\mathbf{k}$ across the plane $z = 0$ and consider the sum of the current vector of two plane waves with wavevectors $\mathbf{k}$ and $\mathbf{k}_r$ we obtain $\mathbf{J} + \mathbf{J}_r = \rho\omega^2 c \sin j\hat{\mathbf{k}}_\parallel$. After normalization by the sum of energy densities, the result (4.14) is recovered. In other words, on average, the energy transported by a body wave mode is simply the sum of the energies transported by the incident and reflected waves, as if the two were independent.

Using the eigenmodes (4.7) and (4.8), one may obtain an exact representation of the Green's function of Helmholtz Eq. with mixed BC in the form:

$$\begin{aligned} G(\mathbf{r}, z, z_0) =& \frac{1}{(2\pi)^3} \int_0^{+\infty} dq \int_{\mathbb{R}^2} \frac{e^{i\mathbf{k}_\parallel \cdot \mathbf{r}} (e^{-iqz} + r(q)e^{iqz})(e^{-iqz_0} + r(q)e^{iqz_0})^*}{k^2 - k_\parallel^2 - q^2 + i\epsilon} d^2k_\parallel \\ &+ \frac{2\alpha e^{-\alpha(z+z_0)}}{(2\pi)^2} \int_{\mathbb{R}^2} \frac{e^{i\mathbf{k}_\parallel \cdot \mathbf{r}}}{k^2 + \alpha^2 - k_\parallel^2 + i\epsilon} d^2k_\parallel \end{aligned} , \tag{4.15}$$

where z_0 denotes the source depth, ϵ is a small positive number which guarantees the convergence of the integrals and the star * denotes complex conjugation. In Eq. (4.15) the first (resp. second) line represents the body wave (resp. surface wave) contribution. As shown in Appendix 4.8.2, the surface wave term can be computed analytically in terms of Hankel functions. The following far-field approximation of the Green's function of the Helmholtz Eq. (4.4) can be obtained using the stationary phase approximation for the body wave term:

$$G(\mathbf{r}, z, z_0) = -\frac{e^{ikR}}{4\pi R} \psi_b(\hat{\mathbf{R}}, z_0) - \frac{\alpha e^{-\alpha(z+z_0) + ik_s r + i\pi/4}}{\sqrt{2\pi k_s r}} \tag{4.16}$$

with $k_s = \omega/c_\phi$, $\hat{\mathbf{R}} = \mathbf{R}/R$ and $\mathbf{R} = \mathbf{r} + z\hat{\mathbf{z}}$. The expansion (4.16) is performed with respect to the midpoint of the source point and its mirror image by the surface $z = 0$. The z dependence of the first term is simply given by the body wave eigenfunction (4.8). For further computational details, the reader may consult Appendix 4.8.2.

4.3.3 Source radiation and density of states

We now compute the energy radiated by a point source located at $(0, 0, z_0)$. To do so, we introduce a cylindrical surface C of radius R_c extending from the free surface to a depth h greater than z_0 and large compared to $1/\alpha$. We close this surface with a hemispherical cap H of radius R centered at the surface point $(0, 0, 0)$. The geometry is schematically depicted in Figure 4.2. The energy flux vector (4.5) of the radiated field contains terms that are purely surface, purely bulk and cross-terms. The contribution of surface waves to the flux across the hemispherical surface is negligible (the error made is exponentially small). The contribution of body waves to the flux across the lateral cylindrical surface is also negligible because this surface subtends a solid angle which goes to 0 as R_c increases. The cross-terms are negligible across the whole surface because the coupled surface/body wave term decays algebraically faster than the surface wave term on the cylindrical surface and exponentially faster than the body wave term on the hemispherical surface. Hence, we may split the flux of radiated waves into a contribution of surface and body waves, respectively.

The energy transported per unit time by body waves through the hemispherical cap H is given by:

$$\begin{aligned}\mathcal{E}_b(z_0) =& \frac{\rho\omega^2 c}{2}\int_H |G_b(\mathbf{r}, z, z_0)|^2 R^2 d\hat{R} \\ =& \frac{\rho\omega^2 c}{32\pi^2}\int_{2\pi} |\psi_b(\hat{\mathbf{R}}, z_0)|^2 d\hat{R},\end{aligned} \tag{4.17}$$

with G_b the body wave part of Green's function. In the second line of Eq. (4.17), the integral is over the space directions subtended by the hemispherical cap. (N.B.: strictly speaking, the total solid angle is not equal to 2π because one should remove the directions corresponding to the cylinder. But as noted before, the measure of this set of directions goes to zero as R_c goes to infinity.) The function defined in Eq. (4.17) oscillates with depth around the following mean value:

$$\langle \mathcal{E}_b \rangle = \frac{\rho\omega^2 c}{8\pi} \tag{4.18}$$

Here the brackets may have at least 2 different meanings. The most obvious is an average over depth, as was done in the calculation of the group velocity. But we may also assume that the surface "scrambles" the phase of the reflected wave ϕ_r so that it becomes a random variable. In this scenario, the brackets would mean an average over all realizations of the random reflection process. Upon averaging over phase or depth, the interference pattern between the incident and reflected wave is smoothed out, so that the two approaches yield the same result. Note that the randomization of the phase does not affect energy conservation because the incident flux is still totally reflected. In particular, the discussion following the interpretation of Eq. (4.14) would still be valid. In practice, the assumption that the phase of the reflected wave is randomized by the surface may not be as unrealistic as it seems. Observations of reflected SH waves by Kinoshita (1993) at borehole stations in Japan indeed suggest that the reflected field is a distorted version of the incident one. This concurs with the general view that the subsurface of the Earth is highly heterogeneous at scales that can be much smaller than the wavelength and brings support to the idea that aberrating fine layers could indeed randomize the phase of the reflected wave as we hypothesize. In what follows, the scrambled-phase assumption will be adopted to simplify the treatment of the reflection of body waves at the surface.

The energy transported per unit time by surface waves through the lateral cylindrical surface C is given by:

$$\begin{aligned}\mathcal{E}_s(z_0) =& \frac{\rho\omega^2 v_g}{2}\int_C |G_s(\mathbf{r},z,z_0)|^2 r d\phi dz \\ =& \frac{\rho\omega^2 v_g \alpha^2 e^{-2\alpha z_0}}{4\pi k_s}\int_0^{2\pi} d\phi \int_0^h e^{-2\alpha z} dz \\ =& \frac{\rho\omega c^2 \alpha}{4} e^{-2\alpha z_0}\end{aligned} \tag{4.19}$$

with G_s the surface wave part of Green's function. Because h is large compared to $1/\alpha$ the integral over depth may be performed from 0 to $+\infty$ (the error incurred is exponentially small). We find the depth dependent surface-to-body energy ratio:

$$R(z_0) = \frac{\mathcal{E}_s(z_0)}{\langle \mathcal{E}_b \rangle} = \frac{2\pi c\alpha}{\omega} e^{-2\alpha z_0} \tag{4.20}$$

Formula (4.20) can also be understood in the light of the local density of states $n_{s,b}$ defined as (Sheng, 2006):

$$n_{s,b}(z_0) = -\left.\frac{\mathrm{Im} G_{s,b}(\mathbf{r},z_0,z_0)}{\pi}\right|_{\mathbf{r}=\mathbf{0},z=z_0} \times \frac{dk_{s,b}^2(\omega)}{d\omega}, \tag{4.21}$$

where $k_{s,b}(\omega)$ stands for the wavenumber of surface or body waves. Using the spectral representation (4.15), one obtains the (exact) formulas:

$$n_b(z_0) = \frac{\omega^2}{8\pi^2 c^3}\int_{2\pi} |\psi_b(\hat{\mathbf{R}},z_0)|^2 d^2\hat{R} \tag{4.22}$$

$$\langle n_b \rangle = \frac{\omega^2}{2\pi c^3} \tag{4.23}$$

$$n_s(z_0) = \frac{\alpha\omega}{c^2} e^{-2\alpha z_0} \tag{4.24}$$

which show that the partitioning of the energy radiated into surface and body waves by the source $R(z_0)$ is given by the ratio of their local density of states $n_s(z_0)/\langle n_b \rangle$. Finally, we may compute the partitioning ratio $\mathcal{R}$ between the modal density of surface and body waves by integrating Eq.(4.24) over z and taking the ratio with (4.23). This yields the simple result:

$$\mathcal{R} = \int_0^\infty \frac{n_s(z)}{\langle n_b \rangle} dz = \frac{\pi c}{\omega} \tag{4.25}$$

where it is to be noted that the modal density ratio $\mathcal{R}$ is independent of the scale length α appearing in the mixed boundary condition of the Helmholtz equation. This result could have been deduced directly from the dispersion relations of body and surface waves using classical mode counting arguments (Kittel, 1976). It is worth noting that the local density of states (4.23) is exactly the same as in the case of the Helmholtz equation in full 3-D space. Although the integral in (4.22) is carried over one hemisphere only, each eigenmode ψ_b is composed of an incident and a reflected wave, which -on average- doubles its contribution compared to a single plane wave state. In the next section, we use our knowledge of the Green's function to derive the scattering properties of surface and body waves including the coupling between the two modes of propagation.

4.4 Single scattering by a point scatterer

In this section, we calculate the energy radiated by a single scatterer in a half-space geometry for incident surface or body waves. For simplicity, we restrict our investigations to point scatterers and employ Born's approximation. The resulting expressions are simplified following the scrambled phase approximation and interpreted in terms of scattering cross-sections.

4.4.1 Scattering of a surface wave

We now consider the following perturbed Helmholtz Eq.:

$$\Delta u(\mathbf{r}, z) + k^2(1 + \epsilon a^3 \delta(\mathbf{r})\delta(z - z_s))u(\mathbf{r}, z) = 0 \tag{4.26}$$

Here a represents the typical linear dimension of the scatterer located at $(0, 0, z_s)$ and it is understood that $ka \ll 1$. ϵ is the local perturbation of inverse squared velocity. Following the standard procedure (Snieder, 1986), we look for solutions of Eq. (4.26) of the form: $u = u_0 + u_s$, where $u_0(\mathbf{r}, z) = e^{-\alpha z + i\sqrt{\alpha^2+\omega^2/c^2}x}$ is a surface wave eigenmode of the Helmholtz equation (the incident field) and u_s is the scattered field. Using the Born approximation, one obtains:

$$u(\mathbf{r}, z) = u_0(\mathbf{r}, z) - k^2 \epsilon a^3 G(\mathbf{r}, z, z_s) u_0(\mathbf{0}, z_s) \tag{4.27}$$

Introducing the coupling strength $S = k^2 a^3 \epsilon e^{-\alpha z_s}$, one may express the energy radiated by the body waves through the hemispherical cap H (per unit time) as:

$$U^{s\to b} = \frac{\rho\omega^2 S^2 c}{2(4\pi)^2 R^2} \int_{2\pi} |\psi_b(\hat{\mathbf{R}}, z_s)|^2 R^2 d\hat{R}. \tag{4.28}$$

Note that the coupling term S depends on both intrinsic properties of the scatterer -size and strength of perturbations- as well as on the properties of the incident wave -depth dependence of eigenfunction and frequency-.

For a unit amplitude surface wave, the vertically-integrated time-averaged energy flux density is given by

$$|\mathbf{J}_s| = \frac{\rho\omega^2 v_g}{4\alpha}. \tag{4.29}$$

The ratio of (4.28) and (4.29) gives the surface-to-body scattering cross-section:

$$\sigma^{s\to b}(z_s) = \frac{\alpha c k^4 a^6 \epsilon^2 e^{-2\alpha z_s}}{8\pi^2 v_g} \int_{2\pi} |\psi_b(\hat{\mathbf{R}}, z_s)|^2 d\hat{R} \tag{4.30}$$

This cross-section has unit of length. In the case where the surface scrambles the phase of the reflected wave, we may compute the mean conversion scattering cross-section by taking the average over the random phase ϕ_r.

$$\langle \sigma^{s\to b}(z_s) \rangle = \frac{c\alpha k^4 a^6 \epsilon^2 e^{-2\alpha z_s}}{2\pi v_g} \tag{4.31}$$

Let us remark again that the averaging smoothes out the interference pattern of the body wave eigenfunction ψ_b but does not affect the conservation of energy. Furthermore, the averaging procedure makes the scattering pattern isotropic since $\langle |\psi_b(\hat{\mathbf{R}}, z_s)|^2 \rangle = 2$ with an equal contribution of upgoing and downgoing waves. The computation of the surface-to-surface scattering cross-section proceeds in a similar way. The surface-wave energy radiated through

the lateral surface is given by:

$$\begin{aligned} U^{s\to s} =& \frac{\rho\omega c^2\alpha^2 S^2}{4\pi}\int_{2\pi}\int_0^{+\infty} e^{-2\alpha(z+z_s)}d\phi dz \\ =& \frac{\rho\omega c^2\alpha S^2 e^{-2\alpha z_s}}{4} \end{aligned} \tag{4.32}$$

Normalizing the result (4.32) by the incident flux yields the surface-to-surface scattering cross section:

$$\sigma^{s\to s}(z_s) = \frac{c\alpha^2 k^3 a^6 \epsilon^2 e^{-4\alpha z_s}}{v_g}, \tag{4.33}$$

again with unit of length. If we have a collection of point scatterers with volume density n, we may define a surface wave scattering mean free path using the independent scattering approximation as (Lagendijk and Van Tiggelen, 1996; Trégourès and Van Tiggelen, 2002; Maeda, Sato, and Nishimura, 2008):

$$\frac{1}{l^s} = \int_0^{\infty} n\left(\sigma^{s\to s}(z) + \sigma^{s\to b}(z)\right) dz \tag{4.34}$$

The approximate formula (4.34) neglects all recurrent interactions between the scatterers, which is valid for sufficiently low concentrations of inclusions.

4.4.2 Scattering of body waves

In the case of an incident body wave mode (4.8), the computation of the energy radiated in the form of body or surface waves can be performed as in the previous section. The definition of the scattering cross-section, however, is problematic if we stick to the modal description. Indeed, the vertically integrated energy flux density of a body wave mode, as defined in Eq. (4.8), diverges. We must therefore come back to a conventional plane wave description. We first consider the situation where the scatterer is located at a large depth in the half-space. In this case, it appears reasonable to think that the scattering of a body wave mode should be equivalent to the scattering of a plane wave in the full-space case, at least in a sense to be specified below. To verify the correctness of this assertion, we start by computing the body wave cross-section in absence of a boundary. Assuming a unit amplitude incident plane wave and using again the Born approximation, one may express the scattered energy as:

$$U_{\text{full}} = \frac{\rho\omega^2 c(k^2\epsilon a^3)^2}{8\pi}, \tag{4.35}$$

Normalizing the result by the energy flux density of the incident wave:

$$|\mathbf{J}_b| = \frac{\rho\omega^2 c}{2} \tag{4.36}$$

we obtain:

$$\sigma_{\text{full}} = \frac{(k^2\epsilon a^3)^2}{4\pi} \tag{4.37}$$

In the half-space geometry, the incident wave has the form (4.8). The total energy scattered in the form of body waves is still given by Eq. (4.28) provided one redefines the coupling constant as $S = k^2 a^3 \epsilon |\psi_b(\hat{\mathbf{R}}_i, z_s)|^2$, where $\hat{\mathbf{R}}_i$ refers to the incidence direction of the body wave. Eq. (4.28) differs from formula (4.35) as a consequence of the interference between the incident and reflected waves. In the case of a scattering medium, we may expect these

interferences to be blurred due to the randomization of the phase by the scattering events. In this scenario, the phase of the incident and reflected waves may be expected to be uncorrelated. Upon averaging the result (4.28) over the random phase of the reflected wave, one obtains:

$$U^{b\to b} = \frac{\rho\omega^2 c(k^2\epsilon a^3)^2}{4\pi}, \tag{4.38}$$

which is exactly the double of the full-space result (4.35). Keeping in mind that the energy flux of the incident plane wave interacts twice with the scatterer (direct interaction + interaction after reflexion) and using the assumption that the energy fluxes of incident and reflected waves do not interfere and may therefore be added, we obtain the result:

$$\langle\sigma^{b\to b}\rangle = \sigma_{\text{full}} \tag{4.39}$$

As announced, the average scattering cross-section of body waves in the half space is the same as in the full space for a scatterer located far away from the boundary. Conceptually, the "scrambled phase" approximation allows us to extend the result (4.39) to a scatterer located at an arbitrary depth in the medium thanks again to the assumption that the incident and reflected waves are statistically independent. In this scenario, on average, the surface does not modify anything to the scattering of body waves into body waves as compared to the full-space case.

Following the same approach and approximation, we can calculate the body-to-surface scattering cross-section. The energy radiated in the form of surface waves is given by:

$$U^{b\to s} = \frac{\rho\omega c^2\alpha(k^2\epsilon a^3)^2 e^{-2\alpha z_s}|\psi_b(\hat{\mathbf{R}}_i, z_s)|^2}{4} \tag{4.40}$$

After averaging and normalization by the total energy flux (incident + reflected), one finds:

$$\langle\sigma^{b\to s}\rangle(z) = \frac{\alpha(k^2\epsilon a^3)^2 e^{-2\alpha z_s}}{2k} \tag{4.41}$$

Note that all the remarks pertaining to the mean scattering pattern made after Eq. (4.30) also apply to the derivation of Eq. (4.39) and (4.41). The scattering cross-sections $\sigma^{b\to b}$ and $\sigma^{b\to s}$ have unit of surface. Using the independent scattering approximation again, we conclude that the inverse scattering mean free path of body waves defined as:

$$\frac{1}{l^b(z)} = n(\sigma^{b\to s}(z) + \sigma^{b\to b}) \tag{4.42}$$

depends on the depth in the medium, as a consequence of the coupling with surface waves. A simple but fundamental reciprocity relation may be established between the surface-to-body and body-to-surface scattering mean free time. The later may be expressed as:

$$\tau^{b\to s}(z) = \frac{2ke^{2\alpha z}}{nc\alpha(k^2a^3\epsilon)^2} \tag{4.43}$$

while the former may be obtained after performing the integral over depth in Eq. (4.34):

$$\tau^{s\to b} = \frac{4\pi}{nc(k^2a^3\epsilon)^2} \tag{4.44}$$

The ratio between the two quantities is given by:

$$\frac{\tau^{s\to b}}{\tau^{b\to s}(z)} = \frac{2\pi\alpha e^{-2\alpha z}}{k} = R(z) \tag{4.45}$$

where Eq. (4.20) has been used. Eq. (4.45) establishes a link between the surface-to-body versus body-to-surface conversion rates and the local density of states. In the case of elastic waves, a similar relation applies (Weaver, 1990; Ryzhik, Papanicolaou, and Keller, 1996): the ratio between the P-to-S and S-to-P scattering mean free times is given by the ratio of the density of states of P and S waves. As shown in the next section, the relation (4.45) plays a key role in the establishment of an equipartion between surface and body waves.

4.5 Equation of radiative transfer

In this section, we employ standard energy balance arguments to derive a set of coupled equations of RT for surface and body waves in a half-space containing a uniform distribution of point-scatterers. A notable feature of our formulation is the appearance of the penetration depth of surface waves as a parameter in the Equations.

4.5.1 Phenomenological derivation

Before we establish the transport equation, a few remarks are in order. It is clear that the transport of surface wave energy is naturally described by a specific surface energy density $\epsilon_s(t, \mathbf{r}, \hat{\mathbf{n}})$ where $\hat{\mathbf{n}}$ is a unit vector in the horizontal plane. The surface energy density of surface waves may in turn be defined as:

$$\varepsilon_s(t, \mathbf{r}) = \int_{2\pi} \epsilon_s(t, \mathbf{r}, \hat{\mathbf{n}}) d\hat{n} \tag{4.46}$$

where the integral is carried over all propagation directions in the horizontal plane. Note that the ϵ_s symbol should not be confused with the strength of fluctuations in Eq. (4.26). In contrast with surface waves, the transport of body waves is described by a specific volumetric energy density $e_b(t, \mathbf{r}, \hat{\mathbf{k}}, z)$ where $\hat{\mathbf{k}}$ is a vector on the unit sphere in 3-D. The volumetric energy density of body waves is again obtained by integration of the specific energy density over all propagation directions in 3-D:

$$E_b(t, \mathbf{r}, z) = \int_{4\pi} e_b(t, \mathbf{r}, z, \hat{\mathbf{k}}) d\hat{k} \tag{4.47}$$

In the usual formulation of transport equations, energy densities have the same unit (either surfacic or volumetric). In order to treat on the same footing surface and body waves, we introduce the following volumetric energy density of surface waves as:

$$e_s(t, \mathbf{r}, z, \hat{\mathbf{n}}) = 2\alpha\epsilon_s(t, \mathbf{r}, \hat{\mathbf{n}}) e^{-2\alpha z} \tag{4.48}$$

It is clear that upon integration of e_s over depth, one recovers the surface density ϵ_s. The exponential decay of the surface wave energy density is directly inherited from the modal shape and implies that the coupling between surface and body waves mostly occurs within a skin layer of typical thickness $1/2\alpha$. For future reference, we introduce the following notation:

$$E_s(t, \mathbf{r}, z) = \int_{2\pi} e_s(t, \mathbf{r}, z, \hat{\mathbf{n}}) d\hat{n} \tag{4.49}$$

to represent the volumetric energy density of surface waves, consistent with Eq. (4.47). Note that the total energy density at a given point will be defined as the sum $(E_b(t,\mathbf{r},z)+E_s(t,\mathbf{r},z))$, thereby implying the incoherence between the two types of waves.

With this definition of the surface wave energy density, the phenomenological derivation of the radiative transport equation follows exactly the same procedure as in the multi-modal case (Turner and Weaver, 1994). A beam of energy followed along its path around direction $\hat{\mathbf{n}}^i$ is affected by (1) conversion of energy into other propagating modes and/or deflection into other propagation directions $\hat{\mathbf{n}}^o \neq \hat{\mathbf{n}}^i$; (2) a gain of energy thanks to the reciprocal process: a wave with mode i propagating in direction $\hat{\mathbf{n}}^i$ can be converted into a wave with mode o propagating in direction $\hat{\mathbf{n}}^o$ by scattering. In the general case of finite size scatterers we may anticipate scattering to be anisotropic. To describe such an angular dependence of the scattering process, we may introduce normalized phase functions $p^{i\to o}(\hat{\mathbf{n}}^o,\hat{\mathbf{n}}^i)$. The phase function may be understood as the probability that a wave of mode i propagating in direction $\hat{\mathbf{n}}^i$ be converted into a wave of mode o propagating in direction $\hat{\mathbf{n}}^o$. To be interpretable probabilistically, its integral over all outgoing directions $(\hat{\mathbf{n}}^o)$ should equal 1. Note that in addition to the incoming and outgoing propagation directions, the phase function may also depend on the depth in the medium as a consequence of the presence of the surface. In the case of point scatterers, this complexity disappears thanks to the scrambled phase assumption and will therefore not be considered in our formalism.

A detailed local balance of energy yields the following system of coupled transport equations:

$$\begin{aligned}
\left(\partial_t + v_g\hat{\mathbf{n}}\cdot\nabla\right) e_s(t,\mathbf{r},z,\hat{\mathbf{n}}) = &-\frac{e_s(t,\mathbf{r},z,\hat{\mathbf{n}})}{\tau^s} + \frac{1}{\tau^{s\to s}}\int_{2\pi} p^{s\to s}(\hat{\mathbf{n}},\hat{\mathbf{n}}')e_s(t,\mathbf{r},z,\hat{\mathbf{n}}')d\hat{n}' \\
&+ \frac{1}{\tau^{b\to s}(z)}\int_{4\pi} p^{b\to s}(\hat{\mathbf{n}},\hat{\mathbf{k}}';z)e_b(t,\mathbf{r},z,\hat{\mathbf{k}}')d\hat{k}' + s_s(t,\mathbf{r},z,\hat{\mathbf{n}}) \\
\left(\partial_t + c\hat{\mathbf{k}}\cdot\nabla\right) e_b(t,\mathbf{r},z,\hat{\mathbf{k}}) = &-\frac{e_b(t,\mathbf{r},z,\hat{\mathbf{k}})}{\tau^b(z)} + \frac{1}{\tau^{b\to b}}\int_{4\pi} p^{b\to b}(\hat{\mathbf{k}},\hat{\mathbf{k}}')e_b(t,\mathbf{r},z,\hat{\mathbf{k}}')d\hat{k}' \\
&+ \frac{1}{\tau^{s\to b}}\int_{2\pi} p^{s\to b}(\hat{\mathbf{k}},\hat{\mathbf{n}}')e_s(t,\mathbf{r},z,\hat{\mathbf{n}}')d\hat{n}' + s_b(t,\mathbf{r},z,\hat{\mathbf{n}})
\end{aligned} \tag{4.50}$$

where the terms $s_{s,b}$ represent sources of surface and body waves. To take into account the reflection of body waves at the surface, the sytem (4.50) is supplemented with the following boundary condition for the energy density e_b:

$$e_b(t,\mathbf{r},0,\hat{\mathbf{k}}) = e_b(t,\mathbf{r},0,\hat{\mathbf{k}}_r) \tag{4.51}$$

where $\hat{\mathbf{k}}_r$ is the mirror image of the incident direction $\hat{\mathbf{k}}$ $(\hat{\mathbf{k}}\cdot\hat{\mathbf{z}} < 0)$ across the horizontal plane $z = 0$. The boundary condition (4.51) is compatible with the assumption that the incident and reflected waves are statistically independent.

In the simple case of a unit point-like source at depth z_0, the terms s_s and s_b are given respectively by:

$$\begin{aligned}
s_s(t,\mathbf{r},z,\hat{\mathbf{n}}) =& \frac{2\alpha R(z_0)e^{-2\alpha z}\delta(\mathbf{r})}{2\pi(1+R(z_0))} \\
s_b(t,\mathbf{r},z,\hat{\mathbf{k}}) =& \frac{\delta(z-z_0)\delta(\mathbf{r})}{4\pi(1+R(z_0))}
\end{aligned} \tag{4.52}$$

where $R(z_0)$ is the energy partitioning ratio defined in Eq. (4.20). Note that s_s follows the

same exponential decay as e_s with depth z (see Eq. 4.48), which takes into account the vertical dependence of the surface wave eigenfunction. In Eq. (4.52), the complex dependence of the body wave radiation with depth has been simplified by averaging the exact result (4.17) over the random phase of the reflected wave. As a consequence, the energy radiation at the source covers uniformly the whole sphere of space directions in 3-D.

A similar remark applies to the scattering from body waves to body waves, which have been treated as if the surface was absent in Eq. (4.50). Again, this approximation is admissible if the scattered upgoing and downgoing energy fluxes are statistically independent, a condition which is guaranteed by the randomization of the phase of the waves upon reflection at the surface in our model. As discussed in the previous section, in the case of point scatterers the phase averaging procedure makes all scattering processes isotropic which allows us to simplify the system of Eqs (4.50) by evaluating the scattering integrals on the right-hand side of Eq. (4.50):

$$\begin{aligned}
(\partial_t + v_g \hat{\mathbf{n}} \cdot \nabla)\, e_s(t, \mathbf{r}, z, \hat{\mathbf{n}}) &= -\frac{e_s(t, \mathbf{r}, z, \hat{\mathbf{n}})}{\tau^s} + \frac{E_s(t, \mathbf{r}, z)}{2\pi \tau^{s\to s}} + \frac{E_b(t, \mathbf{r}, z)}{2\pi \tau^{b\to s}(z)} + s_s(t, \mathbf{r}, z, \hat{\mathbf{n}}) \\
\left(\partial_t + c\hat{\mathbf{k}} \cdot \nabla\right) e_b(t, \mathbf{r}, z, \hat{\mathbf{n}}) &= -\frac{e_b(t, \mathbf{r}, z, \hat{\mathbf{k}})}{\tau^b(z)} + \frac{E_b(t, \mathbf{r}, z)}{4\pi \tau^{b\to b}} + \frac{E_s(t, \mathbf{r}, z)}{4\pi \tau^{s\to b}} + s_b(t, \mathbf{r}, z, \hat{\mathbf{k}})
\end{aligned} \tag{4.53}$$

where we have used the normalization condition of the phase functions. The decreasing efficacy of scattering conversions with depth is guaranteed by the exponential decay of $\tau^{b\to s}(z)^{-1}$ and $E_s(t, \mathbf{r}, z)$ in the first and second Eq. of the coupled sytem (4.53), respectively. It is worth recalling that the depth dependence of the scattering mean free times of body waves $\tau^b(z)$ and $\tau^{b\to s}(z)$ is caused by the coupling with surface waves and not by a stratification of heterogeneity.

4.5.2 Energy conservation and equipartition

A self-consistent formulation of coupled transport equations should verify two elementary principles: energy conservation and equipartition. To demonstrate these properties from the basic set of equations (4.50) or (4.53), we proceed in the usual fashion (Turner and Weaver, 1994). An integration of each equation over all possible propagation directions $\hat{\mathbf{n}}$ (in 2-D) or $\hat{\mathbf{k}}$ (in 3-D) yields:

$$\begin{aligned}
\partial_t E_s(t, \mathbf{r}, z) + \nabla \cdot \mathbf{J}_s(t, \mathbf{r}, z) &= -\frac{E_s(t, \mathbf{r}, z)}{\tau^{s\to b}} + \frac{E_b(t, \mathbf{r}, z)}{\tau^{b\to s}(z)} \\
\partial_t E_b(t, \mathbf{r}, z) + \nabla \cdot \mathbf{J}_b(t, \mathbf{r}, z) &= -\frac{E_b(t, \mathbf{r}, z)}{\tau^{b\to s}(z)} + \frac{E_s(t, \mathbf{r}, z)}{\tau^{s\to b}},
\end{aligned} \tag{4.54}$$

where we have used the definition of the mean free times on the RHS of (4.54). Note that we have dropped the source terms since they are not essential to our argumentation. In Eq. (4.54), we have introduced the energy flux density vector of surface and body waves:

$$\begin{aligned}
\mathbf{J}_s &= \int_{2\pi} e_s(t, \mathbf{r}, z, \hat{\mathbf{n}}) v_g \hat{\mathbf{n}} d\hat{n} \\
\mathbf{J}_b &= \int_{4\pi} e_b(t, \mathbf{r}, z, \hat{\mathbf{k}}) c\hat{\mathbf{k}} d\hat{k}
\end{aligned} \tag{4.55}$$

Note that $\mathbf{J}_s$ is contained in a horizontal plane. Upon integration over the whole half-space, the terms which contain the current density vectors can be converted into surface integrals that vanish. Denoting by a double bar an integration over $\mathbf{r}$ and z, and summing the two Eqs

of the system (4.54) leaves us with:

$$\partial_t \left(\bar{\bar{E}}_s(t) + \bar{\bar{E}}_b(t) \right) = 0 \tag{4.56}$$

which demonstrates the conservation of energy.

In order to prove the existence of equipartition, we integrate each Eq. of the system (4.54) over the horizontal plane and from the surface to a finite depth h, typically large compared to the surface wave penetration depth. To simplify the derivation, we assume that at $z = h$ lies a perfectly reflecting surface through which no energy can flow. Because $\alpha h \gg 1$, the medium may be still be considered as a half-space in the treatment of surface waves. This leads us to:

$$\begin{aligned} \partial_t \bar{\bar{E}}_s(t) &= -\frac{\bar{\bar{E}}_s(t)}{\tau^{s\to b}} + \int_0^h \frac{\bar{E}_b(t,z)}{\tau^{b\to s}(z)} dz \\ \partial_t \int_0^h \bar{E}_b(t,z) dz &= -\int_0^h \frac{\bar{E}_b(t,z)}{\tau^{b\to s}(z)} dz + \frac{\bar{\bar{E}}_s(t)}{\tau^{s\to b}}, \end{aligned} \tag{4.57}$$

where the single bar denotes an integration over $\mathbf{r}$ only. Note that $\bar{\bar{E}}_s$ is the total energy of surface waves (up to an exponentially small correction term), in contrast with $\bar{E}_b$ which represents the body wave energy per unit depth. Our goal is not to solve the system of Eq. (4.57) in its full generality but rather to exhibit an equipartition solution. In this regime, we expect the distribution of body wave energy to become independent of depth. Hence we look for solutions of the system (4.57) of the form:

$$\begin{pmatrix} \bar{\bar{E}}_s(t) \\ \bar{E}_b(t,z) \end{pmatrix} = \begin{pmatrix} \bar{\bar{E}}_s^0 \\ \bar{E}_b^0 \end{pmatrix} e^{-\lambda t} \tag{4.58}$$

Reporting the ansatz (4.58) into the integro-differential system (4.57), one arrives at a linear and homogeneous system of algebraic equations. A non-zero solution is obtained only if the determinant of the sytem vanishes which implies:

$$\lambda \left(\lambda - \frac{1}{\tau^{s\to b}} - \frac{1}{h} \int_0^h \frac{dz}{\tau^{b\to s}(z)} \right) = 0 \tag{4.59}$$

One of the solutions is given by $\lambda = 0$ which corresponds to the asymptotic equipartition state such as:

$$\frac{\bar{\bar{E}}_s^0}{\bar{E}_b^0} = \int_0^h \frac{\tau^{s\to b}}{\tau^{b\to s}(z)} dz \approx \int_0^{+\infty} R(z) dz = \mathcal{R} \tag{4.60}$$

where Eq. (4.25) and (4.45) have been used, and the depth integral is again extended to $+\infty$ thanks to the assumption $\alpha h \gg 1$. Eq. (4.60) illustrates that the ratio between the energy density of surface and body waves approaches the ratio of their density of states $\mathcal{R}$ at long lapse-time. Note that the energy density is not perfectly homogenized spatially, even at equipartition, as a consequence of the decay of the surface wave eigenfunction with depth. This may be related to the depth-dependence of the density of states near the boundary (see e.g. Hennino et al., 2001). The result (4.60) could have been predicted using the usual concept of equipartition which states that when filtered around a narrow frequency band, all the propagating modes of a diffuse field should be excited to equal energy (Weaver, 1982). In the case where the medium is unbounded at depth, there will be a flux of energy across the lower boundary $z = h$ which vanishes as the lapse-time increases. As demonstrated through numerical simulations later in this paper, equipartition also sets in in this configuration, though probably more slowly than in the slab geometry.

4.5.3 Diffusion Approximation

Having established the existence of an equipartition state, we now derive a diffusion approximation for the transport process. At the outset, it should be clear that the volumetric energy density E_s may not be the solution of a diffusion equation because it exhibits a decay with depth which is inherited from the modal shape and therefore independent of the scattering properties. To circumvent the difficulty, we derive a closed diffusion equation for E_b from which we subsequently deduce the energy density of surface waves. To simplify the calculations, we assume that the scattering is isotropic. Proceeding in the usual fashion, we expand the specific energy density into its first two angular moments (Akkermans and Montambaux, 2007):

$$\begin{aligned} e_s(t,\mathbf{r},z,\hat{\mathbf{n}}) =& \frac{E_s(t,\mathbf{r},z)}{2\pi} + \frac{\mathbf{J}_s(t,\mathbf{r},z)\cdot\hat{\mathbf{n}}}{\pi} \\ e_b(t,\mathbf{r},z,\hat{\mathbf{k}}) =& \frac{E_b(t,\mathbf{r},z)}{4\pi} + \frac{3\mathbf{J}_b(t,\mathbf{r},z)\cdot\hat{\mathbf{k}}}{4\pi} \end{aligned}. \tag{4.61}$$

Multiplying, respectively, the first and second line of Eq. (4.53) by the unit vectors $\hat{\mathbf{n}}$ and $\hat{\mathbf{k}}$, integrating over all possible directions and employing the moment expansion (4.61), we obtain the following set of Equations:

$$\begin{aligned} \frac{\partial_t \mathbf{J}_s(t,\mathbf{r},z)}{v_g} + \frac{v_g}{2}\nabla_\parallel E_s(t,\mathbf{r},z) =& -\frac{\mathbf{J}_s(t,\mathbf{r},z)}{v_g\tau^s} \\ \frac{\partial_t \mathbf{J}_b(t,\mathbf{r},z)}{c} + \frac{c}{3}\nabla E_b(t,\mathbf{r},z) =& -\frac{\mathbf{J}_b(t,\mathbf{r},z)}{c\tau^b} \end{aligned}, \tag{4.62}$$

where $\nabla_\parallel$ denotes the gradient operator in the horizontal plane. Note that the expansions (4.61) are used only to evaluate the integral of the gradient on the left-hand side of the RT Equation. All other terms follow directly either from the definition of the energy flux density vector or the assumption of isotropic scattering. Our final approximation consists in neglecting the derivative of the current vector with respect to time which yields the equivalent of Ohm's law for the mutiply-scattered waves:

$$\begin{aligned} \mathbf{J}_s(t,\mathbf{r},z) =& -D_s\nabla_\parallel E_s(t,\mathbf{r},z) \\ \mathbf{J}_b(t,\mathbf{r},z) =& -D_b(z)\nabla E_b(t,\mathbf{r},z) \end{aligned} \tag{4.63}$$

where the following notations have been introduced:

$$\begin{aligned} D_s =& \frac{v_g^2\tau^s}{2} \\ D_b(z) =& \frac{c^2\tau^b(z)}{3} \end{aligned} \tag{4.64}$$

Note that the total reflection condition (4.51) imposes that there is no net flux of body waves across the surface $z = 0$. To make progress, we now invoke the equipartition principle to fix the ratio between the energy densities of surface and body waves:

$$\frac{E_s(t,\mathbf{r},z)}{E_b(t,\mathbf{r},z)} = R(z) \tag{4.65}$$

in agreement with Eq. (4.60). This allows us to express the total energy flux as:

$$\mathbf{J} = \mathbf{J}_b + \mathbf{J}_s = -(R(z)D_s + D_b(z))\nabla_\parallel E_b(t,\mathbf{r},z) + D_b(z)\hat{\mathbf{z}}\partial_z E_b(t,\mathbf{r},z) \tag{4.66}$$

which may be interpreted as a generalization of Ohm's law for diffuse waves. Eq (4.66) demonstrates that the coupling between surface and body waves renders the energy transport both depth-dependent and anisotropic. It is worth emphasizing that depth-dependence and anisotropy are caused neither by specific orientations/shapes of the scatterers nor by the non-homogeneity of the statistical properties. As further discussed below, these properties stem from the coupling between body and surface wave modes.

The conservation equation for the total energy $E = E_s + E_b$ excited by a point source at $t = 0$ is obtained by taking the sum of the set of Eqs (4.54):

$$\partial_t E(t, \mathbf{r}, z) + \nabla \cdot J(t, \mathbf{r}, z) = \delta(t)\delta(z - z_0)\delta(\mathbf{r}), \tag{4.67}$$

where the right-hand side now contains the source term with z_0 the source depth. Making use of Eqs (4.65) and (4.63), we obtain the following diffusion-like equation verified by the body wave energy density:

$$\partial_t E_b(t, \mathbf{r}, z) - \nabla_\parallel \cdot \left(\frac{D_b(z) + R(z)D_s}{1 + R(z)} \nabla_\parallel E_b(t, \mathbf{r}, z) \right) - \frac{1}{1 + R(z)} \partial_z \left(D_b(z) \partial_z E_b(t, \mathbf{r}, z) \right) = \frac{\delta(t)\delta(\mathbf{r})\delta(z - z_0)}{1 + R(z_0)} \tag{4.68}$$

The last term on the left-hand side of Eq. (4.68) differs from the traditional form for the diffusion model due to the $(1 + R(z))^{-1}$ factor in front of the derivative operators. Actually, this difference is purely formal as may be shown by the change of variable $z \to z'$ where z' is defined as:

$$\begin{aligned} z' =& \int_0^z (1 + R(x))dx, \\ =& z + \frac{\pi}{k} \left(e^{-2\alpha z} - 1 \right) \end{aligned} \tag{4.69}$$

where Eq. (4.20) has been used. In the new variables, Eq. (4.68) may be rewritten as:

$$\partial_t E'_b(t, \mathbf{r}, z') - \nabla_\parallel \cdot \left(D_\parallel(z') \nabla_\parallel E'_b(t, \mathbf{r}, z') \right) - \partial_{z'} \left(D_\perp(z') \partial_{z'} E'_b(t, \mathbf{r}, z') \right) = \delta(t)\delta(\mathbf{r})\delta(z' - z'_0) \tag{4.70}$$

In Eq. (4.70), we have introduced the notations $E'_b(t, \mathbf{r}, z') = E_b(t, \mathbf{r}, z)$, $z'_0 = \int_0^{z_0} (1 + R(x))dx$, as well as the following definitions of the horizontal and vertical diffusivities:

$$\begin{aligned} D_\parallel(z') =& \frac{D_b(z) + R(z)D_s}{1 + R(z)} \\ D_\perp(z') =& D_b(z)(1 + R(z)) \end{aligned} \tag{4.71}$$

Hence, a simple change of scale in the vertical direction reduces Eq.(4.68) to the conventional diffusion Eq. (4.70). Note that the $(1 + R(z_0))^{-1}$ factor on the right-hand side has been absorbed by the change of variable (4.69).

We explore the consequences of Eq. (4.71) by first considering the case $z' \to \infty$. According to Eq. (4.69), this implies $z' \approx z$. Since the partitioning ratio $R(z)$ goes to zero at large depth in the medium, Eq. (4.71) indicates that the vertical and horizontal diffusivities become equal and the diffusion tensor isotropic. Furthermore, because the coupling between surface and body waves is negligible at large depth, its magnitude tends to the constant value $D_b^{bulk} = c^2 \tau^{b \to b}/3$, as expected on physical grounds. In other words, the diffusion process at depth is governed by a simple 3-D diffusion equation for body waves with diffusion constant D_b^{bulk}. This

in turn suggests that at long lapse-time, the coda should decay as $t^{-3/2}$ in a non-absorbing medium. This point will be further substantiated by numerical simulations.

In the vicinity of the surface $z = O(\alpha^{-1})$, Eq. (4.71) shows that the diffusivity of coupled body and surface waves is both depth dependent and non-isotropic. The origin of the z-dependence is clear since the efficacy of the coupling between surface and body waves decays exponentially with depth. In the vicinity of the surface, the anisotropy stems from the transport of a fraction of the energy by surface waves whose velocity and scattering mean free time differ from the one of body waves. In Eq. (4.71) the transverse diffusivity is recognized as a weighted average of the surface and body wave diffusivities with coefficients dictated by the equipartition principle. The vertical diffusivity is -up to the $(1+R(z))$ pre-factor inherited from the change of scale in the vertical direction- equal to the diffusivity of body waves. In the next section, we illustrate the transport process of coupled body and surface waves by numerically simulating the system of Eq. (4.50).

4.6 Monte-Carlo Simulations

In this section, we explore some of the key features of our model with the aid of numerical simulations. The approach to equipartition as well as the role of mode coupling in the coda excitation are illustrated.

4.6.1 Overview of the method

As outlined in introduction, Monte-Carlo simulations have been used for more than thirty years in seismology to simulate the transport of seismic energy in heterogeneous media. Our approach to the solution of the coupled set of transport equations (4.53) for surface and body waves follows closely the approach of Margerin, Campillo, and Van Tiggelen (2000), with some appropriate modifications which we outline briefly.

Energy transport is modeled by the simulation of a large number of random trajectories of particles or seismic phonons (Shearer and Earle, 2004). Each particle is described by its mode, position, propagation direction and time. The initial mode of propagation is randomly selected, following the source energy partitioning ratio (4.20), and the initial propagation direction is a uniformly distributed random vector in 2-D (resp. 3-D) for surface (resp. body) waves. Note that when the particle is of surface type, the particle propagates in a horizontal plane and its exact depth is immaterial. In fact, we may say that a particle of surface type is present at all depth with a probability distribution given by $p_s(z) = 2\alpha \exp(-2\alpha z)$ inherited from the modal shape. The lapse-time to the first scattering event is randomly determined and obeys a simple exponential distribution when the particle represents surface waves. In the case of body waves, the selection process is more complicated because their scattering mean free time depends on the depth in the medium. To address this difficulty, we employ the method of delta collisions, which simulates in a simple and exact way a completely general distribution of scattering mean free time. We will not detail the method here and refer the interested reader to the pedagogical treatment by Lux (2018). At each scattering event, the mode of the particle is randomly selected by interpreting probabilistically Eqs (4.34) and (4.42) defining the scattering attenuations. As an example, $(1/l^{s\to b})/(1/l^s)$ may be interpreted as the transition probability from a surface to a body wave mode. Note that when such an event occurs, the particle is reinjected at a random depth in the medium following the probability distribution $p_s(z)$. To obtain energy envelopes, the position and mode of the particle is monitored on a cylindrical grid at regular time intervals. The local energy density is estimated by averaging the number of particles per cell over a sufficiently large number of random walks. For accuracy,

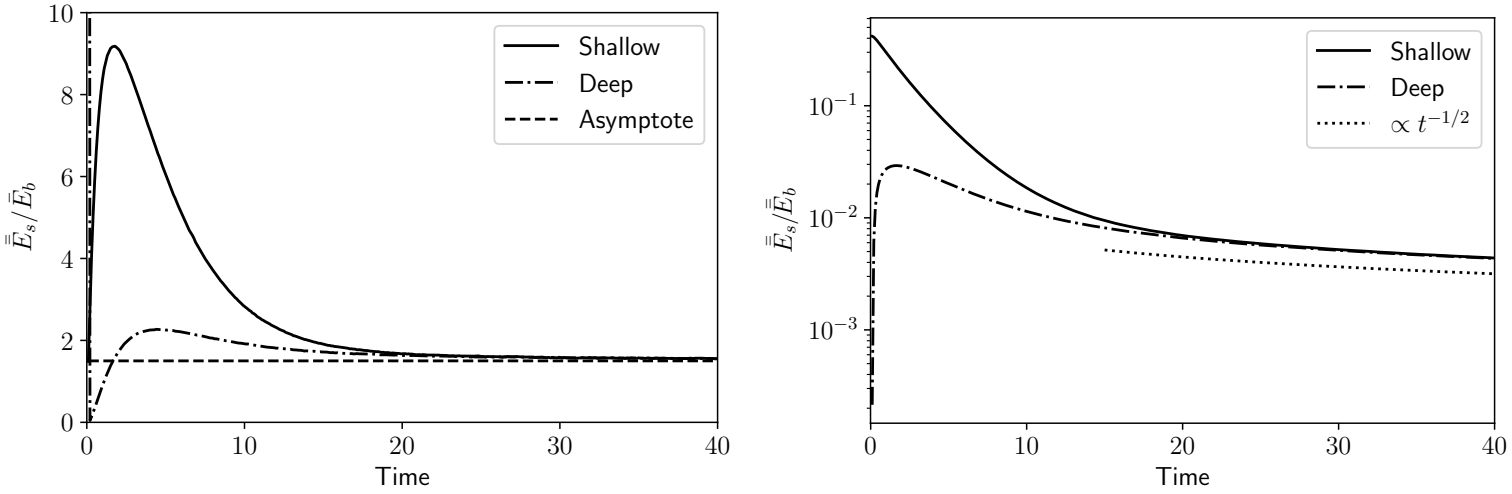

FIGURE 4.3: Local and global evolution of energy partitioning for a shallow (solid line) and a deep (dash-dotted line) source in a heterogeneous half-space filled with point scatterers. The horizontal time scale is the mean free time for surface wave scattering. The penetration depth of surface waves is $\alpha^{-1} = 1$ km and the angular frequency is $\omega = 2\pi$ Hz. The shallow and deep source are located, respectively, at depth α^{-1} and $5\alpha^{-1}$. (Left): Temporal evolution of the ratio between the total energy of surface waves ($\bar{\bar{E}}_s$) and the energy density of body waves integrated over a horizontal plane ($\bar{E}_b$). The body wave energy is evaluated at the surface and averaged over a depth $\Delta z = 1$km. The asymptote (left) is the prediction of Eq. (4.25). (Right) Temporal evolution of the ratio between the total energy of surface ($\bar{\bar{E}}_s$) and body waves ($\bar{\bar{E}}_b$). The dotted line shows an algebraic $t^{-1/2}$ decay.

it is important that the cells be relatively small compared to the shortest mean free path in the medium.

4.6.2 Numerical results

Figure 4.3 illustrates the striking difference between the *global* and *local* partitioning of the seismic energy into surface and body waves. The following parameters have been employed in the simulation: $\alpha = 1\text{km}^{-1}$, $c = 3$km/s and $\tau^{s\to s} = 20$s, $\tau^{s\to b} = 30$s, $\tau^{b\to b} = 30$s, $\tau^{b\to s}(z) = 10\exp(2z)$s. Note that in our model the group velocity of surface waves $v_g \approx 3.32$km/s is slightly faster than the speed of propagation of body waves. Two source depths are considered: a relatively shallow one ($z_0 = 1$km) and a deep one ($z_0 = 5$km), which radiate approximately 29% and 0.01% energy as surface waves, respectively.

On the left, we show the temporal evolution of the ratio between the total energy of surface waves $\bar{\bar{E}}_s$ (see the remarks before Eq. 4.56 for a reminder of the notations), and the horizontally-integrated energy density of body waves $\bar{E}_b$ at the surface $z = 0$, averaged over a depth range $\Delta z = 1$km. Hence, the ratio $\bar{\bar{E}}_s/\bar{E}_b$ has unit of inverse length. Independent of the source depth, we find that the partitioning of the energy density at the surface -into surfacic energy of surface waves and volumetric energy of body waves- converges toward the prediction of equipartition theory, at long lapse-time in the coda (see Eq. 4.25 and 4.60). This numerical result confirms that the analysis of equipartition given in the previous section in slab geometry extends to the half-space geometry. Furthermore, we find that the surface-to-body energy ratio overshoots the prediction of equipartition theory for the two sources at short lapse-time, by a factor which decreases with the source depth z_0.

The stabilization of the local energy density ratio of surface and body waves at the surface of the half-space is to be contrasted with the evolution of the *global* partitioning of the energy into surface and body wave modes. Figure 4.3 (right) shows that after a few mean free times,

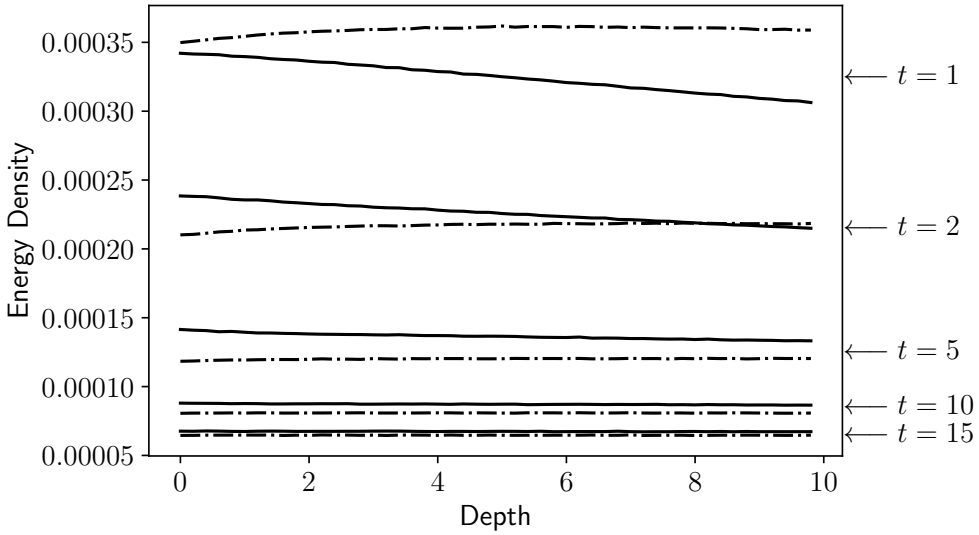

FIGURE 4.4: Horizontally-averaged energy density of body waves $\bar{E}_b$ as a function of depth in a heterogeneous half-space filled with point scatterers. The energy is averaged over a depth range $\Delta z = \alpha^{-1}/5 = 0.2$km and the horizontal axis shows the depth normalized by α^{-1}. The solid and dashed lines correspond to a shallow source ($z_0 = 1$km) and a deep source ($z_0 = 5$km), respectively. The lapse time in the coda in mean free time unit is indicated on the right of the corresponding curves.

most of the energy is carried in the form of body waves in the medium. The Figure also suggests that the global transfer of energy from surface waves to body waves occurs at a rate proportional to $t^{-1/2}$ at long lapse-time.

Further insight into the equipartition process is offered in Figure 4.4, where we show the depth dependence of the horizontally-averaged body wave energy density at different lapse-time in the coda. All the parameters of the simulation are the same as in Figure 4.3, except for the much finer spatial resolution $\Delta z = \alpha^{-1}/5 = 0.2$ km, which allows us to track processes that occur in the skin layer where the coupling between surface and body waves occurs. We observe that after roughly 10 mean free times, the depth distribution of body wave energy becomes homogeneous over a depth range at least as large as $10\alpha^{-1}$, independent of the source depth. This simulation therefore confirms the theoretical analysis performed in slab geometry. The homogenization of the energy of body waves is a dynamic process: the energy density of surface waves increases exponentially near the surface, thereby generating a larger amount of body-wave converted energy; this process is compensated by the exponential increase of the conversion rate from body to surface waves, which eventually yields an equilibrium. Note that the total energy density does *not* homogenize with depth, due to the exponential decay of the surface wave eigenfunction with depth.

In Figure 4.5 and 4.7, we illustrate in greater details the multiple-scattering process by showing snapshots of the surfacic and volumetric energy densities $\varepsilon_s(t, \mathbf{r})$ and $E_b(t, \mathbf{r}, z)|_{z=0}$ at regular time intervals $\Delta t = 1\tau^s$ starting at a lapse time $t = 0.8\tau^s$ for a shallow ($z_0 = 1$km) and a deep ($z_0 = 5$km) source, respectively. The scattering parameters are the same as in Figure 4.3 and the energy is averaged over a range of epicentral distance $\Delta r = 5$km and depth $\Delta z = 5$km. We use a double horizontal axis on Figures 4.5-4.7 to show simultaneously the epicentral distance in kms and in units of mean free path. Note that in the case of body waves, we take the value of the mean free path in the bulk of the medium $\tau^{b\to b}$. For comparison, we show in Figure 4.6, snapshots of energy density of surface waves and body waves when the coupling between the two is deactivated. In the case of surface waves, this amounts to

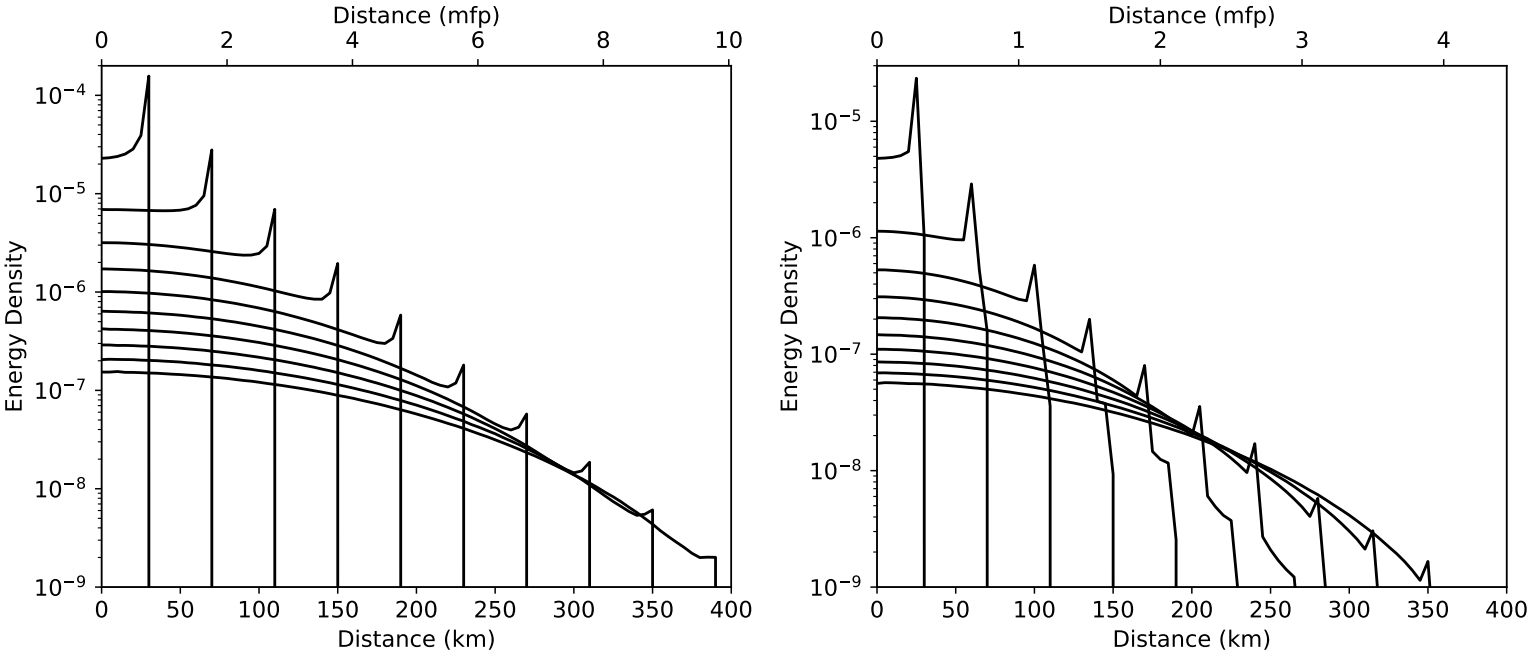

FIGURE 4.5: Snapshots of the energy density of surface waves ϵ_s (left) and of the volumetric energy density of body waves E_b (right) at the surface of a heterogeneous half-space filled with point scatterers in the case of a shallow source ($z_0 = \alpha^{-1}$). The horizontal axes are in units of the scattering mean free path of surface waves (left, top), body waves (right, top) and in kms (bottom). For body waves, we take the mean free path value in the bulk of the medium ($z \to \infty$). The energy is averaged over cylindrical shells of width $\Delta r = 5$km and deph $\Delta z = 5$km.

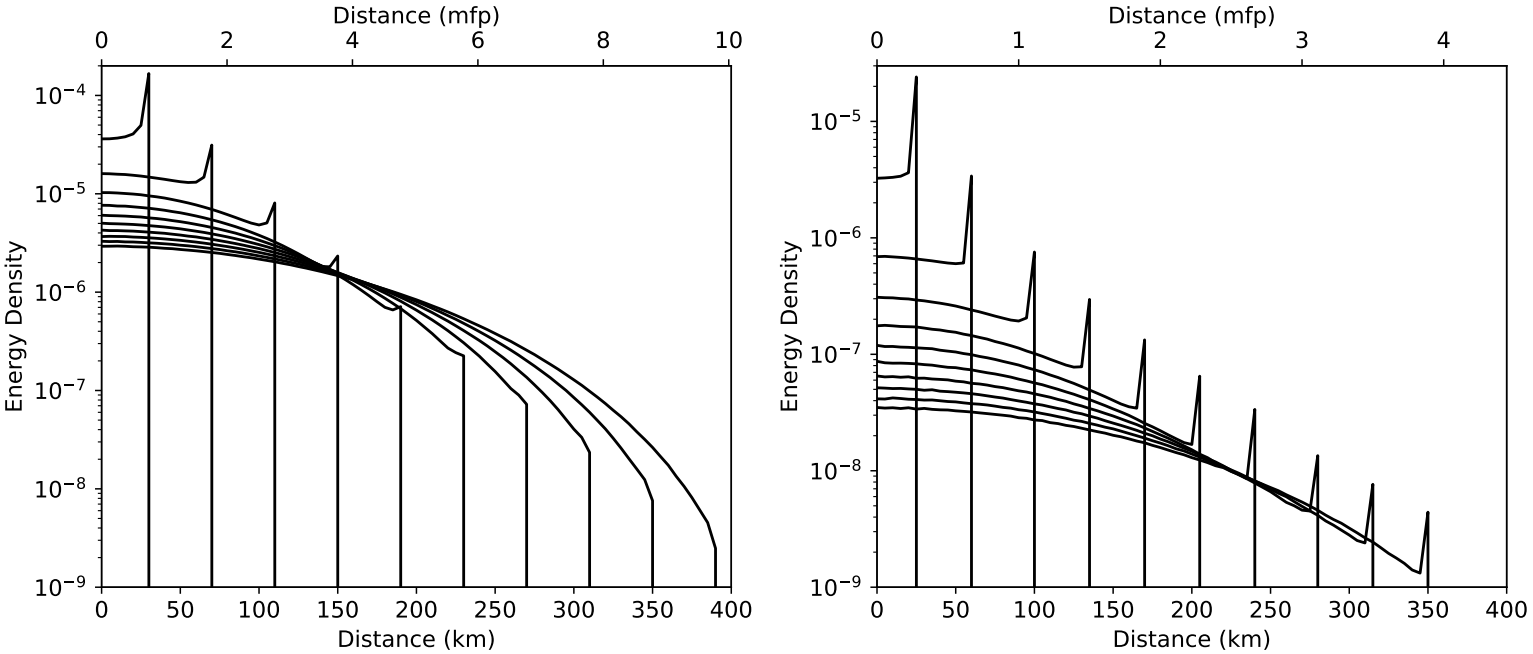

FIGURE 4.6: Same as Figure 4.5 but the coupling between surface and body waves has been deactivated. See text for further explanations.

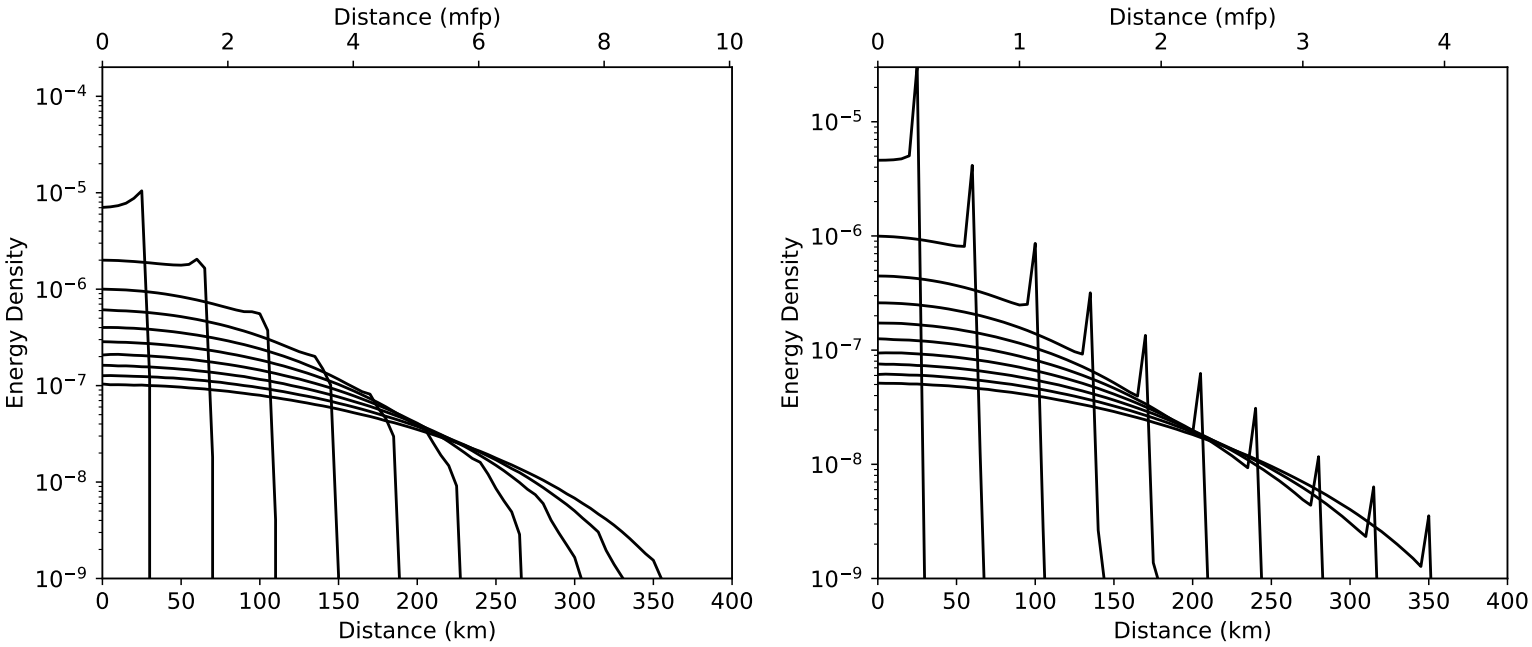

FIGURE 4.7: Snapshots of the energy density of surface waves ϵ_s (left) and of the volumetric energy density of body waves E_b (right) at the surface of a heterogeneous half-space filled with point scatterers in the case of a deep source ($z_0 = 5\alpha^{-1}$). The horizontal axes are in units of the scattering mean free path of surface waves (left, top), body waves (right, top) and in kms (bottom). For body waves, we take the mean free path value in the bulk of the medium ($z \to \infty$). The energy is averaged over cylindrical shells of width $\Delta r = 5$km and depth $\Delta z = 5$km.

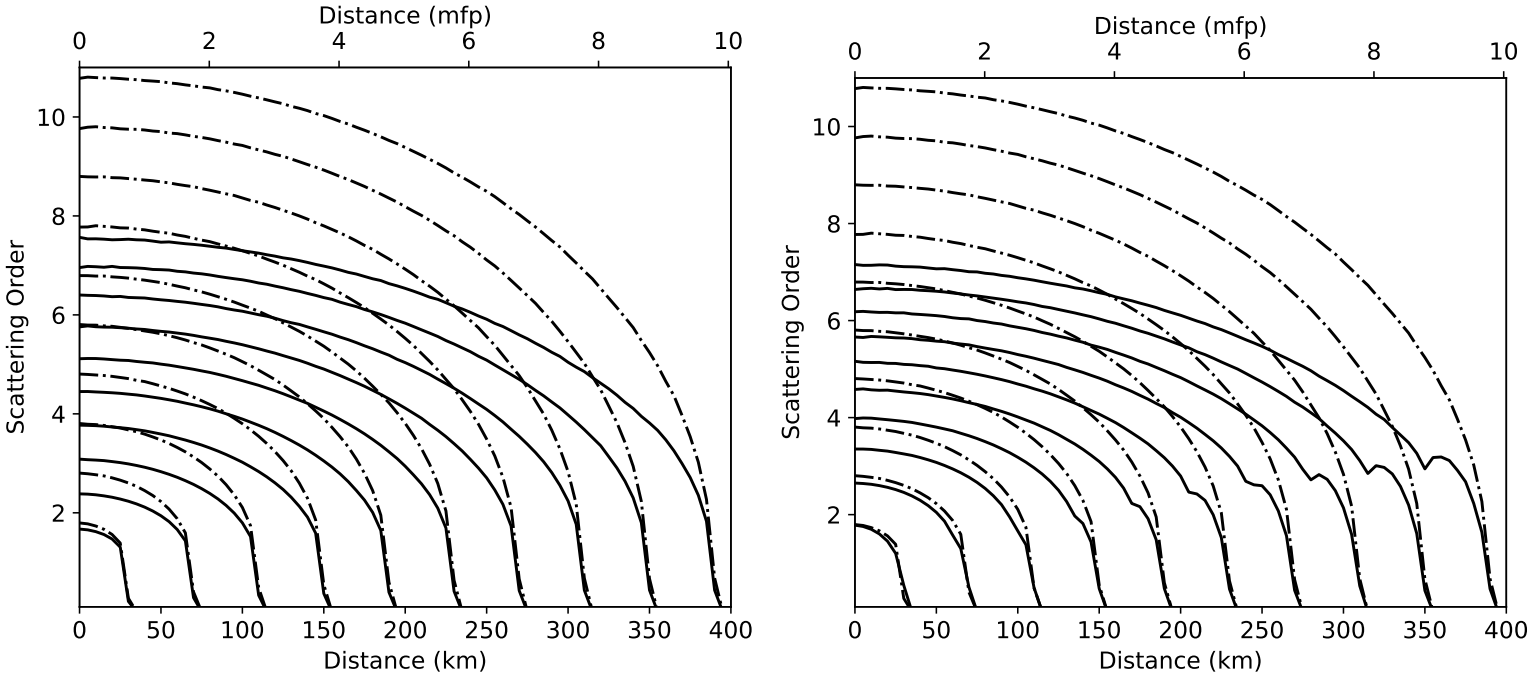

FIGURE 4.8: Contribution of the different orders of scattering to the energy envelopes of surface waves shown in Figure 4.5 (left, solid lines) and 4.7 (right, solid lines). Snapshots of the mean scattering order are represented as a function of the distance from the source. For reference, the dashed line show the same distribution for a conventional transport model in 2-D. The horizontal axes are in units of the scattering mean free path of surface waves (top) and in kms (bottom).

computing the solution of a conventional 2-D multiple-scattering process with the mean free time τ^s. In the case of body waves, we consider a conventional 3-D multiple-scattering process in a half-space with a constant mean free time $\tau^{b\to b}$, i.e., we remove the boundary layer where the coupling with surface waves occurs. To facilitate the comparison between Figure 4.5 and 4.6, we have adjusted the strength of the source term in the conventional multiple-scatttering simulations so that they match exactly the energy released at the source in the form of body and shear waves in the coupled case.

We first analyze the transport of surface waves in the case of a shallow source. As compared to the conventional 2-D case, mode coupling has at least two visible effects on the spatial distribution of the surface wave energy. First, it lowers the energy level in the coda. As an illustration, we observe that after 10 mean free times the coda intensity is reduced by a factor at least equal to 10 in Figure 4.5 compared to Figure 4.6. Second, mode coupling appears to enhance the visibility of ballistic surface waves. In Figure 4.6, the ballistic term is completely masked by the diffuse contribution at roughly 6 mean free path from the source, whereas a small ballistic peak is still visible at roughly 10 mean free paths from the source in Figure 4.5. It is worth noting that the ballistic contribution is exactly identical in Figures 4.5 (left) and 4.6 (left). Again, this is the strong decrease of the energy of scattered coda waves which explains the difference between the two Figures. Figure 4.8, which displays the spatial distribution of the mean order of scattering in the coda, reveals that the coda of coupled surface waves is depleted in high-order multiply-scattered waves compared to a conventional 2-D transport process. In other words, mode conversions entail a strong conversion of multiply-scattered surface waves into body waves which decreases the energy level of surface wave coda and, by comparison, enhances the ballistic contribution. Examination of Figures 4.5 (right) and 4.6 (right) reveals that the effects of mode coupling on body waves are opposite to the ones just described for surface waves. Thus, we observe that the energy level in the coda is slightly increased by the transfer energy from surface wave to body waves. An additional contribution comes from the increase of the scattering strength of body waves near the surface which attenuates the ballistic waves and transfers their energy into the coda. Examination of the decay of the ballistic peak of body waves with epicentral distance in Figures 4.5 and 4.6 confirms the increased attenuation entailed by the coupling with surface waves. Other more exotic phenomena are also visible in Figure 4.5 such as some precursory body waves arrival due to the coupling from surface waves to body waves. However this process is a very peculiar feature of our model, due to the higher wavespeed of surface waves compared to the one of body waves.

Further differences between our coupled model for surface and body waves and conventional transport theory is illustrated in Figure 4.7 where we show snapshots of the energy distribution of surface and body waves in the case of a deep source. Note that in that case, surface waves can only be generated by mode conversions so that ballistic arrivals are absent in Figure 4.7 (left). Interestingly, our numerical simulations indicate that surface waves are rapidly excited to a non-negligible level in the coda. Examination of Figure 4.8 (right) further indicates that multiple-scattering is at the origin of the generation of surface waves in the coda when the source is located at large depth. These observations agree with our theoretical analysis of equipartition, which implies that, independent of the source depth, the coda at the surface of a half-space always appears as a mixture of surface and body waves.

In Figure 4.9, we show envelopes of energy densities for surface and body waves in the case of a shallow source ($z_0 = 1$km) and a deep source ($z_0 = 5$km) at an epicentral distance of 50km. The scattering parameters are the same as in all previous Figures and the spatial resolution of the computation is 5km again. The impact of the depth of the source on the excitation of ballistic waves is obvious in Figure 4.9 and confirms the analysis of Figures 4.5 and 4.7. In particular, it is apparent that the direct body waves are less attenuated in the case

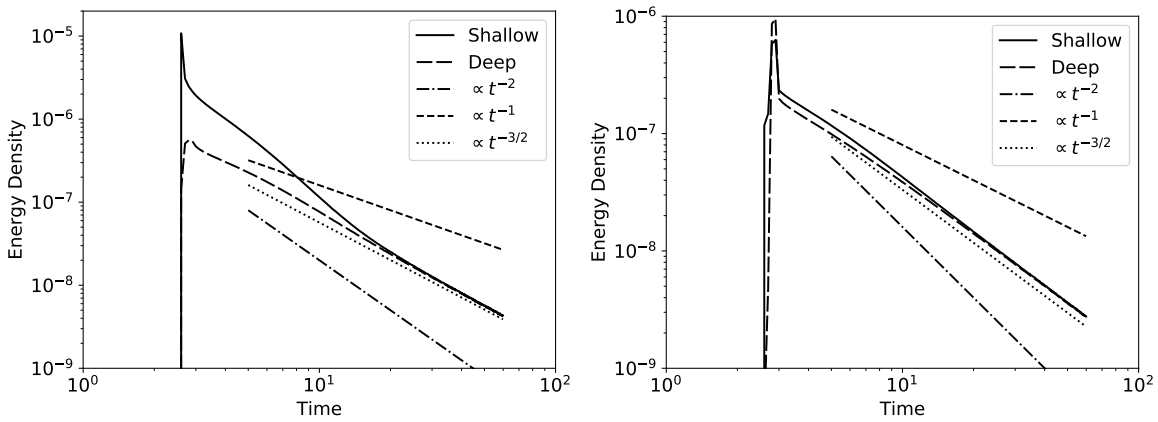

FIGURE 4.9: Energy density of body waves E_b (left) and surface waves ϵ_s (right) at the surface of a heterogeneous half-space filled with point scatterers in the case of a shallow source ($z_0 = \alpha^{-1}$). The enegy is averaged over a depth $\Delta z = 5$km and an epicentral distance range $\Delta r = 5$km. The station is located at an epicentral distance of 50km. The horizontal axis is in units of the scattering mean free time of surface waves in logarithmic scale. Typical algebraic decays are also shown.

of the deep source, as a consequence of the exponential decay of the scattering conversions from body to surface waves with depth. To facilitate the identification of different propagation regimes in the coda, we have superposed on the graphs some typical algebraic decays: t^{-1} for scattering in 2-D (either single or multiple, see e.g. Paasschens, 1997), $t^{-3/2}$ for multiple scattering in 3-D, and t^{-2} for single-scattering in 3-D. In Figure 4.9, we observe that for both body and surface waves the coda obeys a $t^{-3/2}$ decay law at long lapse-time, independent of the source depth, which is characteristic of a 3-D diffusion process. This supports the predictions of the diffusion model and confirms the dominance of body waves in the transport process at large lapse-time. At short lapse-time, we observe a distinct behavior between the two kinds of waves, particularly in the case of a shallow source. After the passage of the ballistic waves, body waves appear to decay slightly more slowly than the asymptotic $t^{-3/2}$ behavior. This may reflect the conversion of surface waves to body waves as discussed in the analysis of Figure 4.5. Two propagation regimes show up clearly on the surface wave energy envelope, with a transition between the two around a lapse-time of 10 mean free times. At short time, the decay of surface waves appears to be faster than the one of body waves, probably as a consequence of the transfer of surface wave energy into the volume as discussed in relation with Figure 4.5. Taken together, Figures 4.5-4.9 illustrate the much richer behavior of the coupled system of transport Eq. (4.50), compared to the conventional transport process without coupling between surface and body waves.

4.7 Conclusions

This work represents a first attempt at formulating a self-consistent theory of RT of seismic waves in a half-space geometry including the coupling between surface and body waves. The main approximation underlying our work is that, upon reflection at the surface, the phase of body waves is randomized so that upgoing and downgoing fluxes may be considered as statistically independent. Our approach distinguishes itself from the standard Eqs of RT for scalar waves found in the literature in one important way: it keeps track - to some extent - of the wave behavior in the vicinity of the surface. This has a number of consequences: (1) surface and body waves are coupled by conversion scattering (2) even in a statistically homogeneous medium it requires that the scattering properties of body waves depend on the depth in

the medium. Furthermore, the reciprocity relation between the surface-to-body vs body-to-surface mean free times plays a prominent role in the establishment of an equipartition regime with a ratio that conforms to the predictions of standard mode counting arguments. Besides equipartition, a notable outcome of our RT equations is the anisotropy of the diffusivity of seismic waves, due to the difference in scattering properties and wave velocities of body and surface waves. We also show that our RT Eqs are operational, in the sense that they are readily amenable to numerical solutions by Monte-Carlo simulations. These simulations could be used in the future to study in more details the dynamics of equipartition, in particular, how the equipartition time varies as a function of the ratio between the penetration depth of surface waves and the scattering mean free path for body-to-surface wave coupling.

Before becoming a viable alternative to current approaches, our theory needs to be tested and improved. In the future, we plan to address the following issues: (1) Evaluate the impact of neglecting the interference between upgoing and downgoing body waves on the scattering cross-section and, if possible, go beyond this approximation. (2) Extend the theory to more realistic finite size scatterers and more general spatial distributions of scatterers. (3) Incorporate polarization effects for elastic waves at a free surface. (4) Absorption of energy is also a very important mechanism of attenuation, which has been entirely neglected in this work for simplicity. Because the sub-surface of the Earth is thought to be very strongly attenuating due to the widespread presence of fluids, we may expect dissipation to affect more severely surface waves than body waves. In turn, this may modify the partitioning of the energy in the coda as was previously shown by Margerin, Van Tiggelen, and Campillo (2001) in the case of coupled S and P waves. Special efforts should be devoted to this important topic before our formalism can be applied to real seismic data.

4.8 Supplementary information

4.8.1 Variational formulation for mixed boundary conditions

Here, we recall briefly on a simple one-dimensional example how mixed boundary conditions of the type used in Eq. (4.2) can be incorporated into a variational formulation. The interested reader will find further details and more examples in the classic book by Gelfand and Fomin (1963), after which our treatment is modeled. For simplicity we consider a vibrating string of density ρ, tension T and length L. For the moment, we do not specify the boundary conditions. The total kinetic energy stored in the string at time t is given by:

$$T[u](t) = \int_0^L \rho(\partial_t u(\mathbf{x},t))^2 dx, \tag{4.72}$$

where u denotes the displacement field. The instantaneous potential energy stored in the string may be expressed as

$$V[u](t) = \int_0^L T(\partial_x u(\mathbf{x},t))^2 dx \tag{4.73}$$

According to Hamilton's principle, among all possible displacement fields, the one that satisfies the actual equations of motion should make the following action integral:

$$I[u] = \int_{t_1}^{t_2} (T-V)[u](t) dt \tag{4.74}$$

stationary. Mathematically, this principle of stationary action may be expressed as:

$$\partial_\epsilon I[u+\epsilon\psi]|_{\epsilon=0} = 0 \tag{4.75}$$

where ψ is an arbitrary function. This is sometimes written as $\delta I = 0$, where δI is known as the first variation of the action integral. Using integration by parts, Gelfand and Fomin (1963) establish that:

$$\begin{aligned}\delta I =& \epsilon \left(\int_{t_0}^{t_1} \int_0^L (-\rho \partial_{tt} u(\mathbf{x},t) + T\partial_{xx} u(\mathbf{x},t))\psi(x,t) dx dt \right. \\ &\left. + T\int_{t_0}^{t_1} (\partial_x u(0,t)\psi(0,t) - \partial_x u(l,t)\psi(l,t)) dt \right)\end{aligned} \tag{4.76}$$

The arbitrariness of the function ψ in Eq. (4.76) implies both the governing wave equation for the vibrating string:

$$\rho \partial_{tt} u(x,t) - T\partial_{xx} u(x,t) = 0 \tag{4.77}$$

as well as the so-called natural boundary conditions:

$$\partial_x u(x,t)|_{x=0} = 0 \text{ and } \partial_x u(x,t)|_{x=l} = 0, \tag{4.78}$$

which correspond to a string with free ends. In order to obtain mixed boundary conditions, it suffices to add to the potential energy (4.73), a term of the form $\chi u(0,t)^2$ where χ is a constant. Eq. (4.76) must be modified accordingly by adding the new contribution $-\epsilon\chi \int_{t_0}^{t_1} u(0,t)\psi(0,t)dt$ which, in turn, implies a natural boundary condition of the mixed type at $x = 0$:

$$\left(\chi \partial_x u(x,t) - T u(x,t)\right)|_{x=0} = 0 \tag{4.79}$$

The total potential energy may be rewritten in integral form as follows:

$$V[u](t) = \int_0^L \left[\chi u(0,t)^2 \delta(x) + T(\partial_x u(\mathbf{x},t))^2\right] dx \tag{4.80}$$

which justifies the appearance of the delta function in Eq. (4.3) and Eq. (4.6) in a simplified context.

4.8.2 Far-field expression of the Green's function for scalar waves in a half-space with mixed B.C.

In this Appendix, we summarize the key steps to the derivation of Eq. (4.16) from Eq. (4.15). We split the computation into two parts and begin with the surface wave contribution:

$$G_s(\mathbf{r}, z, z_0) = \frac{2\alpha e^{-\alpha(z+z_0)}}{(2\pi)^2} \int_{\mathbb{R}^2} \frac{e^{i\mathbf{k}_\parallel \cdot \mathbf{r}}}{k^2 + \alpha^2 - k_\parallel^2 + i\epsilon} d^2 k_\parallel \tag{4.81}$$

Introducing cylindrical coordinates $(k_\parallel, \phi)$ and integrating over angle yields:

$$G_s(\mathbf{r}, z, z_0) = \frac{2\alpha e^{-\alpha(z+z_0)}}{2\pi} \int_0^{+\infty} \frac{J_0(k_\parallel r)}{k^2 + \alpha^2 - k_\parallel^2 + i\epsilon} dk_\parallel \tag{4.82}$$

where J_0 denotes the standard Bessel function of order 0. Using the same trick as in Aki and Richards (2002, Chapter 6), we extend the wavenumber integral over the whole $k_\parallel$ axis using the Hankel function of the first kind instead of the Bessel function:

$$G_s(\mathbf{r}, z, z_0) = \frac{\alpha e^{-\alpha(z+z_0)}}{2\pi} \int_{-\infty}^{+\infty} \frac{H_0^{(1)}(k_\parallel r)}{k^2 + \alpha^2 - k_\parallel^2 + i\epsilon} dk_\parallel \tag{4.83}$$

In the last step, we employ the residue theorem by closing the contour in the upper half of the complex plane with a semi-circle of radius $R \to +\infty$ and note the presence of pole at $k_\parallel = \sqrt{k^2 + \alpha^2} + i\eta$, $(\eta \to 0^+)$. Thanks to the exponential decay of the integrand, the integral on the semi-circle vanishes which yields:

$$G_s(\mathbf{r}, z, z_0) = \frac{-i\alpha}{2\pi} e^{-\alpha(z+z_0)} H_0^{(1)}(\sqrt{k^2 + \alpha^2} r). \tag{4.84}$$

The result (4.84) is exact. The far-field approximation (4.16) follows by application of standard asymptotic expansions to the Hankel function.

The computation of the body wave contribution can also be split into two parts:

$$\begin{aligned} G_b(\mathbf{r}, z, z_0) =& \frac{1}{(2\pi)^3} \int_0^{+\infty} dq \int_{\mathbb{R}^2} \frac{e^{i\mathbf{k}_\parallel \cdot \mathbf{r}} (e^{-iqz} + r(q) e^{iqz})(e^{-iqz_0} + r(q) e^{iqz_0})^*}{k^2 - k_\parallel^2 - q^2 + i\epsilon} d^2 k_\parallel \\ =& \frac{1}{(2\pi)^3} \int_{-\infty}^{+\infty} dq \int_{\mathbb{R}^2} \frac{e^{iq(z-z_0)} e^{i\mathbf{k}_\parallel \cdot \mathbf{r}}}{k^2 - k_\parallel^2 - q^2 + i\epsilon} d^2 k_\parallel \\ &+ \frac{1}{(2\pi)^3} \int_{-\infty}^{+\infty} dq \int_{\mathbb{R}^2} \frac{r(q) e^{iq(z+z_0)} e^{i\mathbf{k}_\parallel \cdot \mathbf{r}}}{k^2 - k_\parallel^2 - q^2 + i\epsilon} d^2 k_\parallel \\ =& G_\infty(\mathbf{r}, z, z_0) + G_r(\mathbf{r}, z, z_0) \end{aligned} \tag{4.85}$$

where the unitarity of the reflection coefficient has been used and the q integral has been extended from $-\infty$ to $+\infty$ thanks to the relation $r(q)^* = r(-q)$. The first term in the second equality of (4.85) may be recognized as the full-space solution to the Helmholtz Eq.:

$$\begin{aligned} G_\infty(\mathbf{r}, z, z_0) =& \frac{1}{(2\pi)^3} \int_{-\infty}^{+\infty} dq \int_{\mathbb{R}^2} \frac{e^{iq(z-z_0)} e^{i\mathbf{k}_\parallel \cdot \mathbf{r}}}{k^2 - k_\parallel^2 - q^2 + i\epsilon} d^2 k_\parallel \\ =& -\frac{e^{ikR_0}}{4\pi R_0}, \end{aligned} \tag{4.86}$$

where $R_0 = \sqrt{r^2 + (z - z_0)^2}$. The second term in the second equality of (4.85) represents the waves reflected at the surface:

$$G_r(\mathbf{r}, z, z_0) = \frac{1}{(2\pi)^3} \int_{-\infty}^{+\infty} dq \int_{\mathbb{R}^2} \frac{r(q) e^{iq(z+z_0)} e^{i\mathbf{k}_\parallel \cdot \mathbf{r}}}{k^2 - k_\parallel^2 - q^2 + i\epsilon} d^2 k_\parallel \tag{4.87}$$

The computation of this integral may be attacked in exactly the same way as we did for the surface wave term G_s to obtain:

$$G_r(\mathbf{r}, z, z_0) = \frac{-i}{8\pi} \int_{-\infty}^{+\infty} r(q) e^{iq(z+z_0)} H_0^{(1)}(\sqrt{k^2 - q^2} r) dq, \tag{4.88}$$

To approximate this last integral in the far-field of the source, we first remark that for $|q| > k$ the cylindrical waves are evanescent so that we may legitimately take $-k$ and $+k$ as integration

limits. We next make use of the far-field expansion of the Hankel function to obtain the following oscillatory integral representation:

$$G_r(\mathbf{r}, z, z_0) \approx \frac{-i}{8\pi}\sqrt{\frac{2}{\pi r}}\int_{-k}^{+k} \frac{r(q)e^{iq(z+z_0)+i\sqrt{k^2-q^2}r-i\pi/4}}{\sqrt{k^2-q^2}}dq \tag{4.89}$$

Further noting that the derivative of the phase term:

$$\phi(q) = q(z+z_0) + \sqrt{k^2-q^2}r \tag{4.90}$$

vanishes at :

$$q_0 = \frac{k(z+z_0)}{R_0'} \tag{4.91}$$

with $R_0' = \sqrt{r^2+(z+z_0)^2}$, we apply the stationary phase formula to obtain after some straightforward algebra:

$$G_r(\mathbf{r}, z, z_0) \approx -\frac{r(q_0)e^{ikR_0'}}{4\pi R_0'}. \tag{4.92}$$

This term may be interpreted as the contribution of the image point of the source with a strength given by the reflection coefficient evaluated at an incidence angle corresponding to the specularly reflected ray connecting the source to the detection point (see Eq. 4.91). To complete the far-field approximation, we first note the following expansions: $R_0 = R - z_0 z/R + o(1/R)$, $R_0' = R + z_0 z/R + o(1/R)$ where $R = \sqrt{r^2+z^2}$. Neglecting all terms smaller than $1/R$ for the amplitude, all terms smaller than z_0/R for the phase and further approximating q_0 as kz/R, formula (4.16) is recovered.

Chapter 5

Sensitivity Kernels

Andres Barajas, Ludovic Margerin, Michel Campillo
Article in preparation

A change in the properties of the crust can generate a perturbation in the propagation velocity of the seismic waves. The phase perturbations of the waveforms registered at the surface depend on the position of this property change. The connection between the two is the sensitivity kernel. Therefore, if we want to localize perturbations at depth we must estimate the sensitivity kernel for the model presented in the previous section: this is the main objective of this chapter. To this end, we first study the changes that generate in the scalar surface wave velocity perturbation in the medium. Later, we extend the travel-time sensitivity kernels theory so it incorporates the propagation and detection and surface and body waves. Then, based on these results and in the radiative transfer equations obtained in the preceding chapter, we estimate the sensitivity kernel for body and surface waves. Although the theory presented here is general for the scalar case, we restrict ourselves for simplicity to a depth description of the sensitivity. Furthermore, thinking in the eventual application of these results to the case study analyzed in chapter 3 where we make measurements from a single station, the estimation of the sensitivity kernel is done for the autocorrelation configuration, it means, with the source and the receiver located in the same location.

5.1 Introduction

The heterogeneities present in the crust interact with the passing seismic waves and scatter them in multiple directions. This phenomenon is directly related to the formation of the coda wave which contains information about the strength and properties of this interaction. The first study in this direction was done by Aki (1969) where he defines for the first time the coda wave and he defines his principal characteristics, and later use it to estimate specific properties of the region (Aki, 1973) and to analyze the attenuation properties related to the structure of the Earth (Sciences, Aki, and Chouet, 1975). More studies followed that showed that the fluctuations in the amplitude and phase of the scattered waves enable the identification of small variations in the properties of the crust (Poupinet, Ellsworth, and Frechet, 1984; Ratdomopurbo and Poupinet, 1995; Schaff and Beroza, 2004). The estimation of these changes from the continuous seismic noise field is one of the fundamental principles of passive image interferometry monitoring which have shown to be effective in detecting velocity variations in fault zones (Wegler and Sens-Schönfelder, 2007; Brenguier et al., 2008a), in volcanoes (Sens-Schönfelder and Wegler, 2006), or as a consequence of a diverse number of meteorological phenomena (Meier, Shapiro, and Brenguier, 2010; Wang et al., 2017; Hillers, Campillo, and Ma, 2014).

The phase differences changes generated in the coda depend on the location of the perturbation and the time that the seismic field has to sample it, or in other words, with the

lapse time. This means that it is possible to locate the perturbation in the crust with the information registered at the surface at different times. Coda wave interferometry establishes the link between the two through the introduction of the sensitivity kernels by Pacheco and Snieder (2005) for the diffusive wave state, and Pacheco and Snieder (2006) for the single scattering case. The sensitivity kernel is a travel-time density function that shows the most probable sectors through which a wave would pass when going from the source to the receiver in a given lapse time. The kernel can be calculated as a convolution of the probabilities of the particle traveling between the source, the receiver, and each part of the medium around them that is sampled by the waves (Pacheco and Snieder, 2005). Each of these probabilities can be interpreted physically as the intensity received at one point of space after a unitary pulse was emitted from another (Margerin et al., 2016). This is the reason why the estimation of the sensitivity pass through the calculation or use of known Green's functions and solutions of the transport equation in different dimensions (Paasschens, 1997; Sato and Fehler, 2012). Later (Margerin et al., 2016) demonstrated the importance of the directionality of the seismic field in the first stages of the system which implied that an analyses of the sensitivity based only in the energy intensities was insufficient; to solve it, they developed the sensitivity kernels through specific intensities overcoming with this the restrictions on the propagation regime that was previously limited to the extreme cases as a diffusive or a single-scattering assumptions, and extending the theory toward anisotropic scattering events.

The sensitivity kernels have been used to localize perturbations in numerical simulations (Planes et al., 2015; Kanu and Snieder, 2015), in a concrete sample (Larose et al., 2010), or generated by changes in the medium preceding volcanic eruptions (Lesage, Reyes-Dávila, and Arámbula-Mendoza, 2014; Obermann et al., 2013b). The coupling between body and surface waves has remained one challenging factor to the development of the sensitivity kernels in a 3-D halfspace that is the usual setting for most seismic applications. Obermann et al. (2013a) and Obermann et al. (2016) approached this problem by expressing the sensitivity as a linear combination of two independent sensitivities, one for surface and another for body waves, with a controlling factor mediating between them that changes with time, and that is estimated through full wavefield numerical simulations. This factor helps to recreate predominance of surface and body wave sensitivities at different lapse times. This method has been extended to localize small scale perturbations in the medium (Obermann et al., 2019).

Recently, Margerin, Bajaras, and Campillo (2019) developed a new scalar model that integrates naturally body and surface waves, making it possible to find the different mean free paths and times between the two modes and therefore, to establish the radiative transfer equations of the system. Based on this model, we reformulate the sensitivity equations from a probabilistic point of view to include the two types of propagation and estimate them statistically through a series of Monte Carlo simulations. This allows us to obtain the travel-time density distributions between the two modes of propagation, for different depths in a 3-D half-space medium. In parallel, we estimate the phase perturbations in the surface waves as a consequence of a perturbation in the medium and integrate it with the results of the simulations to obtain the sensitivity kernel of the system. We compare the performance of this kernel with previous works and analyze its most important features.

5.2 Scalar model

We begin with a quick overview of the scalar model developed by Margerin, Bajaras, and Campillo, 2019. First, we state the wave equation in a 3-D half-space

$$(\rho\partial_{tt} - T\Delta)\, u(t, \mathbf{r}, z) = 0 \tag{5.1}$$

where, t is time, and $(\mathbf{r}, z)$ the position vector $(\mathbf{r}, z \geq 0)$, ρ is the density, T represents the elastic constant of the medium, and u is the displacement. The rise of surface waves is achieved when over the surface is imposed the Robin boundary condition

$$(\partial_z + \alpha)u(t, \mathbf{r}, z)|_{z=0} = 0 \tag{5.2}$$

where α is a positive constant. One of the possible solutions of these equations is the sum of the incident and reflected body wave

$$u_b(t, \mathbf{r}, z) = A(e^{-iqz} + r(q)e^{iqz})e^{i\mathbf{k}_\parallel \cdot \mathbf{r}}, q \geq 0 \tag{5.3}$$

where $\mathbf{k}_\parallel = (k_x, k_y, 0)$ is the horizontal wavenumber, with $q^2 + \mathbf{k}_\parallel \cdot \mathbf{k}_\parallel = \dfrac{\omega^2}{c^2}$ and

$$r(q) = \frac{q + i\alpha}{q - i\alpha}. \tag{5.4}$$

The second possible solution is

$$u_s(t, \mathbf{r}, z) = Ah(z)e^{i(\mathbf{k}_\parallel \cdot \mathbf{r} - \omega t)}; \tag{5.5}$$

where $h(z) = e^{-\alpha z}$ determines automatically the depth penetration of surface wave. The surface phase velocity c_R in this case is

$$c_R = \frac{c}{\sqrt{1 + \dfrac{c^2\alpha^2}{\omega^2}}} \tag{5.6}$$

with c representing the body wave velocity. One particularity of this system is that the surface group velocity v_g, is always higher than both the body and the surface wave velocities

$$v_g = \frac{c^2}{c_R} = c\sqrt{1 + \frac{c^2\alpha^2}{\omega^2}} \tag{5.7}$$

This implies that the ballistic energy received at a point on the surface will come mainly from the surface waves. Thanks to the body and surface eigenfunctions on this system, is possible to calculate the scattering cross-section as a balance of the incoming and outgoing energy of a punctual scatterer and therefore, to estimate the mean free times of all the possible transitions in the system

$$\begin{aligned} \tau^{s\to s} &= \frac{1}{\alpha}\frac{4}{ck^3a^6\epsilon^2} \\ \tau^{s\to b} &= \frac{4\pi}{ck^4a^6\epsilon^2} \\ \tau^{b\to b} &= \frac{4\pi}{ck^4a^6\epsilon^2} \\ \tau^{b\to s}(z) &= \frac{e^{2\alpha z}}{\alpha}\frac{2}{ck^3a^6\epsilon^2} \end{aligned} \tag{5.8}$$

where a represents the linear dimension of the scatterer, and ϵ is the local perturbation of the inverse square velocity. The total mean free paths for each mode are therefore

$$\frac{1}{\tau^s} = \frac{1}{\tau^{s\to s}} + \frac{1}{\tau^{s\to b}};\ \frac{1}{\tau^b(z)} = \frac{1}{\tau^{b\to s}(z)} + \frac{1}{\tau^{b\to b}} \tag{5.9}$$

The dependence of $\tau^{b\to s}$ on the depth is directly related to the surface wave eigenfuntion which changes the probabilities of a scattering event for a body wave depending on its location relative to the surface. The ratio between the energy of surface waves and the depth-integrated energy of body waves generated by a point source:

$$R(z) = \frac{\tau^{s\to b}}{\tau^{b\to s}(z)} = \frac{2\pi c\alpha}{\omega} e^{-2\alpha z}. \tag{5.10}$$

The transport of energy of body waves can be described in terms of the specific volumetric energy density $e_b(t, \mathbf{r}, z, \mathbf{k})$ where $\mathbf{k}$ is a vector on the unit sphere in 3-D. The integration of this specific density over a solid angle gives us the volumetric energy density

$$E_b(t, \mathbf{r}, z) = \int_{4\pi} e_b(t, \mathbf{r}, z, \hat{\mathbf{k}}) \mathrm{d}\hat{k} \tag{5.11}$$

On the other hand, the transport of surface waves can be described in terms of the specific surface energy density $\epsilon_s(t, \mathbf{r}, \mathbf{n})$ where $\mathbf{n}$ is a unit vector in the horizontal plane. To be able to describe the system through the formulation of transport equations, it is necessary to have energy densities of equal dimensions; for this reason, is introduced the specific volumetric energy density of surface waves

$$e_s(t, \mathbf{r}, z, \mathbf{n}) = 2\alpha\epsilon_s(t, \mathbf{r}, \mathbf{n}) e^{-2\alpha z} \tag{5.12}$$

which integrated over depths give us back the specific surface density $\epsilon_s(t, \mathbf{r}, \mathbf{n})$. Using this new specific volumetric density is now possible to define a volumetric energy density of surface wave

$$E_s(t, \mathbf{r}, z) = \int_{2\pi} e_s(t, \mathbf{r}, z, \hat{\mathbf{n}}) \mathrm{d}\hat{n} \tag{5.13}$$

The total energy density at a point in the medium will be the sum of the energy densities of body and surface waves $E_b(t, \mathbf{r}, z) + E_s(t, \mathbf{r}, z)$, which is supported by the orthogonality of their representative eigenfunctions.

From these definitions are constructed the radiative transport equations. The scattering process is assumed to be isotropic and the increase and decay of intensity are stated in terms of the conversion between all the possible modes

$$\begin{aligned}
\left(\partial_t + v_g \hat{\mathbf{n}} \cdot \nabla\right) e_s(t, \mathbf{r}, z, \hat{\mathbf{n}}) = &- \frac{e_s(t, \mathbf{r}, z, \hat{\mathbf{n}})}{\tau^s} + \frac{E_s(t, \mathbf{r}, z)}{2\pi\tau^{s\to s}} \\
&+ \frac{E_b(t, \mathbf{r}, z)}{2\pi\tau^{b\to s}(z)} + s_s(t, \mathbf{r}, z, \hat{\mathbf{n}}) \\
\left(\partial_t + c\hat{\mathbf{k}} \cdot \nabla\right) e_b(t, \mathbf{r}, z, \hat{\mathbf{n}}) = &- \frac{e_b(t, \mathbf{r}, z, \hat{\mathbf{k}})}{\tau^b(z)} + \frac{E_b(t, \mathbf{r}, z)}{4\pi\tau^{b\to b}} \\
&+ \frac{E_s(t, \mathbf{r}, z)}{4\pi\tau^{s\to b}} + s_b(t, \mathbf{r}, z, \hat{\mathbf{k}})
\end{aligned} \tag{5.14}$$

where the terms $s_{s,b}$ represent sources of surface and body waves, which are given in terms of the energy partitioning ratio

$$\begin{aligned}
s_s(t, \mathbf{r}, z, \hat{\mathbf{n}}) &= \frac{2\alpha R\left(z_0\right) e^{-2\alpha z} \delta(\mathbf{r})}{2\pi\left(1 + R\left(z_0\right)\right)} \\
s_b(t, \mathbf{r}, z, \hat{\mathbf{k}}) &= \frac{\delta\left(z - z_0\right) \delta(\mathbf{r})}{4\pi\left(1 + R\left(z_0\right)\right)}
\end{aligned} \tag{5.15}$$

5.3 Penetration depth of the surface wave

One of the fundamental characterizing parameters of the interaction between body and surface waves is the penetration depth of the surface waves. For this reason, finding an equivalence between the scalar model and the elastic model is fundamental to trace parallels between the two systems. For the elastic case we take as reference the Rayleigh waves formed in a homogeneous half-space. The sensitivity of both surface waves to physical variations at depth is a direct function of their respective surface eigenfunctions, or more precisely, to the square of these functions which is related to their energy.The displacement eigenfunctions for the Rayleigh waves can be written as (Ben-Menahem and Singh, 1981):

$$\begin{aligned} u_x(\omega;x,z) =& A r_1(\omega;z)\sin(\omega t - kx) \\ r_1(\omega;z) =& \left[e^{-\gamma_\alpha k_R z} - \left(1 - \frac{c_r^2}{2c_\beta^2}\right) e^{\gamma_\beta k_R z}\right] \\ u_z(\omega;x,z) =& A r_2(\omega;z)\cos(\omega t - kx) \\ r_2(\omega;z) =& \left(1 - \frac{c_r^2}{c_\alpha^2}\right)^{1/2} \left[-e^{-\gamma_\alpha k_R z} + \left(1 - \frac{c_r^2}{2c_\beta^2}\right)^{-1} e^{-\gamma_\beta k_R z}\right] \end{aligned} \tag{5.16}$$

where u_x is the displacement in the direction parallel to the wave propagation, u_z is the displacement perpendicular to the surface, A represents the amplitude of the wave, c_α and c_β are velocities of the P-waves and S-waves respectively, k_R the wavenumber of the Rayleigh waves, and the gamma factors are

$$\gamma_\alpha = \left(1 - \frac{c_r^2}{c_\alpha^2}\right)^{1/2} \qquad \gamma_\beta = \left(1 - \frac{c_r^2}{c_\beta^2}\right)^{1/2} \tag{5.17}$$

The energy density of the Rayleigh wave averaged over one cycle can be written in terms of r_1 and r_2 (Aki and Richards, 2002)

$$\frac{1}{2}\rho\left(r_1^2(\omega;z) + r_2^2(\omega;z)\right) \tag{5.18}$$

where ρ is the density of the medium. We want to find a function in the form of a simple exponential that resembles the shape and especially the reach of the Rayleigh energy density function; the purpose of having a simplified proxy of the elastic surface wave is to mimic the mathematical function that describes the scalar surface eigenfunction. In equation 5.16 the penetration at depth of the energy is dominated by the exponential function with the lower exponent, that in the case for a Poisson solid is $e^{-\gamma_\beta k_R z}$ with $\beta = 0.39$. We take a slightly modified version of this function that resembles a bit better the elastic wave at shallow depths without changing significantly its reach, $e^{-0.3 k_R z}$; this is the equivalent scalar surface eigenfunction. A comparison between them can be seen in figure 5.1. Although their shape is not exactly equal (which would be technically impossible with the simplifications made), they both have fairly similar reaches and shapes.

Since the scalar surface eigenfunction is also $h(z) = e^{-\alpha z}$, it is clear that the parameter α must be equal to $\alpha = 0.3 k_R$. it is important to notice that the behavior here illustrated is completely independent of the Rayleigh wavelength λ_R and that this equivalence between the elastic and the scalar cases gives a natural scaling with frequency to the scalar surface wave.

We take $L_s = 2\alpha^{-1}$ as the penetration distance of the scalar surface wave, as at this depth the amplitude of the eigenfunction is $\sim$14% of its amplitude at the surface. To compare this

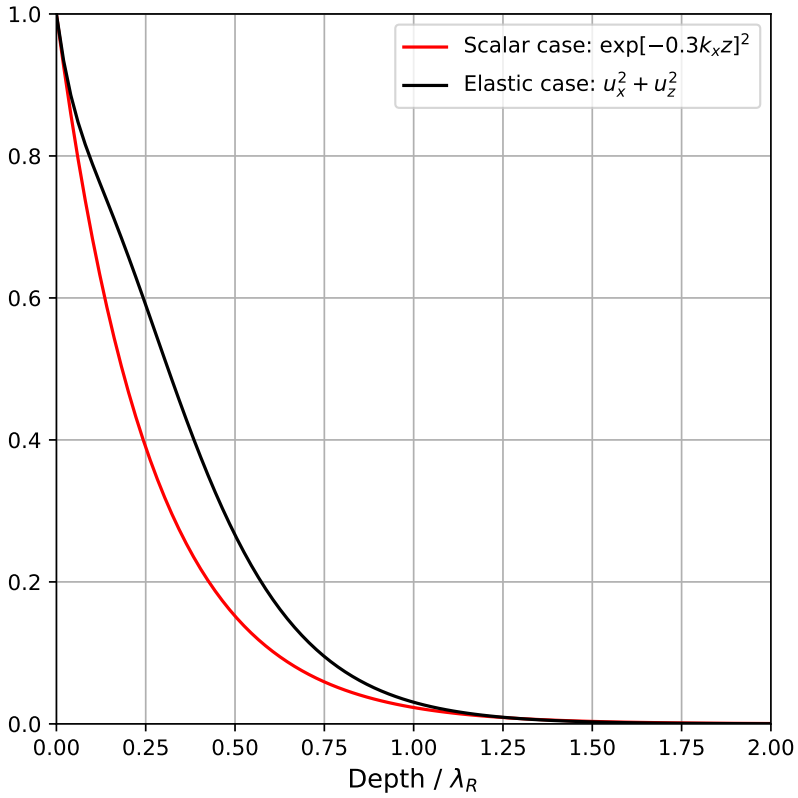

FIGURE 5.1: Comparison of the penetration depth of the energy of Rayleigh waves and a simplified model. Both have the amplitudes normalized.

penetration with the elastic case, we can write L_s in terms of the Rayleigh wavelength using the proposed equivalence between both cases

$$L_s = 2\alpha^{-1} = 2(0.3k_R)^{-1} \approx 1.06\lambda_R \tag{5.19}$$

This result is coherent with the rule of thumb that estimates the penetration of the Rayleigh waves around 1 horizontal wavelength λ_R.

5.4 Phase velocity variation for surface waves

The interaction of a surface wave with a perturbation in the medium is one the principal mechanisms that control the response that is recorded at the surface. This interaction is different from that of the body waves in the sense that the surface waves propagate as a whole over a volume close to the surface, which implies that any small change in one layer of the medium within its penetration depth, should affect all the surface wave without breaking or changing its structure, which should remain the same for a given frequency. In particular, we are interested in determining how the surface phase velocity change with a fractional change in the bulk velocity. To do so, we begin with the Lagrangian that has the usual potential and kinetic terms of a wave scalar field, plus an elastic potential energy at the surface associated with the boundary condition:

$$L = \frac{1}{2}\left[\rho(\partial_t u(t,\mathbf{r}))^2 - T(\nabla u(t,\mathbf{r}))^2 + \alpha T u(t,\mathbf{r})^2\delta(z)\right] \tag{5.20}$$

We integrate the Lagrangian over depth and average over one cycle to put it in terms of the energy integrals

$$\int_0^\infty \langle L\rangle dz = \frac{1}{2}\left[\omega^2 I_1 - k_\parallel^2 I_2 - I_3 + I_s\right] \tag{5.21}$$

where

$$\begin{aligned} I_1 &= \frac{1}{2}\int_0^\infty \rho h^2 dz, & I_2 &= \frac{1}{2}\int_0^\infty T h^2 dz, \\ I_3 &= \frac{1}{2}\int_0^\infty T\left(\frac{dh}{dz}\right)^2 dz, & I_s &= \frac{1}{2}\int_0^\infty \alpha T h^2\delta(z) dz. \end{aligned} \tag{5.22}$$

Now, following Aki and Richards (2002) we find the perturbation of this expression, that is equal to

$$\begin{aligned} &\omega^2\delta I_1 - k_\parallel^2\delta I_2 - \delta I_3 + \delta I_s \\ &\quad = \omega^2\int_0^\infty \rho h\delta h dz - k_\parallel^2\int_0^\infty T h\delta h dz - \int_0^\infty T\frac{dh}{dz}\frac{d\delta h}{dz}dz + \int_0^\infty \alpha T h\delta h\delta(z) \\ &\quad = \int_0^\infty \left\{\omega^2\rho h - k_\parallel^2 T h + \frac{d}{dz}\left(T\frac{dh}{dz}\right)\right\}\delta h dz - T\frac{dh}{dz}\delta h\Big|_0^\infty + \alpha T h\delta h|_{z=0} \end{aligned} \tag{5.23}$$

The terms inside the curly brackets are equal to the application of the equation 5.1 to the surface eigenfunction and therefore, equal to zero

$$-\rho\omega^2 h + T k_\parallel^2 h - T\frac{d^2h}{dz^2} = 0 \tag{5.24}$$

The two remaining terms on the rigth hand side of equation 5.23 can be simplified knowing that $\delta h = 0$ at $z = \infty$ and using the boundary condition $dh/dz|_{z=0} = -\alpha h|_{z=0}$

$$T\frac{dh}{dz}\delta h\Big|_{z=0} + \alpha T h \delta h|_{z=0} = T(-\alpha h)\delta h|_{z=0} + \alpha T h \delta h|_{z=0} = 0 \tag{5.25}$$

Therefore, the integrated Lagrangian is stationary for a perturbation of the surface eigenfunction

$$\omega^2 \delta I_1 - k_\parallel^2 \delta I_2 - \delta I_3 + \delta I_s = 0 \tag{5.26}$$

On the other hand, we can show that the integrated lagrangian 5.21 is equal to zero for the surface eigenfunction as expected from the energy conservation. To do so we multiply 5.24 by $-h/2$ and integrate it over depth to obtain

$$\begin{aligned} 0 &= \frac{1}{2}\int_0^\infty \rho\omega^2 h^2 dz - \frac{1}{2}\int_0^\infty T k_\parallel^2 h^2 dz + \frac{1}{2}\int_0^\infty T h \frac{d^2h}{dz^2} dz \\ &= \frac{1}{2}\int_0^\infty \rho\omega^2 h^2 dz - \frac{1}{2}\int_0^\infty T k_\parallel^2 h^2 dz - \frac{1}{2}\int_0^\infty T\left(\frac{dh}{dz}\right)^2 dz + \frac{1}{2}\,T h\frac{dh}{dz}\Big|_0^\infty \end{aligned} \tag{5.27}$$

The first three terms are I_1, I_2, and I_3 respectively. Using the boundary conditions we can write the last term as follows

$$-\frac{1}{2}\,T h\frac{dh}{dz}\Big|_0 = -\frac{1}{2}\,T h(-\alpha h)|_0 = \frac{1}{2}\int_0^\infty \alpha T h^2 \delta(z) dz = I_s \tag{5.28}$$

and therefore

$$\omega^2 I_1 = k_\parallel^2 I_2 + I_3 - I_s \tag{5.29}$$

Having established this, we proceed to find the change in the phase surface wave velocity as a consequence of a perturbation in the medium. To do so, we make a perturbation in the eigenfunction at fixed frequency $h + \delta h = h(\rho + \delta\rho, T + \delta T, k_\parallel + \delta k_\parallel, \omega)$, in the Lagrangian

$$\begin{aligned} &\omega^2 \int_0^\infty (\rho + \delta\rho)\,(h + \delta h)^2\, dz = (k_\parallel + \delta k_\parallel)^2 \int_0^\infty (T + \delta T)\,(h + \delta h)^2\, dz \\ &+ \int_0^\infty (T + \delta T)\left[\frac{d}{dz}\,(h + \delta h)\right]^2 dz - \int_0^\infty \alpha (T + \delta T)\,(h + \delta h)^2\,\delta(z) dz \end{aligned} \tag{5.30}$$

Eliminating perturbations of second order and subtracting the previous know relations between the energy integrals, we obtain

$$\begin{aligned} \int_0^\infty -2k_\parallel \delta k_\parallel T h^2\, dz = &\int_0^\infty k_\parallel^2 \delta T h^2\, dz + \int_0^\infty \delta T \left(\frac{dh}{dz}\right)^2 dz \\ &- \int_0^\infty \omega^2 \delta\rho h^2\, dz - \int_0^\infty \alpha \delta T h^2 \delta z\, dz \end{aligned} \tag{5.31}$$

From this we can calculate the change in phase velocity

$$\left(\frac{\delta c_R}{c_R}\right)_\omega = -\frac{\delta k_\parallel}{k_\parallel} = \frac{\int_0^\infty \left[k_\parallel^2 h^2 + \left(\frac{dh}{dz}\right)^2\right]\delta T dz - \int_0^\infty \omega^2 h^2 \delta\rho dz - \int_0^\infty \alpha \delta T h^2 \delta z dz}{2k_\parallel^2 \int_0^\infty T h^2 dz} \tag{5.32}$$

We made a series of assumptions to simplify this expression: we assume that there is no perturbation of the density ($\delta\rho = 0$) and that the background elastic constant T does not depend on depth. We also suppose that the elastic constant is not perturbed at the surface ($\delta T(z = 0) = 0$) as a way to avoid perturbations over the boundary condition or over the surface elastic energy that supports the surface waves. We then finally obtain

$$\left(\frac{\delta c_R}{c_R}\right)_\omega = \frac{\rho c^2}{2k_\parallel^2 I_2}\int_0^\infty \left[k_\parallel^2 h^2 + \left(\frac{dh}{dz}\right)^2\right]\frac{\delta c}{c}(z)dz \tag{5.33}$$

where I_2 is the energy integral defined in 5.22, and we made use of the relations between the rigidity and the bulk velocity $\delta T/T = 2\delta c/c,\ T = \rho c^2$. This equation shows that any possible variation of the bulk velocity will change the surface wave velocity as long as it happens within the penetration depth determined by the surface eigenfunction. The weight of this integral will be written as

$$K_{C_{ph}}(z) = \frac{\rho c^2}{2k_\parallel^2 I_2}\left[k_\parallel^2 h^2 + \left(\frac{dh}{dz}\right)^2\right] \tag{5.34}$$

This expression shows us that the effective sensitivity reach of the surface waves at depth is proportional to the square of the eigenfunction and its derivative

5.5 Group velocity

The introduced frequency dependence of the parameter α used to trace a parallel with the elastic case, has a collateral effect over the group velocity of the surface waves. We recalculate this velocity with the variational approach previously introduced. First, we estimate a perturbation of the eigenfunction both in $k_\parallel$ and in ω, $h + \delta h = h(k_\parallel + \delta k_\parallel, \omega + \delta\omega)$, in the energy integrals 5.29 to obtain

$$(\omega + \delta\omega)^2 (I_1 + \delta I_1) = (k_\parallel + \delta k_\parallel)^2 (I_2 + \delta I_2) + (I_3 + \delta I_3) - (I_s + \delta I_s') \tag{5.35}$$

$\delta I_s'$ can be calculated from the definition of I_s' (equation 5.22) keeping in mind that α is a frequency dependent quantity

$$\delta I_s' = \frac{1}{2}\int_0^\infty \alpha T 2h\delta h\delta(z)dz + \frac{1}{2}\int_0^\infty \delta\alpha T h^2\delta(z)dz = \delta I_s + \frac{\delta\alpha}{\alpha}I_s \tag{5.36}$$

Subtracting equations 5.29 and 5.26 from this expression we find that

$$2\omega\delta\omega I_1 = 2k_\parallel\delta k_\parallel I_2 - \frac{\delta\alpha}{\alpha}I_s \tag{5.37}$$

and therefore the group velocity is

$$U = \frac{\delta\omega}{\delta k_\parallel} = \frac{k_\parallel}{\omega}\frac{I_2}{I_1} - \frac{\delta\alpha}{\delta k_\parallel}\frac{1}{2\alpha\omega}\frac{I_s}{I_1} \tag{5.38}$$

We start evaluating some of these integrals. I_2/I_1 can be calculated from their definitions

$$\frac{I_2}{I_1} = \frac{T\int_0^\infty h\delta h dz}{\rho\int_0^\infty h\delta h dz} = c^2 \tag{5.39}$$

On the other hand, from equation 5.6 α is

$$\alpha = \frac{\omega}{c}\sqrt{\left(\frac{c}{c_R}\right)^2 - 1} \tag{5.40}$$

Therefore

$$\frac{\delta\alpha}{\delta k_\parallel} = c_R\frac{\delta\alpha}{\delta\omega} = \frac{c_R}{c}\sqrt{\left(\frac{c}{c_R}\right)^2 - 1} = \frac{c_R\alpha}{\omega} \tag{5.41}$$

Finally, to evaluate I_s and I_1 we make direct use of the eigenfunction $h = e^{-\alpha z}$

$$I_1 = \frac{1}{2}\int_0^\infty \rho h^2 dz = \frac{1}{2}\,\rho\left(-\frac{1}{2\alpha}e^{-2\alpha z}\right)\Big|_0^\infty = \frac{\rho}{4\alpha} \tag{5.42}$$

$$I_s = \frac{1}{2}\int_0^\infty \alpha T h^2\delta(z)dz = \frac{1}{2}\alpha T \tag{5.43}$$

Putting all this together we obtain that

$$U = \frac{\delta\omega}{\delta k_\parallel} = \frac{c^2}{c_R} - c_R\frac{\alpha^2}{\omega^2}c^2 = \frac{c^2}{c_R} - c_R\left(\frac{c^2}{c_R^2} - 1\right) = c_R \tag{5.44}$$

which conveniently fix the group velocity of surface waves with a lower value than the velocity of body waves.

5.6 Time densities

Our objective is to determine how a fluctuation in the background velocity will affect the apparent velocity of the seismic field recorded at the surface. The two are related through the typical time a seismic phonon passes in each part of a medium and the typical time it passes on each mode of propagation (in this case, as a body or as a surface wave). To analyze this we take a probabilistic approach. We begin denoting by A the event of the emission of the seismic phonon at time $t_0 = 0$, B the event of a phonon propagating in time t', and event C the phonon arriving at a receiver. The time will be implicitly included in the differentiation between events A, B, and C marking a temporal transition between them. The probability of each event will be written as $P(E)$ where E represents the event. The state of each phonon in one event is specified with a subindex marking its position $\mathbf{r}$, its direction $\mathbf{k}$, or its mode of propagation m; the mode is b or s when the phonon propagates as a body or surface particle respectively. For example, $P(B_{z',b'})$ is the probability that the phonon is propagating in time t' as a body particle at depth z', independently of its radial position $\mathbf{r}$ of the direction of propagation $\mathbf{k}$. Therefore, $P(B_{b'})$ is the probability that the phonon was propagating in time t' as a body particle, irrespective of its position or its direction. Naturally, $P(B_{b'})$ is the sum of $P(B_{z',b'})$ for all the depths, which for a continuous system can be written as

$$P(B_{b'}) = \int_{z'} P(B_{z',b'})dz' \tag{5.45}$$

In general, removing an index of an event probability implies grouping all the events designed by that index by summing their individual probabilities

$$P(E_{i,j}) = \sum_k P(E_{i,j,k}) \tag{5.46}$$

We can divide specify the event set with any index classification we want as long as it covers the original set completely, or in other words, under the condition that it forms a sample space of the original event (Miller and Childers, 2012).

The probability that a phonon arrives to the receiver at $\mathbf{r}$ under the condition that it was emitted at the source in $\mathbf{r_0}$, can be written as the conditional probability $P(C_\mathbf{r} \mid A_{\mathbf{r_0}})$ (Gut, 2013). We can rewrite this in terms of conditional probabilities with an intermediate state of propagation using the Chapman–Kolmogorov equation (Ross, 2014; Papoulis and Pillai, 2002; Roepstorff, 2012)

$$P(C_\mathbf{r} \mid A_{\mathbf{r_0}}) = \int_\omega P(C_\mathbf{r} \mid B_\omega) P(B_\omega \mid A_{\mathbf{r_0}})\, d\omega \tag{5.47}$$

where ω represents every single outcome of the probability sample space. This equation says that the probability of going from event A to C can be found from the probabilities of the phonon going from A to B and from B to C, as long as we add all the possible intermediate events B. The sample space can be classified in different ways: for example, we could specify the event B uniquely for its position, and this would effectively cover the whole range of possibilities.

$$P(C_\mathbf{r} \mid A_{\mathbf{r_0}}) = \int_{\mathbf{r}'} P(C_\mathbf{r} \mid B_{\mathbf{r}'}) P(B_{\mathbf{r}'} \mid A_{\mathbf{r_0}})\, d\mathbf{r}' \tag{5.48}$$

However, this election would only allow us to describe a system on which the propagation direction of each of the phonons is independent of its position: this is the case of a diffusive system as was proposed by Pacheco and Snieder (2005). If we want to describe the first stages of the system this description is inadequate as they are marked by a strong directionality of the propagation of the waves (Margerin et al., 2016). Therefore, we classify the sample space with a combination of the position, the direction, and the mode of propagation of each phonon

$$P(C_\mathbf{r} \mid A_{\mathbf{r_0}}) = \int_{\mathbf{r}'} \int_{\mathbf{k}'} \sum_m P(C_\mathbf{r} \mid B_{\mathbf{r}',\mathbf{k}',m}) P(B_{\mathbf{r}',\mathbf{k}',m} \mid A_{\mathbf{r_0}})\, d\mathbf{k}'\, d\mathbf{r}' \tag{5.49}$$

$\mathbf{k}'$ was not specified in the source or the arrival events because the direction of propagation of the phonons at those events is not important. Notice that the integration of equation 5.49 over all directions (and modes) does no lead to equation 5.48 because it implies a joint integration between the two conditional probabilities sharing the same $\mathbf{k}'$. Integrating equation 5.49 over the time of the propagation event B (t') for all the possible travel times (between 0 and t), and reorganizing the terms gives

$$t = \int_{\mathbf{r}'} \left[\int_0^t \int_{\mathbf{k}'} \sum_m \frac{P(C_\mathbf{r} \mid B_{\mathbf{r}',\mathbf{k}',m}) P(B_{\mathbf{r}',\mathbf{k}',m} \mid A_{\mathbf{r_0}})}{P(C_\mathbf{r} \mid A_{\mathbf{r_0}})}\, d\mathbf{k}' dt' \right] d\mathbf{r}' \tag{5.50}$$

The parenthesis was added to highlight the fact that the term inside is the time sensitivity kernel (Pacheco and Snieder, 2005; Margerin et al., 2016), extended to track the two possible modes of propagation. To simplify this equation and to approach us to the measurements made in the Monte Carlo simulation, we assume that we're only interested in the phonons emitted by the source at the location $\mathbf{r}' = 0$ (source in the surface), which forms now our whole and only set of particles. This allows us to drop the references to the event A

$$t = \int_0^t \int_{\mathbf{r}'} \int_{\mathbf{k}'} \sum_m \frac{P(C_\mathbf{r} \mid B_{\mathbf{r}',\mathbf{k}',m}) P(B_{\mathbf{r}',\mathbf{k}',m})}{P(C_\mathbf{r})}\, d\mathbf{k}' d\mathbf{r}' dt' \tag{5.51}$$

Using the Bayes formula (Papoulis and Pillai, 2002; Gut, 2013)

$$P(C_{\mathbf{r}} \mid B_{\mathbf{r}',\mathbf{k}',m})P(B_{\mathbf{r}',\mathbf{k}',m}) = P(B_{\mathbf{r}',\mathbf{k}',m} \mid C_{\mathbf{r}})P(C_{\mathbf{r}}) \tag{5.52}$$

we can rewrite equation 5.51 as

$$t = \int_0^t \int_{\mathbf{r}'} \int_{\mathbf{k}'} \sum_m P(B_{\mathbf{r}',\mathbf{k}',m} \mid C_{\mathbf{r}})\, d\mathbf{k}' d\mathbf{r}' dt' \tag{5.53}$$

Thanks to the simplification made, we can now integrate over all directions

$$t = \int_0^t \int_{\mathbf{r}'} \sum_m P(B_{\mathbf{r}',m} \mid C_{\mathbf{r}})\, d\mathbf{r}' dt' \tag{5.54}$$

Now, we proceed to make explicit the contribution of each mode, and to simplify the spatial dependence integrating over the whole space for the surface mode, and over the horizontal plane for the body mode

$$t = \int_0^t P(B_{s'} \mid C_{\mathbf{r}})\, dt' + \int_0^t \int_{z'} P(B_{z',b'} \mid C_{\mathbf{r}})\, dz' dt' \tag{5.55}$$

The surface mode of propagation does not depend on the depth and for that reason, its probability was fully integrated. Before going any further, it is useful to interpret each of these probabilities as a counting process. Let us imagine that we shoot a great number of seismic phonons from the source, some of which reach the receiver at time t; if we receive a number high enough of particles, their travel histories will be representative of all the possible paths to go from the source to the receiver. This is the set of particles that fulfill the condition in each of the conditional probabilities of equation 5.55: arrive to the receiver located at $\mathbf{r}$ in the time t. Because they represent the whole set of possibilities, estimating one probability can be done by counting: for example, if we want $P(B_{z',b'} \mid C_{\mathbf{r}})$, we just have to count the number of body wave particles that were at the position z' in the time t' and divide this number by the total of particles that arrive to the receiver. Therefore, equation 5.55 can be written as

$$t = \int_0^t \frac{N_s(t')}{N}\, dt' + \int_0^t \int_{z'} \frac{N_b(z',t')}{N}\, dz' dt' \tag{5.56}$$

The relationship stated here will be fundamental later on: integrate the probability that a particle propagates in a certain mode between all the possible travel-times is equivalent to sum the time spent by all the particles in that mode and divide it by the total number of particles, or in other words, is equivalent to the average time spent in that mode

$$\int_0^t P(B_{m'} \mid C_{\mathbf{r}})\, dt' = \int_0^t \frac{N_m(t')}{N}\, dt' = \bar{t}_m \tag{5.57}$$

On these terms, equation 5.55 can be written as

$$t = \bar{t}_s + \int_{z'} \bar{t}_b\, dz' \tag{5.58}$$

which makes evident that their sum is equal to the total lapse time. However, before proceeding with this change, let us come back to the probability description of the system in equation 5.55: up until this point, the mode on which the seismic phonon arrives to the receiver has been ignored. However, it can be made explicit adding the probabilities at the arrival point

$$
\begin{aligned}
t = &\frac{P(C_{\mathbf{r},s})}{P(C_{\mathbf{r}})}\int_0^t P(B_{s'} \mid C_{\mathbf{r},s})\,dt' + \frac{P(C_{\mathbf{r},b})}{P(C_{\mathbf{r}})}\int_0^t P(B_{s'} \mid C_{\mathbf{r},b})\,dt' \\
&+ \frac{P(C_{\mathbf{r},s})}{P(C_{\mathbf{r}})}\int_0^t\int_{z'} P(B_{z',b'} \mid C_{\mathbf{r},s})\,dz'dt' + \frac{P(C_{\mathbf{r},b})}{P(C_{\mathbf{r}})}\int_0^t\int_{z'} P(B_{z',b'} \mid C_{\mathbf{r},b})\,dz'dt'
\end{aligned}
\tag{5.59}
$$

being $P(C_{\mathbf{r},m})$ the probability of the phonon arriving at time t and in mode m, to the receiver located at (r, z). Before, the surface mode was not sub-classified at different depths because it propagates as a whole in a parallel direction to the surface. However, at the arrival point it becomes necessary as the energy of the surface waves is highly dependent on the depth and therefore, the position of the receiver will determine how strong it is detected. The quantities in the form $P(C_{\mathbf{r},m})/P(C_{\mathbf{r}})$ can be interpreted as the fraction of particles that arrive in a given mode m with respect to the total of particles that arrive to the receiver; given that each of these phonons represents a package of energy following the propagation scheme described by the transfer equations 5.14, this fractions can be written as $E^m(t,\mathbf{r})/E(t,\mathbf{r})$, being $E^m(t,\mathbf{r})$ the energy that arrives in the mode m to the receiver, and $E(t,\mathbf{r})$ the total energy arriving at the same point. Using this equivalence and integrating for all the possible travel times t' results in

$$
\begin{aligned}
t = &\frac{E^s(t,r,z)}{E(t,r,z)}\bar{t}_{s\to s}(t,r,z) + \frac{E^b(t,r,z)}{E(t,r,z)}\bar{t}_{s\to b}(t,r,z) \\
&+ \frac{E^s(t,r,z)}{E(t,r,z)}\int_0^\infty \bar{t}_{b\to s}(z';t,r,z)\,dz' + \frac{E^b(t,r,z)}{E(t,r,z)}\int_0^\infty \bar{t}_{b\to b}(z';t,r,z)\,dz'
\end{aligned}
\tag{5.60}
$$

The semicolon in the arguments of each average time separates the variables of the propagation, from the variables of the arrival, and the subindex indicates the temporal sequence of propagation and arrival: for example, $\bar{t}_{s\to b}$ is the average time that the particles that arrived in body wave mode, passed in surface wave mode. These times are schematized in figure 5.2 for two simplified cases. Also, the position of the receiver $\mathbf{r}$ was explicitly put in terms of the depth and the radial distance, profiting from the cylindrical symmetry of the system. This equation shows the flight distribution of the particles according to their mode of propagation, and the depth (in the case of body waves) at which they propagate. Notice that how the terms denominated by t in this equation are dimensionally different between them: for the propagation of body particles we have times per unit of depth ($t_{b\to s}$ and $t_{b\to b}$) and for the surface waves they are simply times ($t_{s\to s}$ and $t_{s\to b}$). Equation 5.60 describes what parts of the medium and what modes of propagation are the preferred for the particles traveling from the source to the receiver: a spatial and modal "distribution" of the total travel time. We can simplify this equation by defining the effective time spent in each mode as an energy-weighted average between the two possible modes of arrival

$$
\begin{aligned}
\langle t_s(t,r,z)\rangle &= \frac{E^s(t,r,z)}{E(t,r,z)}\bar{t}_{s\to s}(t,r,z) + \frac{E^b(t,r,z)}{E(t,r,z)}\bar{t}_{s\to b}(t,r,z) \\
\langle t_b(z';t,r,z)\rangle &= \frac{E^s(t,r,z)}{E(t,r,z)}\bar{t}_{b\to s}(z';t,r,z) + \frac{E^b(t,r,z)}{E(t,r,z)}\bar{t}_{b\to b}(z';t,r,z)
\end{aligned}
\tag{5.61}
$$

which will result in a simpler version of equation 5.60

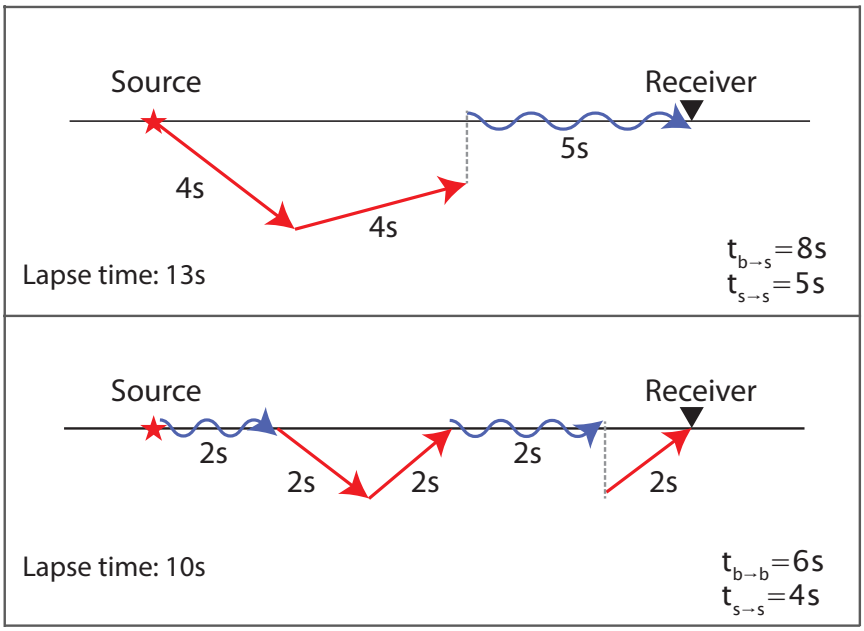

FIGURE 5.2: Representation of the propagation times and modes for two simple cases. In the upper plot we have an arrival in surface wave mode and in the bottom an arrival in body wave mode.

$$t = \langle t_s(t,r,z)\rangle + \int_0^\infty \langle t_b(z';t,r,z)\rangle \, dz' \tag{5.62}$$

Notice how this equation is technically equal to equation 5.58 with the difference that the weighted average process is explicit. Finally, it is worth noticing that equation 5.60 can be re-arranged in a different way

$$\begin{aligned} t = &\frac{E^s(t,r,z)}{E(t,r,z)}\left(\bar{t}_{s\to s}(t,r,z) + \int_0^\infty \bar{t}_{b\to s}(z';t,r,z)\, dz'\right) \\ &+ \frac{E^b(t,r,z)}{E(t,r,z)}\left(\bar{t}_{s\to b}(t,r,z) + \int_0^\infty \bar{t}_{b\to b}(z';t,r,z)\, dz'\right) \end{aligned} \tag{5.63}$$

in which each sum inside the parenthesis is equal to the arrival time t. From this equation is easier to analyze some particular cases: for example if the receiver is located at a great depths, then the surfaces waves will not reach it (which implies that $E^s = 0$ and $E^b = E$) and equation 5.63 will turn into

$$t = \bar{t}_{s\to b}(t,r,z) + \int_0^\infty \bar{t}_{b\to b}(z';t,r,z)\, dz' \tag{5.64}$$

a simplified version of equation 5.62 with the effective times replaced by the averaged times.

5.7 Sensitivity kernels

Let us suppose that on average, the particles propagating as body waves pass an effective time $\langle t_b(z')\rangle$ through a layer at depth z', that has a slight velocity perturbation δc. The overall travel time change is then $\delta t = -\langle t_b(z')\rangle(\delta c/c)$. In the case of the time spent as surface waves,

the travel time perturbation will have an analogous expression using the relative surface wave velocity perturbation $\delta t = -\langle t_s \rangle (\delta c_R / c_R)$. Therefore, the effective travel time delay generated by any set of perturbations in the medium can be written as

$$\delta t = -\langle t_s(t,r,z) \rangle \frac{\delta c_R}{c_R} - \int_0^\infty \langle t_b(z';t,r,z) \rangle \frac{\delta c}{c}(z') dz' \tag{5.65}$$

Putting the relative surface phase velocity perturbation in terms of δc at layer at depth z' with equation 5.33, allow us to calculate the apparent velocity variation ($\delta t/t = -\varepsilon$) in terms of the bulk velocity variation

$$\frac{\delta t}{t}(t,r,z) = \int \left(-\frac{\langle t_s(t,r,z) \rangle}{t} K_{C_{ph}}(z') - \frac{\langle t_b(z';t,r,z) \rangle}{t} \right) \frac{\delta c}{c}(z') dz' \tag{5.66}$$

The term between parenthesis is the sensitivity kernel K; the left part is the surface wave sensitivity K_s and the right one the body wave sensitivity K_b. The negative signs indicate that an increase of the velocity in the medium ($\delta c/c > 0$) generates an early phase arrival ($\delta t/t < 0$). Replacing the effective times by their definitions (equation 5.61) give us

$$\begin{aligned} \frac{\delta t}{t}(t,r,z) = -\int \Bigg(& \frac{E^s(t,r,z)}{E(t,r,z)} K_{s\to s}(z';t,r,z) + \frac{E^b(t,r,z)}{E(t,r,z)} K_{s\to b}(z';t,r,z) \\ & + \frac{E^s(t,r,z)}{E(t,r,z)} K_{b\to s}(z';t,r,z) + \frac{E^b(t,r,z)}{E(t,r,z)} K_{b\to b}(z';t,r,z) \Bigg) \frac{\delta c}{c}(z')\, dz' \end{aligned} \tag{5.67}$$

where

$$\begin{aligned} K_{s\to s}(z';t,r,z) &= \frac{\bar{t}_{s\to s}(t,r,z)}{t} K_{C_{ph}}(z') \\ K_{s\to b}(z';t,r,z) &= \frac{\bar{t}_{s\to b}(t,r,z)}{t} K_{C_{ph}}(z') \\ K_{b\to s}(z';t,r,z) &= \frac{\bar{t}_{b\to s}(z';t,r,z)}{t} \\ K_{b\to b}(z';t,r,z) &= \frac{\bar{t}_{b\to b}(z';t,r,z)}{t} \end{aligned} \tag{5.68}$$

These equations show the contribution of each mode to the sensitivity and the depth dependence on the energy density of surface and body waves.

5.8 Monte Carlo simulations

The use of Monte Carlo simulations to recreate properties of the propagation of seismic waves began with the application in equivalent acoustic systems that showed to be successful reproducing features like coda envelopes generated by earthquakes, or the study of the attenuation in different scattering regimes (Gusev and Abubakirov, 1987; Hoshiba, 1991; Abubakirov and Gusev, 1990). This was later extended to models that include depth dependence of the velocity structure and the mean free path (Hoshiba, 1997; Margerin, Campillo, and Tiggelen, 1998), elastic propagation modes (Margerin, Campillo, and Van Tiggelen, 2000; Przybilla, Korn, and Wegler, 2006), lateral heterogeneous scattering and non-isotropic scattering (Sens–Schönfelder, Margerin, and Campillo, 2009), or coupling between surface and body scalar

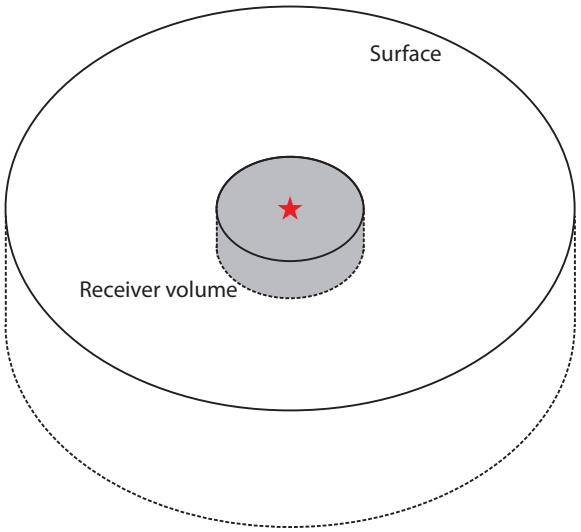

FIGURE 5.3: Model of the Monte Carlo simulations. The red star marks the location of the source, and the grey volume represents the receiver zone.

waves (Margerin, Bajaras, and Campillo, 2019). Here, the last case will be further explored towards the estimation of the time sensitivity kernels of both body and surface waves

5.8.1 General outline

The objective of the Monte Carlo simulations is to recreate the conditions set by the energy transport equations shown in 5.14, and to make measurements of the time spent at each depth and mode in a layered system. The general procedure consists in shooting many seismic particles from the source, and allow them to travel in a straight line until they are scattered; after each of these scattering events, a new direction and mode are chosen randomly following certain probability distribution, and the particle continues its propagation. The time between scattering events is statistically controlled by the mean free time of each mode. The receiver is defined as a small finite volume through which the particles must cross in order to contribute to the energy density and to the sensitivity measured from that point, at that particular time. This is the particle counting method (Sens–Schönfelder, Margerin, and Campillo, 2009; Gusev and Abubakirov, 1987). One of the main disadvantages of this method is that the probability that a particle doing a random walk will pass through the receiver at a given time is low; this is partially compensated by shooting many particles from the source, and exploiting the symmetries of the system which may allow to turn the receiver into bigger volume. For example, if we have a completely symmetric full-space, the receiver can be turned into a spherical shell. In our case, the half-space symmetry allows us to have a ring-shaped receiver around the source. it is worth noticing however that this symmetry can be broken if the sources are non-isotropic, although this is not our case. The geometry used here if illustrated in figure 5.3.

Nonetheless, maybe the main advantage of this method is that it allows us to follow the trajectories of all the phonons and measure the time that each of them passes on every part of the medium and on every mode. With these measurements, we can calculate the time densities for each mode and depth that are the basis of the sensitivity kernel as was explained in the previous sections. Next, we present the most important aspects of the simulations

Propagation: A big number of particles are shot from a source located at the surface in random directions, with initial modes chosen probabilistically to follow equations 5.15. The body mode propagates in three dimensions and the surface mode in two; this means that the surface particles do not have any depth coordinate. Each particle propagates in a straight line in a random isotropic direction assigned at the beginning. The time of propagation or free time of flight is also chosen randomly in such a way that its distribution reconstructs the exponential probability density function $\tau^{-1}e^{t/\tau}$ (Welch, Van Gemert, and Others, 2011) where τ is the mean free time. This means free time is chosen according to the mode and depth of the particle (for the case of the body particles) as indicated in equation 5.9. For the case of body waves, the dependence of the mean free time on the depth is simplified through the method of delta collisions which introduce virtual scattering events that do not modify the direction of propagation (Lux, 2018). If a body particle reaches the surface, its movement is completely reflected into the half-space without modifying any other parameter.

Scattering: Once the simulation time reaches the the free time of flight, a scattering event occurs. A new propagation direction and mode are chosen. The mode is chosen randomly between the two possible outcomes using their respective mean free times as weights for each option. For example, the probability that a body wave scatter into a surface wave is

$$p^{b\to s}(z) = \frac{(\tau^{b\to s}(z))^{-1}}{(\tau^{b\to s}(z))^{-1} + (\tau^{b\to b})^{-1}} \tag{5.69}$$

It follows then that the probability that a body wave scatters into another body wave is $p^{b\to b} = 1 - p^{b\to s}$. Notice that for this particular case, when the body particle is far away from the surface, the probability of changing into a surface particle is practically zero. When a surface particle scatters into a body particle, the depth of the particle is defined randomly following the probability density function $2\alpha e^{-2\alpha z}$, which represents the normalized energy density of the surface waves.

Time bookkeeping: In order to measure the time densities in equation 5.60, the half-space is virtually segmented in horizontal layers. When the particle is propagating as a body wave, we keep track of the time spent in each of these layers; these times t_b, are added between them when the particle passes several times through the same layer. If the particle propagates as a surface wave, the time is registered and accumulated as the independent value t_s. This process is illustrated in figure 5.4. it is important to remember that although from the bookkeeping process the times recorded in a body or surface modes seem equivalent, for the body waves case we are technically registering the time per unit of layer length, contrary to the case of the surface waves where we're registering directly the total time as was explained in the section 5.6.

Detection and averaging: The source and the receiver are both located in the same position over the surface to reproduce measurements of the seismic field obtained through the auto-correlation. However in the practice, the receiver is a cylindrical volume: if the particle is inside it, then it is assumed that it arrived to the receiver. This is illustrated in figure 5.3. At the times at which we want to measure the sensitivity (the lapse times), the simulation evaluates if the particle is inside the receiver volume: if that's the case, the bookkept times are registered along with the mode of the particle at that instant as this is the arrival mode. If not, no registering process is performed but the simulation

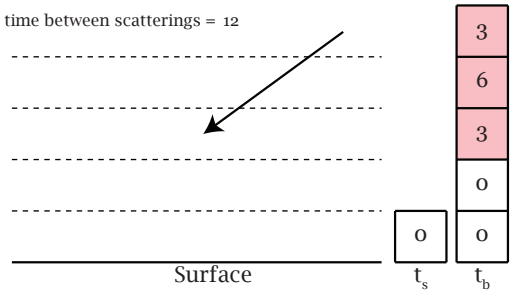

(A) The time spent by the body particle is recorded independently for each layer

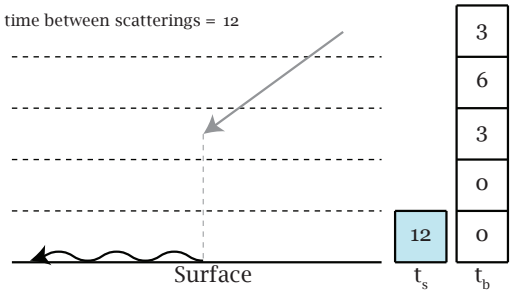

(B) The time spent as a surface particle is recorded independently

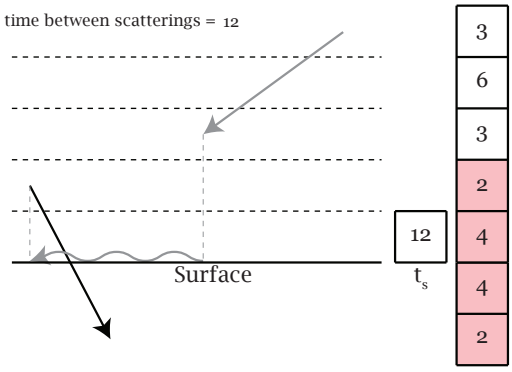

(C) If the body particle reaches the surface, the time is recorded temporarily beyond it

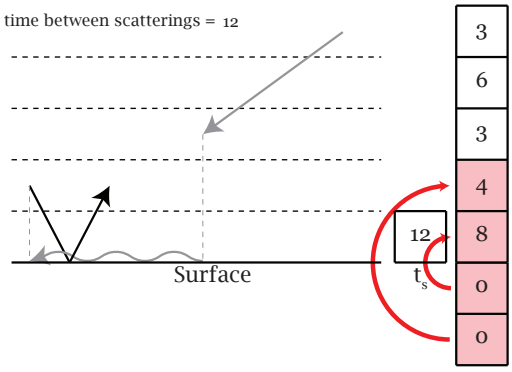

(D) The times beyond the surface are summed to the layers within the half-space

FIGURE 5.4: Time bookkeeping for body and surface waves. The probabilistic character of the time between scatterings events has been simplified.

Variable	Monte Carlo
frequency* (Hz)	5.25
α* (km^{-1})	2.86
Surface penetration depth L_s (km)	0.7
B. energy velocity c_E (km/s)	3.9
S. energy velocity c_R (km/s)	3.7
Mean free time $\tau^{b\to b}$ (s)	0.35
Mean free path $l^{b\to b}$ (km)	1.37
Grid spacing g_r (m)	50
Receiver radius* (km)	5.7
Receiver depth* (m)	20
Model depth (km)	6
Model radius* (km)	5.7

TABLE 5.1: Parameters used in the Monte Carlo simulations. The half-space has no bounds; the last two parameters are only relevant for the absorbing boundary conditions. The parameters with an asterisk may differ from Obermann et al. (2016) for reasons explained in the text; α is included in this list as it has no equivalent in the elastic case.

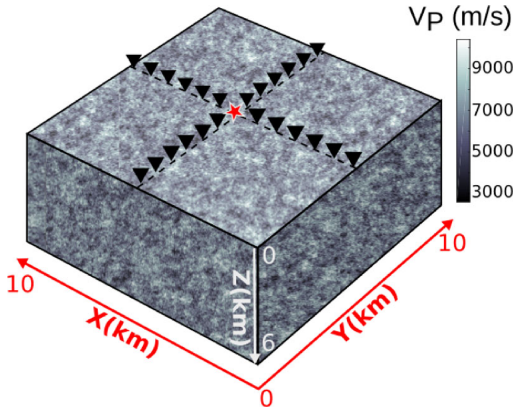

FIGURE 5.5: Model used by (taken from) Obermann et al. (2016). The red star marks the source positions and the inverted triangles the receiver positions

continues because it is still possible that the particle will be within the receiver volume for another measurement at a later lapse time.

After all the particle paths have been simulated, the registered times are averaged between them for particles that arrived in the same mode to the receiver at a given time t, and that propagated at the same mode and at the same depth (for body waves). This procedure gives us all the averaged times present in equation 5.60.

5.9 Surface and body wave sensitivity

We begin making a quick summary of the method used by Obermann et al. (2016) in an elastic 3-D half-space; the model used can be seen in figure 5.5 They first estimate the surface and body wave contributions to the apparent velocity variation independently. The surface contribution $\varepsilon^{\text{Surf}}$ is determined with a series of simulations in a 3-D homogeneous half-space

elastic medium, where a source pulse is generated, and the resulting seismic field is recorded at the surface. The apparent velocity perturbation is estimated by comparing the waveforms obtained with and without a horizontal velocity perturbation located at different depths. In particular, in this first set of simulations, the medium does not allow conversions into bulk waves. The body wave contribution $\varepsilon^{\text{Body}}$ is estimated with the kernel for the diffusive regime by Pacheco and Snieder (2005). Afterward, a similar series of simulations is performed, but this time including all the types of waves in an heterogeneous medium. From this is obtained the total observed apparent velocity variation. They propose that the total apparent velocity variation can be modeled as a linear combination of the independent contributions of body and surface waves

$$\varepsilon^{\text{Theo}}(z,t) = \alpha'(t)\varepsilon^{\text{Surf}}(z) + (1-\alpha'(t))\varepsilon^{\text{Body}}(z,t) \tag{5.70}$$

where α' is the fitting parameter that they called partition coefficient (the prime was added to differentiate it from the surface penetration factor of the scalar case α). For each lapse time, they search for the best partition coefficient that optimizes the fit between $\varepsilon^{\text{Theo}}$ and observed total apparent velocity variation at depths.

The parameters used initially in the Monte Carlo simulation were chosen to resemble the physical variables of Obermann et al. (2016) in order to compare with the results there presented. They are shown in table 5.1. Some clarifications must be made about some of these values: α was chosen to match the reach of the surface wave sensitivity reported in Obermann et al. (2016) of $L_s = 0.7km$; this automatically fixed a value of the frequency given their relationship explained in the section 5.3. The frequency in SPECFEM3D is not directly controlled. Furthermore, the model used there had absorbing boundary conditions which can be easily implemented in a random walk simulation by adding the condition that the simulation ends once a particle leaves the allowed zone. In the case of Obermann et al. (2016) this zone is rectangular (with a side length of $10km$) while we make use of a symmetric cylindrical zone; therefore, although the depth in both cases is the same, in our case we choose the radius in such a way the total horizontal area would be approximately the same ($100km^2$). However, here the boundary conditions will be used only when explicitly stated for making comparisons between the two studies; in general, there will be no absorption of the energy.

We estimate the apparent velocity variation $(-\delta t/t)$ for a velocity perturbation of 20% with a thickness of $50m$ (the grid spacing of the medium) located at different depths; the result is represented as the yellow line in the figure 5.6. This is equivalent to take each of the values of the discretized version of equation 5.66 and multiply them by $\delta c/c = 0.02$. Therefore, the obtained velocity variations are proportional to the sensitivity kernels at depth. Given that the sensitivity is the additive results of the surface and body sensitivities, we can track what part of this velocity variation is due to which of them: this is represented by the solid blue and red lines. The body and surface sensitivities show some expected characteristics: the surface sensitivity disappears around $0.7km$ which is the imposed reach of the surface waves. On the other hand, the body sensitivity shows a deeper reach that is related to the transit of body wave particles to deeper zones of the medium and their eventual return. This snapshot of the sensitivity at an early stage of the system shows a dominance of the surface sensitivity in the zones closer to the surface, (the first $300m$ to be precise) and a limited reach of the body wave sensitivity to the first couple of kilometers. Overall, a perturbation in the first hundreds of meters of the medium can produce changes in the apparent velocity variation at the surface one order of magnitude bigger than the same perturbation located below $1km$.

figure 5.6 also shows the contribution of each sensitivity to the apparent velocity variation, classified by their propagation and arrival modes. For example, the dotted blue line (contribution of $K_{s\to b}$) shows the contribution of the surface wave particles that arrived in

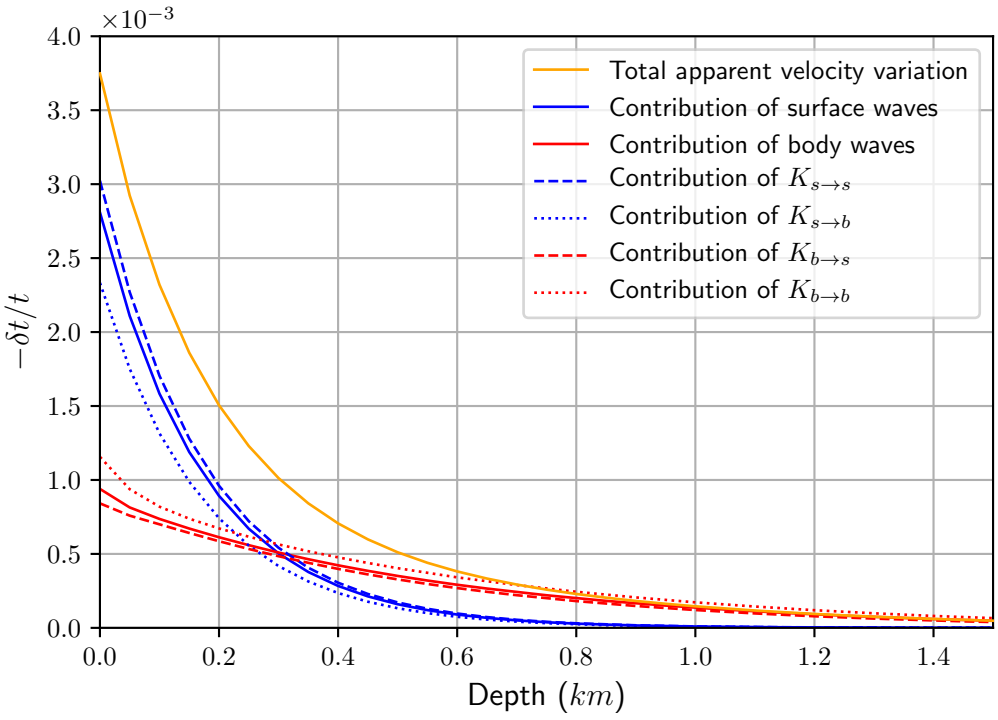

FIGURE 5.6: Total apparent velocity variation (yellow), associated to the body waves sensitivity (red), to the surface waves sensitivity (blue) and to each of the times densities in equations 5.67 and 5.68 at a lapse time of $2s$ (normalized time of $t/\tau^{b\to b} = 5.7$) with a velocity perturbation of $\delta c/c = 0.02$

body wave mode, and the dashed blue line (contribution of $K_{s\to s}$) shows the contribution of the surface wave particles that arrived in the surface wave mode; the solid blue line is the weighted average between the two of them (as can be seen in equations 5.67 and 5.68). The sensitivity on a given mode is always higher when the arrival happens in the same mode; for example the contribution of $K_{b\to b}$ is higher than the contribution of $K_{b\to s}$. At this lapse time ($t/\tau^{b\to b} = 5.7$), there is still a low number of scattering events and therefore, a low probability of changing mode. However, the total surface and body wave sensitivities (the solid blue and red lines) seem the be closer to the surface mode arrivals (the dashed lines) indicating that the number of surface particles at the receiver is higher. This is related to the location of the receiver on the surface and is a common featured for all the results obtained with his configuration.

The sensitivity at depth was obtained by Obermann et al. (2016) with a similar configuration except for the presence of absorbing boundary conditions: it can be seen on the left in figure 5.7. The yellow line represents the observed apparent velocity variation measured in full elastic simulations, the dashed black line is the result of the fitted model with equation 5.70, and the dashed red line represents the estimation only due to the body sensitivity kernel calculated from the equation of Pacheco and Snieder (2005). To compare with our case, we imposed also boundary conditions (the bounded geometry is indicated in the last two rows of table 5.1 and recalculated the apparent velocity variation; the result is shown in the right of figure 5.7 (right panel). The resemblance between the two of them is remarkable, especially if we keep in mind that one of them is obtained in an elastic propagation field and the other in a scalar one. A quick comparison between this result and the one obtained without absorbing boundary conditions (figure 5.6) shows virtually no differences: although at this lapse time

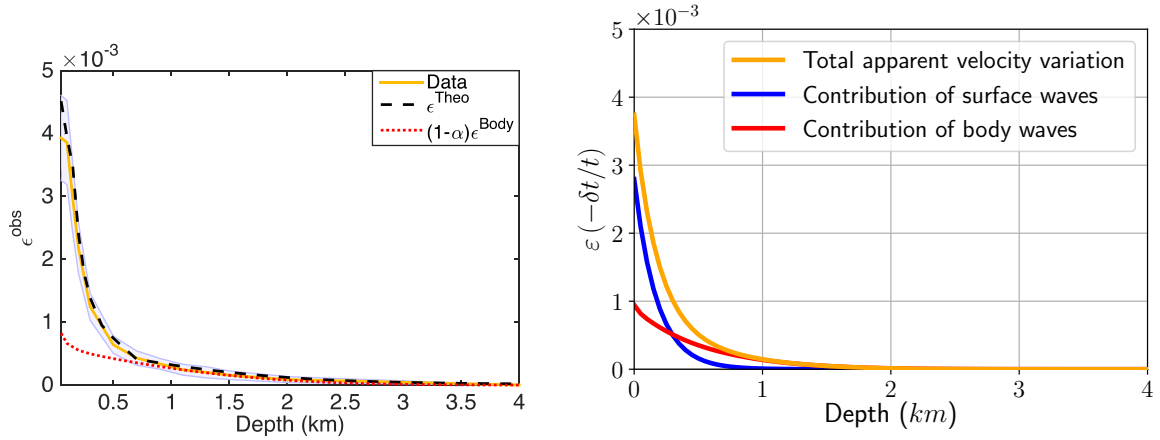

FIGURE 5.7: Apparent relative velocity variation with absorbing boundary conditions. Left: Observed apparent velocity variation (yellow), estimated contribution using only the body wave sensitivity (red), and modeled total apparent velocity variation(black) - modified from Obermann et al. (2016). Right: Total apparent velocity variation (yellow), contribution of body waves (red) and surface waves (blue) sensitivities.

the ballistic part of the wave already reach the boundaries, most of the energy it is still a very early stage of the system.

The temporal evolution of the profile for the surface and body sensitivity kernels can be seen in figure 5.8. In this case, the factor $\delta c/c = 0.02$ was not multiplied so these are the kernels themselves and not the apparent velocity variation. In general, there is a decrease of surface sensitivity and an increase of body sensitivity related to the radiation of this type of wave into the bulk of the medium (Margerin, Bajaras, and Campillo, 2019). The amplitude of the surface wave sensitivity changes gradually but its shape remains the same: this peculiarity comes from the manifest independence between $K_{C_{ph}}(z')$ that contains the information of the depth of the perturbation and $\langle t_s(t,r,z)\rangle$ that acts as a modulating pre-factor (see equation 5.66). The deeper zones of the medium are sampled only by the body waves, as its sensitivity extends over these regions at later lapse times. The surface wave sensitivity dominates in regions close surface, especially at early lapse times and both types of sensitivities decrease in the vicinity of the surface at longer lapse times.

5.9.1 Time partition coefficient

The contributions of the surface and body waves to the apparent velocity variation are proportional to their corresponding sensitivities. We can represent the total contribution of each of them rewriting equation 5.62 as

$$1 = \frac{\langle t_s(t,r,z)\rangle}{t} + \frac{\langle t_b(t,r,z)\rangle}{t} = \eta_s + \eta_b \tag{5.71}$$

where the average time spent as a body particle was integrated for all depths. The fractions in the right hand side of this equation are the time partition coefficients. They represent the time that the system passed on each mode (as a fraction between 0 and 1), and are, therefore, proportional to the total sensitivity on each mode. Any change that increases the total time spent in the body wave mode (for example moving the receiver at a deeper layer) will necessarily produce a decrease in the total time spent in the surface wave mode. We could make an analogous definition of the partition coefficients in terms of K_s and K_b (which implies including the variation of the surface wave velocity with perturbations at depth $K_{C_{ph}}$), but we

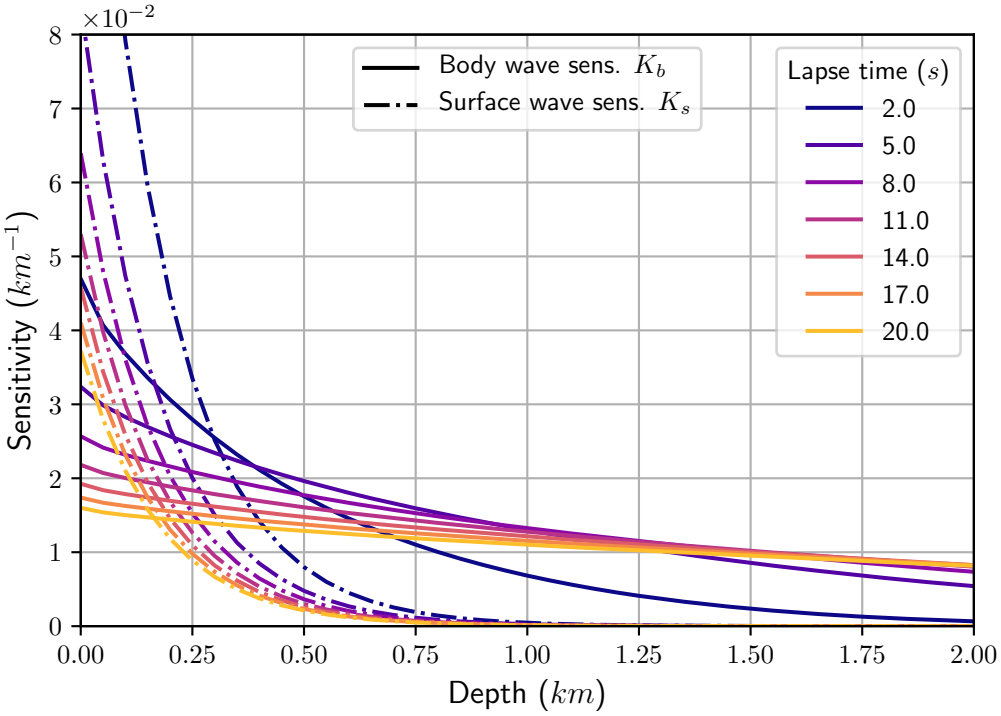

FIGURE 5.8: Profile of the surface (dashed lines) and body (solid lines) waves sensitivity kernels at depths, for different lapse times (indicated with colors)

will keep it in terms of the time densities as their interpretation is more immediate and it does not produce relevant changes in the result. We can extend this definition to the classification by mode of propagation and arrival using the equation 5.63

$$1 = \frac{E^s(t,r,z)}{E(t,r,z)}(\eta_{s\to s} + \eta_{b\to s}) + \frac{E^b(t,r,z)}{E(t,r,z)}(\eta_{s\to b} + \eta_{b\to b}) \tag{5.72}$$

where each sum inside the parenthesis is equal to 1. We can write the time partition coefficient for body and surface waves as a weighted average of these time partition coefficients following equations 5.61

$$\begin{aligned}\eta_s &= \frac{E^s(t,r,z)}{E(t,r,z)}\eta_{s\to s} + \frac{E^b(t,r,z)}{E(t,r,z)}\eta_{s\to b} \\ \eta_b &= \frac{E^s(t,r,z)}{E(t,r,z)}\eta_{b\to s} + \frac{E^b(t,r,z)}{E(t,r,z)}\eta_{b\to b}\end{aligned} \tag{5.73}$$

The evolution of the partition coefficients in time can be seen in plot 5.9. At very early lapse times, the time partition coefficient is strongly dominated by the surface waves because the location of the source favors the excitation of surface wave modes; this implies a predominance of the total surface wave sensitivity. The partition coefficients of body and surface waves are equal (the crossing point) around 6 mean free times: this marks the moment in which the body wave sensitivity starts dominating the total sensitivity.

figure 5.9 also shows the dynamics of the coefficients classified by modes of propagation and arrival. Just as before, the coefficients associated with the arrivals in the surface mode (the

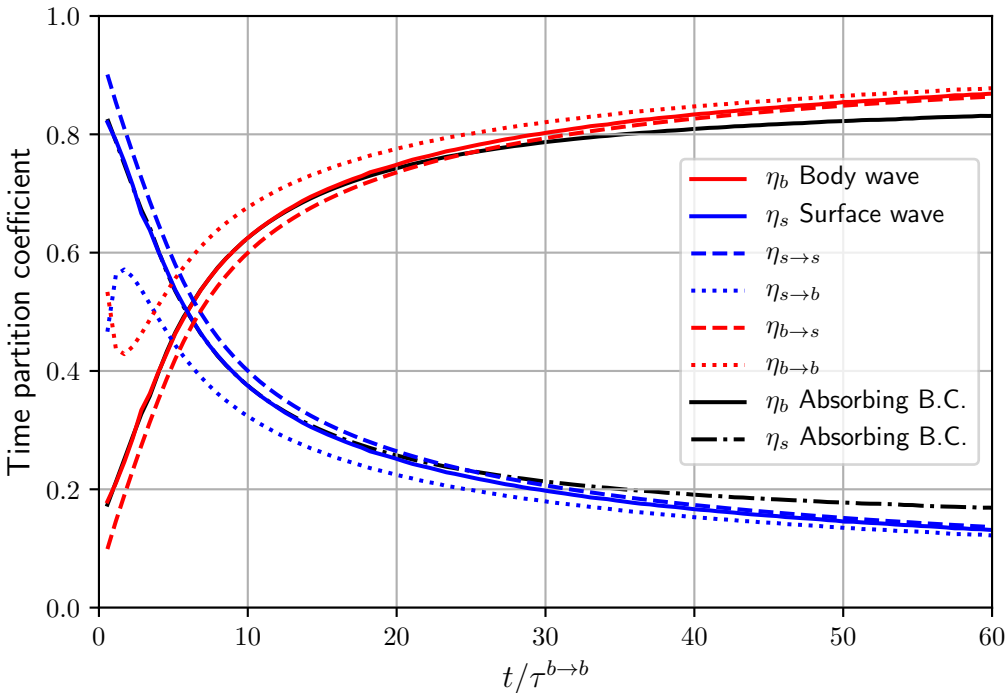

FIGURE 5.9: Evolution of the time partition coefficient for the surface (blue) and body (red) waves sensitivities, and associated with each possible combination of modes of propagation and arrival (dashed lines). The black lines represent the evolution of the partition coefficients for the surface and body sensitivities with absorbing boundary conditions. The time has been normalized by the body-to-body mean free time.

dashed blue $\eta_{s\to s}$ and red $\eta_{b\to s}$ lines) seem to be closer to the total average (the solid lines), especially at early lapse times. This indicates a bigger weight in the averages in equation 5.73 as a consequence of a higher level of energy surface at the receiver. Let us focus on the particles that arrive in the surface wave mode: the time partition $\eta_{b\to s}$ (red dashed line) is greater than $\eta_{s\to s}$ (blue dashed line) for long lapse times. Therefore, at this stage of the system, a surface particle arriving to the receiver has actually passed most of its travel time propagating as a body particle. At this point, the difference of the time partition coefficient between the two arrival modes tends to disappear: for example, the difference between $\eta_{b\to s}$ (red dashed line) and $\eta_{b\to b}$ (red dotted line) is minimum at after 60 mean free times. This indicates that the system has spent a relatively large time in the diffusive state.

The application of absorbing boundary conditions (represented by the black lines) comes to be evident only after 30 mean free times, where we start seeing a decrease of the sensitivity of the body waves and an increase of the surface waves sensitivity. The absorption implies removing the paths between the source and the receiver that pass outside of the allowed volume at any point. figure 5.10 shows the effect of the boundary conditions in the balance between the total surface and body waves energies for the whole space: as the surface particles can only escape through the lateral side of the volume, while the body particles can do it by the sides and the bottom, the rate of body phonons leaving the simulation is higher. It is then clear that the surface sensitivity for the system with the absorbing boundary conditions in figure 5.9 is higher because there is an over-representation of the paths that remain in the surface wave mode of propagation. Although just a fraction of the phonons represented in figure 5.10 participate in the sensitivity and in the time partition coefficients measured in the surface, for long lapse times the amount of energy sampling the medium is just a small fraction of the total energy emitted by the source.

figure 5.11 shows a comparison of the evolution of the partition coefficient between the elastic case calculated by Obermann et al. (2016) (left) and the times partition coefficient in scalar case (right). In the elastic case, the time is normalized with the transport mean free time, that is, the time over which a particle loses all information about the initial direction of propagation (Margerin, 2011; Sheng and Tiggelen, 2007). When the scattering is isotropic, as in our case, the transport mean free path and the mean free path are equal. Therefore, the time in the Monte Carlo simulation is normalized with the body-to-body mean free time. The surface and body partition coefficients reach equal values (the crossing point) approximately at the same time for both cases; that this point is reached a bit later for the elastic case may be related to the high surface sensitivity of the system at the beginning of the simulation in comparison with the scalar case. This is probably due to a strong excitation of surface wave modes by the source whereas in our case this is statistically controlled to follow the energy partitioning ratio in the source radiation (equation 5.15). The other important difference comes from the partitioning coefficient at long lapse times: the elastic case seems to show a strong tendency towards the disappearance of the surface sensitivity. In the scalar case, this process is more gradual as it shows a rate of energy transfer of surface wave energy into body wave energy proportional to the squared root of time (Margerin, Bajaras, and Campillo, 2019).

5.10 Spatial scaling parameter

The mean free time is a natural scaling factor for the time as it quantifies the degree of scattering in the system. In a propagation medium without boundaries, two systems with different mean free times, but at the same normalized time t/τ, will have similar distributions of energy and sensitivities in a system spatially scaled with mean free path. However, the

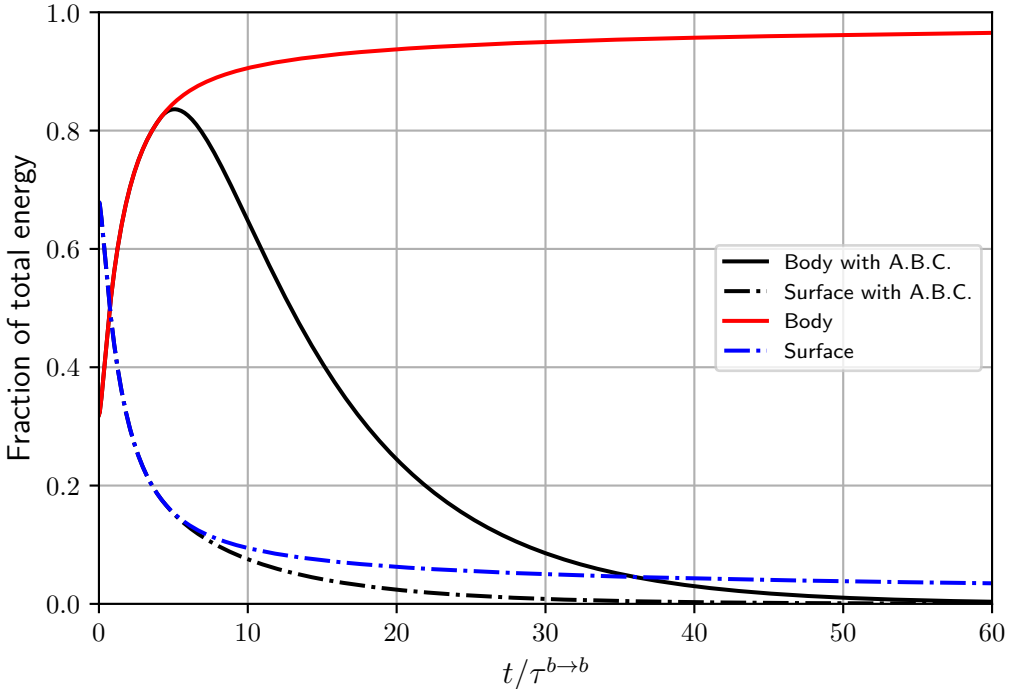

FIGURE 5.10: Fraction of the total energy in body (solid lines) and in surface wave mode (dashed lines) with absorbing boundary conditions (black lines) and without (red and blue lines).

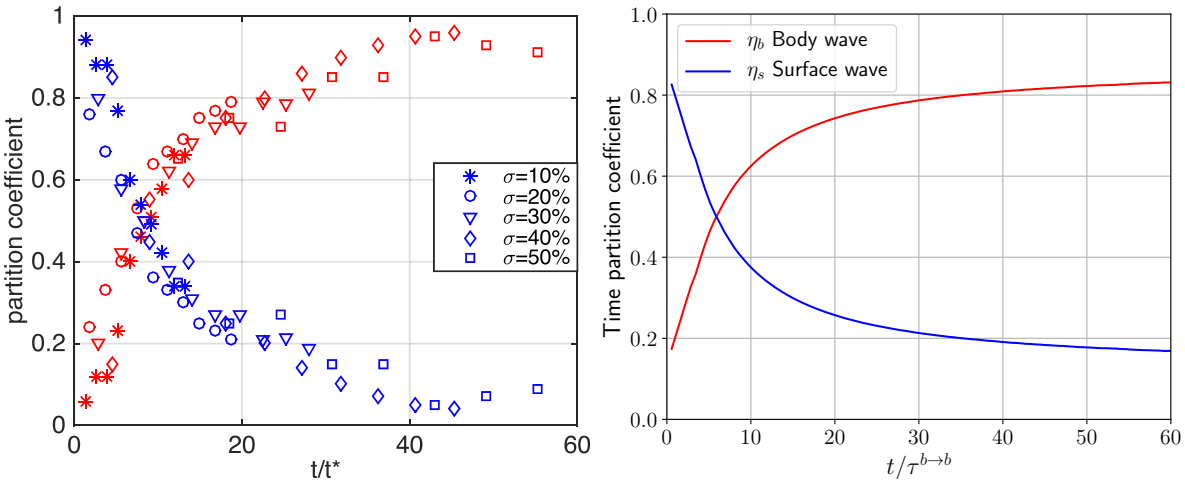

FIGURE 5.11: Partition coefficients with absorbing boundaries condition. Left: partition coefficient for different degrees of heterogeneity. The time has been normalized by the transport mean free time. (modified from Obermann et al. (2016)). Right: time partition coefficient for the configuration presented in table 5.1.The time has been normalized with the body-to-body mean free path. In both cases the red correspond to the body wave and blue line to the surface wave.

Variable	Monte Carlo
Surface penetration depth L_s (km)	$1, 2, 10, 20, 100$
B. energy velocity c_E (km/s)	3.9
S. energy velocity c_R (km/s)	4.1
Mean free path $l^{b\to b}$ (km)	$1, 5, 10, 50, 100$
Grid spacing g_r (m)	50
Receiver radius (km)	$4l^{b\to b}$
Receiver depth (m)	20

TABLE 5.2: Parameters used in the Monte Carlo simulations for the scaling parameter section. The radius of the receiver zone is scaled with the mean free path.

introduction of the surface boundary in the half-space problem breaks this symmetry. To see why, let us think about the energy proportions between the two types of waves, which are controlled through two parallel mechanisms happening in parallel: the first one, the continuous energy exchange between the two modes happening through scattering. This process is confined to the region close to the surface and is controlled by the surface-to-body and body-to-surface mean free times. The second, the continuous propagation of the body waves towards deeper levels of the medium, which implies that a smaller amount of body wave energy is available to convert to surface wave at longer times. In general, the shorter is the time the body particle passes in the region close to the surface, the lowest is the probability of scattering into surface wave mode. Therefore, two systems with the same mean free times and source will have very different energy distributions if the exchange zone for scattering into surface waves is of different sizes between them. The region on which the energy exchange happens is delimited by the penetration of the surface waves, and therefore, the natural quantity to compare this length is the body-to-body mean free path.

We study the time partition coefficient for different proportions between the penetration length of the surface wave and the body-to-body mean free path, fixing the first one at $10km$ and modifying the mean free path with values ranging from $1km$ to $100km$; the result for the body wave coefficient is shown in figure 5.12 as the solid lines. The curves representing the coefficients of the surface wave was omitted for simplicity as it contains the same information of the body coefficients. The general parameters used in this set of simulations are shown in table 5.2. It is worth remembering at this point that the partition coefficients are calculated only with the particles that arrive to the receiver. Despite that the conditions of the source are equal between all the configurations (and therefore the initial proportion of energies between the two modes) the partition coefficient show drastic differences after one lapse time between different configurations. From there on, the total surface sensitivity decreases quicker for the configurations with the higher mean free paths (represented in this case by the purple $l^{b\to b} = 100km$ and the red line $l^{b\to b} = 50km$) as in those cases the particles have higher chances of escape exchange zone and the energy feedback into surface energy is lower, as was discussed before.

Evaluate how the proportion between $l^{b\to b}$ and L_s affects the evolution of the system can also be done by fixing the mean free path and modifying the penetration depth of the surface waves. This is shown also in figure 5.12 as the scatter plots. it is evident that the evolution of the system follows the same path as before. However, the interesting aspect of these results lies in the proportions: notice, for example, that the values of $l^{b\to b}$ and L_s for the configuration represented by the blue line are ten times smaller than for the configuration represented by the blue scatter plot. In the opposite case, these values for the purple lines are ten times bigger than their purple scatter plot counterpart. This means that the evolution

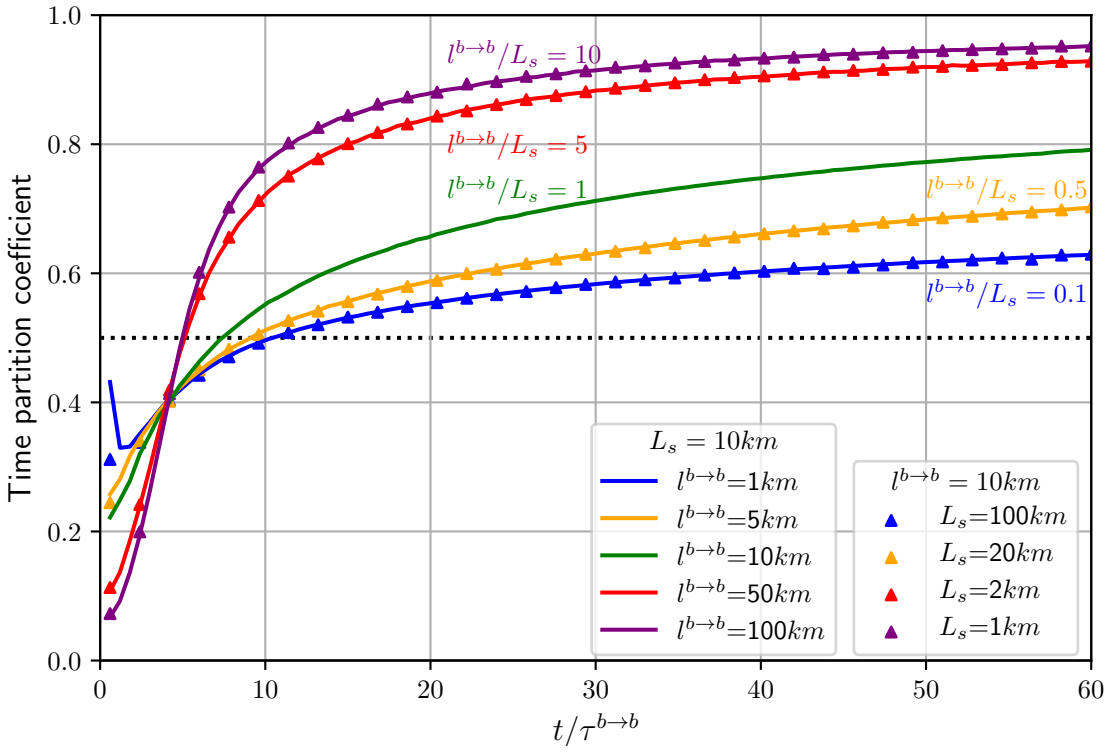

FIGURE 5.12: Body partition coefficient for different values of L_s and $l^{b\to b}$. Lines: time partition coefficient of body waves for a penetration length of $L_s = 10km$ and different values of $l^{b\to b}$. Triangle scatter plots: time partition coefficient of body waves for a body-to-body mean free path of $l^{b\to b} = 10km$ and different values of L_s. The time has been normalized by the body-to-body mean free time. The dotted black line indicate the level at which the body and surface time partition coefficients are equal (the crossing points)

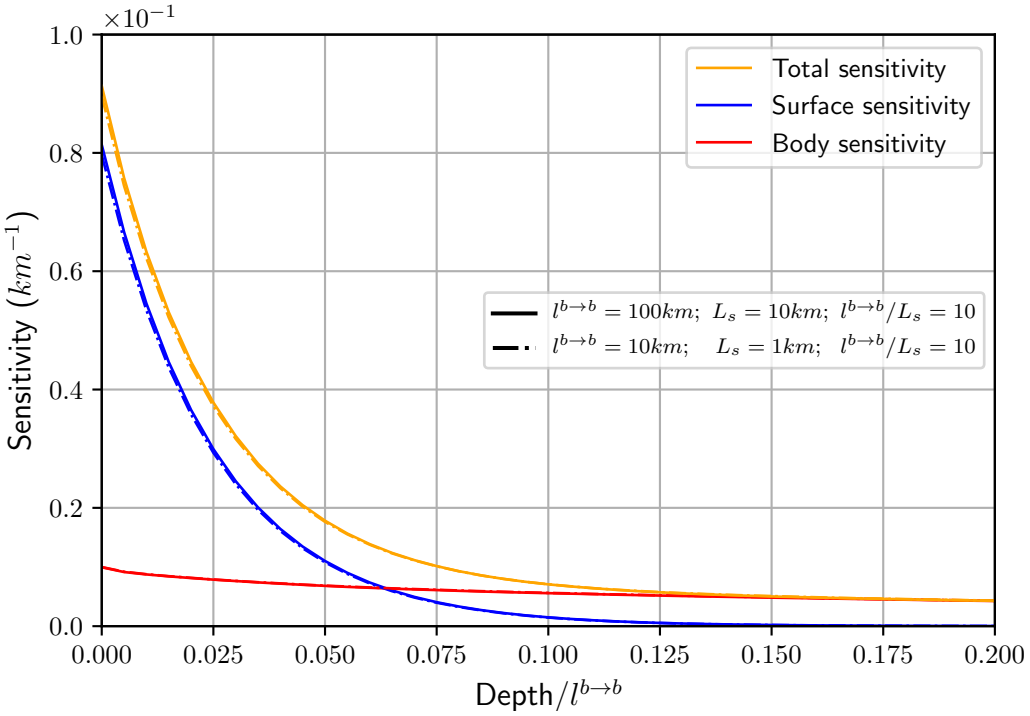

FIGURE 5.13: Total sensitivity (yellow), body waves sensitivity (red), and surface waves sensitivity (blue) for configurations with $l^{b\to b} = 100km$; $L_s = 10km$ (solid lines) and with $l^{b\to b} = 10km$; $L_s = 1km$ (dashed lines), for a lapse time of $t/\tau^{bb} = 6$. The depth was scaled with their respective body-to-body mean free paths.

of the system is determined by the ratio $l^{b\to b}/L_s$, in addition to the normalized time $t/\tau^{b\to b}$. All the configurations that share the same color in figure 5.12, have the same value for this spatial scaling parameter.

The comparison of the sensitivity profile with depth for the configurations in purple in the plot 5.12, can be seen in the figure 5.13; the sensitivities are virtually equal. As expected, the sensitivity extends through very different scales of length and therefore is necessary to scale them down with their respective body-to-body mean free paths. The time densities (and therefore the sensitivities) are also affected by the difference of scale as the grid spacing g_r is not proportional with the mean free paths. To equalize them we should have a layering ten times thicker for the configuration with the largest mean free path, or to add the sensitivity for several layers over a distance that makes the grid proportional to the mean free path, as was done in this case. For the configuration with $l^{b\to b} = 100km$ the sensitivity was added every ten layers so the ratio $l^{b\to b}/g_r = 200$ is equal for the two configurations.

The crossing time of the time partition coefficient (the normalized time in which the surface and body wave coefficients are equal to 0.5) marks the moment where the body sensitivity starts being predominant over the surface sensitivity. We can see from figure 5.12 that this moment varies depending on the value of $l^{b\to b}/L_s$. figure 5.14 shows the normalized time of the crossing point for systems in which the spatial scaling parameter $l^{b\to b}/L_s$ goes from 0.1 to 10. When the mean free path is several times bigger than the penetration length ($l^{b\to b}/L_s \gg 1$) the coupling between surface and body waves is weak and the crossing time seems to approach asymptotically a minimum possible value. In the opposite case, when the mean free path is several times smaller than the penetration length ($l^{b\to b}/L_s \ll 1$) the

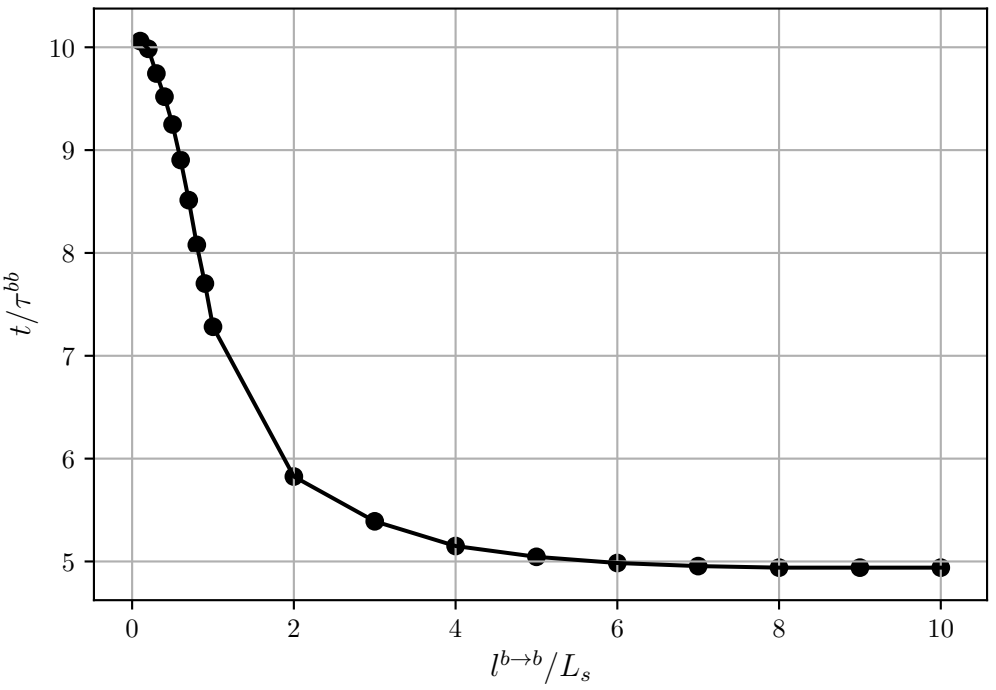

FIGURE 5.14: Normalized time at which the body and surface wave partition coefficients are equal for different ratios of $l^{b\to b}/L_s$

sensitivity transition between surface and body waves happens more slowly since most of the body wave energy gets confined inside the energy exchange zone delimited by the surface wave. The biggest change of the system happens around the point where the mean free path and the penetration length are similar to each other. This overall behavior is not present in the results of Obermann et al. (2016) shown in figure 5.7

5.11 Conclusions

We develop over the scalar model with mixed boundary conditions recently proposed by Margerin, Bajaras, and Campillo (2019) for the estimation of the travel-time sensitivity kernels in 3-D for body and surface waves. First, we apply a variational approach in the scalar case to determine the response of the surface wave velocity to perturbations of the bulk velocity. After some simplifications, we reach an expression that relates them through the eigenfunction of the surface wave which automatically sets a sensitivity depth limit for the surface waves.

As part of the effort to build parallels with the elastic case, we find an equivalence between the penetration depths of the surface wave in the scalar model and the Rayleigh wave. We find that they have a similar reach within the medium when the parameter α that configures the boundary condition, is equal to $0.3k_R$, a fraction of the wavenumber of the Rayleigh wave. This parallel between the two of them has the advantage of giving the scalar surface wave a scaling behavior with the Rayleigh wavelength and a natural dependency with the frequency. Furthermore, we propose $L_s = 2\alpha^{-1}$ as the effective penetration that the surface wave has in the medium for the scalar case. Then, we reconstruct the sensitivity kernel formalism to include the two possible modes of propagation, as surface and as body waves. To do so, we

start with a classic probabilistic description of the transit of phonons from the source to the receiver, which we extend towards different modes and depths. This includes also the modes of arrival to the receiver, and the corresponding equivalence to the energies ratios at this point. The conceptual link of each of these probabilities with the possible paths going from the source to the receiver is developed to establish a link with the time densities and with the Monte Carlo simulations to measure them. The formalism here presented has the advantage that it can be easily extended to a full vectorial distribution of travel-time densities. These results are used to construct an equation for the travel-time sensitivity kernel of the system that integrates the body and the surface wave sensitivities in a natural way.

A crucial part of the estimation of this kernel is the measurement of the time densities with the Monte Carlo simulations which are described in detail. The initial set of parameters used are chosen to mimic as close as possible the work of Obermann et al. (2016) where estimations of the body and surface sensitivities were made with the help of full wavefield numerical simulations. We evaluate the apparent velocity variation at the surface generated by a bulk velocity perturbation located at different depths. As the kernel is a linear combination of the sensitivities of body and surface waves, the contribution of each of them to the apparent velocity change can be estimated independently. The contribution of the surface waves is limited to an effective penetration equal to L_s as expected, while the body contribution is less dominant at the surface but has a longer reach within the medium. The total sensitivity of the seismic field can be one order of magnitude stronger for perturbations close to the surface, than to perturbations located deeper in the medium.

The apparent velocity variation obtained by the scalar kernel with absorbing boundary conditions holds a remarkable resemblance with the reported results by Obermann et al. (2016) both in amplitude and shape. The increase of lapse time in the system produces a decrease of the surface wave sensitivity that does not alter its shape but only its amplitude; this is a consequence of the independence between the depth and the temporal variables of the surface kernel. On the other hand, the body wave sensitivity increases its reach towards deeper levels of the medium. However, the sensitivity of both of them decreases progressively at the surface with time.

The time partition coefficients represent the total contribution of each of the modes of propagation to the total sensitivity of the system. The evolution of the coefficients characterizes the influence of one or other type of wave in the sampling of the perturbations at depth in different moments of the system. At very short lapse times the surface waves dominate the sensitivity because the location of both the source and the receiver in the surface excites predominately the surface wave modes. After, there is a decrease of the surface wave sensitivity coupled with an increase of the body wave sensitivity related to the progressive transformation of surface wave energy into body energy and the continuous radiation of this last one into the bulk of the medium (Margerin, Bajaras, and Campillo, 2019).

The inclusion of the absorbing boundary conditions is only evident after around 30 mean free times, the point at which there seems to be a higher surface sensitivity (and lower body sensitivity) with respect to the unbounded case. This can be explained in light of the energy losses generated by the absorption: although we observe a decrease in both types of energy, it is more accentuated for the body energy because the total area through which it can escape is bigger that for the surface case. This implies that the higher surface sensitivity in the absorbing case is just an artificial effect of the over-representation of the surface wave particles in the calculation of the time densities. The comparison with the partition coefficient evolution obtained by Obermann et al. (2016) leads to similar crossing points but differs at long lapse times where the scalar case tends to show a more gradual process of decrease (increase) of the surface (body) wave sensitivity.

The classification of the travel-time densities by their mode of propagation and arrival gives a deeper view into the dynamics of the system: there is a natural higher contribution of the mode of arrival that coincides with the mode of propagation for both cases. This is a feature characteristic of an early stage of the system where the number of scattering events is still low, and therefore, there is a lower probability of changing mode arriving to the receiver than to keep the same mode of propagation. At later stages we also see an equalization between the partition coefficient for different arrival modes; this is a consequence of the system passing an increasing amount of time in a diffusive state on which there is no predominance of any mode on the arrival point beyond the one dictated by the modes density.

The evolution of a scattering system can be measured in terms of the normalized time. However, the introduction of the surface breaks this principle as the time that each body phonon passes in the exchange zone increases the probabilities of being scattered into a surface particle, and therefore, affect drastically the overall energy balance between the two modes. The natural quantities that characterize this process are the body-to-body mean free path and the thickness of the exchange zone, that is, the penetration of the surface wave. We perform a series of simulations with different proportions between these two quantities that show that the evolution of time partition coefficient is highly dependent on them. When the mean free path is considerably bigger than the penetration of the surface waves, the body and the surface waves are weakly coupled which implies that the body wave energy has more chances to radiate away from the exchange zone which accelerates the overall decrease of the surface wave sensitivity. In the opposite case, this process is more gradual as there is a continuous energy feedback between the two modes of propagation. We also observe an invariance in the evolution of the time partition coefficient between systems that share the same scaling parameter $l^{b\to b}/L_s$ independently of the absolute values of $l^{b\to b}$ and L_s. We show that this invariance extends to their sensitivities profiles with depth as long as the distance is normalized with their respective mean free paths $l^{b\to b}$, and the thickness of the grid used to measure the time sensitivities is proportional to $l^{b\to b}$.

The crossing time (i.e. the moment on which the total body and surface wave sensitivities are equal to each other) marks the moment in which the body sensitivity starts dominating in the system. An analysis of the dependence of this moment with the adimensional scale of the system $l^{b\to b}/L_s$ shows that the strongest qualitative change happens when this last value is between 1 and 2; increasing this ratio decreases the coupling between the two modes and accelerates the domination of the body waves in the sensitivity. However, this process quickly reaches a minimum limit around 5 mean free times. On the other hand, decreasing this ratio implies confining the body wave energy within the penetration zone of the surface waves, which generates a continuous feedback that delays the overtake of the body wave time partition coefficient.

Despite the natural limitations of the scalar description of wave propagation (like the lack of polarization of the existence of a single mode of propagation for the body waves) our approach reproduces know features of the overall sensitivity in the system with the advantage of requiring low computational resources.

Chapter 6

Recovery of velocity variations at depth

Andres Barajas, Ludovic Margerin, Michel Campillo
Article in preparation

Our objective now is to use the sensitivity kernels obtained in the preceding chapter to localize in depth the perturbations in the medium from a set of observations at the surface; this is the inversion problem. In this chapter we test the capabilities and limitations of the kernel to identify velocity variations in the crust under real-life conditions. In this section we focus in the effect of three variables within the inversion: the depth of the perturbation, the duration of the coda segment to invert and the level of noise in the system. The results here presented are obtained for the autocorrelation configuration as the will be applied to the single-station measurements obtained in the chapter 3

6.1 Introduction

The seismic wavefronts propagating through the earth get distorted by the interaction with heterogeneities that scatter a fraction of their energy in different directions. This process produces the characteristic coda wave segments after the main arrivals in the seismograms (Aki, 1969). Although complicated to analyze, the coda wave is not random and can be understood as the superposition of all the possible wave fronts that propagated through many different paths when going from the source to the receiver (Snieder, 1999; Pacheco and Snieder, 2005; Pacheco and Snieder, 2006). This implies that a complex seismogram generated by an seismic event can be reproduced if, by some mean, we repeat the same seismic source at the same position; this has been observed with two of more earthquakes that occur in the same location with very similar magnitudes (Geller and Mueller, 1980; Poupinet, Ellsworth, and Frechet, 1984; Beroza, Cole, and Ellsworth, 1995). However, although very similar, the received waveforms at the surface are not exactly equal: small variations are produced as a consequence of small changes of the properties of the medium that happen in the period of time between the two seismic events. This is the main principle behind some studies that use these alike earthquakes, called doublets, to track the changes in the velocity (Poupinet, Ellsworth, and Frechet, 1984; Ratdomopurbo and Poupinet, 1995) or in the attenuation (Beroza, Cole, and Ellsworth, 1995) of the crust.

The natural limitations of this approach are the scarce occurrence of doublets, and the impossibility of applying this technique to zones where there is not strong seismic activity. This problem can be circumvented with Passive Image Interferometry (Sens-Schönfelder and Wegler, 2006) which shows that the Green's function of a random medium can be obtained by cross-correlating the diffuse seismic fields registered by two receiver located in the surface

(Campillo and Paul, 2003; Weaver and Lobkis, 2004). This means that a cross correlation between continuous recordings of noise at two stations is equal to what would be observed by one of the stations, if there were a unitary impulsive force at the other. The obtained waveforms have not only the ballistic part of the wave but also the coda, meaning that the seismic noise samples the medium in the same way a seismic event would do. The fluctuation of the phases in the coda of the cross correlations has allowed to estimate changes in the velocity in the crust related to a variety of phenomena, like earthquakes (Brenguier et al., 2008a), volcanic activity (Rivet, Brenguier, and Cappa, 2015; Brenguier et al., 2008b), the thermoelastic response of the soil (Meier, Shapiro, and Brenguier, 2010), the earth tides produced by the sun and the moon (Sens-Schönfelder and Eulenfeld, 2019), among others.

The particular way in which the coda is perturbed is closely related to the lapse time that the wave had to travel from the source to the receiver, and the location of the perturbation in the medium. Coda wave interferometry establishes the link between the perturbations of the waveform at the receiver point and the location of the perturbation, through the introduction of the sensitivity kernels by Pacheco and Snieder (2005) and Pacheco and Snieder (2006). The sensitivity kernel is a travel-time density function that shows the most probable sectors through which a wave would pass when going from the source to the receiver in a given lapse time. The kernel can be calculated as a convolution of the probabilities of the particle traveling between the source, the receiver, and each part of the medium around them that is sampled by the waves (Pacheco and Snieder, 2005; Margerin et al., 2016; Pacheco and Snieder, 2003). Obermann et al. (2013a) and Obermann et al. (2016) proposed a sensitivity kernel for wave propagation in a 3-D half space as a linear combination of two independent sensitivities, one for surface and other for body waves, with a controlling factor mediating between them that changes on time, and that is estimated through full wavefield numerical simulations. . This factor helps to recreate predominance of surface and body wave sensitivities at different lapse times. In this work we use the sensitivity kernel described in the preceding chapter (based on the scalar model of Margerin, Bajaras, and Campillo (2019)) which estimates the probabilities of propagation in surface and body modes with a series of Monte Carlo simulation that integrates them simultaneously.

However, the process to obtain the parameters or sources, from the kernel and a series of observations is not straightforward: this is the inverse problem. The quality of the obtained results depends on the levels of noise in the system and on the specific conditions of the mathematical function that relate the sources and the observations. For that reason it is important to know the capabilities and limitations of the kernel when applied to inversions. Towards that objective we perform a series of synthetic tests that are aimed at assessing the capacity of the time sensitivity kernels to retrieve a velocity perturbation in different scenarios that involve the depth of the perturbation in the medium, the set of measurements used, or the level of noise in the system, for a setting where the source and the receiver are located in the same position at the surface.

6.1.1 The inversion problem

Let's imagine a system where we can define two physical quantities. When measured at different positions or moments, these two quantities take a series of values that we can store in two vectors $\mathbf{d}$ and $\mathbf{m}$, each of which have a number d and m of elements respectively. Let's suppose now that there is a causal relationship between the two variables: this means that the variation of the values in one of the variables $\mathbf{m}$, that we will call the model, will generate changes in the other variable $\mathbf{d}$, that we will call the observations. This relationship between them can be written as $\mathbf{d} = \mathbf{G}(\mathbf{m})$, where $\mathbf{G}$ is a mathematical representation of the physical mechanism that acts between the model and the observations, and that we will call generically

the operator. If the relation between the model and the observations is linear, this relation can be written simply as a matrix multiplication

$$\mathbf{d} = \mathbf{G}\mathbf{m} \tag{6.1}$$

where $\mathbf{G}$ represents a d by m matrix. We assume that we can have access to the series of observations $\mathbf{d}$, and that we can make a good mathematical representation of the physical mechanism mediating between them, $\mathbf{G}$. Then, the inversion problem consists in estimating the series of values of the model that generate the observations, or in other words, to obtain $\mathbf{m}$. This problem can be seen as a minimization of the difference between the observed and the calculated values of $\mathbf{d}$, where the later is the multiplication between the operator and the estimation we make of the model

$$\|\mathbf{G}\widetilde{\mathbf{m}} - \mathbf{d}\| \tag{6.2}$$

the accent in $\widetilde{\mathbf{m}}$ highlights the fact that this is an estimated model. This minimization problem can be solved by the least-squares method, which provides us with the following equation (Aster, Borchers, and Thurber, 2018; Snieder and Trampert, 1999)

$$\widetilde{\mathbf{m}} = \left(\mathbf{G}^T\mathbf{G}\right)^{-1}\mathbf{G}^T\mathbf{d} \tag{6.3}$$

In an ideal case, the estimated and the real model parameters are equal $\widetilde{\mathbf{m}} = \mathbf{m}$. One of the main difficulties related to the application of the inversion is the presence of noise which may produce unreliable or simply wrong estimations. The stability of the solution 6.3 to the noise, lies in the intrinsic characteristics of the operator $\mathbf{G}$; if the application of this formula produces the amplification of the noise (that is usually the case) the inverse problem is said to be ill-conditioned.

Assessing the instability of the operator in the inversion can be done through its singular value decomposition (SVD), which allow us to write the d by m matrix $\mathbf{G}$, as the product of three matrices:

$$\mathbf{G} = \mathbf{U}\mathbf{S}\mathbf{V}^T \tag{6.4}$$

where $\mathbf{U}$ is a d by d orthogonal matrix whose columns $\mathbf{U}_{\cdot,\mathbf{i}}$ span the data space, $\mathbf{V}$ is a m by m orthogonal matrix whose columns $\mathbf{V}_{\cdot,\mathbf{i}}$ span the model space, and $\mathbf{S}$ is a d by m diagonal matrix whose diagonal elements s_i are the so called singular values. It can be shown that given the SVD, the estimated model $\widetilde{\mathbf{m}}$ can written as (Aster, Borchers, and Thurber, 2018):

$$\widetilde{\mathbf{m}} = \sum_{i=1}^{p} \frac{\mathbf{U}_{\cdot,i}^T \cdot \mathbf{d}}{s_i}\mathbf{V}_{\cdot,i} \tag{6.5}$$

where p is the number of non-zero singular values. From this equation, it is clear that the solution is a linear superposition of the basis $\mathbf{V}_{\cdot,\mathbf{i}}$, with factors inversely proportional to the singular values. If one of these singular values is unusually small in comparison with the others, the introduction of a small amount of noise in the observations ($\mathbf{d}$) will be amplified, and its associated term in the sum 6.4 will likely dominate the others. The condition number of the operator is usually quantified by dividing the biggest singular value, that is also the first one, in the smallest one, that corresponds to the last one s_1/s_p; if this ratio is big, then the matrix G is probably ill-conditioned.

Qualitatively speaking, the problem is that the minimization of $\|\mathbf{G}\widetilde{\mathbf{m}} - \mathbf{d}\|$ may produce a result that overfits $\widetilde{\mathbf{m}}$ to the noise, generating estimations with big fluctuations, and therefore, unstable. This can be fixed if we try to minimize not only this quantity but also the norm of

the solution itself $\|\widetilde{\mathbf{m}}\|$. This ensures that the solution will be close enough to the observations, but at the same time that its amplitude will be controlled. The quantity to minimize will be then

$$\|\mathbf{G}\widetilde{\mathbf{m}} - \mathbf{d}\|^2 + \mu^2\|\widetilde{\mathbf{m}}\|^2 \tag{6.6}$$

where μ is the regularization or damping parameter, in charge of controlling the trade-off between the minimization of the first and the second term. The least-squares approach for this situation gives us the following solution

$$\widetilde{\mathbf{m}} = \left(\mathbf{G}^T\mathbf{G} + \mu^2\mathbf{I}\right)^{-1}\mathbf{G}^T\mathbf{d} \tag{6.7}$$

where $\mathbf{I}$ is a m by m identity matrix. The stabilization of the estimation through the introduction of the new term can be seen explicitly if we write this equation in terms of the singular value decomposition (Aster, Borchers, and Thurber, 2018)

$$\widetilde{\mathbf{m}} = \sum_{i=1}^{p} \frac{s_i^2}{s_i^2 + \mu^2} \frac{\mathbf{U}_{\cdot,i}^T \cdot \mathbf{d}}{s_i} \mathbf{V}_{\cdot,i} \tag{6.8}$$

where

$$f_i = \frac{s_i^2}{s_i^2 + \mu^2} \tag{6.9}$$

are the filter factors. The introduction of the damping parameter helps to modulate the contribution of the smallest singular values: if $\mu \gg s_i$ the filter factor will be close to zero $f_i \approx 0$ and therefore there will be no contribution of the associated basis vector $\mathbf{V}_{\cdot,\mathbf{i}}$. On the contrary, if $\mu \ll s_i$ then $f_i \approx 1$ and the respective vector will contribute like in the no-damped solution. In this sense, the damping parameter works as a threshold value below which the singular values, and their associated basis vector, are gradually excluded from the solution. Although this helps to control the influence of the noise, it inevitably reduces the precision of the estimated model, rendering it smoother and less complex.

In general, we search for a solution that can reproduce the observations with good precision, without overfitting it to the presence of noise, or in other words, a solution with good stability. The precision can be quantified through the the residual norm $\|\mathbf{G}\widetilde{\mathbf{m}} - \mathbf{d}\|$ and the stability through the norm of the solution itself $\|\widetilde{\mathbf{m}}\|$; when performing inversions, we search to balance the trade-off between them. In practice, different damping values minimize the solution or the residual norm in such a way that plotting them simultaneously will give the characteristic trade-off L-curve that can be seen in figure 6.1; the dot marks the point that effectively minimizes both parameters, although, in the practice, the best performing damping parameter may not be necessarily exactly at this position, but close to it.

In the minimization problem can also be introduced a certain weight to each of the observations or each of the parameters of the model, changing

$$\widetilde{\mathbf{m}} \to \mathbf{L}\widetilde{\mathbf{m}} \qquad \mathbf{d} \to \mathbf{Q}\mathbf{d} \tag{6.10}$$

This is a way to introduce information about the measurements uncertainties or about features that we know (or want) our model should have (REF ASTER). Under these changes, the quantity to minimize is

$$\begin{aligned} &\|\mathbf{Q}(\mathbf{G}\widetilde{\mathbf{m}} - \mathbf{d})\|^2 + \mu^2\|\mathbf{L}\widetilde{\mathbf{m}}\|^2 \\ &= (\mathbf{G}\widetilde{\mathbf{m}} - \mathbf{d})^T\mathbf{W}_\mathbf{d}(\mathbf{G}\widetilde{\mathbf{m}} - \mathbf{d}) + \mu^2\widetilde{\mathbf{m}}^T\mathbf{W}_\mathbf{m}\widetilde{\mathbf{m}} \end{aligned} \tag{6.11}$$

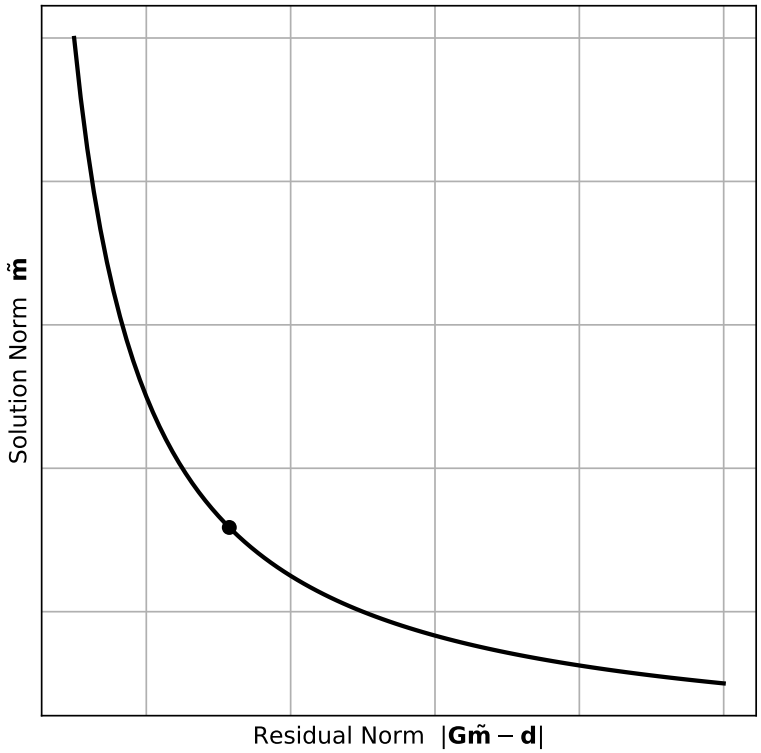

FIGURE 6.1: Characteristic trade-off curve between the norm of the solution $\widetilde{\mathbf{m}}$ and the residue $\|\mathbf{G}\widetilde{\mathbf{m}} - \mathbf{d}\|$

where $\mathbf{W_d} = \mathbf{Q}^T\mathbf{Q}$ and $\mathbf{W_m} = \mathbf{L}^T\mathbf{L}$. Notice that this equations is a more general version of equation 6.6. The solution of this equation is a weighted version of equation 6.7

$$\widetilde{\mathbf{m}} = \left(\mathbf{G}^T\mathbf{W_d}\mathbf{G} + \mu^2\mathbf{W_m}\right)^{-1}\mathbf{G}^T\mathbf{W_d}\mathbf{d} \tag{6.12}$$

The weight matrices can be related to the covariances matrices of the model and the data (Snieder and Trampert, 1999)

$$\mathbf{W_d} = {\mathbf{C_d}}^{-1} \qquad \mathbf{W_m} = {\mathbf{C_m}}^{-1} \tag{6.13}$$

For example, the uncertainties of d measurements can be included in the inversion as the elements of a diagonal matrix $\mathbf{C_d}$ as long as they are independent between them; otherwise, the elements off the diagonal won't be necessarily equal to zero. This perspective is especially useful if there is a priori information on the system, case on which both the model and its covariance can be calculated as (Tarantola, 2005)

$$\begin{aligned} \widetilde{\mathbf{m}} &= \widetilde{\mathbf{m}}_{\mathbf{prior}} + \left(\mathbf{G}^T{\mathbf{C_d}}^{-1}\mathbf{G} + \mu^2{\mathbf{C_m}}^{-1}\right)^{-1}\mathbf{G}^T{\mathbf{C_d}}^{-1}(\mathbf{d} - \mathbf{G}\widetilde{\mathbf{m}}_{\mathbf{prior}}) \\ \widetilde{\mathbf{C}}_{\mathbf{m}} &= \left(\mathbf{G}^t{\mathbf{C_d}}^{-1}\mathbf{G} + {\mathbf{C_m}}^{-1}\right)^{-1} \end{aligned} \tag{6.14}$$

where $\widetilde{\mathbf{m}}_{\mathbf{prior}}$ represents a priori model information, with its respective covariance $\mathbf{C_d}$. Finally, for the sake of completeness, we make some last remarks about the relative proportions between the number of parameters in the model m and the number of observations d. The solutions presented previously are for cases where the number of unknowns is less than the

number of observations ($m > d$), with exception of the equations in terms of the singular value decomposition, that are applicable for all the cases. When there are more unknowns than observations ($m > d$) there are many possible solutions and the optimization criteria is the minimization of $\|\widetilde{\mathbf{m}}\|$ which leads to slightly different versions of the equations 6.3, 6.7 and 6.12 . However, most of the cases of interest for us are over-determined, mixed-determined, or weakly under-determined and for all of these cases, the best approach is the one that was presented here. The interested reader can find an extensive discussion about both the over-determined and the under-determined problem and its solutions in Menke (2018).

6.2 Setting of the seismic inverse problem

If we compare two seismograms obtained before and after the inclusion of a small velocity perturbation in a heterogeneous medium, we would notice a small phase shift between them (Obermann et al., 2013a). These phase perturbations can be interpreted as an apparent velocity variation of the seismic field ($\varepsilon = -\delta t/t$). Our objective is to deduce the variations of velocity generated in the crust from the measured apparent velocity variations at the surface. Therefore, the changes in velocity at depth are the components of the model vector

$$\mathbf{m} = \left(\frac{\delta c}{c}(z_1), \frac{\delta c}{c}(z_2), \cdots, \frac{\delta c}{c}(z_m) \right) \tag{6.15}$$

and the apparent velocities measured at the receptor at different lapse times are the components of the vector of observations

$$\mathbf{d} = (\varepsilon(t_1), \varepsilon(t_2), \cdots, \varepsilon(t_d)) \tag{6.16}$$

For most of practical applications, the coda wave of the seismograms is retrieve with seismic interferometry, which is obtaining the medium's Green's function from the cross-correlation of continuous records of the ambient seismic noise in the surface (Weaver and Lobkis, 2004; Campillo and Paul, 2003). Each segment of the coda of these correlations is representative of a part of the energy that traveled from the source to the receiver. Then, in theory, measuring this phase delay for every point in a long enough coda would give us as many measures as we want which would be advantageous to perform the inversion. However, in practice, the obtained correlations are far from perfect due to factors like unstable or non-symmetric noise sources (Snieder, 2004; Liu and Ben-Zion, 2013). Even with ideal noise-free correlations, it is desirable to limit the observations of the apparent velocity variations to a certain frequency range which implies dividing the coda in windows wide enough to contain several oscillations of the desired frequencies. This means that every estimation of $\delta t/t$ is not made with a very specific lapse time but with a portion of the coda around it. The limitations are also related to the overall portion of the coda that can be used to measure the phase delay: at later lapse times there is a natural decrease of signal-to-noise ratio so the measurements become unreliable. All these factors limit the useful portion of the coda to make the inversion, and the number of measurements we can take from it.

6.2.1 Construction of the operator G

The relation between the apparent velocity measurements in the surface and the velocity variations at depth can be represented as

$$\begin{matrix} \mathbf{d} & = & & \mathbf{G} & & & \mathbf{m} \end{matrix}$$
$$\begin{pmatrix} \varepsilon(t_1) \\ \varepsilon(t_2) \\ \vdots \\ \varepsilon(t_d) \end{pmatrix} = \begin{pmatrix} \mathbf{G}_{1,1} & \mathbf{G}_{1,2} & \cdots & \mathbf{G}_{1,m} \\ \mathbf{G}_{2,1} & \mathbf{G}_{2,2} & & \\ \vdots & & \ddots & \\ \mathbf{G}_{d,1} & & & \mathbf{G}_{d,m} \end{pmatrix} \begin{pmatrix} (\delta c/c)(z_1) \\ (\delta c/c)(z_2) \\ \vdots \\ (\delta c/c)(z_m) \end{pmatrix} \tag{6.17}$$

The operator $\mathbf{G}$ can be constructed with the sensitivity kernel obtained previously in 5.66, but adapted to a discretized medium

$$\mathbf{G} = (\mathbf{G}_{i,j}) = \left(\frac{\langle t_s(t_i) \rangle}{t_i} K_{C_{ph}}(z_j) + \frac{\langle t_b(z_j; t_i) \rangle}{t_i} \right) \tag{6.18}$$

where the source and the receiver were assumed to be at the same place in the surface ($z = 0$, $r = 0$). Each row of the operator is related to the travel-time of the phonons going from the source to the receiver t_i, and each column to the depth through which they passed during this process at any time z_j; this is the reason why a colon has been preserved in the notation of $t_b(z_j; t_i)$, making a clear distinction between the variables that refer to the transit of the phonon through the medium, and the variables that make reference to the arrival event. From this equation is clear that the dimensions of the operator are dependent of the amount of observations made d, and on the desired layers to resolve through the inversion m. The first term of the right hand side of the equation 6.18 is representative of the surface waves sensitivity, and the second one of the body waves sensitivity.

The quantities $t_s(t_i)$ and $t_b(z_j; t_i)$ are estimated through the Monte Carlo simulation as was explained in the preceding chapter. For a chosen set of parameters, a single simulation is run registering t_s and t_b, in many different lapse times t_i, with a very high depth resolution which is obtained dividing the half space in many thin layers z_j. The operator $\mathbf{G}$ formed with all the registered lapse times over a set of very thin layers, will be referred to as the high-resolution operator. However, real applications of the inversion will be done over a more sparse set of lapse times (equal to the measurements of $\delta t/t$), to obtain velocity perturbations in a relatively thick layered system (with every layer in the order of kilometers or hundreds of meters). The full-resolution operator can be adapted for these applications as follows:

Time axis: The closest lapse time of the simulation is chosen, and its respective row in the operator is preserve, meaning that all the others are simply removed. This decrease the number of rows of the operator to the same number of measurements of the apparent velocity variation or $\delta t/t$.

Depth axis: The sensitivity between different columns is grouped and summed to match the desired thickness. For example, from an operator layered every $0.2km$, can be constructed a new operator layered every $1km$, summing every 5 columns of the operator.

After this procedure the resulting operator will have less columns than the full-resolution original operator. We will refer to the operator with both axis reduced, as the down-sampled operator $\mathbf{G^{ds}}$.

6.2.2 Parameters election

With the purpose of obtaining velocity perturbations in the crust from real data obtained in the region of Pollino, in the south of Italy, the parameters of the construction of the kernel were chosen to resemble as close as possible the actual physical conditions found there. The

Variable	Monte Carlo simulation
frequency (Hz)	0.75
B. velocity (km/s)	$c = 3.48$
S. velocity (km/s)	$c_R = 3.7$ (group v.)
α (km^{-1})	0.49
Penetration depth L_s (km)	4.1
Mean free time (s)	$\tau^{b\to b} = 30.4$
Mean free path l (km)	$l^{b\to b} = 100$
Thickness receiver layer (km)	0.2
Radius receiver layer (km)	50

TABLE 6.1: Parameters of the Monte Carlo simulations used in all the inversions. The source and the receiver volume are located in the same point.

P-wave velocity in this region of Italy is around $c_\alpha = 5.8km/s$ (Orecchio et al., 2011). The S-wave velocity is calculated from the P-wave velocity assuming that the Lamé constants are equal, or in other words, that we're working with a Poisson solid on which $c_\alpha/c_\beta = \sqrt{3}$. Therefore, $c_\beta = 3.35km/s$. The velocity of the body waves in the scalar case is calculated from both of these velocities: the time the energy travels between two points can be calculated as an averaged time between the two types of body waves, using the energy ratios as weigths

$$t_E = \frac{E_\beta}{E_\beta + E_\alpha} t_\beta + \frac{E_\alpha}{E_\beta + E_\alpha} t_\alpha \tag{6.19}$$

where E_β is the energy of the S-waves, E_α is the energy of the S-waves. For the Poisson solid the energy ratio between both modes of body waves is $r_p = E_\beta/E_\alpha = 10.39$ (Hennino et al., 2001), so the energy velocity, understood as an effective average velocity, is

$$\frac{1}{c_E} = \frac{r_p}{(r_p+1)}\frac{1}{v_\beta} + \frac{1}{(r_p+1)}\frac{1}{v_\alpha} = \frac{0.91}{v_\beta} + \frac{0.09}{v_\alpha} \tag{6.20}$$

All the used parameters are listed in the table 6.1. These same configuration is used for all the following tests.

6.3 Performance of the inversion in synthetic tests

To determine how susceptible is the inversion to the presence of noise and to have an idea of its resolution capacity, we perform a series of synthetic tests. Each test consists first in creating a simple velocity perturbation profile $\mathbf{m}$. After, with the help of the full-resolution operator, we deduce what would be the measured $\delta t/t$ at the surface at different times, leading to the synthetic data vector $\mathbf{d}$. Finally, the inversion is applied over this vector $\mathbf{d}$ to obtain an estimation of the original model $\widetilde{\mathbf{m}}$. In perfect conditions, the original perturbation model and the model estimated through the inversion would be equal. However, the presence of noise and finite time window for observations may create big differences between the two.

The synthetic test, illustrated in detail in figures 6.2 and 6.3, is as follows:

I. A model $\mathbf{m}$ is created containing a single velocity perturbation as shown in the figure 6.2a. In this case, the perturbation is $10km$ of thick and is located between $10km$ and $20km$ depth. This profile is defined over a finely discretized grid of $0.2km$ thick although it is not evident from the figure given the simple shape. it is also important to note that the depths extend up to $180km$ to cover all the positions at which the sensitivity

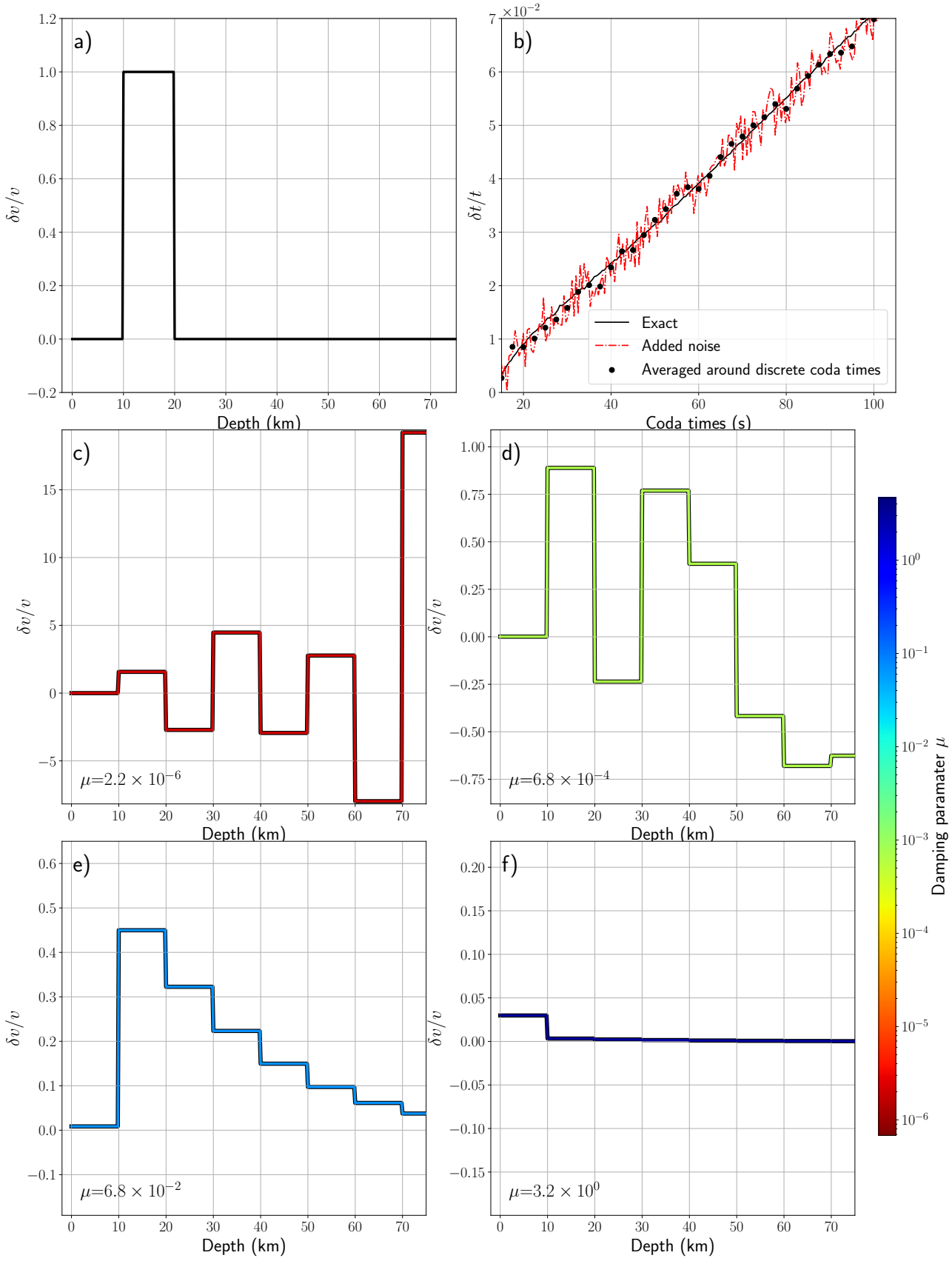

FIGURE 6.2: Synthetic tests procedure. a) Original velocity perturbation profile $\delta v/v$. b) Exact $\delta t/t$ calculated from $\delta v/v$ and the operator, after the addition of noise, and passed through moving average window of $10s$ every $2.5s$. c)- f) Selected estimated models retrieved from the inversion with their respective damping value. The color of the line is related to a damping value as shown in the color bar at the right. Continued in figure 6.3

.

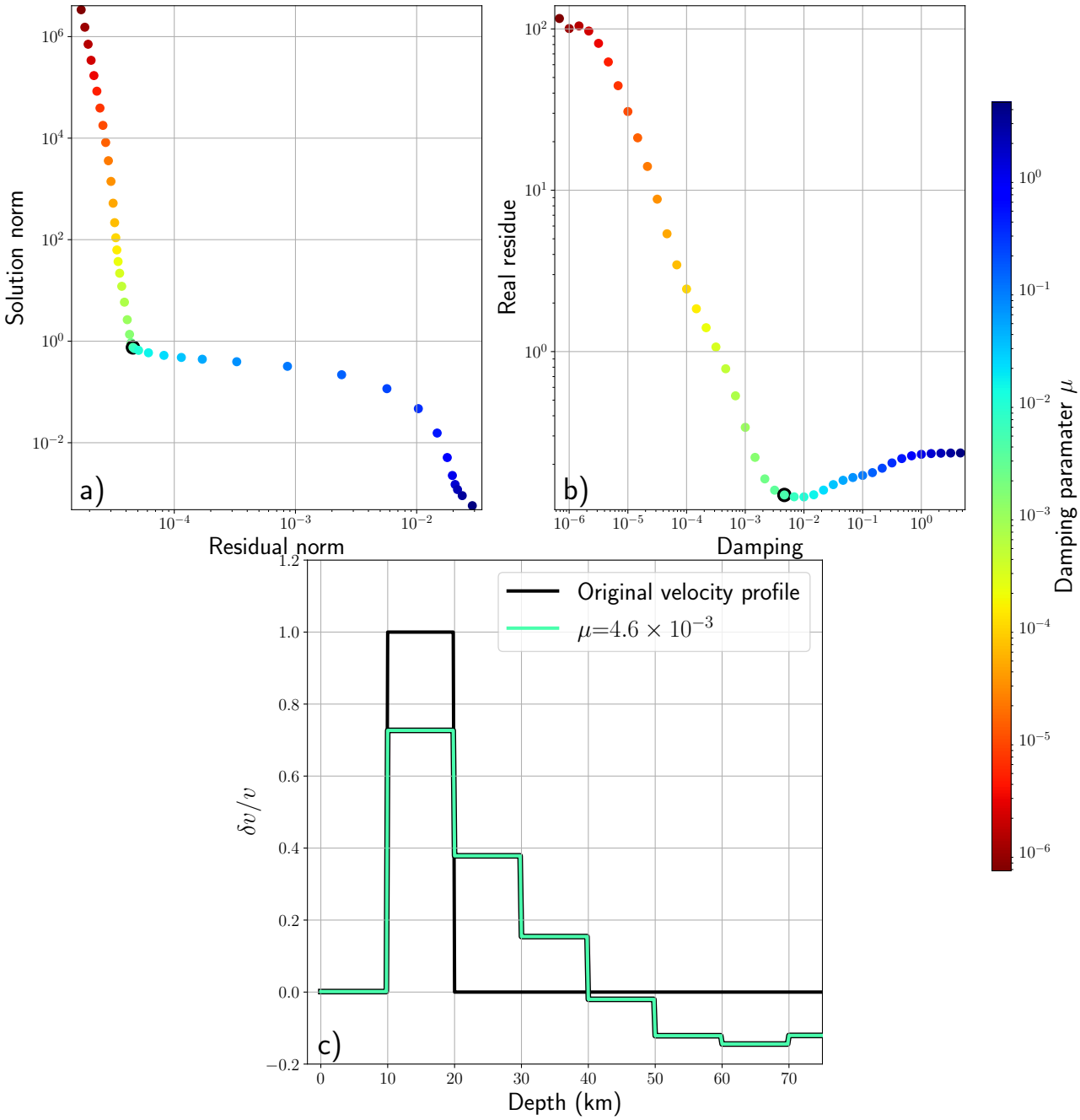

FIGURE 6.3: Synthetic tests procedure, continuation. a) Trade-off curve. Each point represents an inversion. b) Real residue calculated for the same set of estimated models. c) Estimated velocity perturbations for the best inversion as chosen by the trade-off criteria, along with its damping parameter. This configuration is highlighted in the two upper plots with a black border. The colors of the dots and line are related to the value of the damping parameter.

is significant, although in the figure only the first $75km$ are shown for visualization purposes

II. We calculate what would be the exact $\delta t/t$ measured at the surface making a matrix multiplication between the model and the full-resolution operator $\mathbf{G}$ as schematized in the equation 6.17. Then we add to this exact $\delta t/t$ a randomly generated noise. Both of these sets of $\delta t/t$ are defined over a dense set of lapse times. To mimic real-life measurements taken from a cross-correlation, we make a moving average going from $15s$ to $105s$, every $2.5s$ over the $\delta t/t$ with noise. The three $\delta t/t$ are shown in figure 6.2b

III. The operator is down-sampled with the averaged lapse times and a new layering (in this case, of thickness of $10km$)

IV. The inversion is performed following equation 6.7 with a set of damping values that are chosen to be between the maximum and the minimum singular value of the down-sampled operator. In figures 6.2c-f can be seen the result of 4 of these inversions with their respective damping values.

V. For each of these estimated models $\widetilde{\mathbf{m}}$ we calculate the residual norm $\|\mathbf{G}\widetilde{\mathbf{m}} - \mathbf{d}\|$ and the solution norm $\|\widetilde{\mathbf{m}}\|$ to make a trade-off curve shown in the figure 6.1: in our case the result of this trade-off curve is shown in the figure 6.3a.

VI. We increase the depth resolution of the estimated model over the more dense set of depths (with thickness of $0.2km$) to make a direct comparison between the $\mathbf{m}$ and $\widetilde{\mathbf{m}}$ with the root-mean-square error, for each damping value:

$$R_r = \sqrt{\frac{1}{N}\sum_{i=0}^{N}\left(\frac{\delta v}{v}(i)_{real} - \frac{\delta v}{v}(i)_{estimated}\right)^2} \tag{6.21}$$

where R_r is what we call the real residue and N is the total number of layers. The smaller is this value, the closer is the estimated model from the real one. We plot each damping value with its respective real residue to compare their performance as shown in figure 6.3b.

VII. Finally, imitating what would be a real case scenario, we chose the model whose damping value is closer to the elbow of the trade-off curve as the correct one. This particular model is highlighted with a black border in the plots 6.3a and 6.3b, and is plotted in the figure 6.3c. In this example this configuration happens to have the smaller real residue which means that the trade-off criteria is appropriate. Although this won't be necessarily always the case, in general, this "elbow" configuration is always close to the best performing one.

This simple example shows the known effect of μ in the inversion: as can be seen in figures 6.2c-f, the lowest is the damping parameter the highest is the amplitude and the oscillation of the estimated model. Although this parameter helps to damp the estimated model limiting the influence of noise, it does it sacrificing its resolution. This trade-off behavior can be seen in the plot 6.3a where low damping values result in models with strong oscillations (big solution norms) that may be overfitting the presence of noise (low residual norm), whereas high damping values results in models with weak oscillations (low solution norms) that may not be fitting good enough to the observations (high residual norm). Before continuing we define the zero-residue R_0 as the residue that would produce an estimated model in which all $(\delta v/v)_{estimated} = 0$:

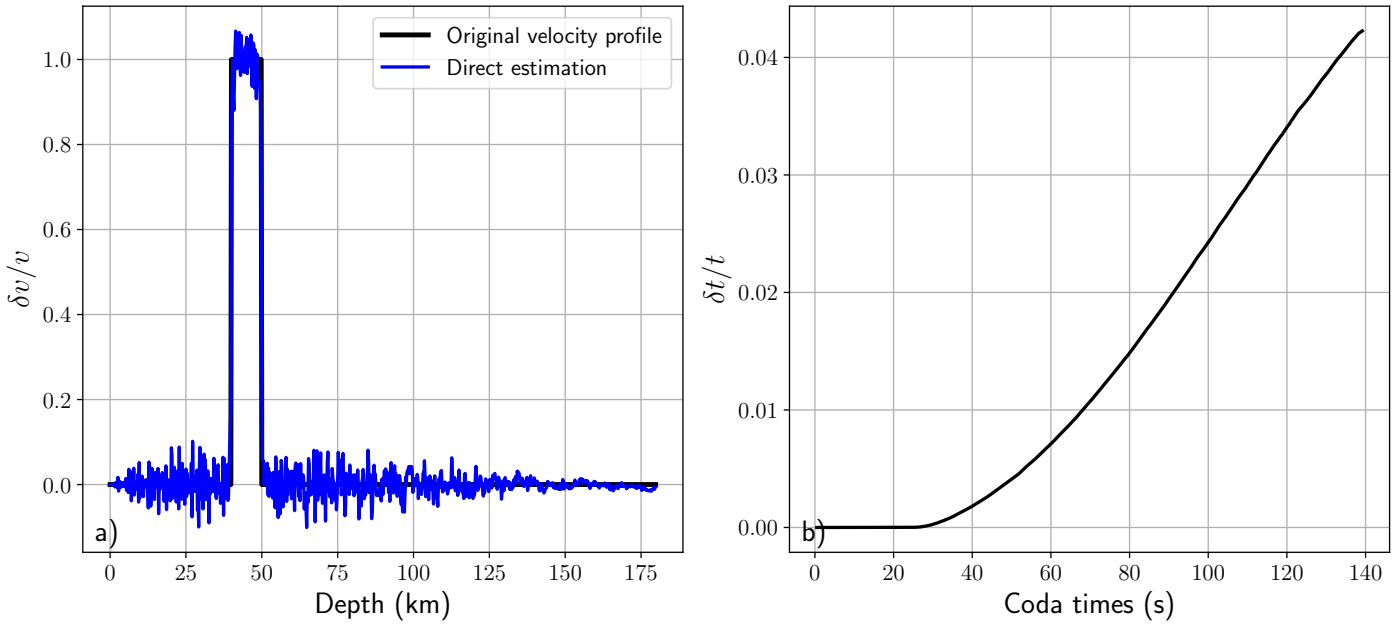

FIGURE 6.4: Direct inversion without artifical noise. a) Real model and estimated model for the inversion made with the full-resolution operator from the $\delta t/t$. b) $\delta t/t$ obtained with the full-resolution operator

$$R_0 = \sqrt{\frac{1}{N}\sum_{i=0}^{N}\left(\frac{\delta v}{v}(i)_{real}\right)^2} = \frac{\|\mathbf{m}\|}{\sqrt{N}} \tag{6.22}$$

This value will be used as a reference point: an estimated model with a higher residue than R_0 has lost all information.

6.3.1 Noise-free inversion: Effects of the downsampling process

We make a control test where no noise is introduced. It consists of estimating the model using the full-resolution operator, it means, applying the equation 6.5 directly over $\mathbf{d}$. The result of this is shown in figure 6.4a. Although the result shows the presence of fluctuations most likely generated by numerical imprecisions, it reproduces the original sharp velocity perturbation. The produced phase perturbations at the surface (figure 6.4b) is consistent with a wave propagation understanding of the sensitivity: $\delta t/t$ deviates from zero at later lapse times because of the seismic field samples progressively deeper zones of the medium, where the perturbation is located. It is worth noticing that this inversion makes full use of all the available lapse times, a feature that in real applications is not possible.

The next test consists in making the inversion over the averaged measurement of $\delta t/t$ using the down-sampled operator, for two cases: the first one, analyzing big perturbations at depth, and the second case analyzing smaller perturbations close to the surface. In figures 6.5a and 6.5b can be seen the real model and the produced $\delta t/t$ respectively. The original model is the same used in figure 6.4.

In this case the inversion is done with a down-sampled operator over a set of $\delta t/t$ between $15s$ and $65s$, with a spacing of $2.5s$ between them, represented by the dots in the figure 6.5b; the duration of the window in this moving window average is $10s$. The half-space is divided

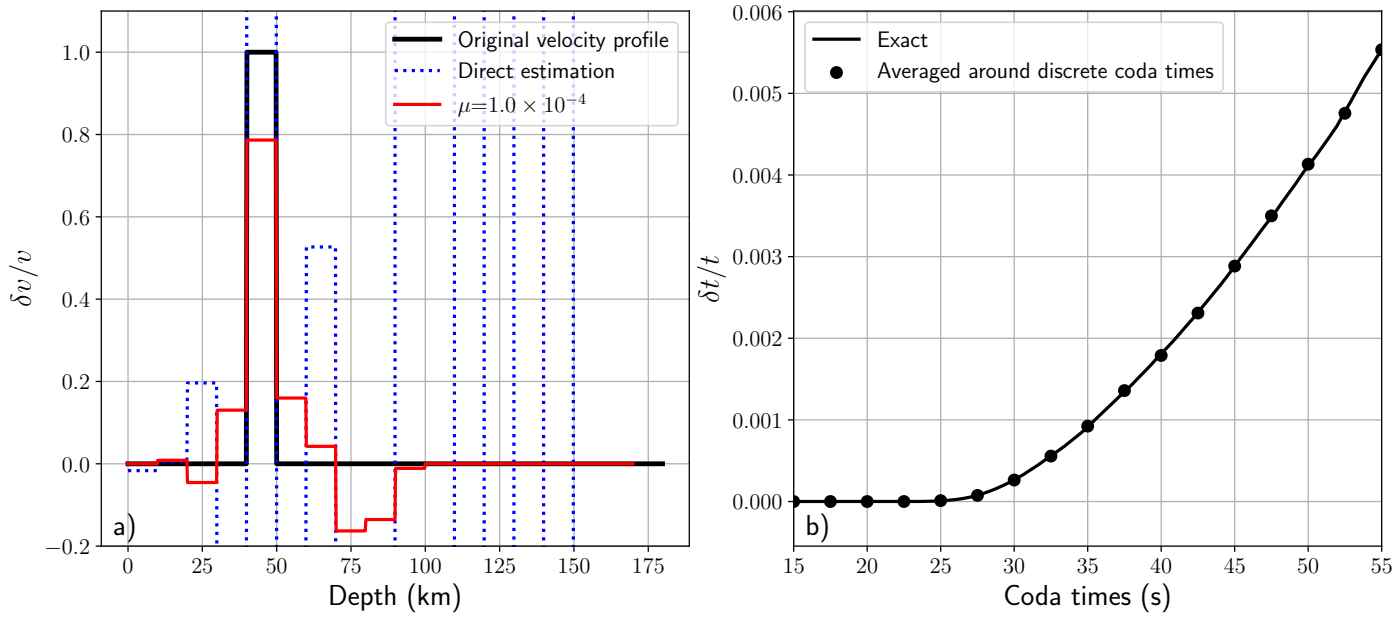

FIGURE 6.5: Inversion without artificial noise for a deep perturbation. a) Original model, estimated model for the inversion made directly with the down-sampled operator, and estimated model for the inversion made with the down-sampled operator including a damping parameter. b) $\delta t/t$ obtained with the full-resolution operator and averaged $\delta t/t$ around the measurements points.

with a regular layering of $10km$ spanning from $0km$ to $180km$ depth. A first inversion can be made directly over the averaged $\delta t/t$ using the down-sampled operator with the equation 6.5; this produces the very unstable model estimation represented by the dotted blue line in figure 6.5a. The wide amplitude of this solution seems to suggest that the reduction of the resolution of the data and the operator, acts as a noise introduction in the system. This means that its overall effect can be controlled through the introduction of the damping parameter; in effect, making a full set of inversions, and choosing the best one according to the L-curve criteria (as was described in the previous section), leads to the solution in red in figure 6.5a, which resembles more closely the real model. However, this solution shows already a loss of resolution which is characteristic of the introduction of the damping parameter. This helps to illustrate that even in a noise-free scenario, the regularization process is necessary.

Now, we test how the inversion performs over a $1km$ perturbation within the first kilometers of depth, as the one shown in figure 6.6a. The layering of the downsampled operator is has a thickness of $1km$. The generated $\delta t/t$ and its averaged version are represented by the line and the dots in figure 6.6b respectively; in this case, the $\delta t/t$ diverges from 0 at an early lapse time, as expected from a perturbation located close to the surface. As occurred before, the inversion made directly with the down-sampled operator produces a very irregular estimation, represented by the blue dotted line in figure 6.6a. However, the introduction of the damping parameter does not produce a reliable estimation either: in this case, the damped estimated model (green line in figure 6.6a) does not show any distinctive feature that can be related to the original perturbation.

To increase the performance of the inversion, we introduce a weighting factor that searches for models that have velocity perturbations within the first layers of depth and penalizes solutions that show fluctuations at deeper levels. The idea is to prioritize solutions that lie in what would be the crust, and ignore the rest; this is a reasonable expectation as most

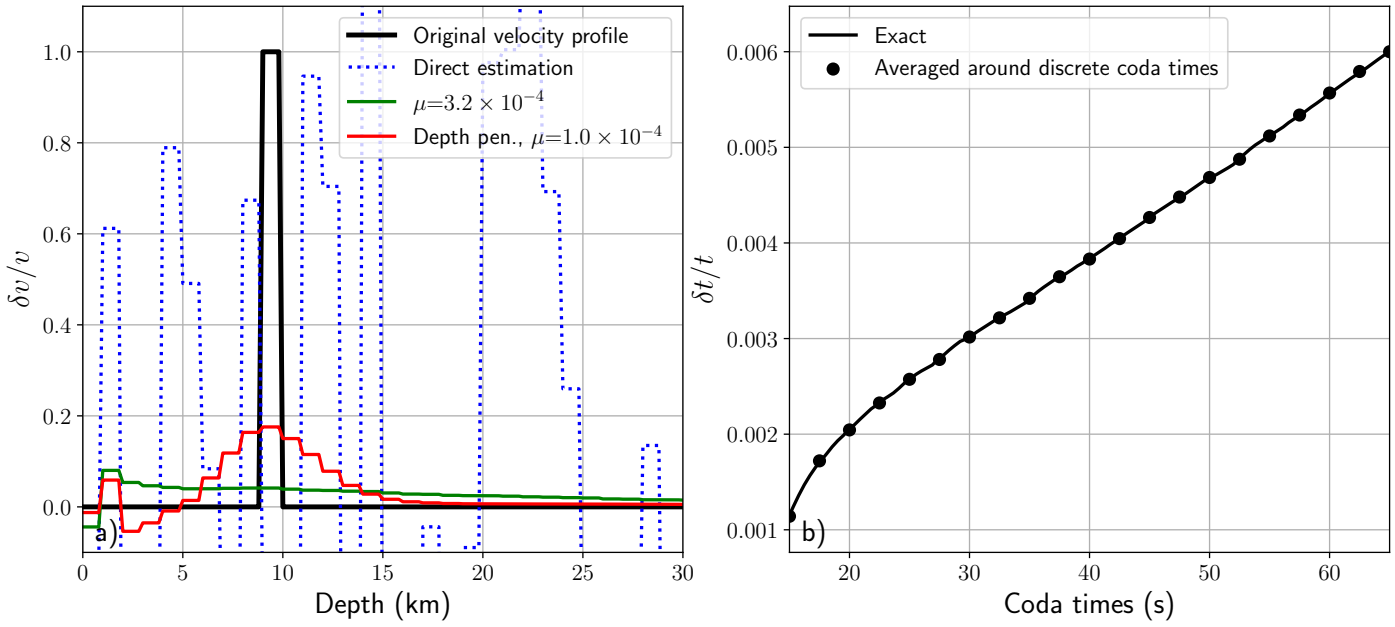

FIGURE 6.6: Inversion without artificial noise for a shallow perturbation. a) Original model and estimated models for the inversion made directly with the down-sampled operator, with the down-sampled operator including a damping parameter, and with the down-sampled operator including a damping parameter and a depth penalization. b) $\delta t/t$ obtained with the full-resolution operator and averaged $\delta t/t$ around the measurements points.

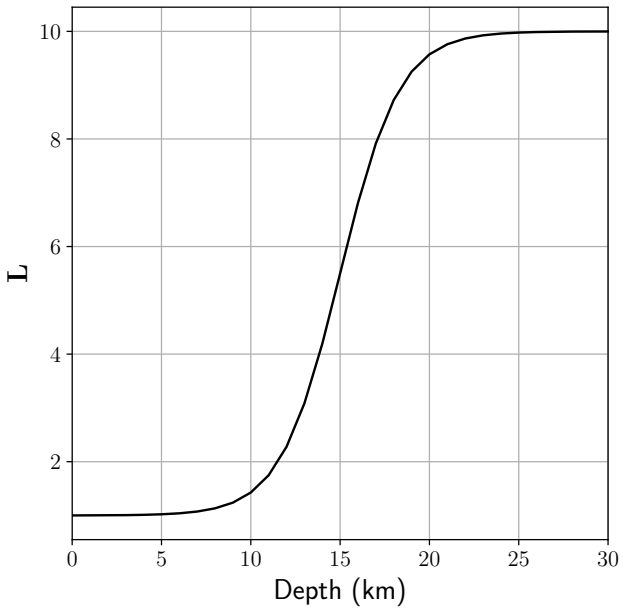

FIGURE 6.7: Depth penalization on the parameters in the model. Sigmoid function centered around 15km. The higher is the value, the stronger will be the minimization process on the estimated model at this depth.

of the known factors that generate fluctuations in the $\delta t/t$ come from phenomena located within these first kilometers of the crust, like earthquakes and weather-related cycles. In the practice, this is done multiplying $\mathbf{m}$ with a smooth sigmoid function $\mathbf{L}$ (equation 6.10) that leaves the component of $\mathbf{m}$ equal if it is located between $0km$ and $15km$, but penalizes them by a factor of 10 if they are at deeper levels than this threshold. This function can be seen in figure 6.7. The introduction of the associated matrix W_m in the equation 6.12 produces the solution represented by the red line in figure 6.6a. This increases the capacity of the inversion to resolve thinner perturbations, at the expense of being unable to locate changes at a deeper layer. In a practical setting, a simultaneous inversion for deep thick velocity structures, complemented with other for thin shallow ones, should be enough to obtain a comprehensive set of observations of the dynamic in the medium.

6.3.2 Performance at different depths

The performance of the inversion is tested moving the perturbation at depths without artificial noise. The used set of measurements $\delta t/t$ ranges from $15s$ to $65s$ every $2.5s$. The result of some selected depths is shown in figure 6.8. As we move deeper, the best performant configuration (as selected by the L-curve criteria) is generated by a systematically lower damping parameter. This indicates that when the perturbation is close to the surface the estimated models are more robust but have less resolution. Figure 6.8b shows a case where the velocity perturbation is located between two layers of the inversion, which leads to more unstable results.

Figure 6.9a shows the residues (equation 6.21) for different depths without noise: the oscillation is generated by the location of the perturbation between layers, having the lower values when the perturbation is aligned to the layering. At deeper levels, the residue of the aligned cases is progressively lower as these configurations use a lower damping value, that produces higher resolution estimations. In figure 6.9b we see the residues of a set of inversions under the same conditions but with an artificial level of noise added to the $\delta t/t$; the residues increase at depth as the noise make the less robust inversions unstable. Below $80km$ there are no more residues because for these configurations the trade-off curve does not have anymore its characteristic L-shape, and therefore, it is impossible to know what is the best configuration between different damping parameters. This is also a sign of the low quality of the estimations. Interestingly enough, this suggests that the level of noise limits the practical reach of the inversion, as will be seen afterwards in detail. In the case where there is no noise, the inversion seems to reach a limit at around $110km$ location at which the sensitivity values are too low. it is worth mentioning that the big instabilities that are produced when the perturbation is close to the surface between layers (at depths of $2km$, $4km$, and $6km$ to be precise) are one of the reasons why a second configuration with thinner layers is analyzed independently.

Figure 6.10 illustrates how the noise weakens and can drown completely the information contained in the perturbation of the phase. The $\delta t/t$ for the deeper layer is around one order of magnitude smaller that for the shallow layer, which makes it more susceptible to the noise; the noise amplitude for the former is comparable with the changes in $\delta t/t$, and therefore, almost all the information is gone.

The same analysis is performed over the inversion with thinner and shallower layers, making use of the depth penalization in the minimization as was previously explained. In this case, the perturbation has $1km$ thickness and is shifted by steps of $200m$. The half-space is divided into layers of $1km$. Four selected inversions are shown in figure 6.11 (a fifth one can be seen in figure 6.6a). The inversion shown in 6.11a is made for a perturbation that is not aligned with the layering, and contrary to what we saw in the thicker case, this does not lead to an unstable estimation. We see as in the first case, a migration of the damping parameter

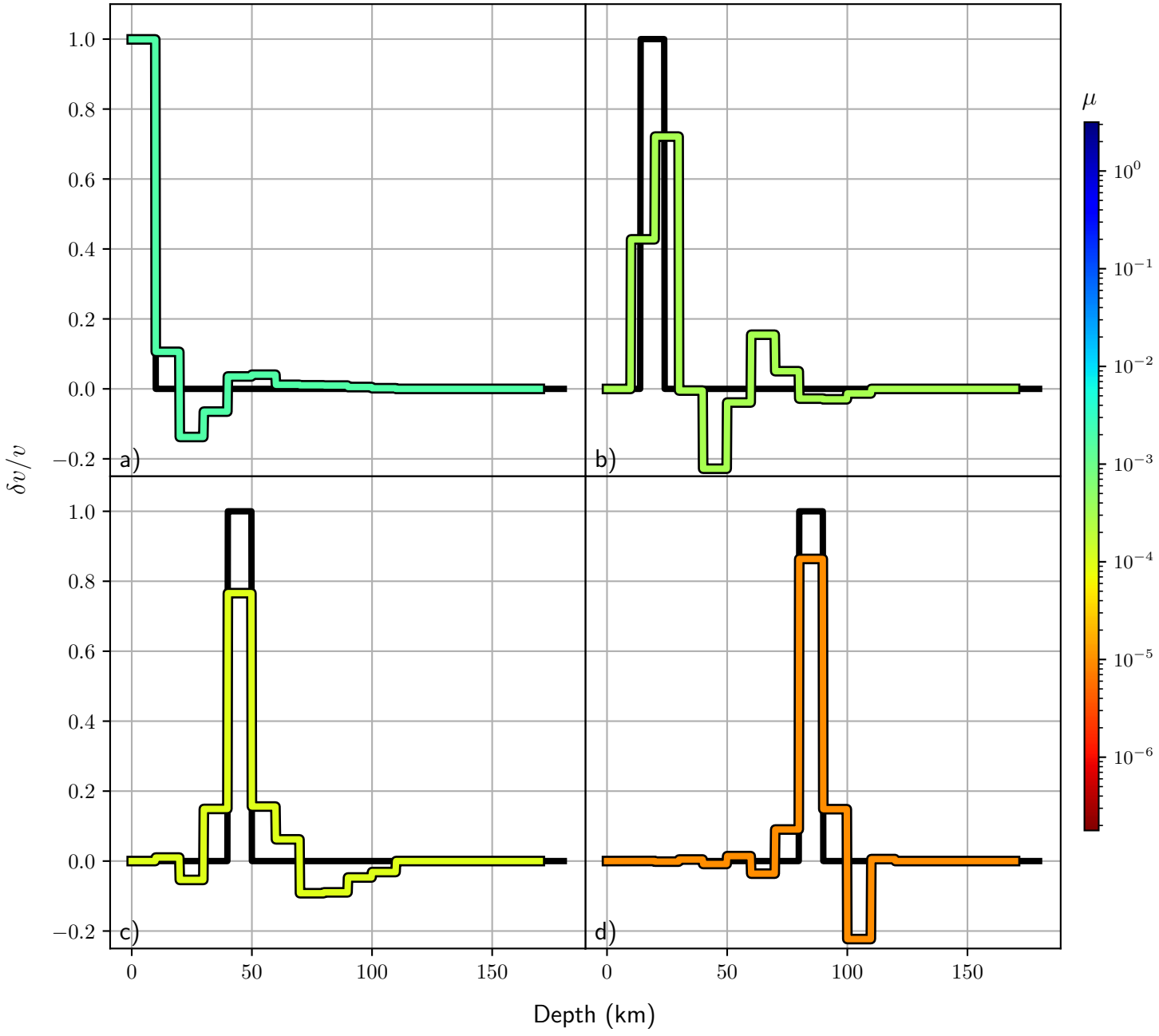

FIGURE 6.8: Result of the inversion without noise for the velocity perturbation located at a) $0km$, b) $14km$, c) $40km$ and d) $80km$. The black and the color lines represent the original and the estimated model respectively for each case. Each color is associated to a damping value as shown in the colorbar.

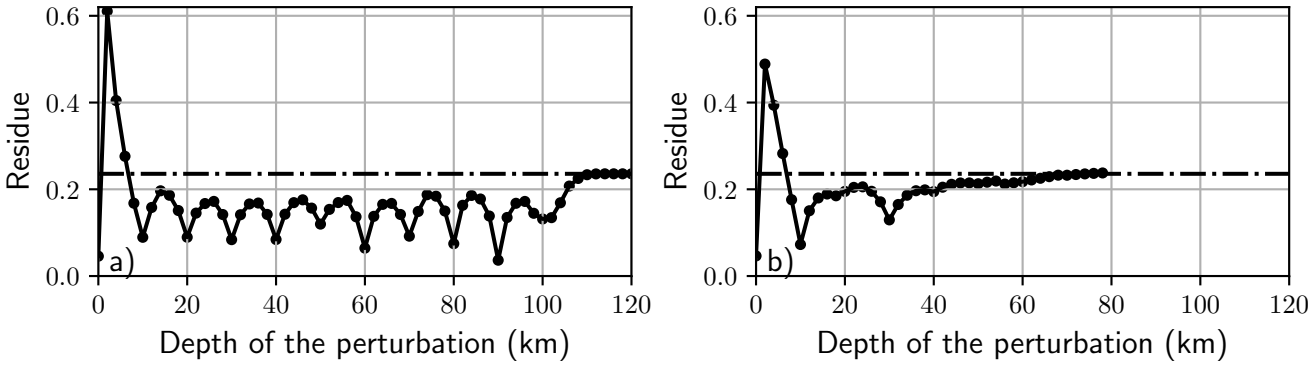

FIGURE 6.9: Real residue for the perturbation at several depths for a system a) without noise b)with added artificial noise of 10^{-3} of amplitude. The dashed line marks the value of R_0.

towards lower values when inverting for deeper layers. However, the general resolution of all the solutions is lower and the estimations seem to be poorly located. When the perturbation is located below $9km$ (6.11d), it appears a bias in the estimated model because at this depth it starts increasing the amplitude of the sigmoidal penalization function (shown in figure 6.7.

The residue plot for the cases with and without noise (figure 6.12) lead to similar conclusions as before: the addition of noise limits the reach of the inversion, in this case, shortening the range that was set by the depth penalization. In the first kilometer is present the oscillation generated when the perturbation is not aligned with the layering system. However, in this case, we obtain an acceptable estimation as the residue values are below R_0.

6.3.3 Performance with different lapse times

Next, we analyze an important question: how the coda window duration used in the inversion affects the final model estimation. To test this, we use a perturbation fixed at $50km$ depth, and we start with a set of measurements of $\delta t/t$ that goes from $15s$ to $45s$. Then we progressively add a new $\delta t/t$ measurements at later coda times ($47.5s$, $50s$, ...) and redo the inversion. This means the segment of the coda used begins always at $15s$ but finish a different lapse times; this last lapse time will be used as the identifier of the set. This process mimics what would be a real case-scenario where the length of the coda time to include in the apparent $\delta v/v$ at the surface is usually chosen with a trial-and-error process.

A sample of two inversions with different coda times sets is shown in figure 6.13. These two estimated solutions show a general behavior: using a smaller set of lapse times leads to solutions with a lower damping parameter, and therefore, more sensitive to noise. However, when using lower coda segments what is gained in robustness is lost in resolution. This can also be seen in figure 6.14a where the residue increases with the number of measurements, because of this loss of precision. As expected, this tendency in the residue is reversed when noise is introduced as shown in 6.14b: the inversions made with the smaller lapse time sets, i.e., using a smaller section of the coda, produce unstable model estimations. Although this last plot suggests that after adding $60s$ to the set of $\delta t/t$ the results are almost the same, in reality, there are important quantitative differences between them, as can be seen in the figure 6.15. This shows that the residue estimation, although useful, is not the best way to assess the performance of the inversion when the features of the system are being smoothed at very different degrees. The case with the thinner and shallower perturbations shows the same trends (longer lapse times leads to more robust and smoothed solutions) and therefore

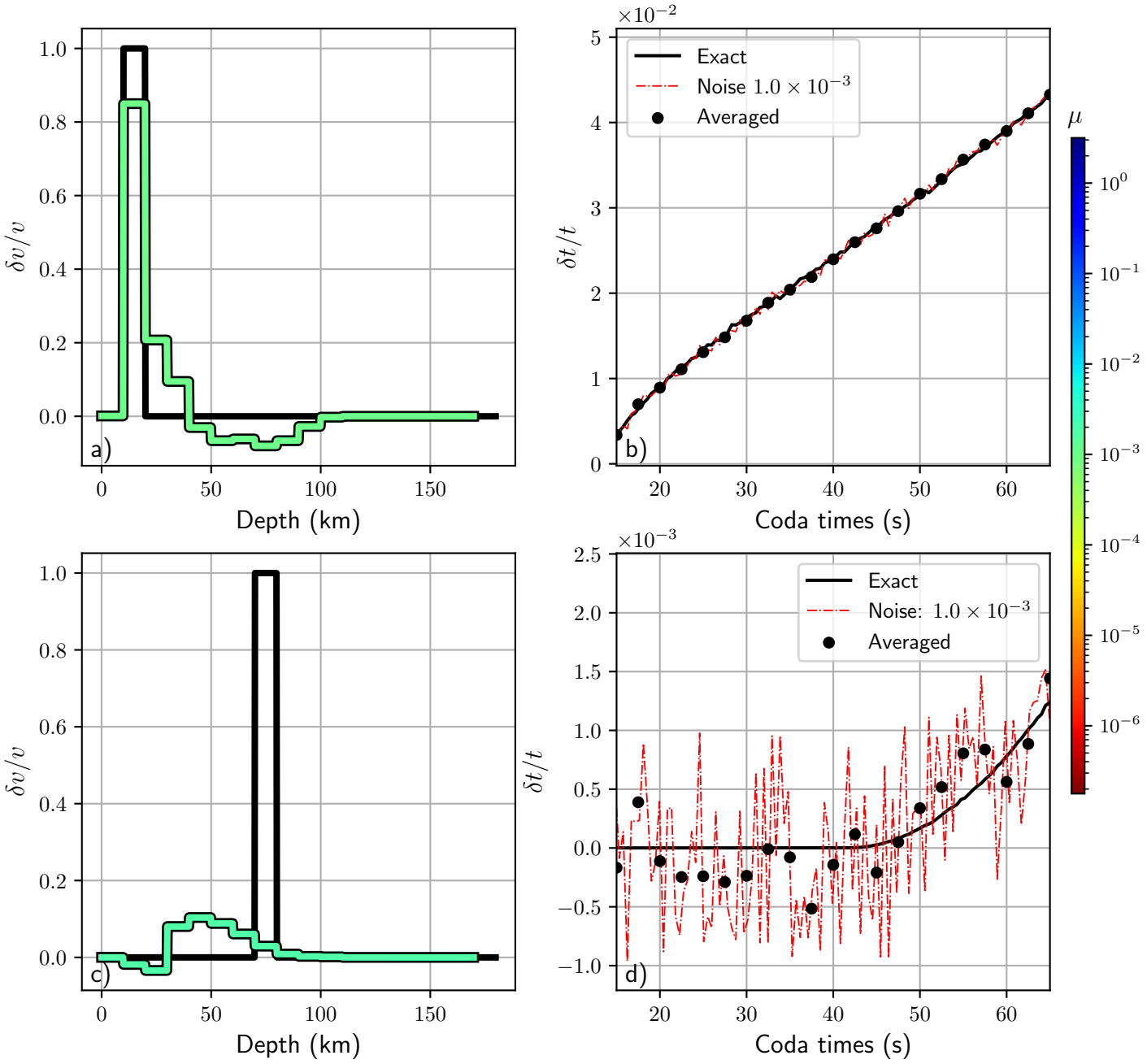

FIGURE 6.10: Inversion results at two selected depths with artificial noise in the system. Original velocity perturbation located at a) $10km$, c)$70km$. Exact $\delta t/t$, after the addition of noise, and passed through moving average window of $10s$ every $2.5s$ for the perturbation at b) $10km$, d)$70km$.

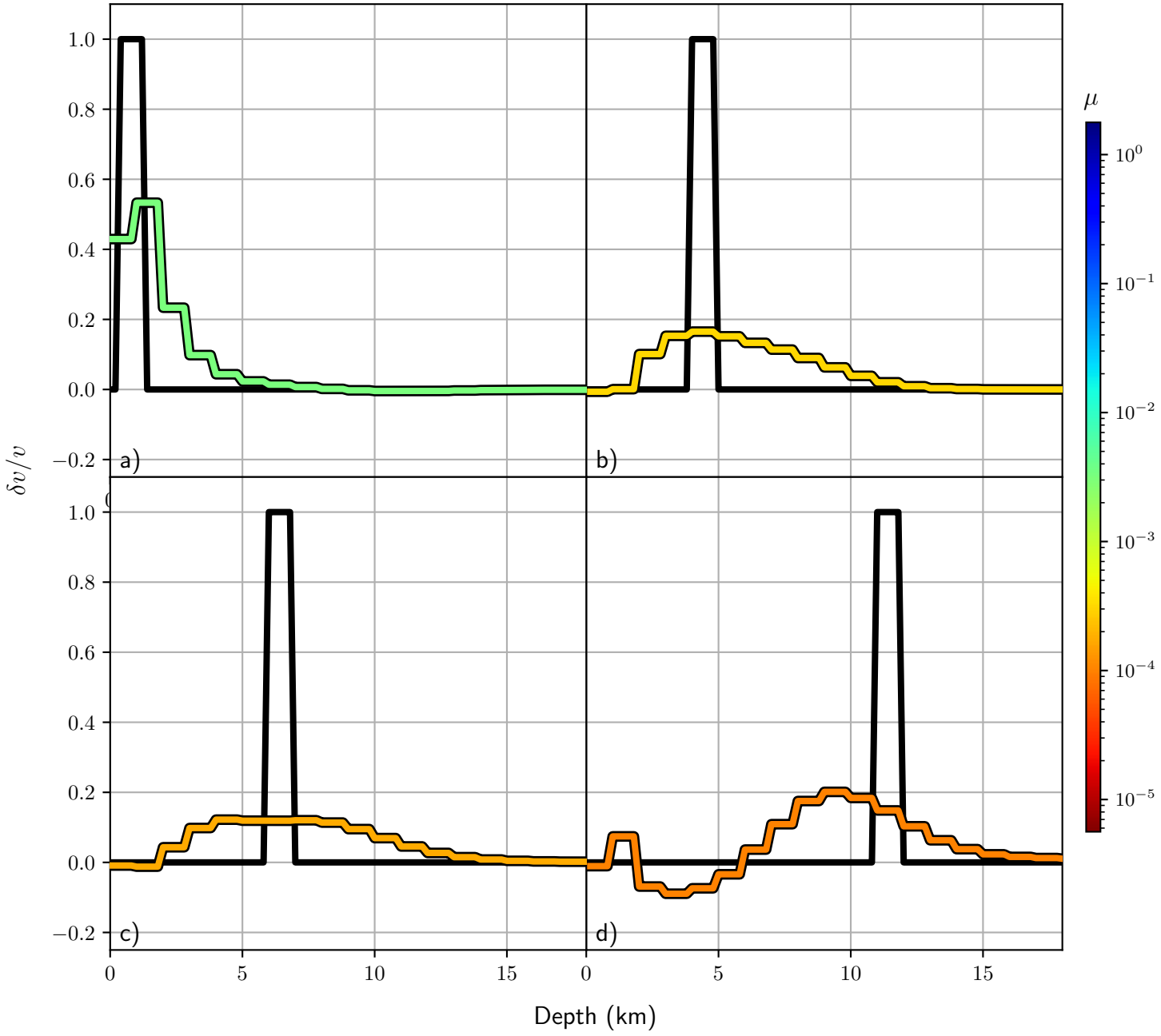

FIGURE 6.11: Result of the inversion without noise for the velocity perturbation located at a) $0.4km$, b) $4km$, c) $6km$ and d) $11km$. The black and the color lines represent the original and the estimated model respectively for each case. Each color is associated to a damping value as shown in the colorbar.

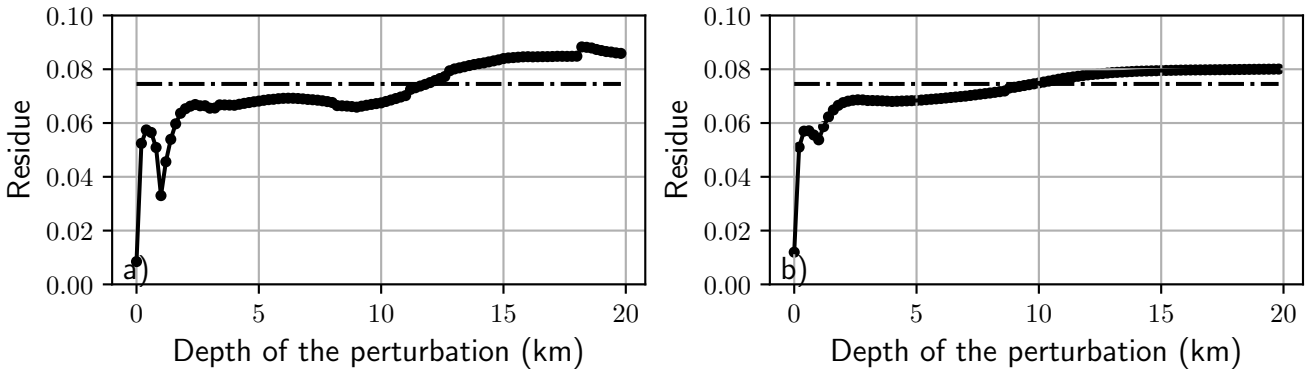

FIGURE 6.12: Real residue for the perturbation at several depths for a system a) without noise b)with added artificial noise of 10^{-3} of amplitude. The dashed line marks the value of R_0.

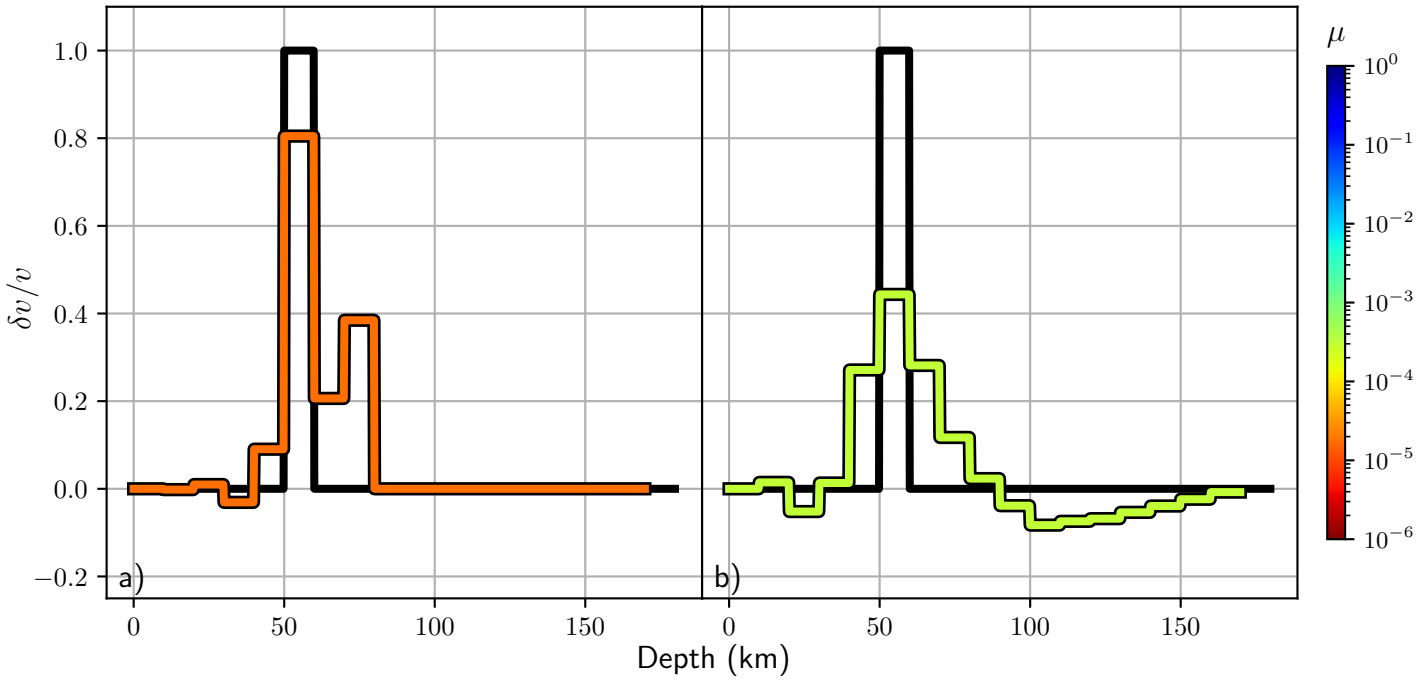

FIGURE 6.13: Result of the inversion for a set of $\delta t/t$ measurements from a) 15s to 45s, b) 15s to 100s. The black and the color lines represent the original and the estimated model respectively for each case. Each color is associated to a damping value as shown in the colorbar.

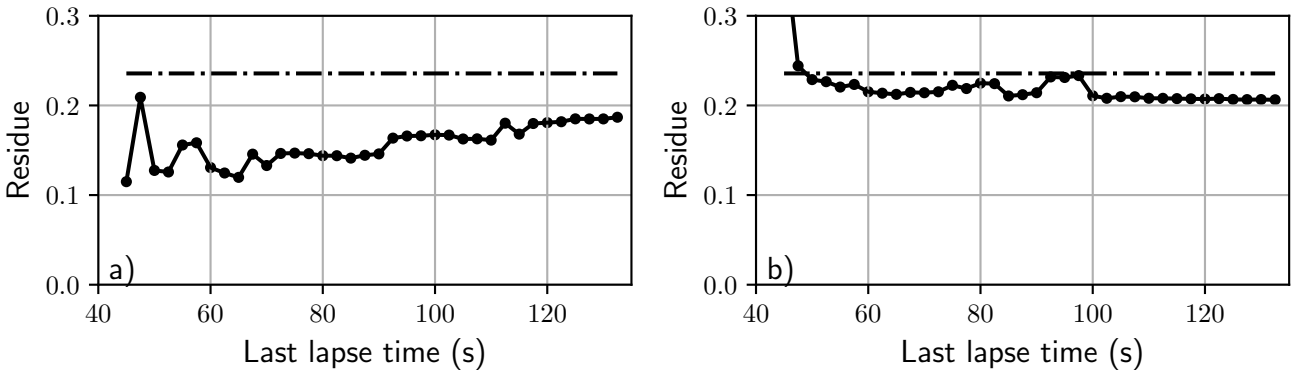

FIGURE 6.14: Real residue for different lapse time ranges starting at 15s and ending at the lapse time given in the horizontal axis a) without noise b) with added artificial noise of 10^{-3} of amplitude. The dashed line marks the value of R_0.

are not shown. However, as in that case the solutions are already smoothed, adding too many measurements of $\delta t/t$ may degrade critically the resolution of the model. This also means that this case is even more sensitive to noise.

6.3.4 Performance with different levels of noise

Let's think that we generate a perturbation at a certain depth and that we try to retrieve it through the inversion. We know that the quality of the estimated model will depend on the level of noise that we add to the system; in fact, we have seen that if we keep increasing the level of noise systematically, at some point the information of the $\delta t/t$ is completely lost and the inversion will be unable to retrieve the original model. Even more, we saw that this also depends on the depth of the layer as that may change the amplitude of the $\delta t/t$ itself.

We want to find for each depth the maximum level of noise under which the inversion makes an acceptable job. For this, we make a series of inversions using always the coda between between $15s$ and $125s$. We proceed as follows: we create a perturbation of $10km$ and calculate the zero-residue R_0. We choose a value a bit lower, $0.92R_0$, as a symbolic threshold under which the results are still acceptable. Now, with the perturbation located at a certain depth, we proceed to perform inversions increasing gradually the level of noise in the system. Once the residue threshold is reached, the noise amplitude is registered: this is the maximum amplitude of noise that the system can tolerates at this depth. However, this maximum amplitude may be different for the same model with different realizations of the noise given its random nature. For this reason, the process is repeated for the same model with 50 different realizations of noise, and all the maximum-amplitudes are averaged between them. Finally, the whole operation is repeated for the perturbation located at another position. The maximum amplitude of the noise for each depth is shown as the scatter plot in figure 6.16. It is clear that the deeper is the perturbation, the lower is the maximum level of noise that can introduce into the system without losing the original information. However, the interesting aspect of this behavior is that the maximum tolerable amplitude of noise can be related to the sensitivity kernel itself.

From 6.17 can be seen that an unitary perturbation at different positions produce measurements of $\delta t/t$ that are proportional to the the sensitivity. As the noise is added to the $\delta t/t$, its effect on the inversion depends on to the relative amplitudes between the two: if the sensitivity is high compared with the level of noise, most of the features of the $\delta t/t$ are

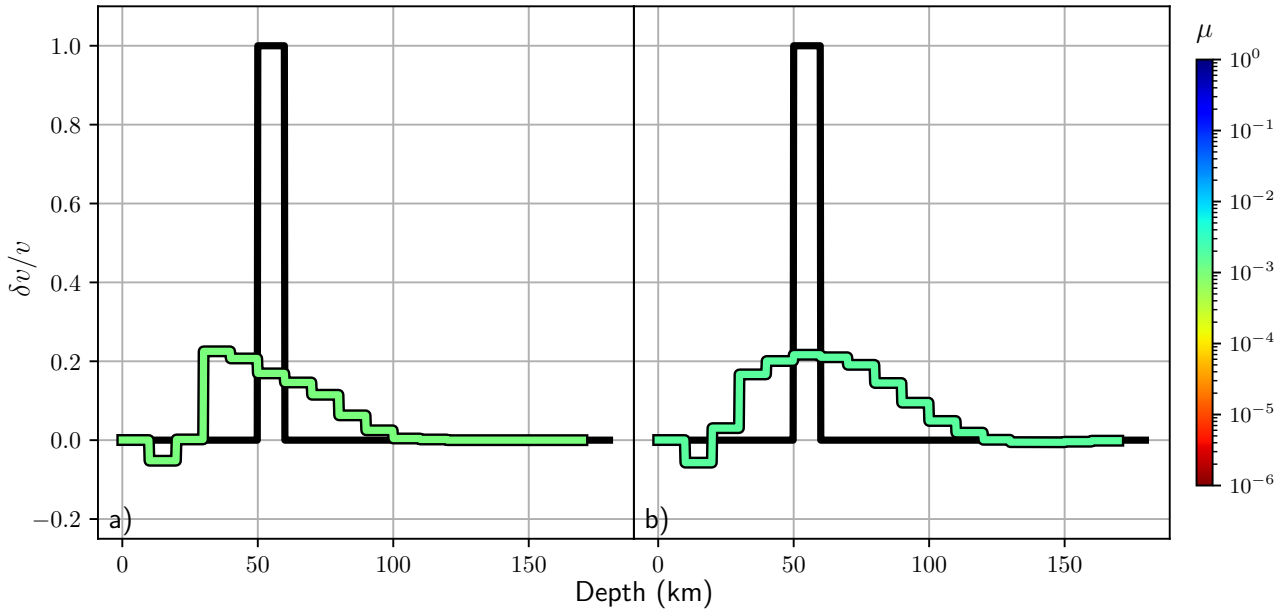

FIGURE 6.15: Result of the inversion for a set of $\delta t/t$ measurements from a) $15s$ to $45s$, b) $15s$ to $100s$. Artificial noise was added to both configurations. The black and the color lines represent the original and the estimated model respectively for each case. Each color is associated to a damping value as shown in the colorbar.

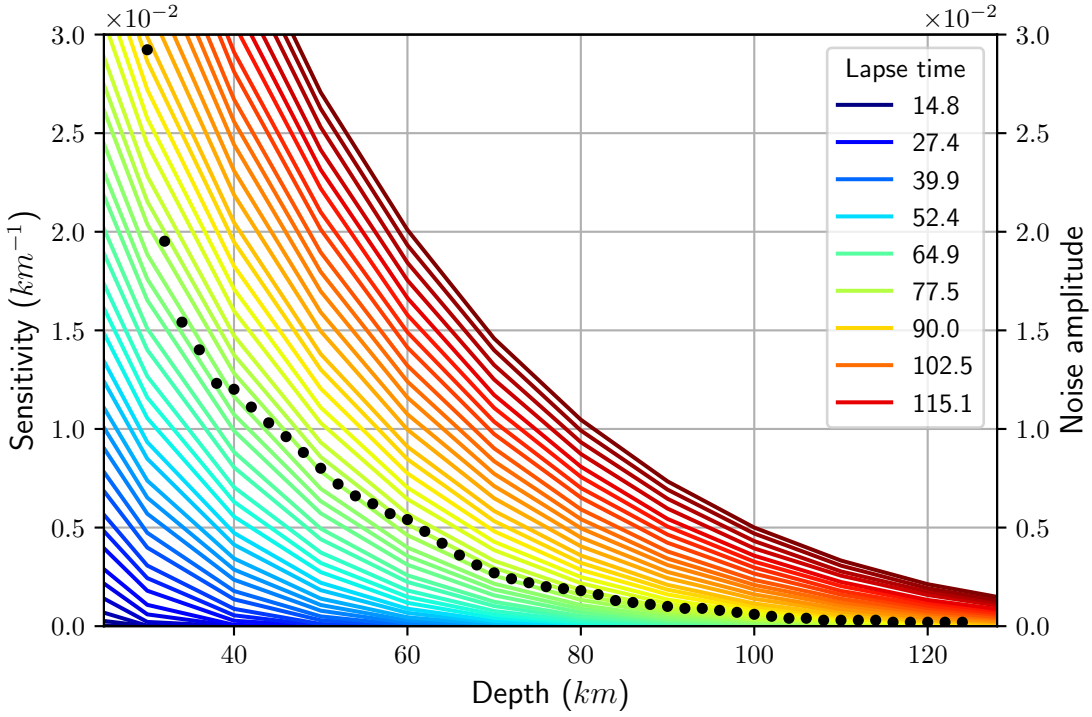

FIGURE 6.16: Color lines: Profiles of the down-sampled kernel for different times, at different depths. Scatter plot: Maximum amplitude of noise before trespassing the good-quality limit of $0.92R_0$ for each depth. The set of $\delta t/t$ is taken between $15s$ and $125s$ for all the inversions.

preserved and the inversion performs well. If both are comparable, the behavior of the $\delta t/t$ is masked and it is impossible to recover the velocity perturbation with the inversion. In figure 6.16 is also plotted the kernel profile for different times at different depths, which shows this proportionality. This means that the maximum level of noise that we can add to the system without losing completely the information is a fraction of the maximum sensitivity at that point. This practical relation can be quite useful to determine the possibilities of retrieving information at a certain depth, by analyzing the kernel profile and the general level of noise in the signals.

Nonetheless, it must be pointed out that the actual proportion between the amplitude of the noise and the amplitude of the sensitivity may be altered by the actual value of the velocity perturbation (that will be a number much smaller than 1) and by the averaging process in the temporal dimension that may affect the effective noise amplitude of the system. Below $30km$ the relation does not hold because at those depths there is a dramatic change in the sensitivity due to the surfaces waves and because the shape itself of the $\delta t/t$ may change a lot and be quite different from the characteristic shape generated by having the perturbation at depth (see for example 6.5b). Finally, this same analysis cannot be done close to the surface with the surface waves sensitivity because the parameter we use to determine the quality of the inversion (the residue R_r) does not work well with smoothed shapes as was seen in the previous section.

6.4 Conclusions

Based on the scalar model that couples body and surface waves, a linear relationship can be established between the changes of velocity on the crust, and the changes of phase in the cross-correlations obtained by seismic-noise based methods at the surface: this is the sensitivity kernel. This particular kernel is obtained for the case where the source and the receiver are located at the same position. With it we can construct a discrete matrix operator that connects a series of measurements $\delta t/t$, with its sources $\delta v/v$. However, this first operator is defined over a dense set of lapse times and depths, and in practice, we have a limited number of observations. We discuss the process to reduce the dimensions of this full-resolution operator to obtain a down-sampled version that is the one that we would use in applications.

We design a general procedure under which we test the performance and limitations of the inversion. This is based on obtaining an estimated model for a range of values of the damping parameter, and choosing automatically the best one following the L-curve criteria. We test the precision of the criteria calculating the residual difference between the original model and the estimated model and observe an overall good performance. We also conclude that downsampling the set of measurements available for the inversion acts like a noise introduction in the system. Therefore the utilization of the damping parameter is necessary. However, this has as side-effect the inevitable loss of resolution of the original model.

We separate the analysis in two systems of layering of $10km$ and $1km$ thick, and we use perturbations of similar size ($10km$ and $1km$ respectively) to test the inversion. The second one is desgined to image interesting phenomena like seismic events or seasonal-driven fluid movements in the crust, that happen in the first kilometers close to the surface. The use of the damping parameter is not sufficient to recover the original model in the thinner layering system. To increase the capacity of the inversion the introduce a penalization function that prioritize solutions with perturbations located in the first layers of the half-space. This is done through a smooth sigmoid function that assigns a larger weight to the deeper parameters of the model in the minimization process of the least square solution. We find that this

depth penalization helps us to retrieve the location of the original perturbation, although the estimated models are of lower resolution.

The performance of the inversion is tested when the perturbation is located at different depths. We find that in noise-free conditions, the deeper is the $\delta v/v$ the lower is the damping value of the estimated model. This has two main implications: first, it means on these conditions the estimated model at depth is a bit more precise than close to the surface, where the estimations are smoother. The second one is that closer to the surface the solutions are less vulnerable to the effect of the noise. In effect, we find that the introduction of an artificial random generated noise in the system leads to a dramatic loss of precision when we are trying to resolve the velocity structure deeper in the medium. This effect is so strong, that there is a depth after which the original information is completely lost. This is product of the levels of $\delta t/t$ falling under the levels of noise, or in other words, of a low signal-to-noise ratio. This same behavior is observed in the thinner layering system, with the difference that on this case the maximum depth to which the inversion can recover the perturbation is determined by the penalization sigmoid function.

We are also interested in knowing how the duration of the coda used in the inversion affects the quality of the calculated models. For this, we compare the results of a series of inversions, that use a progressively bigger set of measurements of $\delta t/t$. This is done by attaching a new measurement in a slightly later lapse time. Both cases (the thicker and thinner layering system) show that the smaller is the number of measurements, the lower is the damping value of the estimated model; as before, this leads to models with higher precision but quite unstable to the introduction of noise. A large set of measurements will generate very stable results that have unfortunately lower resolution. In the practice making tests starting with a large number of $\delta t/t$ measurements, could reveal the presence of structures, that can after be resolved with higher resolution decreasing progressively the used coda in the inversion. In the thinner layering case, the use of long segments of the coda can deteriorate beyond recognition the velocity perturbations, so in that case the search of the equilibrium point between stability and precision should start with the smallest possible set of $\delta t/t$.

Finally, the overall role of the noise in the inversion is analyzed. For each depth, we make a series of inversions where the noise is gradually increased until the original velocity perturbation is almost completely gone. This is the maximum level of noise that the system can tolerate without losing completely the information. We find that in general, this level is proportional with the sensitivity. This gives a very convenient tool to assess the eventual robustness of the inversion based on the characteristics of the kernel itself. However this does not hold for points close to the surface due to the presence of the surface waves, and to the varied shapes that the $\delta t/t$ takes in those regions

Chapter 7

Conclusions and perspectives

We present in this thesis a study focus on the development of tools for the analysis of ambient seismic noise. Our main interest is to have a deeper understanding of the mechanisms that are responsible for the well-known velocity perturbations of the seismic waves in the crust. This means separating and localizing each of these processes with the information that is usually recorded on the surface. In the first part, we analyzed a particular case in the south of Italy. This region shows a very particular set of characteristics that makes it an interesting study case: the presence of an aquifer, a limited period of seismic activity that included slow slip events and a $M5.0$ earthquake, and a convenient deployment of GPS and meteorological stations along with a seismic station located very close to the fault system. We proposed some simple physical models that allow us to predict the observed velocity variations in the zone from the rainfall of the region, and validate our physical interpretation of the process inside the crust with geodetic data. We successfully separate and recognize the independent influence of seasonal and tectonic phenomena in the measurements obtained from the analysis the ambient seismic noise.

On the other hand, we address one of the main objectives of Passive Image Interferometry: localize the changes in the crust from the phase delays registered at the surface. This objective is complementary to the previous analysis as we expect that different processes affect different parts of the crust. We develop this part of the project in three stages: the study of a scalar model that allows the coupling between surface and body waves, the estimation of the sensitivity kernel of this system, and the technical study of inverse problem with this kernel to locate velocity perturbations in a real-life like scenario.

In the first stage, we use a scalar model with a mixed boundary condition that sustains the natural propagation of surface waves. We study the scattering cross sections between all the possible combinations of propagation in this system, and from it, we estimate the scattering mean free times. Based on this we construct the radiative transfer equations of the system and test them in a Monte Carlo simulation. The results show that the scalar model reproduces expected behaviors in the limit cases, and gives us an insightful perspective of the energy exchange between body and surface waves in the first stages of propagation after the activation of an impulsive source.

In the second stage, we reconstruct the sensitivity framework including the directionality of the energy and add into it the two modes of propagation. At the same time, we use a variational approach to quantify how a velocity perturbation in the medium affects the propagation velocity of the surface waves. We use once again Monte Carlo simulations, this time to estimate the travel-time distribution of the energy when propagating from a source to a receiver, both of them located at the same spot on the surface. All of these results are integrated into the construction of a sensitivity kernel that accounts simultaneously for both types of waves. Basic tests on this newly found kernel found good agreement with previous results based on full wavefield elastic simulations and theoretical solutions in 3-D full space propagation. However, we also observe disagreements related to the evolution of the system,

caused by the introduction of the coupling or exchange region delimited by the penetration of the surface waves. Furthermore, we find evidence that shows that the coupled system is invariant when the ratio between the mean free path and the penetration depth of the surface wave is maintained.

Finally, in the third stage, we study the capabilities and limitations of the kernel to identify velocity variations in the crust under real-life conditions within the framework of the inverse problem. In this section, we focus on the effect of three variables within the inversion: the depth of the perturbation, the duration of the coda segment to invert, and the level of noise in the system. We find useful relations for each of these cases to make a more effective interpretation of the result of an inversion performed with the scalar sensitivity kernel.

In figure 7.1 we present a first result of the inversion over measurements of $\delta t/t$ obtained from the station MMNO in the region of Pollino, Italy, described in Chapter 3. On top, we have the apparent velocity variation, and at the bottom the actual velocity variation in the crust for several depths, ranging from $0km$ to $1.2km$ depth. Each of these curves was smoothed using a moving average of 10 days. The parameters used for the measurements of the time densities are shown in table 6.1 on page 112. We use a frequency band between $0.5Hz$ and $1.0Hz$ and measurements of the apparent velocity variation obtained with the Moving Cross Spectral Window technique between $10s$ and $40s$ each $0.4s$ with a window of $8s$ around each lapse time. The apparent velocity variation is usually obtained with the average between all the possible correlations between the three available channels for the stations. However, for the inversion, we use only the measurements of $\delta t/t$ of the correlation North-North as it shows the closest estimations to the final apparent velocity variation

For each day we have a measurement of values of $\delta t/t$ and therefore the inversion is performed for each date independently. This means that the damping parameter chosen automatically with the L-curve criteria may be different for different days; however, in figure 7.1 we present the inversion made with the average damping parameter obtained from all the dates. This decision is justified if we recognize that the velocity perturbations appear and remain in the same position in the crust over long lapse times, in this case, in the order of months. This allows us to obtain results from days when the trade-off curve of the inversion is poor. In this case, the perturbations in the medium seem to be constrained to the first kilometers of depth. This is possibly a consequence of the predominance of the surface waves on this part of the coda: when normalize by the body-to-body mean free time, the later lapse time $40s$ is equal to $t/\tau_{b\to b} = 1.39$, a very early stage of the system where the sensitivity of the system is almost completely determined by the surface wave sensitivity (see figure 5.12 on page 100). However, the recovered model shows an interesting feature: from some times before the earthquake (September-October 2012), until the reported last slow slip event in the zone (mid 2013, see figure 3.3 on page 26) the velocity variation passes through its strongest decrease of the whole 10-year period, accentuated by an overall decrease of the natural fluctuation of the time series. Although the behavior at depth is not really distinctive, the inversion seems to highlight the period in which there is the most notable stress redistribution of the zone.

Figure 7.2 shows the results of the inversion at deeper zones of the medium. These first results indicate that the annual variations and long-term trend are associated with the most superficial layers, more precisely the first kilometer. This is in line with our interpretation in terms of the filling of the karstic system. Note that these fluctuations are not incorrectly projected at depth. Unfortunately, due to the dominance of the sensitivity of surface waves, the effects of changes in the deep layers are of small amplitude at short lapse times and our measurements seem to be contaminated by errors that are projected at depth. At this stage it is clear that these instabilities in the delay measurements need to be reanalyzed and reduced by extended time averaging and by the use of noise reduction techniques such as those proposed by Baig, Campillo, and Brenguier (2009) or Moreau et al. (2017). We

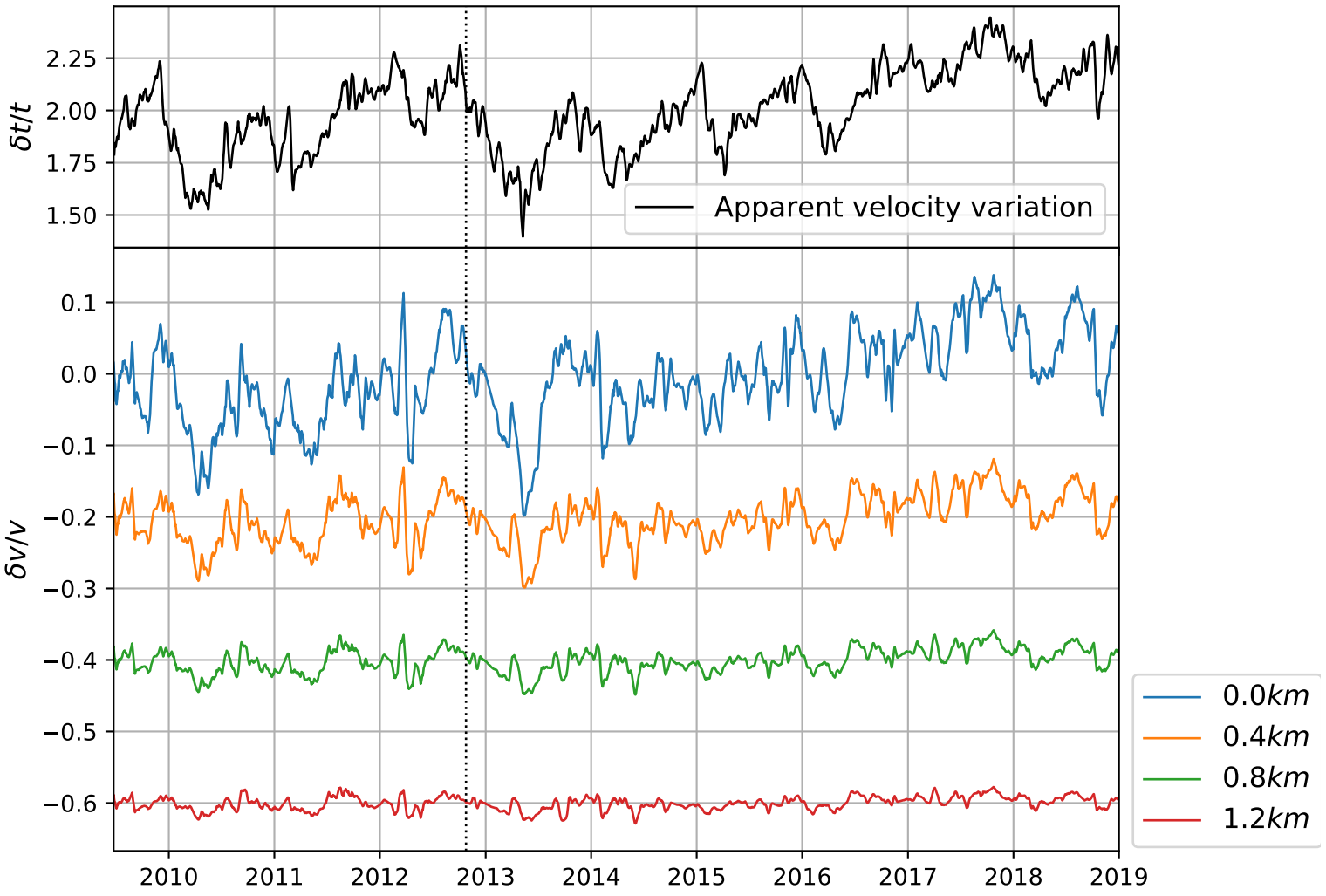

FIGURE 7.1: Top: average apparent velocity variation measures from continuous seismic records in the station MMNO at Pollino, Italy. Bottom: velocity variation at several depths obtained from the inversion. A shift of 0.2 was added between them for visualization purposes. The dashed line marks the date of the $M5.0$ seismic event.

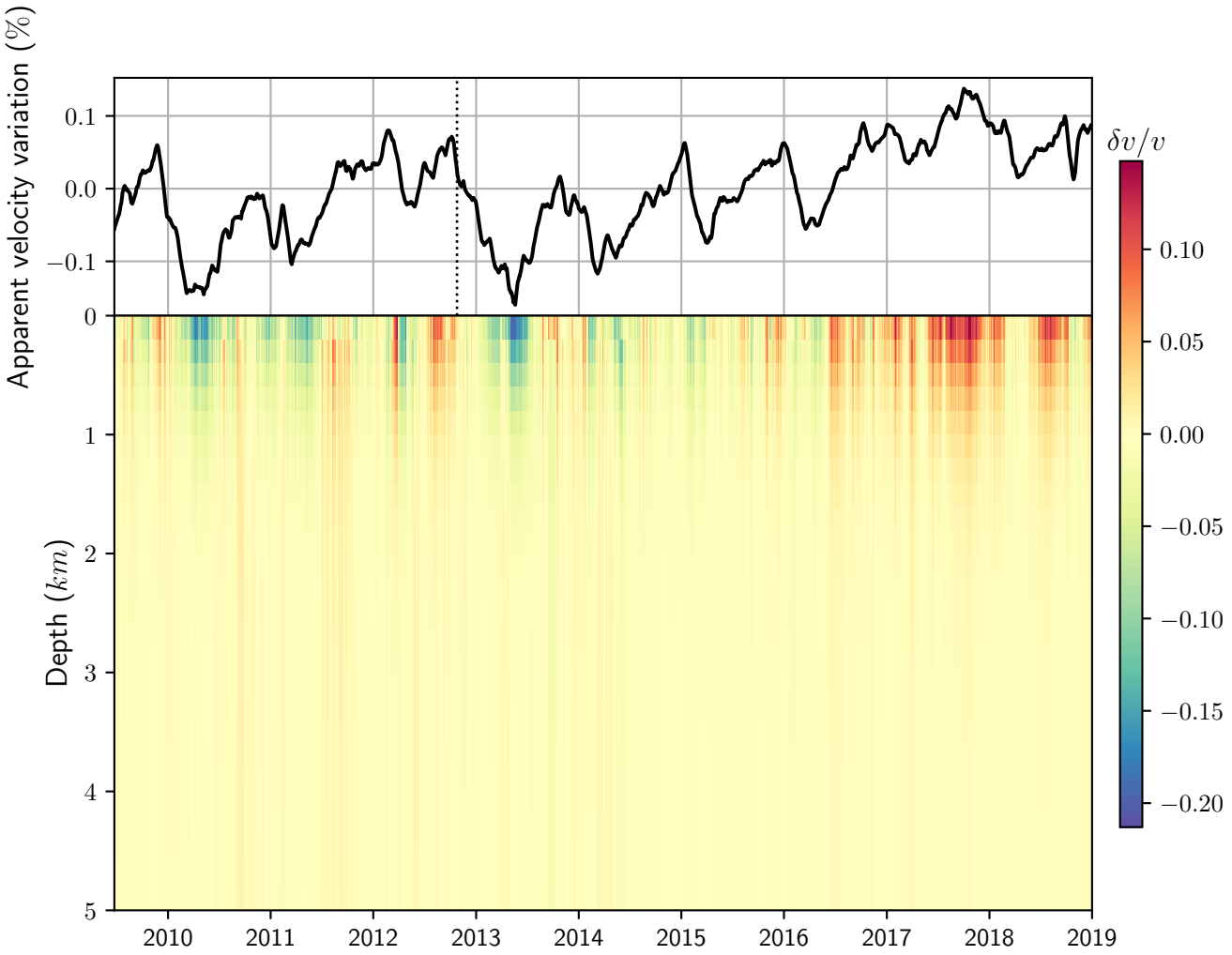

FIGURE 7.2: Top: average apparent velocity variation measures from continuous seismic records in the station MMNO at Pollino, Italy. Bottom: velocity variation at several depths obtained from the inversion with their values indicated by the colorbar. The dashed line marks the date of the $M5.0$ seismic event.

will also consider using the continuous wavelet method of Mao et al. (2020) in place of the MWCS method considered so far. Prior to these studies we cannot conclude on a possible tectonic origin of the differences observed in Chapter 3 between observations and models derived from meteorological observations. It is also clear that in situation where the surface wave sensitivity is strong, it could be mandatory to use measurements in different frequency bands to constraint the depth distribution of the changes.

There are many directions of improvement for the work here presented, that go from conceptual aspects like the introduction of two types of body wave modes of propagation or the development and estimation of the sensitivity kernel for a full-spatial description, to technical aspects like the use of dense seismic networks or more advance methods for the inversion. The first results show encouraging aspects that may lead in the future to accurate applications of ambient seismic noise as a regular imaging tool of the crust.

Bibliography

Abubakirov, I R and A A Gusev (1990). "Estimation of scattering properties of lithosphere of Kamchatka based on Monte-Carlo simulation of record envelope of a near earthquake". In: *Physics of the Earth and Planetary Interiors* 64.1, pp. 52–67. ISSN: 0031-9201. DOI: https://doi.org/10.1016/0031-9201(90)90005-I. URL: http://www.sciencedirect.com/science/article/pii/003192019090005I.

Akasaka, Chitoshi and Shigetaka Nakanishi (2000). "Correction of background gravity changes due to precipitation: Oguni geothermal field, Japan". In:

Aki, K and P G Richards (2002). *Quantitative Seismology, 2d Ed.* University Science Book.

Aki, Keiiti (1969). "Analysis of the seismic coda of local earthquakes as scattered waves". In: *Journal of Geophysical Research (1896-1977)* 74.2, pp. 615–631. ISSN: 0148-0227. DOI: https://doi.org/10.1029/JB074i002p00615. URL: https://doi.org/10.1029/JB074i002p00615.

— (1973). "Scattering of P Waves under the Montana Lasa". In: *J. Geophys. Res.* 78.8, pp. 1334–1346.

Akkermans, E and G Montambaux (2007). *Mesoscopic Physics of Electrons and Photons*. Cambridge: Cambridge University press.

Amoruso, A et al. (2014). "Correlation between groundwater flow and deformation in the fractured carbonate Gran Sasso aquifer (INFN underground laboratories, central Italy)". In: *Water Resources Research* 50.6, pp. 4858–4876. DOI: https://doi.org/10.1002/2013WR014491. URL: https://agupubs.onlinelibrary.wiley.com/doi/abs/10.1002/2013WR014491.

Amos, Colin B et al. (2014). "Uplift and seismicity driven by groundwater depletion in central California". In: *Nature* 509.7501, pp. 483–486. ISSN: 1476-4687. DOI: 10.1038/nature13275. URL: https://doi.org/10.1038/nature13275.

Argus, Donald F, Yuning Fu, and Felix W Landerer (2014). "Seasonal variation in total water storage in California inferred from GPS observations of vertical land motion". In: *Geophysical Research Letters* 41.6, pp. 1971–1980. DOI: 10.1002/2014GL059570. URL: https://agupubs.onlinelibrary.wiley.com/doi/abs/10.1002/2014GL059570.

ARPACAL. *Centro funzionale multirischi della Calabria*. http://www.cfd.calabria.it/. URL: http://www.cfd.calabria.it/.

Aster, Richard C, Brian Borchers, and Clifford H Thurber (2018). *Parameter estimation and inverse problems*. Elsevier.

Baig, Adam M, Michel Campillo, and Florent Brenguier (2009). "Denoising seismic noise cross correlations". In: *Journal of Geophysical Research: Solid Earth* 114.B8.

Bal, Guillaume, George Papanicolaou, and Leonid Ryzhik (2000). "Probabilistic Theory of Transport Processes with Polarization". In: *SIAM Journal on Applied Mathematics* 60.5, pp. 1639–1666. ISSN: 00361399. URL: http://www.jstor.org/stable/3061704.

Bawden, Gerald W et al. (2001). "Tectonic contraction across Los Angeles after removal of groundwater pumping effects". In: *Nature* 412.6849, pp. 812–815. ISSN: 1476-4687. DOI: 10.1038/35090558. URL: https://doi.org/10.1038/35090558.

Ben-Menahem, Ari and Sarva Jit Singh (1981). *Seismic Waves and Sources*. ISBN: 978-1-4612-5858-2. DOI: 10.1007/978-1-4612-5856-8. URL: http://link.springer.com/10.1007/978-1-4612-5856-8.

Bergman, Theodore L et al. (2011). *Fundamentals of heat and mass transfer*. John Wiley and Sons.

Beroza, Gregory C, Alex T Cole, and William L Ellsworth (1995). "Stability of coda wave attenuation during the Loma Prieta, California, earthquake sequence". In: *Journal of Geophysical Research: Solid Earth* 100.B3, pp. 3977–3987. ISSN: 0148-0227. DOI: https://doi.org/10.1029/94JB02574. URL: https://doi.org/10.1029/94JB02574.

Borsa, Adrian Antal, Duncan Carr Agnew, and Daniel R Cayan (2014). "Ongoing drought-induced uplift in the western United States". In: *Science* 345.6204, pp. 1587–1590. ISSN: 0036-8075. DOI: 10.1126/science.1260279. URL: https://science.sciencemag.org/content/345/6204/1587.

Brenguier, F et al. (2008a). "Postseismic Relaxation Along the San Andreas Fault at Parkfield from Continuous Seismological Observations". In: *Science* 321.5895, 1478 LP –1481. DOI: 10.1126/science.1160943. URL: http://science.sciencemag.org/content/321/5895/1478.abstract.

Brenguier, Florent et al. (2008b). "Towards forecasting volcanic eruptions using seismic noise". In: *Nature Geoscience* 1.2, pp. 126–130. ISSN: 1752-0908. DOI: 10.1038/ngeo104. URL: https://doi.org/10.1038/ngeo104.

Campillo, Michel (2006). "Phase and Correlation in 'Random' Seismic Fields and the Reconstruction of the Green Function". In: *pure and applied geophysics* 163.2, pp. 475–502. ISSN: 1420-9136. DOI: 10.1007/s00024-005-0032-8. URL: https://doi.org/10.1007/s00024-005-0032-8.

Campillo, Michel and Anne Paul (2003). "Long-Range Correlations in the Diffuse Seismic Coda". In: *Science (New York, N.Y.)* 299, pp. 547–549. DOI: 10.1126/science.1078551.

Carcolé, E and H Sato (2010). "Spatial distribution of scattering loss and intrinsic absorption of short-period s waves in the lithosphere of japan on the basis of the multiple lapse time window analysis of hi-net data". In: *Geophysical Journal International* 180, pp. 268–290.

Chanard, K et al. (2014). "Modeling deformation induced by seasonal variations of continental water in the Himalaya region: Sensitivity to Earth elastic structure". In: *Journal of Geophysical Research: Solid Earth* 119.6, pp. 5097–5113. DOI: 10.1002/2013JB010451. URL: https://agupubs.onlinelibrary.wiley.com/doi/abs/10.1002/2013JB010451.

Chapman, Sydney, Thomas George Cowling, and David Burnett (1990). *The mathematical theory of non-uniform gases: an account of the kinetic theory of viscosity, thermal conduction and diffusion in gases*. Cambridge university press.

Cheloni, Daniele et al. (2017). "Aseismic transient during the 2010-2014 seismic swarm: evidence for longer recurrence of M >/= 6.5 earthquakes in the Pollino gap (Southern Italy)?" In: *Scientific reports* 7.1, p. 576. ISSN: 2045-2322 (Electronic). DOI: 10.1038/s41598-017-00649-z.

Cheng, Alexander (2000). *Multilayered Aquifer Systems: Fundamentals and Applications*. Vol. 4. 1, pp. 64–75. ISBN: 0824798759.

D'Agostino, N et al. (2018). "Crustal Deformation and Seismicity Modulated by Groundwater Recharge of Karst Aquifers". In: *Geophysical Research Letters* 45.22, pp. 12,212–253,262. DOI: 10.1029/2018GL079794. URL: https://agupubs.onlinelibrary.wiley.com/doi/abs/10.1029/2018GL079794.

Dainty, Anton M. et al. (1974). "Seismic scattering and shallow structure of the moon in oceanus procellarum". In: *The Moon*. ISSN: 00270903. DOI: 10.1007/BF00565388.

Daniele, Tenze, Carla Braitenberg, and Ildikò Nagy (2012). "Karst deformations due to environmental factors: Evidences from the horizontal pendulums of Grotta Gigante, Italy". In: *Bollettino di Geofisica Teorica ed Applicata* 53, pp. 331–345. DOI: 10.4430/bgta0049.

Duvall, T L et al. (1993). "Time–distance helioseismology". In: *Nature* 362.6419, pp. 430–432. ISSN: 1476-4687. DOI: 10.1038/362430a0. URL: https://doi.org/10.1038/362430a0.

Economou, Eleftherios N (2006). *Green's functions in quantum physics*. Vol. 7. Springer Science and Business Media.

Eulenfeld, T and U Wegler (2017). "Crustal intrinsic and scattering attenuation of high-frequency shear waves in the contiguous united states". In: *Journal of Geophysical Research: Solid Earth* 122, pp. 4676–4690.

Fehler, Michael et al. (1992). "Separation of scattering and intrinsic attenuation for the Kanto-Tokai region, Japan, using measurements of S-wave energy versus hypocentral distance". In: *Geophysical Journal International*. ISSN: 1365246X. DOI: 10.1111/j.1365-246X.1992.tb03470.x.

Fiorillo, Francesco (2011). "Tank-reservoir drainage as a simulation of the recession limb of karst spring hydrographs". In: *Hydrogeology Journal* 19, pp. 1009–1019. DOI: 10.1007/s10040-011-0737-y.

Froment, Bérénice (2011). "Utilisation du bruit sismique ambiant dans le suivi temporel de structures géologiques". Theses. Université de Grenoble. URL: https://tel.archives-ouvertes.fr/tel-00648796.

Gaebler, P J, C Sens-Schönfelder, and M Korn (2015). "The influence of crustal scattering on translational and rotational motions in regional and teleseismic coda waves". In: *Geophysical Journal International* 201, pp. 355–371.

Galloway, Devin and Thomas Burbey (2011). "Review: Regional land subsidence accompanying groundwater extraction". In: *Hydrogeology Journal - HYDROGEOL J* 19. DOI: 10.1007/s10040-011-0775-5.

Garnier, Josselin and George Papanicolaou (2009). "Passive Sensor Imaging Using Cross Correlations of Noisy Signals in a Scattering Medium". In: *SIAM J. Imaging Sciences* 2, pp. 396–437. DOI: 10.1137/080723454.

Gelfand, I and S Fomin (1963). *Calculus of Variations*. New Jersey: Prentice Hall.

Geller, Robert J and Charles S Mueller (1980). "Four similar earthquakes in central California". In: *Geophysical Research Letters* 7.10, pp. 821–824.

Giles, P.∼M. et al. (1997). "A subsurface flow of material from the Sun's equator to its poles". In: *Nature* 390.6655, pp. 52–54. DOI: 10.1038/36294.

Grêt, Alexander et al. (2005). "Monitoring rapid temporal change in a volcano with coda wave interferometry". In: *Geophysical Research Letters*. ISSN: 00948276. DOI: 10.1029/2004GL021143.

Grêt, Alexandre, Roel Snieder, and John Scales (2006). "Time-lapse monitoring of rock properties with coda wave interferometry". In: *Journal of Geophysical Research: Solid Earth*. ISSN: 21699356. DOI: 10.1029/2004JB003354.

Gusev, A and I Abubakirov (1996). "Simulated envelopes of non-isotropically scattered body waves as compared to observed ones: another manifestation of fractal heterogeneity". In: *Geophysical Journal International* 127, pp. 49–60.

Gusev, A A and I R Abubakirov (1987). "Monte-Carlo simulation of record envelope of a near earthquake". In: *Physics of the Earth and Planetary Interiors* 49.1, pp. 30–36. ISSN: 0031-9201. DOI: https://doi.org/10.1016/0031-9201(87)90130-0. URL: http://www.sciencedirect.com/science/article/pii/0031920187901300.

Gut, Allan (2013). *Probability: a graduate course*. Vol. 75. Springer Science and Business Media.

Hadziioannou, Céline (2011). "Ondes sismiques en milieu complexe : mesure des variations temporelles des vitesses". Theses. Université de Grenoble. URL: https://tel.archives-ouvertes.fr/tel-00564110.

Hadziioannou, Céline et al. (2009). "Stability of monitoring weak changes in multiply scattering media with ambient noise correlation: Laboratory experiments". In: *The Journal of the Acoustical Society of America* 125.6, pp. 3688–3695.

Hein, Ricardo and Hein R. (2010). "Green's functions and integral equations for the Laplace and Helmholtz operators in impedance half-spaces". PhD thesis. Ecole Polytechnique.

Hennino, R et al. (2001). "Observation of equipartition of seismic waves". In: *Physical Review Letters*. ISSN: 00319007. DOI: 10.1103/PhysRevLett.86.3447.

Hill, Terrell L (1986). *An introduction to statistical thermodynamics*. Courier Corporation.

Hillers, G, M Campillo, and K.-F. Ma (2014). "Seismic velocity variations at TCDP are controlled by MJO driven precipitation pattern and high fluid discharge properties". In: *Earth and Planetary Science Letters* 391, pp. 121–127. ISSN: 0012-821X. DOI: https://doi.org/10.1016/j.epsl.2014.01.040. URL: http://www.sciencedirect.com/science/article/pii/S0012821X14000569.

Hillers, G et al. (2019). "Seismic Velocity Change Patterns Along the San Jacinto Fault Zone Following the 2010 M7.2 El Mayor-Cucapah and M5.4 Collins Valley Earthquakes". In: *Journal of Geophysical Research: Solid Earth* 124.7, pp. 7171–7192. DOI: 10.1029/2018JB017143. URL: https://agupubs.onlinelibrary.wiley.com/doi/abs/10.1029/2018JB017143.

Hillers, Gregor et al. (2015). "Noise-based monitoring and imaging of aseismic transient deformation induced by the 2006 Basel reservoir stimulation". In: *GEOPHYSICS*. ISSN: 19422156. DOI: 10.1190/geo2014-0455.1.

Hoshiba, M (1993). "Separation of scattering attenuation and intrinsic absorption in japan using the multiple lapse time window analysis of full seismogram envelope". In: *Journal of geophysical research* 98, pp. 15809–15824.

— (1995). "Estimation of nonisotropic scattering in western Japan using coda wave envelopes: Application of a multiple nonisotropic scattering model". In: *Journal of Geophysical Research* 100, pp. 645–657.

Hoshiba, Mitsuyuki (1991). "Simulation of multiple-scattered coda wave excitation based on the energy conservation law". In: *Physics of the Earth and Planetary Interiors* 67.1-2, pp. 123–136.

— (1997). "Seismic coda wave envelope in depth-dependent S wave velocity structure". In: *Physics of the Earth and Planetary Interiors* 104.1-3, pp. 15–22.

INGV Seismological Data Centre (2006). *Italian National Seismic Network*. DOI: https://doi.org/10.13127/SD/X0FXnH7QfY.

Ishimaru, Akira (1978). *Wave propagation and scattering in random media*. Vol. 2. Academic press New York.

Jing, Y, Y Zeng, and G Lin (2014). "High-frequency seismogram envelope inversion using a multiple nonisotropic scattering model: Application to aftershocks of the 2008 wells earthquake". In: *Bulletin of the Seismological Society of America* 104, pp. 823–839.

Kanu, Chinaemerem and Roel Snieder (2015). "Time-lapse imaging of a localized weak change with multiply scattered waves using numerical-based sensitivity kernel". In: *Journal of Geophysical Research: Solid Earth* 120.8, pp. 5595–5605. ISSN: 2169-9313. DOI: https://doi.org/10.1002/2015JB011871. URL: https://doi.org/10.1002/2015JB011871.

Khan, Taufiquar and Huabei Jiang (2003). "A new diffusion approximation to the radiative transfer equation for scattering media with spatially varying refractive indices". In: *Journal of Optics A: Pure and Applied Optics* 5.2, pp. 137–141. ISSN: 1464-4258. DOI: 10.1088/1464-4258/5/2/310. URL: http://dx.doi.org/10.1088/1464-4258/5/2/310.

King, N E et al. (2007). "Space geodetic observation of expansion of the San Gabriel Valley, California, aquifer system, during heavy rainfall in winter 2004 2005". In: *Journal of Geophysical Research: Solid Earth* 112.B3. DOI: 10.1029/2006JB004448. URL: https://agupubs.onlinelibrary.wiley.com/doi/abs/10.1029/2006JB004448.

Kinoshita, S (1993). "Evaluation of site factor and propagation characteristics by means of earthquake observation". In: *Zisin: Journal of the Seismological Society of Japan* 46, pp. 161–170.

Kittel, C al. (1976). *Introduction to solid state physics*. Vol. 8. New York: Wiley.

Lagendijk, A and B A Van Tiggelen (1996). "Resonant multiple scattering of light". In: *Physics Reports* 270, pp. 143–215.

Larose, Eric et al. (2006). "Observation of multiple scattering of kHz vibrations in a concrete structure and application to monitoring weak changes". In: *Physical Review E - Statistical, Nonlinear, and Soft Matter Physics*. ISSN: 15502376. DOI: 10.1103/PhysRevE.73.016609.

Larose, Eric et al. (2010). "Locating a small change in a multiple scattering environment". In: *Applied Physics Letters* 96.20, p. 204101. ISSN: 0003-6951. DOI: 10.1063/1.3431269. URL: https://doi.org/10.1063/1.3431269.

Lecocq, Thomas et al. (2017). "Monitoring ground water storage at mesoscale using seismic noise: 30 years of continuous observation and thermo-elastic and hydrological modeling". In: *Scientific Reports* 7.1, p. 14241. ISSN: 2045-2322. DOI: 10.1038/s41598-017-14468-9. URL: https://doi.org/10.1038/s41598-017-14468-9.

Lesage, Philippe, Gabriel Reyes-Dávila, and Raúl Arámbula-Mendoza (2014). "Large tectonic earthquakes induce sharp temporary decreases in seismic velocity in Volcán de Colima, Mexico". In: *Journal of Geophysical Research: Solid Earth* 119.5, pp. 4360–4376. ISSN: 2169-9313. DOI: https://doi.org/10.1002/2013JB010884. URL: https://doi.org/10.1002/2013JB010884.

Liu, Xin and Yehuda Ben-Zion (2013). "Theoretical and numerical results on effects of attenuation on correlation functions of ambient seismic noise". In: *Geophysical Journal International* 194.3, pp. 1966–1983. ISSN: 0956-540X. DOI: 10.1093/gji/ggt215. URL: https://doi.org/10.1093/gji/ggt215.

Lobkis, Oleg I and Richard L Weaver (2001). "On the emergence of the Green's function in the correlations of a diffuse field". In: *The Journal of the Acoustical Society of America* 110.6, pp. 3011–3017. ISSN: 0001-4966. DOI: 10.1121/1.1417528. URL: https://doi.org/10.1121/1.1417528.

Lux, Ivan (2018). *Monte Carlo particle transport methods*. CRC press.

Maeda, T, H Sato, and T Nishimura (2008). "Synthesis of coda wave envelopes in randomly inhomogeneous elastic media in a half-space: single scattering model including rayleigh waves". In: *Geophysical Journal International* 172, pp. 130–154.

Maeda, Takuto, Haruo Sato, and Masakazu Ohtake (2003). "Synthesis of Rayleigh-wave envelope on the spherical Earth: Analytic solution of the single isotropic-scattering model for a circular source radiation". In: *Geophysical Research Letters*. ISSN: 00948276. DOI: 10.1029/2002GL016629.

Mainsant, Guénolé et al. (2012). "Ambient seismic noise monitoring of a clay landslide: Toward failure prediction". In: *Journal of Geophysical Research: Earth Surface*. ISSN: 21699011. DOI: 10.1029/2011JF002159.

Mancinelli, N, P Shearer, and C Thomas. "On the frequency dependence and spatial coherence of pkp precursor amplitudes". In: *On the frequency dependence and spatial coherence of pkp precursor amplitudes* 121 (), pp. 1873–1889.

Mancinelli, N J and P M Shearer (2013). "Reconciling discrepancies among estimates of small-scale mantle heterogeneity from pkp precursors". In: *Geophysical Journal International* 195, pp. 1721–1729.

Mancinelli, Nicholas, Peter Shearer, and Qinya Liu (2016). "Constraints on the heterogeneity spectrum of Earth's upper mantle". In: *Journal of Geophysical Research: Solid Earth*. ISSN: 21699356. DOI: 10.1002/2015JB012641.

Mao, Shujuan et al. (2020). "On the measurement of seismic traveltime changes in the time–frequency domain with wavelet cross-spectrum analysis". In: *Geophysical Journal International* 221.1, pp. 550–568.

Margerin, L. (2003). "Multiple scattering of high-frequency seismic waves in the deep Earth: PKP precursor analysis and inversion for mantle granularity". In: *Journal of Geophysical Research*. ISSN: 0148-0227. DOI: 10.1029/2003jb002455.

Margerin, L, B Van Tiggelen, and M Campillo (2001). "Effect of absorption on energy partition of elastic waves in the seismic coda". In: *Bulletin of the Seismological Society of America* 91, pp. 624–627.

Margerin, L et al. (2016). "Sensitivity kernels for coda-wave interferometry and scattering tomography: theory and numerical evaluation in two-dimensional anisotropically scattering media". In: *Geophysical Journal International* 204, pp. 650–666.

Margerin, Ludovic (2005). "Introduction to radiative transfer of seismic waves". In: *Geophysical Monograph-American Geophysical Union* 157, p. 229.

— (2011). "Seismic Waves, Scattering". In: *Encyclopedia of Solid Earth Geophysics*. Ed. by Harsh K Gupta. Dordrecht: Springer Netherlands, pp. 1210–1223. ISBN: 978-90-481-8702-7. DOI: 10.1007/978-90-481-8702-7_54. URL: https://doi.org/10.1007/978-90-481-8702-7_54.

Margerin, Ludovic, Andres Bajaras, and Michel Campillo (2019). "A scalar radiative transfer model including the coupling between surface and body waves". In: *Geophysical Journal International* 219.2, pp. 1092–1108. ISSN: 1365246X. DOI: 10.1093/gji/ggz348. arXiv: 1907.05624.

Margerin, Ludovic, Michel Campillo, and Bart Tiggelen (1998). "Radiative transfer and diffusion of waves in a layered medium: new insight into coda Q". In: *Geophysical Journal International* 134.2, pp. 596–612. ISSN: 0956-540X. DOI: 10.1111/j.1365-246X.1998.tb07142.x. URL: https://doi.org/10.1111/j.1365-246X.1998.tb07142.x.

Margerin, Ludovic, Michel Campillo, and Bart Van Tiggelen (2000). "Monte Carlo simulation of multiple scattering of elastic waves". In: *Journal of Geophysical Research: Solid Earth* 105.B4, pp. 7873–7892.

Margerin, Ludovic and Guust Nolet (2003). "Multiple scattering of high-frequency seismic waves in the deep Earth: Modeling and numerical examples". In: *Journal of Geophysical Research: Solid Earth* 108.B5.

Mayeda, K. et al. (1992). "A comparative study of scattering, intrinsic, and coda Q-1 for Hawaii, Long Valley, and central California between 1.5 and 15.0 hz". In: *Journal of Geophysical Research*. ISSN: 01480227. DOI: 10.1029/91JB03094.

Meier, Ueli, Nikolai M Shapiro, and Florent Brenguier (2010). "Detecting seasonal variations in seismic velocities within Los Angeles basin from correlations of ambient seismic noise". In: *Geophysical Journal International* 181.2, pp. 985–996. ISSN: 0956-540X. DOI: 10.1111/j.1365-246X.2010.04550.x. URL: https://doi.org/10.1111/j.1365-246X.2010.04550.x.

Menke, William (2018). *Geophysical data analysis: Discrete inverse theory*. Academic press.

Miller, Scott and Donald Childers (2012). *Probability and random processes: With applications to signal processing and communications*. Academic Press.

Mordret, Aurélien et al. (2016). "Monitoring southwest Greenland's ice sheet melt with ambient seismic noise". In: *Science Advances*. ISSN: 23752548. DOI: 10.1126/sciadv.1501538.

Moreau, L et al. (2017). "Improving ambient noise correlation functions with an SVD-based Wiener filter". In: *Geophysical Journal International* 211.1, pp. 418–426.

Morse, P M and K U Ingard (1986). *Theoretical acoustics*. Princeton: university press.

Morse, Philip M and Richard H Bolt (1944). "Sound Waves in Rooms". In: *Reviews of Modern Physics* 16.2, pp. 69–150. DOI: 10.1103/RevModPhys.16.69. URL: https://link.aps.org/doi/10.1103/RevModPhys.16.69.

Nakahara, Hisashi et al. (1998). "Seismogram envelope inversion for the spatial distribution of high-frequency energy radiation from the earthquake fault: Application to the 1994 far east off Sanriku earthquake, Japan". In: *Journal of Geophysical Research: Solid Earth* 103.B1, pp. 855–867.

Nakata, N. and R. Snieder (2011). "Near-surface weakening in Japan after the 2011 Tohoku-Oki earthquake". In: *Geophysical Research Letters*. ISSN: 00948276. DOI: 10.1029/2011GL048800.

Nakata, Nori, Lucia Gualtieri, and Andreas Fichtner (2019). *Seismic Ambient Noise*. Cambridge: Cambridge University Press. ISBN: 9781108417082. DOI: DOI:10.1017/9781108264808. URL: https://www.cambridge.org/core/books/seismic-ambient-noise/6D9AE0CC68897330A27DB7FF

Nakata, Nori et al. (2013). "Monitoring a building using deconvolution Interferometry. I: Earthquake-data analysis". In: *Bulletin of the Seismological Society of America*. ISSN: 00371106. DOI: 10.1785/0120120291.

Nishimura, T. et al. (2000). "Temporal changes of the crustal structure associated with the M6.1 earthquake on September 3, 1998, and the volcanic activity of Mount Iwate, Japan". In: *Geophysical Research Letters*. ISSN: 00948276. DOI: 10.1029/1999GL005439.

Nof, Ran et al. (2012). "Rising of the lowest place on Earth due to Dead Sea water-level drop: Evidence from SAR interferometry and GPS". In: *Journal of Geophysical Research (Solid Earth)* 117, pp. 5412–. DOI: 10.1029/2011JB008961.

Obermann, A et al. (2013a). "Depth sensitivity of seismic coda waves to velocity perturbations in an elastic heterogeneous medium". In: *Geophysical Journal International* 194, pp. 372–382.

Obermann, A et al. (2013b). "Imaging preeruptive and coeruptive structural and mechanical changes of a volcano with ambient seismic noise". In: *Journal of Geophysical Research: Solid Earth* 118.12, pp. 6285–6294. ISSN: 21699356. DOI: 10.1002/2013JB010399.

Obermann, A et al. (2016). "Lapse-time-dependent coda-wave depth sensitivity to local velocity perturbations in 3-d heterogeneous elastic media". In: *Geophysical Journal International* 207, pp. 59–66.

Obermann, Anne et al. (2019). "4-D Imaging of Subsurface Changes with Coda Waves: Numerical Studies of 3-D Combined Sensitivity Kernels and Applications to the Mw 7.9, 2008 Wenchuan Earthquake". In: *Pure and Applied Geophysics* 176.3, pp. 1243–1254. ISSN: 14209136. DOI: 10.1007/s00024-018-2014-7.

Orecchio, B et al. (2011). "Imaging the velocity structure of the calabrian arc region (southern Italy) through the integration of different seismological data". In: *Bollettino di Geofisica Teorica ed Applicata*. ISSN: 00066729. DOI: 10.4430/bgta0023.

Paasschens, J C J (1997). "Solution of the time-dependent Boltzmann equation". In: *Physical Review E* 56.1, pp. 1135–1141. DOI: 10.1103/PhysRevE.56.1135. URL: https://link.aps.org/doi/10.1103/PhysRevE.56.1135.

Pacheco, C and R Snieder (2006). "Time-lapse traveltime change of singly scattered acoustic waves". In: *Geophysical Journal International* 165.2, pp. 485–500. ISSN: 0956540X. DOI: 10.1111/j.1365-246X.2006.02856.x.

Pacheco, Carlos and Roel Snieder (2003). *CWP-459 Localizing change with Coda Wave Interferometry: Derivation and validation of the sensitivity kernel*.

— (2005). "Time-lapse travel time change of multiply scattered acoustic waves". In: *The Journal of the Acoustical Society of America* 118.3, pp. 1300–1310. DOI: 10.1121/1.2000827. URL: https://doi.org/10.1121/1.2000827.

Papoulis, Athanasios and S Unnikrishna Pillai (2002). *Probability, random variables, and stochastic processes*. Tata McGraw-Hill Education.

Parotidis, M, E Rothert, and S A Shapiro (2003). "Pore-pressure diffusion: A possible triggering mechanism for the earthquake swarms 2000 in Vogtland/NW-Bohemia, central Europe". In: *Geophysical Research Letters* 30.20. DOI: 10.1029/2003GL018110. URL: https://agupubs.onlinelibrary.wiley.com/doi/abs/10.1029/2003GL018110.

Passarelli, Luigi et al. (2015). "Aseismic transient driving the swarm-like seismic sequence in the Pollino range, Southern Italy". In: *Geophysical Journal International* 201.3, pp. 1553–1567. ISSN: 1365-246X. DOI: 10.1093/gji/ggv111. URL: http://academic.oup.com/gji/article/201/3/1553/776740/Aseismic-transient-driving-the-swarmlike-seismic.

Paul, Anne et al. (2005). "Empirical synthesis of time-asymmetrical Green functions from the correlation of coda waves". In: *Journal of Geophysical Research: Solid Earth* 110.B8. ISSN: 0148-0227. DOI: https://doi.org/10.1029/2004JB003521. URL: https://doi.org/10.1029/2004JB003521.

Peng, Zhigang and Yehuda Ben-Zion (2006). "Temporal changes of shallow seismic velocity around the Karadere-Düzce branch of the north Anatolian fault and strong ground motion". In: *Pure and Applied Geophysics*. ISSN: 00334553. DOI: 10.1007/s00024-005-0034-6.

Peng, Zhigang and Joan Gomberg (2010). "An integrated perspective of the continuum between earthquakes and slow-slip phenomena". In: *Nature Geoscience* 3.9, pp. 599–607. ISSN: 1752-0908. DOI: 10.1038/ngeo940. URL: https://doi.org/10.1038/ngeo940.

Peraiah, Annamaneni (2002). *An Introduction to Radiative Transfer: Methods and applications in astrophysics*. Cambridge University Press.

Pinsky, Mark A (2008). *Introduction to Fourier analysis and wavelets*. Vol. 102. American Mathematical Soc.

Planès, T. et al. (2016). "Time-lapse monitoring of internal erosion in earthen dams and levees using ambient seismic noise". In: *Geotechnique*. ISSN: 17517656. DOI: 10.1680/jgeot.14.P.268.

Planès, Thomas et al. (2014). "Decorrelation and phase-shift of coda waves induced by local changes: Multiple scattering approach and numerical validation". In: *Waves in Random and Complex Media*. ISSN: 17455049. DOI: 10.1080/17455030.2014.880821.

Planes, Thomas et al. (2015). "Imaging multiple local changes in heterogeneous media with diffuse waves". In: *The Journal of the Acoustical Society of America* 137, p. 660. DOI: 10.1121/1.4906824.

Poli, Piero et al. (2020). "Seasonal and Coseismic Velocity Variation in the Region of L'Aquila From Single Station Measurements and Implications for Crustal Rheology". In: *Journal of Geophysical Research: Solid Earth* 125.7, e2019JB019316. DOI: 10.1029/2019JB019316. URL: https://agupubs.onlinelibrary.wiley.com/doi/abs/10.1029/2019JB019316.

Poupinet, G, W L Ellsworth, and J Frechet (1984). "Monitoring velocity variations in the crust using earthquake doublets: An application to the Calaveras Fault, California". In: *Journal of Geophysical Research: Solid Earth* 89.B7, pp. 5719–5731. DOI: 10.1029/JB089iB07p05719. URL: https://agupubs.onlinelibrary.wiley.com/doi/abs/10.1029/JB089iB07p05719.

Poupinet, G, J.-L. Got, and F Brenguier (2008). *Earth Heterogeneity and Scattering Effects on Seismic Waves*. Vol. 50. of **Advances in Geophysics**.

Prieto, Germán A and Gregory C Beroza (2008). "Earthquake ground motion prediction using the ambient seismic field". In: *Geophysical Research Letters* 35.14, pp. 1–5. ISSN: 00948276. DOI: 10.1029/2008GL034428.

Prieto, German A et al. (2010). "Impulse response of civil structures from ambient noise analysis". In: *Bulletin of the Seismological Society of America* 100.5 A, pp. 2322–2328. ISSN: 00371106. DOI: 10.1785/0120090285.

Przybilla, J, M Korn, and U Wegler (2006). "Radiative transfer of elastic waves versus finite difference simulations in two-dimensional random media". In: *Journal of Geophysical Research: Solid Earth* 111.4, pp. 1–13. ISSN: 21699356. DOI: 10.1029/2005JB003952.

Przybilla, J, U Wegler, and M Korn (2009). "Estimation of crustal scattering parameters with elastic radiative transfer theory". In: *Geophysical Journal International* 178, pp. 1105–1111.

Przybilla, Jens and Michael Korn (2008). "Monte Carlo simulation of radiative energy transfer in continuous elastic random media-three-component envelopes and numerical validation". In: *Geophysical Journal International*. ISSN: 0956540X. DOI: 10.1111/j.1365-246X.2008.03747.x.

Ratdomopurbo, Antonius and Georges Poupinet (1995). "Monitoring a temporal change of seismic velocity in a volcano: Application to the 1992 eruption of Mt. Merapi (Indonesia)". In: *Geophysical Research Letters* 22.7, pp. 775–778. DOI: https://doi.org/10.1029/95GL00302. URL: https://agupubs.onlinelibrary.wiley.com/doi/abs/10.1029/95GL00302.

Rivet, Diane, Florent Brenguier, and Frédéric Cappa (2015). "Improved detection of preeruptive seismic velocity drops at the Piton de La Fournaise volcano". In: *Geophysical Research Letters* 42.15, pp. 6332–6339. DOI: 10.1002/2015GL064835. URL: https://agupubs.onlinelibrary.wiley.com/doi/abs/10.1002/2015GL064835.

Roepstorff, Gert (2012). *Path integral approach to quantum physics: an introduction*. Springer Science and Business Media.

Ross, Sheldon M (2014). *Introduction to probability models*. Academic press.

Roux, Philippe et al. (2005a). "Ambient noise cross correlation in free space: Theoretical approach". In: *The Journal of the Acoustical Society of America* 117.1, pp. 79–84. ISSN: 0001-4966. DOI: 10.1121/1.1830673. URL: https://doi.org/10.1121/1.1830673.

Roux, Philippe et al. (2005b). "P-waves from cross-correlation of seismic noise". In: *Geophysical Research Letters*. ISSN: 00948276. DOI: 10.1029/2005GL023803.

Ryzhik, Leonid, George Papanicolaou, and Joseph B Keller (1996). "Transport equations for elastic and other waves in random media". In: *Wave Motion* 24.4, pp. 327–370. ISSN: 0165-2125. DOI: https://doi.org/10.1016/S0165-2125(96)00021-2. URL: http://www.sciencedirect.com/science/article/pii/S0165212596000212.

Sanborn, C J, V F Cormier, and M Fitzpatrick (2017). "Combined effects of deterministic and statistical structure on high-frequency regional seismograms". In: *Geophysical Journal International* 210, pp. 1143–1159.

Sanborn, Christopher J. and Vernon F. Cormier (2018). "Modelling the blockage of Lg waves from three-dimensional variations in crustal structure". In: *Geophysical Journal International*. ISSN: 1365246X. DOI: 10.1093/gji/ggy206.

Sato, H and K Emoto (2018). "Synthesis of a scalar wavelet intensity propagating through von kármán-type random media: Radiative transfer theory using the born and phase-screen approximations". In: *Geophysical Journal International* 215, pp. 909–923.

Sato, Haruo (1977). "Energy propagation including scattering effects single isotropic scattering approximation". In: *Journal of Physics of the Earth*. ISSN: 00223743. DOI: 10.4294/jpe1952.25.27.

— (1988). "Temporal change in scattering and attenuation associated with the earthquake occurrence—A review of recent studies on coda waves". In: *pure and applied geophysics* 126.2, pp. 465–497.

Sato, Haruo (1993). "Energy Transportation In One- and Two-Dimensional Scattering Media: Analytic Solutions of the Multiple Isotropic Scattering Model: Energy transportation in one- and two-dimensional scattering media". In: *Geophysical Journal International*. ISSN: 1365246X. DOI: 10.1111/j.1365-246X.1993.tb01443.x.

— (1994a). "Formulation of the multiple non-isotropic scattering process in 2-D space on the basis of energy-transport theory". In: *Geophysical Journal International* 117.3, pp. 727–732. ISSN: 0956-540X. DOI: 10.1111/j.1365-246X.1994.tb02465.x. URL: https://doi.org/10.1111/j.1365-246X.1994.tb02465.x.

— (1994b). "Multiple Isotropic Scattering Model Including P-S Conversions For the Seismogram Envelope Formation". In: *Geophysical Journal International*. ISSN: 1365246X. DOI: 10.1111/j.1365-246X.1994.tb03946.x.

— (1995). "Formulation of the multiple non-isotropic scattering process in 3-D space on the basis of energy transport theory". In: *Geophysical Journal International*. ISSN: 1365246X. DOI: 10.1111/j.1365-246X.1995.tb05730.x.

Sato, Haruo and Michael C Fehler (2012). *Seismic Wave Propagation and Scattering in the Heterogeneous Earth*. Springer Berlin Heidelberg. ISBN: 9783540896227.

Sato, Haruo, Hisashi Nakahara, and Masakazu Ohtake (1997). "Synthesis of scattered energy density for nonspherical radiation from a point shear-dislocation source based on the radiative transfer theory". In: *Physics of the Earth and Planetary Interiors*. ISSN: 00319201. DOI: 10.1016/S0031-9201(97)00050-2.

Sato, Haruo and Makiko Nohechi (2001). "Envelope formation of long-period Rayleigh waves in vertical component seismograms: Single isotropic scattering model". In: *Journal of Geophysical Research: Solid Earth*. ISSN: 21699356. DOI: 10.1029/2000jb900383.

Schaff, David P and Gregory C Beroza (2004). "Coseismic and postseismic velocity changes measured by repeating earthquakes". In: *Journal of Geophysical Research: Solid Earth* 109.B10. DOI: https://doi.org/10.1029/2004JB003011. URL: https://agupubs.onlinelibrary.wiley.com/doi/abs/10.1029/2004JB003011.

Sciences, Planetary, Keiiti Aki, and Bernard Chouet (1975). "Origin of coda waves: Source, attenuation, and scattering effects". In: *Journal of Geophysical Research* 80.23, pp. 3322–3342. ISSN: 01480227. DOI: 10.1029/JB080i023p03322. URL: http://doi.wiley.com/10.1029/JB080i023p03322.

Sens-Schönfelder, C and U Wegler (2006). "Passive image interferometry and seasonal variations of seismic velocities at Merapi Volcano, Indonesia". In: *Geophysical Research Letters* 33.21. DOI: 10.1029/2006GL027797. URL: https://agupubs.onlinelibrary.wiley.com/doi/abs/10.1029/2006GL027797.

Sens-Schönfelder, Christoph and Tom Eulenfeld (2019). "Probing the in situ Elastic Nonlinearity of Rocks with Earth Tides and Seismic Noise". In: *Physical Review Letters* 122.13, p. 138501. DOI: 10.1103/PhysRevLett.122.138501. URL: https://link.aps.org/doi/10.1103/PhysRevLett.122.138501.

Sens-Schönfelder, Christoph and Eric Larose (2008). "Temporal changes in the lunar soil from correlation of diffuse vibrations". In: *Physical Review E - Statistical, Nonlinear, and Soft Matter Physics*. ISSN: 15393755. DOI: 10.1103/PhysRevE.78.045601.

Sens–Schönfelder, C, L Margerin, and M Campillo (2009). "Laterally heterogeneous scattering explains Lg blockage in the Pyrenees". In: *JGR* 114.

Seydoux, Léonard, Julien de Rosny, and Nikolai M Shapiro (2017). "Pre-processing ambient noise cross-correlations with equalizing the covariance matrix eigenspectrum". In: *Geophysical Journal International* 210.3, pp. 1432–1449. ISSN: 1365246X. DOI: 10.1093/gji/ggx250.

SHANG, TIELIANG and LONGSHENG GAO (1988). "TRANSPORTATION THEORY OF MULTIPLE SCATTERING AND ITS APPLICATION TO SEISMIC CODA WAVES OF

IMPULSE SOURCE". In: *Science in China Series B-Chemistry, Biological, Agricultural, Medical and Earth Sciences* 31.12, pp. 1503–1514. ISSN: 0253-5823. DOI: https://doi.org/10.1360/yb1988-31-12-1503. URL: https://engine.scichina.com/doi/10.1360/yb1988-31-12-1503.

Shapiro, N M and M Campillo (2004). "Emergence of broadband Rayleigh waves from correlations of the ambient seismic noise". In: *Geophysical Research Letters* 31.7. DOI: 10.1029/2004GL019491. URL: https://agupubs.onlinelibrary.wiley.com/doi/abs/10.1029/2004GL019491.

Shapiro, Nikolai et al. (2000). "The Energy Partitioning and the Diffusive Character of the Seismic Coda". In: *Bulletin of The Seismological Society of America - BULL SEISMOL SOC AMER* 90, pp. 655–665. DOI: 10.1785/0119990021.

Shearer, P and P Earle (2004). "The global short-period wavefield modelled with a Monte Carlo seismic phonon method". In: *Geophysical Journal International* 158, pp. 1103–1117.

Sheng, P (2006). *Introduction to wave scattering, localization and mesoscopic phenomena*. Vol. 88. Science and Business Media: Springer.

Sheng, Ping and Bart van Tiggelen (2007). *Introduction to Wave Scattering, Localization and Mesoscopic Phenomena*.

Silverii, Francesca et al. (2016). "Transient deformation of karst aquifers due to seasonal and multiyear groundwater variations observed by GPS in southern Apennines (Italy)". In: *Journal of Geophysical Research: Solid Earth* 121.11, pp. 8315–8337. DOI: 10.1002/2016JB013361. URL: https://agupubs.onlinelibrary.wiley.com/doi/abs/10.1002/2016JB013361.

Snieder, R (1986). "3-D linearized scattering of surface waves and a formalism for surface wave holography". In: *Geophysical Journal International* 84, pp. 581–605.

Snieder, Roel (1999). "Imaging and Averaging in Complex Media BT - Diffuse Waves in Complex Media". In: ed. by Jean-Pierre Fouque. Dordrecht: Springer Netherlands, pp. 405–454. ISBN: 978-94-011-4572-5. DOI: 10.1007/978-94-011-4572-5_14. URL: https://doi.org/10.1007/978-94-011-4572-5_14.

— (2004). "Extracting the Green's function from the correlation of coda waves: A derivation based on stationary phase". In: DOI: 10.1103/PhysRevE.69.046610.

— (2006). "The Theory of Coda Wave Interferometry". In: *pure and applied geophysics* 163.2, pp. 455–473. ISSN: 1420-9136. DOI: 10.1007/s00024-005-0026-6. URL: https://doi.org/10.1007/s00024-005-0026-6.

Snieder, Roel and Jeannot Trampert (1999). "Inverse problems in geophysics". In: *Wavefield inversion*. Springer, pp. 119–190.

Snieder, Roel et al. (2002). "Coda Wave Interferometry for Estimating Nonlinear Behavior in Seismic Velocity". In: *Science (New York, N.Y.)* 295, pp. 2253–2255. DOI: 10.1126/science.1070015.

Stehly, L et al. (2008). "Reconstructing Green's function by correlation of the coda of the correlation (C3) of ambient seismic noise". In: *Journal of Geophysical Research: Solid Earth* 113.B11. ISSN: 0148-0227. DOI: https://doi.org/10.1029/2008JB005693. URL: https://doi.org/10.1029/2008JB005693.

Stein, Seth and Michael Wysession (2009). *An introduction to seismology, earthquakes, and earth structure*. John Wiley and Sons.

Takeuchi, N et al. (2017). "Determination of intrinsic attenuation in the oceanic lithosphere-asthenosphere system". In: *Science* 358, pp. 1593–1596.

Tarantola, Albert (2005). *Inverse problem theory and methods for model parameter estimation*. SIAM.

Trégourès, N P and B A Van Tiggelen (2002). "Quasi-two-dimensional transfer of elastic waves". In: *Physical Review E* 66.

Tsai, Victor C (2011). "A model for seasonal changes in GPS positions and seismic wave speeds due to thermoelastic and hydrologic variations". In: *Journal of Geophysical Research: Solid Earth* 116.B4. DOI: 10.1029/2010JB008156. URL: https://agupubs.onlinelibrary.wiley.com/doi/abs/10.1029/2010JB008156.

Turner, J A and R L Weaver (1994). "Radiative transfer of ultrasound". In: *The Journal of the Acoustical Society of America* 96, pp. 3654–3674.

Wang, Qing Yu et al. (2017). "Seasonal Crustal Seismic Velocity Changes Throughout Japan". In: *Journal of Geophysical Research: Solid Earth* 122.10, pp. 7987–8002. ISSN: 21699356. DOI: 10.1002/2017JB014307.

Wang, Qing Yu et al. (2019). "Evidence of Changes of Seismic Properties in the Entire Crust Beneath Japan After the Mw 9.0, 2011 Tohoku-oki Earthquake". In: *Journal of Geophysical Research: Solid Earth*. ISSN: 21699356. DOI: 10.1029/2019JB017803.

Wapenaar, Kees (2004). "Retrieving the Elastodynamic Green's Function of an Arbitrary Inhomogeneous Medium by Cross Correlation". In: *Physical Review Letters* 93.25, p. 254301. DOI: 10.1103/PhysRevLett.93.254301. URL: https://link.aps.org/doi/10.1103/PhysRevLett.93.254301.

Watson, Karen M, Yehuda Bock, and David T Sandwell (2002). "Satellite interferometric observations of displacements associated with seasonal groundwater in the Los Angeles basin". In: *Journal of Geophysical Research: Solid Earth* 107.B4, ETG 8–1–ETG 8–15. DOI: 10.1029/2001JB000470. URL: https://agupubs.onlinelibrary.wiley.com/doi/abs/10.1029/2001JB000470.

Weaver, Richard L (1982). "On diffuse waves in solid media". In: *The Journal of the Acoustical Society of America* 71.6, pp. 1608–1609. ISSN: 0001-4966. DOI: 10.1121/1.387816. URL: https://doi.org/10.1121/1.387816.

— (1990). "Diffusivity of ultrasound in polycrystals". In: *Journal of the Mechanics and Physics of Solids* 38.1, pp. 55–86.

Weaver, Richard L and Oleg I Lobkis (2004). "Diffuse fields in open systems and the emergence of the Green's function (L)". In: *The Journal of the Acoustical Society of America* 116.5, pp. 2731–2734. ISSN: 0001-4966. DOI: 10.1121/1.1810232. URL: https://doi.org/10.1121/1.1810232.

Wegler, U and C Sens-Schönfelder (2007). "Fault zone monitoring with passive image interferometry". In: *Geophysical Journal International* 168.3, pp. 1029–1033. ISSN: 0956-540X. DOI: 10.1111/j.1365-246X.2006.03284.x. URL: https://doi.org/10.1111/j.1365-246X.2006.03284.x.

Wegler, U. et al. (2009). "Sudden drop of seismic velocity after the 2004 Mw 6.6 mid-Niigata earthquake, Japan, observed with Passive Image Interferometry B06305". In: *Journal of Geophysical Research: Solid Earth*. ISSN: 21699356. DOI: 10.1029/2008JB005869.

Wegler, Uli et al. (2006). "Increase of shear wave velocity before the 1998 eruption of Merapi volcano (Indonesia)". In: *Geophysical Research Letters*. ISSN: 00948276. DOI: 10.1029/2006GL025928.

Welch, Ashley J, Martin J C Van Gemert, and Others (2011). *Optical-thermal response of laser-irradiated tissue*. Vol. 2. Springer.

Wu, Chunquan et al. (2016). "Constraining depth range of S wave velocity decrease after large earthquakes near Parkfield, California". In: *Geophysical Research Letters*. ISSN: 19448007. DOI: 10.1002/2016GL069145.

Wu, Ru Shan and Keiiti Aki (1988). "Multiple scattering and energy transfer of seismic waves-Separation of scattering effect from intrinsic attenuation II. Application of the theory to Hindu Kush region". In: *Pure and Applied Geophysics PAGEOPH*. ISSN: 00334553. DOI: 10.1007/BF01772590.

Wu, Ru-Shan -S (1985). "Multiple scattering and energy transfer of seismic waves – separation of scattering effect from intrinsic attenuation – I. Theoretical modelling". In: *Geophysical Journal of the Royal Astronomical Society*. ISSN: 1365246X. DOI: 10.1111/j.1365-246X.1985.tb05128.x.

Yamamoto, M and H Sato (2010). "Multiple scattering and mode conversion revealed by an active seismic experiment at asama volcano, japan". In: *Journal of Geophysical Research: Solid Earth* 115.

Yoshimoto, K (2000). "Monte Carlo simulation of seismogram envelopes in scattering media". In: *Journal of Geophysical Research* 105, pp. 6153–6161.

Yuehua Zeng (1993). "Theory of scattered P- and S-wave energy in a random isotropic scattering medium". In: *Bulletin - Seismological Society of America*.

Yuehua Zeng, Feng Su, and K. Aki (1991). "Scattering wave energy propagation in a random isotropic scattering medium: 1. Theory". In: *Journal of Geophysical Research*. ISSN: 01480227. DOI: 10.1029/90jb02012.

Zeng, Y (2006). "Scattered surface wave energy in the seismic coda". In: *Pure and Applied Geophysics* 163, pp. 533–548.

Zhao, Li, Thomas H. Jordan, and Chris H. Chapman (2000). "Three-dimensional Frechet differential kernels for seismic delay times". In: *Geophysical Journal International*. ISSN: 0956540X. DOI: 10.1046/j.1365-246X.2000.00085.x.